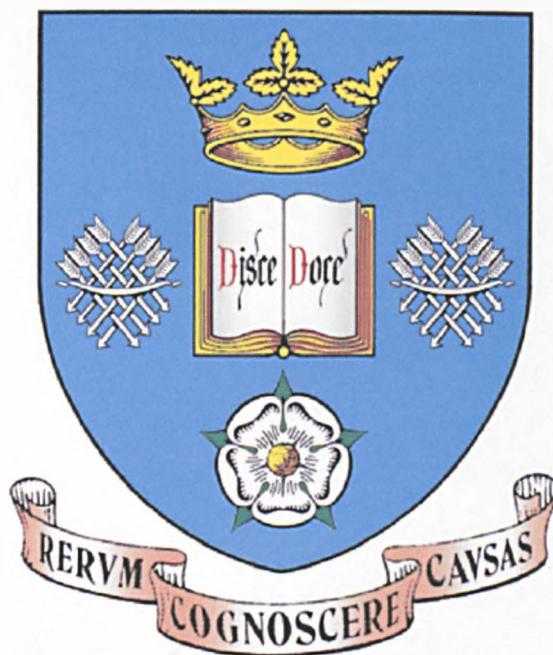


---

# Optical Studies of Three Dimensional Confinement in Photonic and Electronic Systems

Ali Mohammad Ahmad Adawi



Thesis presented for the degree of PhD

Department of Physics and Astronomy

University of Sheffield

June 2002

---

# Optical Studies of Three Dimensional Confinement in Photonic and Electronic Systems

Ali Mohammad Ahmad Adawi

## Abstract

In the first part of this thesis the optical properties of three dimensional opal photonic crystals are investigated. The samples were grown by sedimentation of silica spheres into a face centred cubic structure. Structural studies show that self assembled opal photonic crystals are polycrystalline materials consisting of misoriented domains of size 50  $\mu\text{m}$  to 100  $\mu\text{m}$ . The angle dependent transmission technique is used to characterise the stop band of the samples. Due to the weak refractive index contrast in opal photonic crystals, only stop bands along the [111] direction are observed. The experimental transmission spectra are compared with theoretical transmission spectra calculated according to a three dimensional model based on the transfer matrix method. The experimental stop band is found to be six times broader than the calculated one, and also the experimental Bragg attenuation length is found to be five to seven times larger than the calculated one. Angle resolved diffraction and scattering techniques are used to investigate the origin of the discrepancies between experiment and theory. Analysis of the diffraction spectra indicate that the samples consist of misoriented domains of thickness 10  $\mu\text{m}$  with a Gaussian distribution of 10° FWHM around the [111] direction. The scattering spectra show a strong resonant enhancement at the centre or edges (depending on the refractive index contrast) of the stop band. This observation is attributed to the multiple incoherent backward/forward reflections between the sample domains. By analysing the balance of photon flux originating from a slab of opal the shape of the experimental transmission stop band is fully explained.

To investigate the effect of an incomplete photonic structure on the emission properties of light sources located inside the photonic crystal, the samples were infiltrated with solutions of laser dyes having fluorescence bands which overlap with the photonic gap of the host crystal. The optical fluorescence spectra reveal a stop band region with a centre varying with angle according to Bragg's law. It is found that the fluorescence stop band is much shallower and narrower than that observed in

---

transmission spectra. The gap narrowing in the fluorescence spectra is attributed to the scattering events inside the opal taking into account the spectral dependence of the Bragg attenuation length.

High refractive index contrast opal photonic crystals are achieved by infiltration with chalcogenide glasses ( $\text{As}_2\text{S}_3$  and  $\text{AsSe}$ ) by precipitation from solution. Optical imaging of the samples after infiltration shows that chalcogenide glasses tend to aggregate into submillimeter areas inside opals. Spatially resolved reflectivity spectroscopy is used to characterise the infiltrated areas. Large shifts (up to 80 nm) in the position of the stop band has been achieved from the infiltrated samples in comparison to the samples before infiltration.

In the second part of this thesis, mid-infrared (2.5  $\mu\text{m}$ -25  $\mu\text{m}$ ) intersubband transitions in the conduction band of uncoupled and vertically coupled and also in the valence band of self assembled  $\text{In}(\text{Ga})\text{As}/\text{GaAs}$  quantum dots are investigated using direct absorption measurements and photocurrent spectroscopy. The investigated dots show three dimensional electronic confinement. Intersubband transitions are investigated as a function of the polarisation angle of the incident radiation, external electric field and temperature. The experimental results indicate that intersubband transitions in the conduction band of the uncoupled dots are allowed for radiation polarised in the growth direction, similar to that found for quantum wells. By strongly coupling quantum dots in the growth direction (10 Å GaAs barrier between the dots) we have achieved a reversal of the intersubband selection rule for optical transitions between conduction band states, compared with that observed for uncoupled dots. We find that for strongly coupled dots the dominant absorption occurs for light polarised perpendicular to the growth direction (*s*-polarised), consistent with eight-band strain dependent  $\mathbf{k}\cdot\mathbf{p}$  calculations. This contrasting behaviour results from the very different composition of the basis wave functions in the conduction band states for coupled and uncoupled dots due to differences in the conduction-valence band mixing. This effect enhances the oscillator strength of transitions between the ground and excited states in the conduction band for coupled dots. The results from p-type samples show that intersubband transitions in the valence band of self assembled quantum dots are strongly polarised perpendicular to the growth direction (*s* polarised). The results are attributed to the anisotropy of the hole subbands and also to the strong band mixing

---

between the valence subbands. The results suggest the suitability of strongly coupled self assembled quantum dots and p-type quantum dots for high efficiency normal incidence infrared photodetectors.

---

To my parents.

---

## Acknowledgements

First of all I would like to thank my supervisor Professor Maurice Skolnick, without whom this work would not have been possible. I would like to thank Maurice for giving me the opportunity to work within his group, also I would like to thank him for all the effort he made to make my return to Sheffield to complete my study possible. Also I would like to thank Maurice for the unlimited support which he gave me throughout my time in Sheffield. I would also like to thank Dr Vasily Astratov, Dr John Cockburn, Dr Aristide Lemaitre, Dr Luke Wilson, and Dr Evgeny Zibik for their guidance, advice, help and useful discussions throughout this work. My thanks have to go to Dr Andrew Reynolds for allowing me to use his code (translight) to calculate the transmission and reflection spectra presented in this thesis, Professor John Pendry and Dr David Whittaker for their help in interpreting the scattering puzzle, and also to Weidong Sheng and Dr Jean Leburton for providing me by their eight band  $k_p$  calculations. Thank you to Dr David Mowbray and Dr John Finley for very useful discussions and help especially with the equipment, and to Dr Mark Hopkinson, Dr Mathew Steer and Dr Geoff Hill for the dot samples. Thanks to Dr David Lidzey for allowing me to use his optical microscope. I would also like to thank Dr Mark Fox, Dr Dmitry Revin, Dr Raphael Butte, Dr Paul Fry, Dr Alexander Tratakovskii, Dr Adamo Monte and Dr Wenhui Fan for their support.

My great thanks to my fellow PhD students, Ian Sellers, Alan Bristow, Damian Carder, Kris Groom, Mohammad Emam-Ismail (he got his PhD), Ruth Oulton, Yago Olaizola, Adam Ashmore, Richard Green, Agoney Garcia-Deniz, and Richard White for their help and support especially during my writing. In addition, I would like to thank Ian for reading my thesis and correcting my English.

My great thanks to University of Sheffield (Ward Lewis Fee Waiver Award) for funding my study.

On a personal level, I would like to thank all my friends here in Sheffield for making my life throughout the last three years enjoyable. Very especial thank has to go to Mufied and Amna for their support (and of course the coffee, I can not forget that).

Finally, and most importantly, thank you to my mother and father for every thing they have done to me since I came to this life, also my brothers Ahmad, Mahmoud, Sa'id, A'bed Al-fatah, Hussain, A'laa Al-dean, A'dawi and my sisters Layla, Ahlam, and of course the little one *Lolo*.

---

## Publications

1. Interplay of Order and Disorder in the Optical Properties of Opal Photonic Crystals, V.N.Astratov, A.M.Adawi, S.Fricker, M.S.Skolnick, D.M.Whittaker, and P.N.Pusey, Accepted for publication in Phys. Rev. B.
2. Opal photonic Crystals Infiltrated with Chalcogenide Glasses, V. N. Astratov, A. M. Adawi, M. S. Skolnick, V. K. Tikhomirov, V. Lyubin, D. G. Lidzey, M. Ariu and A. L. Reynolds, Appl. Phys. Lett. **78**, 4094 (2001).
3. Inversion of the Intersublevel Optical Selection Rule in Strongly Coupled InGaAs/GaAs Self Assembled Quantum Dots, A. M. Adawi, E. A. Zibik, L. R. Wilson, A. Lemaitre, W. D. Sheng, J. W. Cockburn, M. S. Skolnick, J. P. Leburton, M. J. Steer, M. Hopkinson, G. Hill, S. L. Liew, and A. G. Cullis, Proceeding of the 26<sup>th</sup> International Conference on the Physics of Semiconductors (ICPS), Edinburgh 2002.
4. Observation of In-plane Polarized Intersubband Absorption in Strongly Coupled InGaAs/GaAs Self Assembled Quantum Dots, A. M. Adawi, E. A. Zibik, L. R. Wilson, A. Lemaitre, W. D. Sheng, J. W. Cockburn, M. S. Skolnick, J. P. Leburton, M. J. Steer, M. Hopkinson, G. Hill, S. L. Liew, and A. G. Cullis, to be submitted to Applied Physics Letters.
5. Temperature Dependence of Intersubband Photocurrent in InAs/GaAs Self Assembled Quantum Dots, A. M. Adawi, E. A. Zibik, L. R. Wilson, A. Lemaitre, J. W. Cockburn, M. S. Skolnick, M. Hopkinson and G. Hill, to be submitted to Applied Physics Letters.
6. Enhancement of In-Plane Polarized Absorption by Strongly Coupling InGaAs/GaAs Quantum Dots, A.M.Adawi, E.A.Zibik, L.R.Wilson, A.Lemaitre, M.S.Skolnick, J.W.Cockburn, W.D.Sheng, J.P.Leburton, M.J.Steer, M.Hopkinson and G.Hill, to be published in Physica Status Solidi as a part of the proceeding of the 2<sup>nd</sup> international conference on semiconductor quantum dots Japan 2002.

---

# Contents

<b>Chapter 1 Introduction and Outline of Thesis</b>	<b>1</b>
<b>1.1 Motivation</b>	<b>1</b>
1.1.1 Three Dimensional Confinement in Photonic Systems: Photonic Crystals	1
1.1.2 Three Dimensional Confinement in Electronic Systems: Quantum Dots	4
<b>1.2 References</b>	<b>7</b>
<b>Chapter 2 Characterisation of Three Dimensional Self Assembled Opal Photonic Crystals</b>	<b>8</b>
<b>2.1 Introduction</b>	<b>8</b>
<b>2.2 Theory</b>	<b>11</b>
2.2.1 Electromagnetic Waves in a Periodic Structure	11
2.2.2 Properties of the Master Equation	13
2.2.3 Solution of the Master Equation	14
2.2.4 Band Structure of Opal Photonic Crystals	18
<b>2.3 Fabrication of Photonic Crystals</b>	<b>19</b>
2.3.1 Hole Drilling	19
2.3.2 Layer by Layer Fabrication	20
2.3.3 Self Assembled Photonic Crystals	21
<b>2.4 Calculation Approach</b>	<b>23</b>
<b>2.5 Experimental Setup</b>	<b>23</b>
<b>2.6 Samples</b>	<b>25</b>
<b>2.7 Structural Properties of Self Assembled Opals</b>	<b>25</b>
<b>2.8 Optical Properties of Opal Photonic Crystals</b>	<b>30</b>
2.8.1 Dependence of the Stop Band on the Refractive Index Contrast	33
2.8.2 Angular Dependence of the Stop Band	38

2.8.3	Thickness Dependence of the Stop Band	42
2.9	Conclusions	46
2.10	References	48
<b>Chapter 3 Diffraction and Scattering of Light in Self Assembled</b>		
<b>Opals</b>		
		<b>50</b>
3.1	Introduction	50
3.2	Review of the Transmission Spectra	53
3.3	Experimental Details	57
3.3.1	Diffraction Measurement Setup	57
3.3.2	Scattering Measurement Setup	57
3.4	Diffraction Results	59
3.4.1	Results in Ethanol	59
3.4.2	Results in Cyclohexane	65
3.4.3	Interpretation of the Broadening Effect in the Transmission Spectra	67
3.4.3	Ethanol Case	67
3.4.3.2	Cyclohexane Case	70
3.5	Scattering Results	72
3.5.1	Scattering in the Regime of Weak Bragg Attenuation Length	72
3.5.2	Interpretation of the Scattering Results in Ethanol	78
3.5.3	Scattering in the Regime of Strong Bragg Attenuation Length	82
3.5.4	The Spatial Pattern of the Scattered Light in the Regime of Strong Bragg	
	Attenuation Length	86
3.6	Conclusions	90
3.7	References	92

<b>Chapter 4 Self Assembled Opal Photonic Crystals Infiltrated with Fluorescent Materials and Chalcogenide Glasses</b>	<b>93</b>
<b>4.1 Introduction</b>	<b>93</b>
<b>4.2 Experimental Details</b>	<b>95</b>
4.2.1 Fluorescence Measurement Setup	95
4.2.2 Spatial Resolved Reflectivity Spectroscopy of Infiltrated Opals	96
<b>4.3 Opal Infiltrated with Fluorescence Materials</b>	<b>97</b>
<b>4.4 Opal Infiltrated with Chalcogenide Glasses</b>	<b>105</b>
4.4.1 Sample Characteristics	105
4.4.2 Results of Infiltration of Opals with Chalcogenide Glasses	110
<b>4.5 Conclusions</b>	<b>118</b>
<b>4.6 References</b>	<b>119</b>
<b>Chapter 5 Intersubband Spectroscopy of In(Ga)As/GaAs Self Assembled Quantum Dots</b>	<b>121</b>
<b>5.1 Introduction</b>	<b>121</b>
<b>5.2 Growth of Self Assembled Quantum Dots</b>	<b>124</b>
<b>5.3 Theory</b>	<b>126</b>
5.3.1 Electronics of Quantum Dots	126
5.3.1.1 Strain in Self Assembled Quantum Dots	126
5.3.1.2 Effect of the Strain on the Band Structure of Quantum Dots	129
5.3.1.3 Energy Levels in Quantum Dots	131
<b>5.4 Optical Transitions in Quantum Dots</b>	<b>134</b>
<b>5.5 Experimental Methods</b>	<b>145</b>
5.5.1 FTIR Spectroscopy	145
5.5.2 Direct Absorption Measurements	149

---

5.5.3 Photocurrent Measurements	151
<b>5.6 Samples</b>	<b>153</b>
<b>5.7 Results</b>	<b>155</b>
5.7.1 Intersubband Transitions in the Conduction Band of Quantum Dots	155
5.7.1.1 Photoluminescence	157
5.7.1.2 Direct Absorption	159
5.7.1.3 Photocurrent	162
5.7.2 Intersubband Transitions in the Valence Band of Quantum Dots	174
5.7.3 Intersubband Absorption in Strongly Coupled Quantum Dots	182
<b>5.8 Conclusions</b>	<b>195</b>
<b>5.9 References</b>	<b>197</b>
<b>Chapter 6 Future Work</b>	<b>200</b>

# Chapter 1

## Introduction and Outline of Thesis

### 1.1 Motivation

Over the last decade there has been considerable worldwide effort to develop new physical structures to confine photons or electrons in all directions. The structures used to confine photons in three dimensions are called three dimensional photonic crystals, while the structures used to confine electrons in three dimensions are called quantum dots. These two systems are of great interest, both for the physical understanding of fundamental phenomena such as the interaction of light with matter, and for the development of novel optoelectronic devices such as low threshold lasers. The experimental work presented in this thesis is devoted towards investigating the three dimensional confinement in such systems. Due to the broad scope of this thesis, the detailed structure, experimental procedure, and theoretical information of the investigated systems will not be presented in this introduction. Instead they will be presented in the relevant experimental chapter.

#### 1.1.1 Three Dimensional Confinement in Photonic Systems: Photonic Crystals

Confining light in three dimensions requires a structure (photonic crystal) with three dimensional variations in refractive index on the scale of the order of the wavelength of light. Much like electronic states in an electronic crystal, photonic states inside a photonic crystal are classified into bands and gaps, frequency ranges over which photons are allowed or forbidden, respectively, to propagate. If the refractive index contrast of the photonic crystal is high enough ( $\approx 2.8$ ) propagation of photons will be prevented in all directions within a certain range of frequencies (the so-called

complete photonic band gap). Essentially the photonic crystal alters the density of the available states for photons within a certain range of frequencies. Within the bands photons behave like free particles. However, within the gaps there are no available states for photons to exist. The drastic change in the density of states between bands and gaps opens the door to confine photons within a volume of the order of a cubic wavelength<sup>1</sup>. Creating a point defect<sup>1</sup> in the periodic structure of the photonic crystal may be used to trap light at a point within a three dimensional photonic crystal. Also light can be guided<sup>1</sup> from one location to another by creating a line defect in the periodic structure of the crystal.

In chapters 2, 3 and 4 the studies of the optical properties of three dimensional self assembled opal photonic crystals are presented, motivated by the potential of using this type of photonic crystal to control light in the visible region. The samples were grown by sedimentation of silica spheres into a face centre cubic structure (fcc) under gravity.

In chapter 2 structural and optical properties of opal photonic crystals are investigated. The structural studies showed that self assembled opals are polycrystalline materials consisting of misoriented domains of size 50  $\mu\text{m}$ -100  $\mu\text{m}$ . The angle dependent transmission technique was used to characterise the stop band of the samples in different liquids. Due to the weak refractive index contrast in self assembled opals only stop gaps along the [111] direction were observed, indicating that self assembled opals behave essentially like one dimensional photonic crystals. The experimental transmission spectra were compared with theoretical transmission spectra. The theoretical transmission spectra were calculated according to a three dimensional model based on the transfer matrix method<sup>2</sup>. The experimental stop band

is found to be six times broader than the theoretical one, and also the experimental Bragg attenuation length is found to be five to seven times larger than the calculated one.

To understand the discrepancies between experiment and theory, diffraction and scattering measurements were performed in all directions around the sample. The results of the diffraction and scattering measurements are discussed in detail in chapter 3. The experimental results revealed that the diffracted and scattered light play an important role in the understanding of the spectral form of the transmission stop band. The diffraction measurements indicated that the opals under study consist of misoriented domains with a Gaussian distribution of  $10^\circ$  FWHM around the [111] direction. Also the measurements indicated that the thickness of the domains is about  $10\ \mu\text{m}$ . The scattering spectra revealed that due to the polycrystalline nature of self assembled opals, spectral enhancement at the centre or edges (depending on the refractive index contrast) of the stop band is possible. Such phenomena are of interest for emission and laser applications.

The effect of opal stop gap(s) on the emission properties of laser dyes were investigated. The results are presented in chapter 4. The experimental results showed that propagation of light generated inside opal photonic crystals is strongly controlled by the structural disorder of the material.

The three dimensional confinement in as-grown opals can be improved by infiltrating opals with high refractive index materials<sup>3</sup>. High refractive index chalcogenide glasses ( $n \sim 2.5\text{-}3.6$ ) were used to infiltrate the pore system of opals in order to enhance the confinement in opals. Another motivation for using chalcogenide glasses

is that chalcogenide glasses have a strong photorefractive effect ( $\Delta n$  up to 0.2 easily achievable) which make them of high interest for developing tunable band gap photonic crystals. In addition chalcogenide glasses have a large optical nonlinearity index (nonlinear index  $n_2 \sim 10^{-14} \text{ cm}^2/\text{W}$ ) which makes them suitable for optical switching applications. The results of the infiltration of opals with chalcogenide glasses will be presented in chapter 4.

### 1.1.2 Three Dimensional Confinement in Electronic Systems: Quantum Dots

The band structure of any semiconductor consists of two main bands; the valence band and the conduction band. Carriers in each band (electrons in the conduction band and holes in the valence band) behave like free particles in each band with density of states proportional to square root of their energy. The density of states in each band can be altered by confining the carrier motion to the order of the carrier de Broglie wavelength in one direction or more<sup>4</sup>. Experimentally carriers can be confined in one dimension by making a sandwich of a thin layer of low band gap material such as GaAs between two thick layers of high band gap material such as AlGaAs. Such structures are called quantum wells. The same idea can be used to confine carriers in three dimensions by burying low band gap material in high band gap material. Experimentally this can be achieved by epitaxially growing two semiconductors whose lattice constants are different on the top of each other (InAs/GaAs). In this method the second material initially grows as strained planar layers (called wetting layers) until it reaches a critical thickness ( $\sim 2\text{ML}$ ). After reaching the critical thickness, it becomes energetically favorable for the strain to relax forming three dimensional islands (dots). To complete the confinement another layer of the first material should be grown on top of the dots. Structures like this are called self assembled quantum dots (SAQDs). Three dimensional confinement in the dots quantizes the available energy states for the carriers in the conduction band and

valence band, and thereby the density of states is altered to atomic like delta function. The atomic like density of states in quantum dots makes them of high interest for the development of novel optoelectronic devices such as low threshold quantum dot lasers<sup>5</sup>, optical memory systems<sup>6</sup> and large area quantum dot infrared photodetectors<sup>7</sup>.

In chapter 5 the results of intersubband absorption and photocurrent spectroscopy from In(Ga)As/GaAs quantum dots are presented. The motivation of using intersubband spectroscopy to investigate the three dimensional confinement in In(Ga)As/GaAs quantum dots is that electron and hole transitions can be studied independently. The confinement potential for electrons in the conduction band is different from the confinement potential for the holes in the valence band, and also the effective mass of the electron is different from the effective mass of the hole. Thus the effect of the three dimensional confinement on the electrons is different from the effect of the three dimensional confinement on the holes. The valence band is much more complicated than the conduction band due to the anisotropy of the hole subbands and the strong band mixing between the valence subbands.

The results of intersubband spectroscopy from the conduction band of isolated quantum dots showed that intersubband transitions in the conduction band are polarised in the growth direction indicating that electrons in the conduction band behave essentially like particles confined in one dimension. By coupling dots in the vertical direction the confinement potential in the conduction band can be changed, and thus in-plane absorption can be improved. The results of intersubband absorption measurements from two strongly coupled InGaAs dots showed a strong enhancement in the in-plane absorption due to the dot coupling in the vertical direction. These

results are of significant importance for development of normal incidence infrared photodetectors.

The results of intersubband spectroscopy from the valence band of SAQDs indicated that intersubband transitions in the valence band are strongly polarised in the dot plane. The results are attributed to the anisotropy of the hole subbands and also to the strong band mixing between the valence subbands.

## 1.2 References

- 
- <sup>1</sup> - J. Joannopoulos, P. Villeneuve and S. Fan, *Nature* **386**,143 (1997).
  - <sup>2</sup> - J. B. Pendry and A. Mackinnon, *Phys. Rev. Lett.* **69**, 2772 (1992), and A. Reynolds, F. Lopez-Tejeira, D. Cassagne, F. J. Garcia-Vidal, C. Joanin, and J. Sanchez-Daheza, *Phys. Rev.B* **60**, 11422 (1999).
  - <sup>3</sup> - K. Busch and S. John, *Phys. Rev. E* **58**, 3896 (1998).
  - <sup>4</sup> - D. Bimberg, M. Grundmann, and N. N. Ledentsov, *Quantum Dot Heterostructures*, John Wiley and Sons (1998).
  - <sup>5</sup> - Y. Arakawa and S. Sakaki, *Appl. Phys. Lett.* **40**, 939 (1982).
  - <sup>6</sup> - G. Yusa and H. Sakaki, *Appl. Phys. Lett.* **70**, 345 (1997).
  - <sup>7</sup> - S. Tang, S. Lin and S. Lee, *Appl. Phys. Lett.* **78**, 2428 (2001).

## Chapter 2

# Characterisation of Three Dimensional Self Assembled Opal Photonic Crystals

### 2.1 Introduction

It is well known that if an x-ray is incident on the planes of an electronic crystal with an angle  $\phi$ , the reflection of the x-ray from the planes of the crystal will appear for a specific wavelength  $\lambda$  and an angle  $\phi$ , given by Bragg's law  $2d\cos(\phi) = m\lambda$ , where  $d$  is the distance between the planes and  $m$  is an integer number related to the order of the Bragg reflections. The concept of Bragg reflection applies equally well to visible radiation, except that such phenomena do not occur in electronic crystals as a result of the very small size of the crystal lattice constant. Therefore Yablonovitch<sup>1</sup> suggested fabricating material with periodic refractive index structure on the scale of the wavelength of light, in order to control the propagation of light. This structure can be designed from dielectric materials in one, two or three dimensions and is called a photonic crystal (see Figure 2-1). If the photonic crystal is highly ordered, reflections from the many lattice planes interfere constructively, and the Bragg reflection will be very strong. The photonic crystal also can be designed in such a way to reflect light within a certain range of wavelengths in all directions. In such a case the photonic crystal has a complete photonic band gap.

This special property of a photonic crystal does not arise just because the light can not penetrate through the surface, but also because the light generated inside photonic crystal can not propagate out. There are no electromagnetic states available inside the

material. Material with this property can be used to control spontaneous emission, which leads to possibilities for more efficient light emitters like thresholdless lasers and single-mode light-emitting diodes.

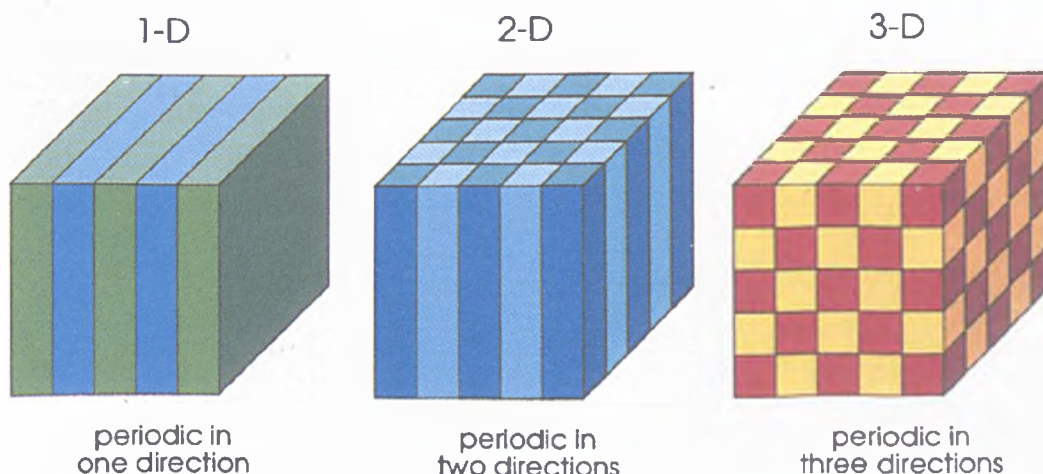


**Figure 2-1 Periodic photonic structures in one dimension, two dimensions and three dimensions. (Reference 2)**

However, the fabrication of photonic crystals suitable for visible or ultraviolet light still remains a challenge, because of the difficulty of realising periodic dielectric structures with a submicrometer lattice constant. Three main methods are used to fabricate photonic crystals: hole drilling<sup>3,4</sup>, layer by layer fabrication<sup>5</sup>, and self-assembly<sup>6,7</sup>. Among these methods, self-assembling is highly promising for the fabrication of photonic crystals for the visible and ultraviolet region. At the same time the system of interconnected pores in the self assembling photonic crystal can be easily infiltrated with active/nonlinear materials for nonlinear or optical switching applications<sup>8,9</sup>, or to use as a template to fabricate an inverted opal<sup>10</sup> which is expected to have a complete photonic band gap if the refractive index of the infiltrated material is more than 2.8. However, the final quality of these novel devices depends strongly on the initial ordering quality of the self-assembling photonic crystal.

In this chapter the structural and optical properties of self-assembled opal photonic crystals will be investigated. First a brief theoretical introduction to the concept of photonic crystals and the propagation of light in a periodic structure will be given. The three main methods (hole drilling, layer by layer fabrication, and self-assembly) used to fabricate three dimensional photonic crystal will be discussed. The structural properties of the samples are investigated using Optical Microscope Imaging and Scanning Electron Microscope (SEM). The angle dependent transmission technique used to study the optical properties of the samples will be presented. The optical properties of self-assembled opals have been studied as a function of the pore refractive index, angle of incidence and sample thickness. The experimental spectra are compared with three dimensional calculations for a perfectly ordered fcc photonic crystal using the transfer matrix methods<sup>11,12</sup>. The comparison between the measured and calculated spectra indicates that the optical properties of self-assembled opals are strongly controlled by the disorder in the material.

## 2.2 Theory

In this section an introduction to the theory of photonic crystals will be given. Subjects such as propagation of electromagnetic waves in a periodic structure, the band structure of photonic crystals, the concept of complete band gap and the conditions which are required to achieve it will be discussed.

### 2.2.1 Electromagnetic Waves in a Periodic Structure

The equations that govern all macroscopic electromagnetism, including the propagation of light in a periodic structure (photonic crystal), are the four macroscopic Maxwell equations<sup>13,2</sup>. They are

$$\begin{aligned}
 \nabla \cdot \mathbf{B}(\mathbf{r}, t) &= 0 \\
 \nabla \times \mathbf{E}(\mathbf{r}, t) + \frac{\partial \mathbf{B}(\mathbf{r}, t)}{\partial t} &= 0 \\
 \nabla \cdot \mathbf{D}(\mathbf{r}, t) &= \rho \\
 \nabla \times \mathbf{H}(\mathbf{r}, t) - \frac{\partial \mathbf{D}(\mathbf{r}, t)}{\partial t} &= \mathbf{J}
 \end{aligned} \tag{2.1}$$

where  $\mathbf{E}$  and  $\mathbf{H}$  are the macroscopic electric and magnetic fields,  $\mathbf{D}$  and  $\mathbf{B}$  are the displacement and magnetic induction fields,  $\rho$  and  $\mathbf{J}$  are the free charges and currents. Consider the structure of the photonic crystal fabricated from linear, lossless, nonmagnetic dielectrics. Assuming that there are no free charges or current sources, and the dielectric constant ( $\epsilon$ ) is frequency independent, the relations between  $\mathbf{E}$  and  $\mathbf{D}$ ,  $\mathbf{B}$  and  $\mathbf{H}$  are given by<sup>2</sup>

$$\begin{aligned}
 \mathbf{D}(\mathbf{r}) &= \epsilon_0 \epsilon(\mathbf{r}) \mathbf{E}(\mathbf{r}) \\
 \mathbf{B}(\mathbf{r}) &= \mu_0 \mathbf{H}(\mathbf{r})
 \end{aligned} \tag{2.2}$$

With all of these assumptions in place, Maxwell equations read<sup>2</sup>

$$\begin{aligned}
 \nabla \cdot \mathbf{H}(\mathbf{r}, t) &= 0 \\
 \nabla \times \mathbf{E}(\mathbf{r}, t) + \mu_0 \frac{\partial \mathbf{H}(\mathbf{r}, t)}{\partial t} &= 0 \\
 \nabla \cdot \epsilon(\mathbf{r}) \mathbf{E}(\mathbf{r}, t) &= 0 \\
 \nabla \times \mathbf{H}(\mathbf{r}, t) - \epsilon_0 \epsilon(\mathbf{r}) \frac{\partial \mathbf{E}(\mathbf{r}, t)}{\partial t} &= 0
 \end{aligned} \tag{2.3}$$

For fields varying as  $\exp(-i\omega t)$  Maxwell equations become<sup>2</sup>

$$\nabla \cdot \epsilon_0 \epsilon(\mathbf{r}) \mathbf{E}(\mathbf{r}) = 0 \quad (2.4a)$$

$$\nabla \cdot \mathbf{H}(\mathbf{r}) = 0 \quad (2.4b)$$

$$\nabla \times \mathbf{E}(\mathbf{r}) - i\omega \mu_0 \mathbf{H}(\mathbf{r}) = 0 \quad (2.4c)$$

$$\nabla \times \mathbf{H}(\mathbf{r}) + i\omega \epsilon_0 \epsilon(\mathbf{r}) \mathbf{E}(\mathbf{r}) = 0 \quad (2.4d)$$

One can decouple these equations by dividing equation (2.4d) by  $\epsilon_0 \epsilon(\mathbf{r})$  and then take the curl. Then use equation (2.4c) to eliminate  $\mathbf{E}(\mathbf{r})$  to get

$$\nabla \times \left( \frac{1}{\epsilon(\mathbf{r})} \nabla \times \mathbf{H}(\mathbf{r}) \right) = \frac{\omega^2}{c^2} \mathbf{H}(\mathbf{r}) \quad (2.5)$$

Equation (2.5) is often termed the master equation for the propagation of photons<sup>2</sup> and it is equivalent to the Schrodinger equation for electrons. From equations (2.4b) and (2.5),  $\mathbf{H}(\mathbf{r})$  can be determined. Once we know  $\mathbf{H}(\mathbf{r})$  we can obtain  $\mathbf{E}(\mathbf{r})$  and  $\mathbf{D}(\mathbf{r})$  from equation (2.4d) via

$$\mathbf{E}(\mathbf{r}) = \left( \frac{i}{\omega \epsilon_0 \epsilon(\mathbf{r})} \nabla \times \mathbf{H}(\mathbf{r}) \right) \quad (2.6)$$

### 2.2.2 Properties of the Master Equation

The master equation has the following properties<sup>2</sup>

1. It is an eigenvalue problem. Therefore, we can rewrite the master equation as

$$\Theta \mathbf{H}(\mathbf{r}) = \frac{\omega^2}{c^2} \mathbf{H}(\mathbf{r}) \quad (2.7)$$

where  $\Theta$  is a differential operator,  $\mathbf{H}(\mathbf{r})$  is the eigenfunction and  $\frac{\omega^2}{c^2}$  is the eigenvalue.

2. The operator  $\Theta$  is linear and hermitian and therefore the eigenvalues are real.
3. Scale invariance

Maxwell's equations for macroscopic media have no fundamental length scale, and consequently neither does the master equation. Suppose we know the solution for the dielectric function  $\varepsilon(\mathbf{r})$ . Then for a dielectric function  $\varepsilon'(\mathbf{r}) = \varepsilon\left(\frac{\mathbf{r}}{s}\right)$ , the master equation is

$$\nabla_x \left( \frac{1}{\varepsilon\left(\frac{\mathbf{r}}{s}\right)} \nabla_x \mathbf{H}'(\mathbf{r}) \right) = \frac{\omega'^2}{c^2} \mathbf{H}'(\mathbf{r}) \quad (2.8)$$

But if  $\mathbf{H}_n(\mathbf{r})$  are the solutions of the original equation with frequencies  $\omega_n$ , then the solutions of equation (2.8) are  $\mathbf{H}'_n(\mathbf{r}) = \mathbf{H}_n\left(\frac{\mathbf{r}}{s}\right)$  with  $\omega'_n = \frac{\omega_n}{s}$ . The solution of the master equation at one scale determines the solutions at all other length scales.

### 2.2.3 Solution of the Master Equation

There is an interesting analogy between electron waves in a natural crystal and light waves in a three-dimensional photonic crystal. Both should be described by the band theory. The concepts of reciprocal space, Brillouin zone, dispersion relation, Bloch functions, etc., can also be applied to optical waves<sup>3</sup>. Yablonovitch<sup>1</sup> and John<sup>14</sup> independently proposed the face centred cubic (fcc) as the best candidate to fabricate photonic crystals, since this structure has the most spherical Brillouin zone. The solution of the master equation is given by Bloch functions  $\mathbf{H}_k(\mathbf{r}) = \mathbf{u}_k(\mathbf{r})e^{i\mathbf{k}\cdot\mathbf{r}}$ , where  $\mathbf{u}_k(\mathbf{r})$  is a periodic function on the lattice. Several methods have been applied to solve the master equation in an fcc photonic structure such as the plane-wave method<sup>15</sup> and the Korringa-Kohn-Rostoker method<sup>16</sup>. Figure 2-2a<sup>16</sup> shows the dispersion relation between the wave vector  $\mathbf{k}$  and the frequency  $\omega$  for a photonic crystal of identical spheres of dielectric constant  $\epsilon_s = 1$  and radius  $R_s$  embedded in a background dielectric with  $\epsilon_b = 9$ . The filling fraction of the spheres is  $f = 74\%$ . The periodic variation of the dielectric constant causes splitting (band gap) at the edges of the Brillouin zone. To understand the origin of the photonic band gap we will discuss it in the case of one dimensional photonic crystals which can be generalized to the 2D and 3D PC. In the discussion we will concentrate on the first two bands in the band structure as in Figure 2-3a. In the bands (away from the edges  $k = \frac{\pi}{a}$ , where  $a$  is the lattice constant of the crystal) the modes behave as plane waves ( $e^{ikx}$ ) see Figure 2-3a. Towards the edges of the bands ( $k = \frac{\pi}{a}$ ) the modes become standing waves ( $\cos(\frac{\pi x}{a})$  or  $\sin(\frac{\pi x}{a})$ ). The  $\cos(\frac{\pi x}{a})$  standing waves have nodes centred in each low refractive index dielectric layer as in Figure 2-3b, while the  $\sin(\frac{\pi x}{a})$  standing waves have nodes centred in each high

refractive index dielectric layer as in Figure 2-3c. From the electromagnetic variational theorem<sup>2</sup> the low-frequency modes concentrate their energy in the high dielectric (refractive index) regions, and the high-frequency modes concentrate their energy in the low dielectric (refractive index) regions as in Figure 2-3d and e respectively, opening a gap between band 1 and band 2. Waves with frequencies within the gaps are Bragg reflected and can not propagate through the crystal.

Theoretical<sup>15,16</sup> calculations for 3D fcc photonic crystals also indicate that a full band gap will open between the 8th and 9th bands if the refractive index contrast  $= \max\left(\frac{n_s}{n_b}, \frac{n_b}{n_s}\right) \geq 2.8$ , where  $n_s$  is the refractive index of the spheres and  $n_b$  is the refractive index of the background. A low filling fraction of the high refractive index material ( $f \sim 20\%$ ) is required in order to enhance interference, and the optical path lengths in the low index material and the high index material should be equal. Therefore, a low filling fraction of the high index material is favorable. Figure 2-2b<sup>16</sup> illustrates the relation between the relative band gap width and the refractive index contrast for several values of the filling fraction. The relative width of the gap decreases monotonically as the refractive index contrast decreases.

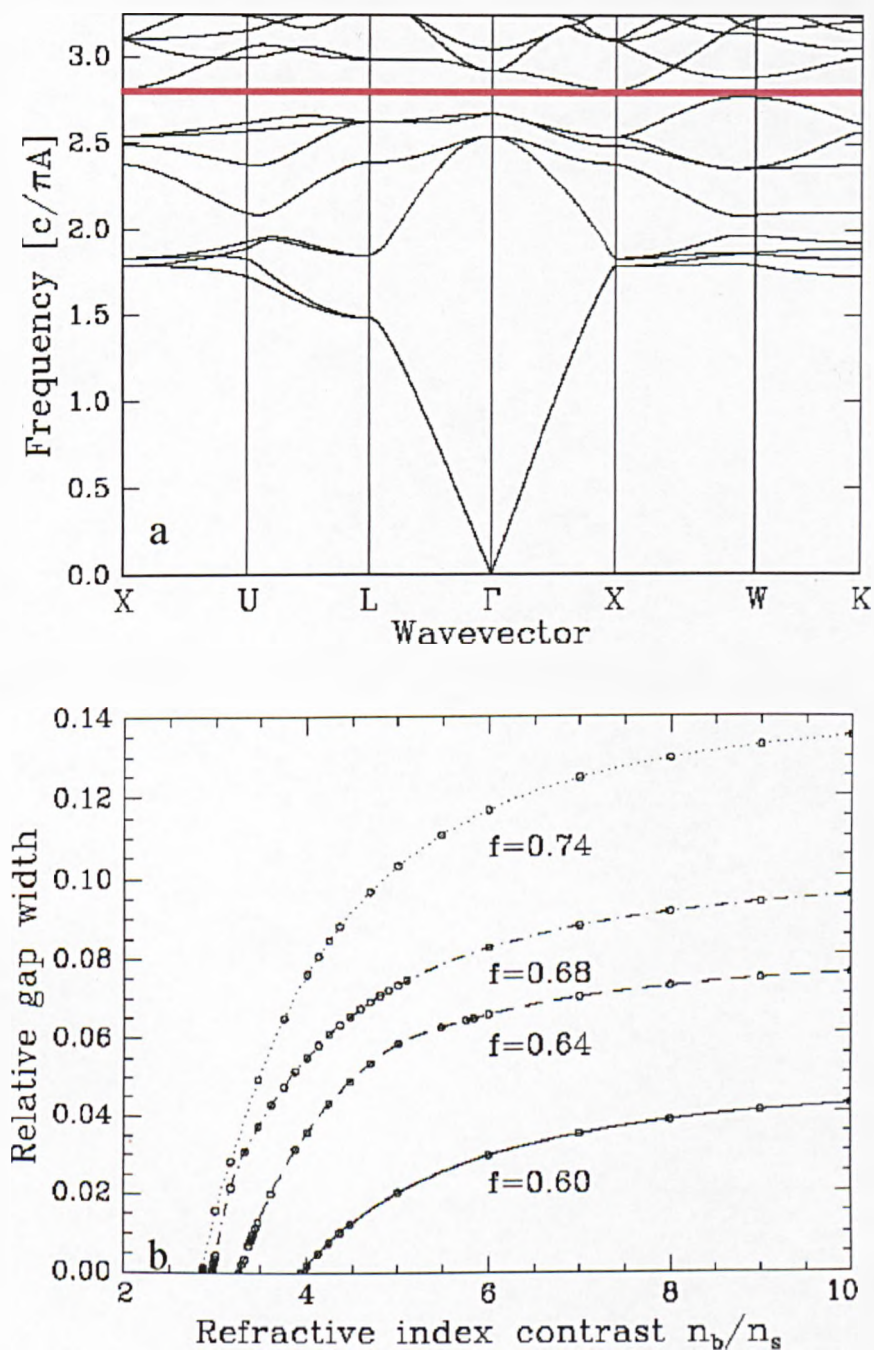
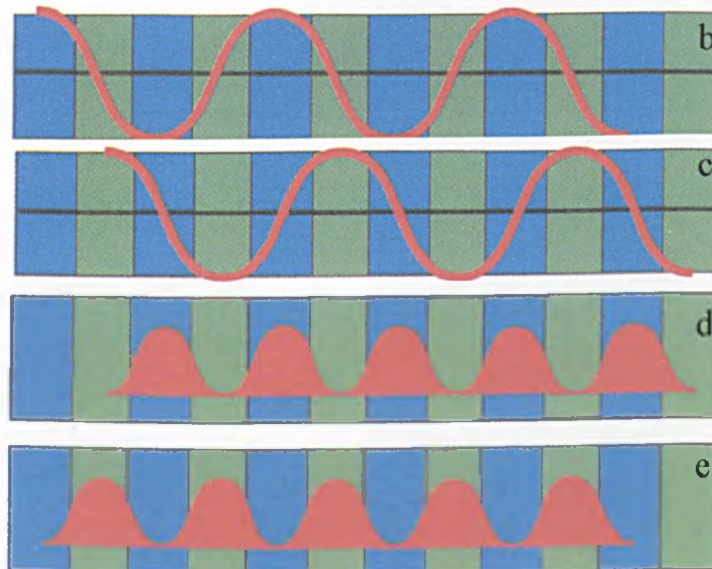
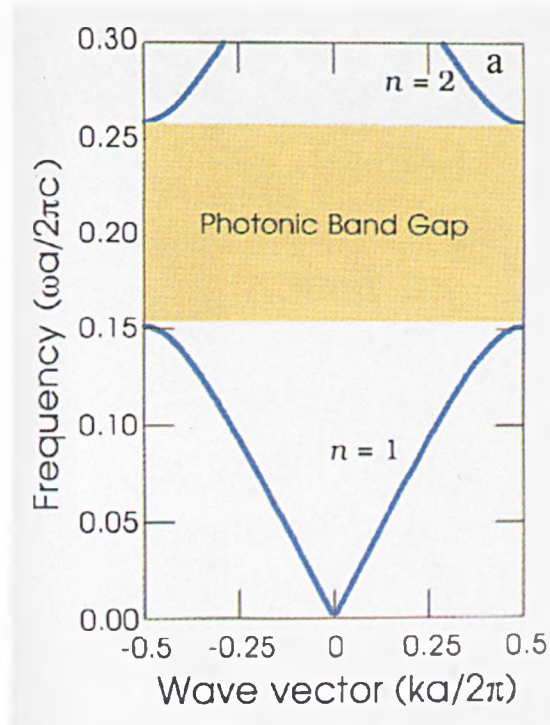


Figure 2-2 (a) The photonic band structure for a closed-packed fcc lattice of air spheres in a background of  $\epsilon_b=9$ . (b) The relative band gap width as a function of the refractive index contrast for different filling fractions. (a and b are from reference16).



**Figure 2-3 (a) Schematic presentation of the band gap in 1D PC (b) electric field of band 1 (c) electric Field of band 2 (d) local energy of band 1 (e) local energy of band 2 at the edge of the Brillouin zone. In b, c, d and e blue represents high refractive index material and green represents low refractive index material. (Reference 2).**

### 2.2.4 Band Structure of Opal Photonic Crystals

The opal photonic crystal is a three-dimensional self-ordered system of  $\text{SiO}_2$  spheres in an fcc structure. The periodicity of the opal crystal is comparable to the wavelength of light in the visible region. The refractive index contrast between silica spheres and air is weak (1.5:1). Therefore bare opal exhibits no complete gaps. Figure 2-4<sup>17</sup> shows the band structure of an opal crystal. Only stop gaps along particular directions occur, especially at the L point ([111] direction) of the Brillouin zone. The relative width of the first stop gap at the L point is 5.7%. As we move from the L point to the X point ([100] direction) the stop band shifts to higher frequencies (shorter wavelengths) and becomes narrower as can be seen in Figure 2-4.

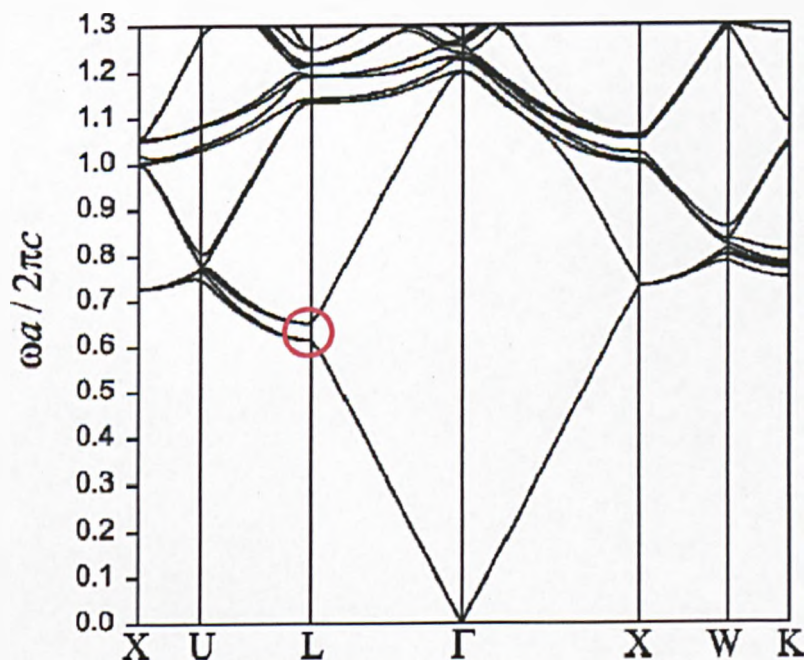


**Figure 2-4** The band structure of bare opal photonic crystal (refractive index contrast =1.5). (Reference 17).

### 2.3 Fabrication of Photonic Crystals

The design and fabrication of photonic crystals is a very difficult challenge, because the lattice dimensions must be of the order of the wavelength of the incident light. It is a real technological problem, and several ways have been investigated in order to synthesise a photonic crystal with a full photonic band gap. The three main routes used to fabricate photonic crystal are hole drilling<sup>3,4</sup>, layer by layer fabrication<sup>5</sup>, and self-assembly<sup>6,7</sup> will be summarised in this section.

#### 2.3.1 Hole Drilling

This structure is known as Yablonovite, after its inventor<sup>3</sup>. It was the first photonic crystal fabricated, and measured, which gave a complete photonic band gap. This structure has been fabricated from a slab of material of refractive index 3.6 and is covered by a mask consisting of a triangular array of holes. Each hole is drilled through three times at an angle  $35.26^\circ$  away from the normal and spread out by  $120^\circ$  on the azimuth, Figure 2-5. The resulting criss-cross of holes below the surface of the slab produces a full 3-D periodic fcc structure. The resulting structure has a 17% band gap in the microwave region. To scale down the band gap to the visible region the drilling can be done by reactive ion etching, for a material which has a refractive index of 3.6 in the visible region such as Si, GaAs or Chalcogenide glasses. Zavieh and Mayer<sup>4</sup> have used nonselective dry etching and selective wet etching to fabricate a simple cubic photonic crystal from multilayer of GaAs/Al<sub>0.6</sub>Ga<sub>0.4</sub>As. The angular transmission measurements indicated a complete photonic band gap between 10  $\mu\text{m}$  and 14  $\mu\text{m}$  with 10 dB depth. Recently an elegant approach to fabricate three dimensional photonic crystal in the visible region is proposed by Campbell *et al*<sup>18</sup> using a four laser holographic method to create a three dimensional interference pattern in a block of photoresistance. The high intensity regions in the interference pattern render the photoresist, allowing the 3D periodic structure to be formed.

Because the refractive index of the photoresistance is low ( $n \sim 1.6$ ), this structure does not exhibit complete band gap. However, this structure can be used as a template to form an inverted structure, which is expected to have a complete band gap. The holographic technique has the advantage of speed since the entire pattern in the photoresist is created in nanoseconds. Also, a variety of crystal structures can be created by varying the orientation and polarisation of the four laser beams. However, it remains to be tested to what degree ideal defect-free structures can be experimentally realized, how absorption of the laser beams affects uniformity in thickness, and how intentional defects and waveguides could be incorporated in the structure.

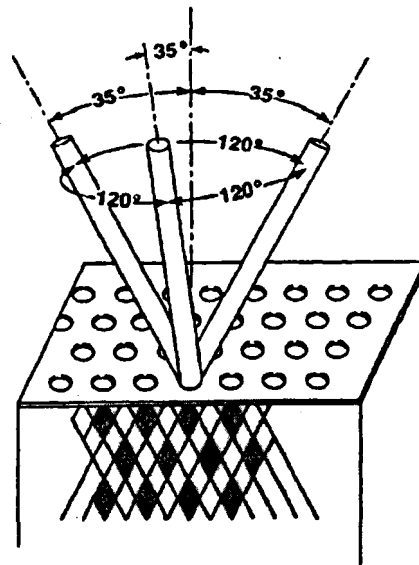


**Figure 2-5 Schematic presentation of hole drilling method (reference 3).**

### 2.3.2 Layer by Layer Fabrication

The principle of this method is illustrated in Figure 2-6. It consists of layers of one-dimensional rods with a stacking sequence that repeats itself every four layers. Within each layer the axes of the rods are parallel to each other. The orientations of the axes are rotated by  $90^\circ$  between adjacent layers. To obtain an fcc structure, the third layer

is shifted by half a period with respect to the first one, and also the fourth layer with respect to the second. Defects can be easily introduced in this type of structure by removing a section (or rod) of the dielectric material<sup>19</sup>. Several materials such as Si<sup>5</sup>, GaAs<sup>20</sup>, InP<sup>20</sup> and Chalcogenide glasses<sup>21</sup> have been used to fabricate layer by layer photonic crystals with a complete photonic band gap. The process of producing these crystals utilises techniques such as selective etching and wafer bonding. Nada *et al*<sup>20</sup> have fabricated four layers and eight layers GaAs or InP photonic crystal with complete photonic band gap around 1.2  $\mu\text{m}$ .

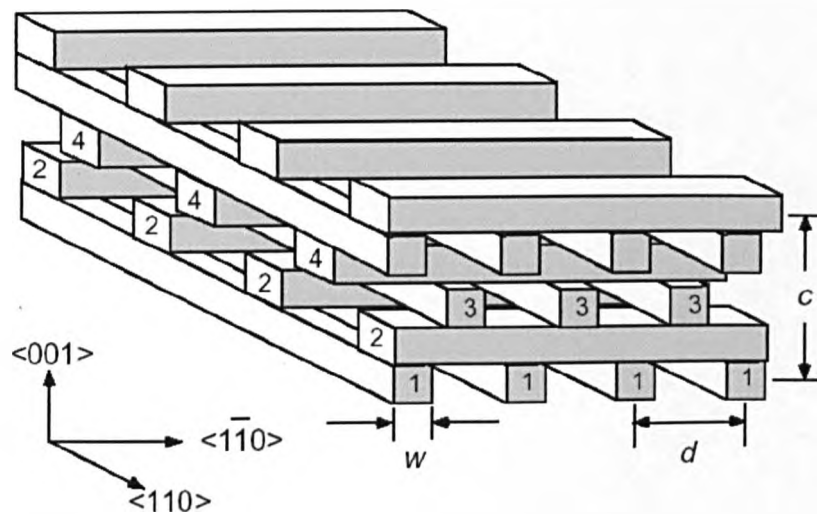


**Figure 2-6 Scheme of layer by layer photonic crystal (Reference 5)**

### 2.3.3 Self Assembled Photonic Crystals

Self-assembled colloidal particles provide a good candidate for the fabrication of 3-D photonic crystals in the visible and ultraviolet regions. They have been synthesised from a wide variety of materials, as monodispersed spheres having precisely controlled diameters in the range of a few nanometers to a few hundred micrometers. Polystyrene spheres<sup>22</sup> and silica particles<sup>6,7</sup> are examples of the materials which can be used to fabricate colloidal crystals. Several methods have been used to crystallize colloidal particles into highly ordered 3-D lattices such as sedimentation growth under gravity<sup>6,7</sup>, and self-assembled by electrophoretic deposition<sup>23</sup>.

Self assembled photonic crystals have advantages and disadvantages in comparison with the other methods. The technology of self assembled crystals allows crystal plates of very large size  $\sim 5 \text{ cm}^3$  to be obtained. It is easy to fill the pores with high refractive index materials or active/nonlinear materials such as dyes, liquid crystals or Chalcogenide glasses. They can be used as a template to fabricate inverse opal structures that are expected to have a complete photonic band gap. The main disadvantages of the self assembled crystals are that the refractive index contrast is not large enough to give a complete band gap, and they possess a large concentration of defects due to the uncertainty in the diameter of the spheres and the stacking faults. As a result of these defects the stop band of the self assembled crystal is much broader and weaker in comparison with the theoretical calculations.

Recently, two new methods<sup>24,25</sup> have been used to grow self assembled crystals. In the first method<sup>24</sup> a vertical silicon substrate has been used. The silica particles are forced into an ordered arrangement on the surface of the substrate as the meniscus is swept downwards by evaporation of the solvent. This method is very efficient in growing crystals from spheres of a diameter less than  $0.4 \mu\text{m}$ . Vlasov *et al*<sup>24</sup> managed to grow crystals from spheres of diameter greater than  $0.8 \mu\text{m}$ , through adding a temperature gradient to the sol to minimize sedimentation and to provide a continuous flow of particles toward the meniscus region. In the second method<sup>25</sup> a lithographically patterned silicon substrate has been utilised to grow colloidal crystals in the [100] direction instead of the conventional [111] growth direction. By using these two methods the stacking faults are reduced from 20% to 1% and the point defect concentration is reduced by a factor of 10 in comparison with the other methods.

## 2.4 Calculation Approach

To compare our experimental results with theoretical calculations, we have used the publically available Translight code<sup>9,12,17</sup> to model the transmission of light through a perfectly periodic fcc lattice. This code was developed by A. L. Reynolds as a part of his PhD thesis<sup>12</sup>. The calculations in this code are based on three dimensional modeling of the propagation of light through an fcc lattice of spheres using the transfer matrix method (TMM), which originally was introduced by J. B. Pendry and A. Mackinnon<sup>11</sup>. The code allows us to calculate transmission and/or reflection spectra along the [111] direction of an fcc photonic crystal as a function of the slab thickness, and refractive index of the pores. Also transmission or reflection spectra can be calculated as a function of the angle of incidence with respect to the [111] direction. This type of calculation is complex and requires a very long time to perform. The typical time to calculate one transmission and reflection spectrum consisting of 80 frequency points in the spectrum for a slab of thickness 1536 layers (this number of layers is equivalent to 300  $\mu\text{m}$ ) is 9 hours.

## 2.5 Experimental Setup

In this part of the work, a transmission technique has been used to characterise the samples. The experimental setup used to study the transmission spectra of the samples along the [111] direction (normal incidence) and in oblique incidence, is shown in Figure 2-7a. The sample was illuminated by collimated white light from a 24 V, 150 W tungsten lamp. The divergence of the collimated incident beam was less than  $2^\circ$ . The transmitted light through the sample was collected using a flexible fiber directed toward the propagation direction. The fiber was coupled to a spectrometer (40 $\text{\AA}$ /mm resolution) plus photomultiplier (PMT) combination using a 5 cm Achromatic doublet lens. To measure the zero-order transmission beam only, a pinhole of diameter 600  $\mu\text{m}$  was placed immediately after the sample. To reduce incoherent scattering on the

sample surfaces, and from crystal defects, the sample was immersed in liquids such as ethanol or cyclohexane throughout the measurements. A high optical quality cuvette is used for this propose. To measure the transmission spectra as a function of the external angle of incidence  $\theta$  with respect to the [111] direction, the sample was mounted on a rotation stage. Illuminating the sample along the [111] direction is not a straightforward task, since the (111) plane may not be exactly parallel to the surface of the sample. To determine the [111] direction precisely, we used the Bragg reflection pattern (which can be seen by eye) as a criteria, simply by rotating the sample to centre the Bragg reflection spot with the optical axis, as can be seen in Figure 2-7b.

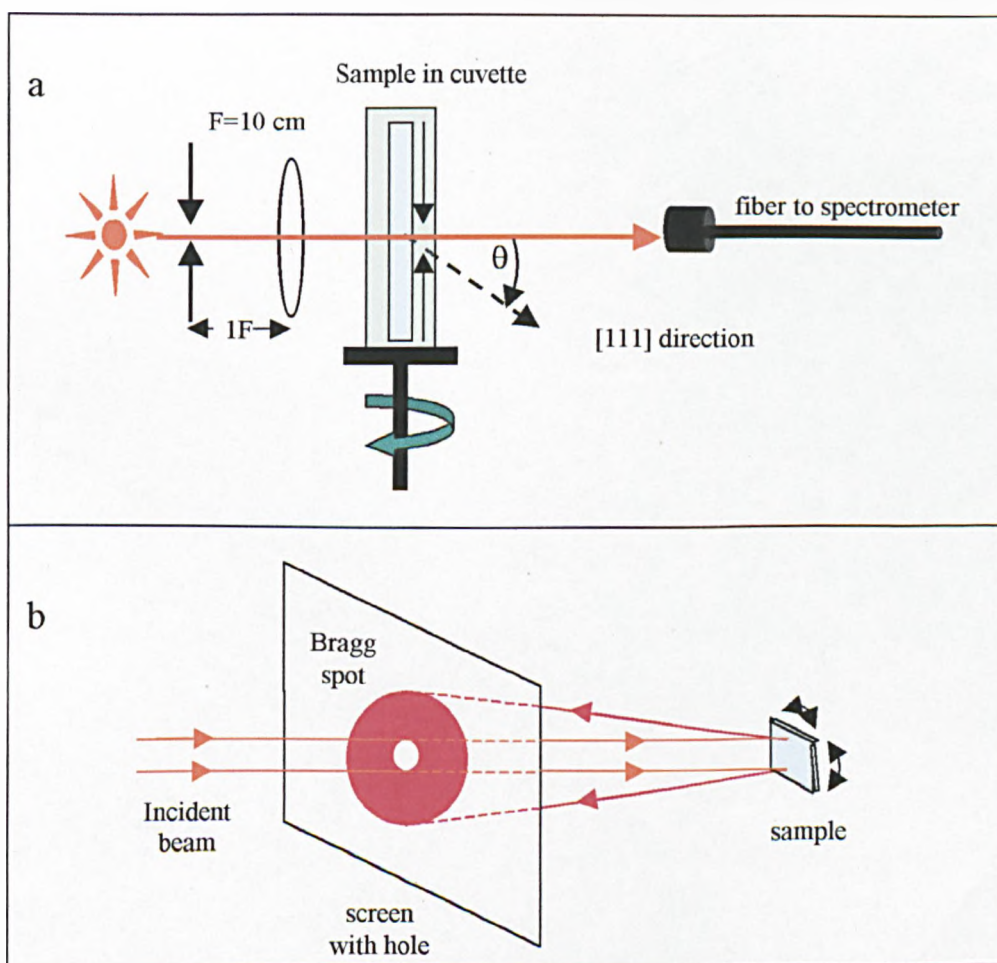


**Figure 2-7 (a) Transmission measurement setup (b) Method of alignment of the sample.**

## 2.6 Samples

The samples<sup>26</sup> used in this work were fabricated by sedimentation of silica spheres under gravity. This routine gives good optical quality samples with dimensions around 5  $\mu\text{m}$ . The  $\text{SiO}_2$  spheres with standard deviation less than 5% are obtained from a sol produced by hydrolysis of organic esters of ortho-silicic acid in alcohol<sup>6</sup>. The  $\text{SiO}_2$  spheres are suspended in DI water and the monodisperse solution is permitted to sediment under gravity. Under these conditions the spheres settle in three dimensional face centered cubic structures. This process takes several weeks to several months (depending on the sphere size).

The samples used in this study cover the whole visible region. The samples are termed A (with green Bragg reflection), B (with dark green Bragg reflection), C (with red Bragg reflection) and D (with blue Bragg reflection). Each sample was sawed into slices perpendicular to the growth direction with (111) orientation of the base plane. The thickness of the slices of the samples varies between 300-500  $\mu\text{m}$  and the surface area of each sample is about 0.25  $\text{cm}^2$ .

## 2.7 Structural Properties of Self Assembled Opals

According to the amount of disorder in any solid, it can be classified as crystalline, amorphous or polycrystalline. In crystals, atomic positions form a geometrical pattern that is exactly repeated throughout the solid without change in composition, dimension, or orientation. Atomic positions in an amorphous solid do not form such a repeating pattern. A polycrystalline solid is made up of a large number of small crystals called crystallites or domains. The atoms form a regular array just as in a crystal but the orientation changes abruptly at crystallite boundaries. Using the same terminology, photonic materials can be classified as crystalline, polycrystalline or amorphous.

In this section the structural properties of self assembled opals will be investigated. To do so, two techniques have been used namely Optical Microscopy Imaging and Scanning Electron Microscope (SEM).

To obtain a general idea about the structural quality of the samples, an optical microscope (LEICA DML) operating in reflection mode was used. The experiment was performed by illuminating the samples with a white light source at normal or oblique incidence. Figure 2-8 shows the optical images of one of our samples. In the normal incidence configuration, bright yellow reflections are observed from some areas on the sample surface (Figure 2-8a). Under oblique incidence (angle of incidence of  $\sim 40^\circ$ ) blue reflections are observed from other areas on the sample surface (Figure 2-8b). Figure 2-8c shows the image of the sample under normal and oblique incidence at the same time. The result in Figure 2-8c is a superposition of the images in a and b. From Figure 2-8 we conclude that our samples consist of domains with different orientation with respect to the [111] direction. We attributed the yellow spots as a specular Bragg reflection from the stop band of the (111) planes of those domains parallel to the sample surface, and the blue spots as a specular Bragg reflection from the (111) planes of domains which deviate by half of the angle of incidence ( $\sim 20^\circ$ ) from the [111] direction. Optical microscope scanning over the surface of the samples indicated that the size of the domains in our samples varied between 50 to 100  $\mu\text{m}$ .

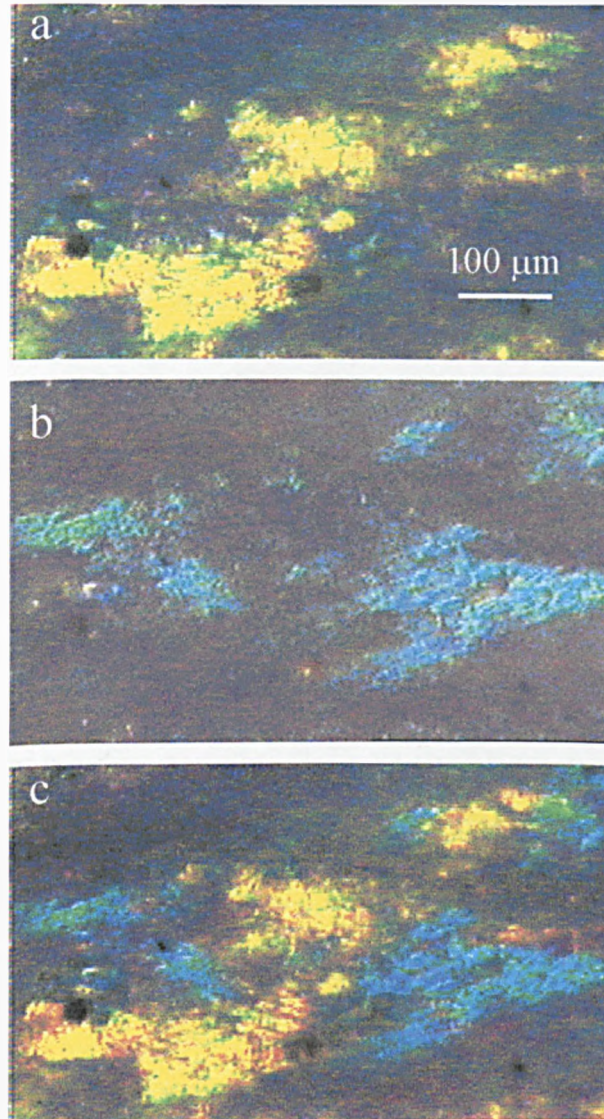


**Figure 2-8 (a) Optical micrograph image at normal incidence, (b) at oblique illumination ( $\theta \sim 40^\circ$ ) and (c) at normal and oblique illumination at the same time of the same area on the surface of the sample. The yellow and blue areas represent domains with different orientation of highly reflective (111) system of planes.**

An SEM was also used to study the structural properties of the self assembled opals. Figure 2-9 represents the results of the SEM study. A clear close-packed triangular array can be seen in Figure 2-9a which represents the {111} type face of an fcc structure. A closer look at the boundaries indicates that the domain boundaries could arise from a simple deviation of the ordering direction (Figure 2-9a) or could be another type of ordering such as (100) as in Figure 2-9b. There are also completely disordered areas as in Figure 2-9c. By using a larger magnification we were able to study the disorder inside the domains. Several kinds of defects have been observed such as vacancies (missing spheres), interstitial defects (spheres in places where they should not be). We have also observed some positions which have been occupied by smaller or bigger spheres in comparison with their neighbors. Most of these types of defects are illustrated in Figure 2-9d. The number of such point defects varies in different samples. However, typical values are estimated to be  $\sim 10^7 \text{ cm}^{-2}$  or  $10^{-2}$  defect per unit cell. Other structural studies<sup>27</sup> on opals indicate that dislocations and plane stacking faults are the most common structural faults along directions perpendicular to the growth direction. Therefore we expect that all these type of defects and faults to contribute strongly to the optical properties of opals.

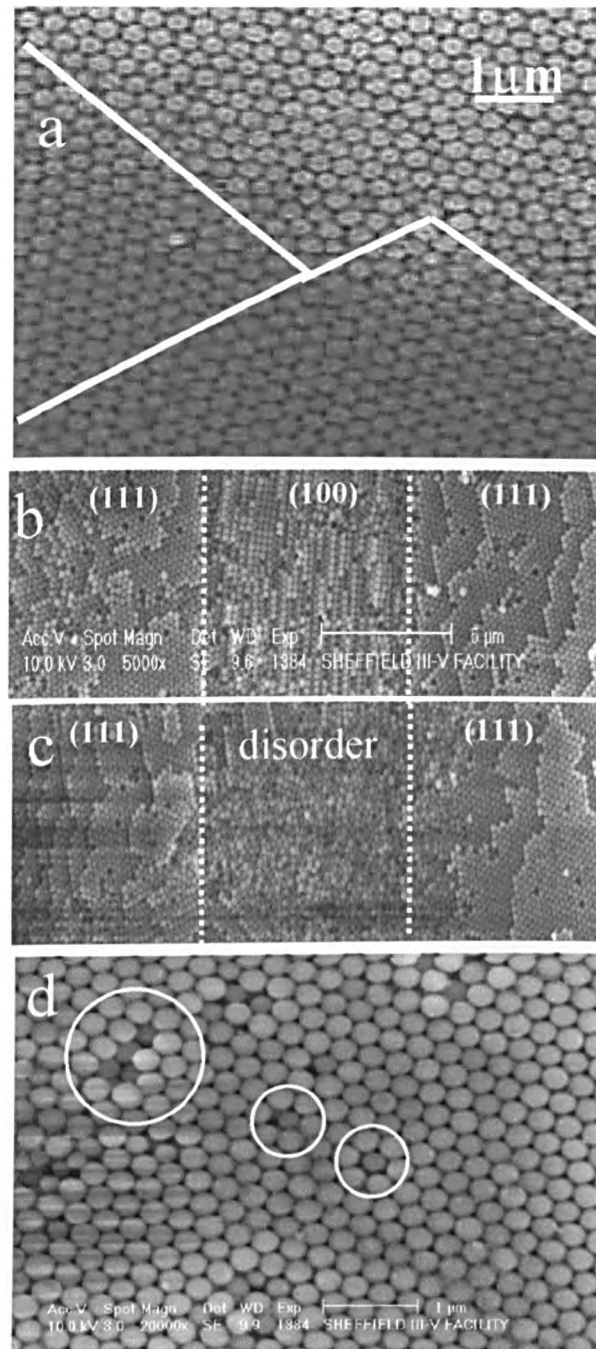


**Figure 2-9 (a) SEM of the surface of a self assembled opal showing individual crystal domains. The hexagonal packing represents domains with (111) planes. (b) SEM showing (100) orientation at the domain boundaries. (c) SEM showing disorder domain boundaries. (d) SEM images exhibiting possible types of defects inside domains.**

## 2.8 Optical Properties of Opal Photonic Crystals

To obtain general information about the optical quality of our samples, transmission spectra at normal incidence to the (111) plane were measured from all samples. The bare opal is not transparent (they have milky appearance) in the visible region, despite the fact that the silica spheres are transparent in the visible region. This arises because of the small transport mean free path of photons<sup>28</sup> ~15-20  $\mu\text{m}$ , which is much smaller than the thickness of the samples 300-500  $\mu\text{m}$ . Therefore photons undergo multiple scattering events near the surface of the sample and are finally scattered out of the surface of the sample. The reason behind the small value of the transport mean free path of photons in bare opal is the relatively large refractive index contrast between silica spheres and air.

To reduce the incoherent scattering (by increasing the transport mean free path of photons) the pores of the samples were infiltrated with cyclohexane ( $n_{\text{cy}}=1.43$ ) during the measurements. Figure 2-10 represents the transmission spectra of all samples (A, B, C and D). To compare the transmission spectra of samples with different lattice constants and different thicknesses, the y-axis of Figure 2-10 is presented in units  $\text{cm}^{-1}$

of the reciprocal of the Bragg attenuation length,  $\alpha = \frac{1}{L_{\text{Bragg}}} = \frac{\ln(\frac{1}{I_0})}{t}$ , where  $t$  is the

thickness of the sample. A clear attenuation band in the optical transmission can be observed from each sample. Since we are in the transparency region of silica, the attenuation in the transmission can not be attributed to the absorption. At the same time the dip in transmission from each sample is accompanied by an intense reflected spot, which compensates the decrease in the transmission intensity. This means that the light can not propagate through the sample at a certain range of wavelengths, but is totally reflected as a result of Bragg reflection from the periodic opal lattice. The

shift in the position of the stop band from one sample to another arises from the difference in the lattice constant (size of the silica spheres) from one sample to another. From the transmission spectra, it appears that sample A and B are the best, because sample A has the deepest stop band and sample B has the narrowest stop band.

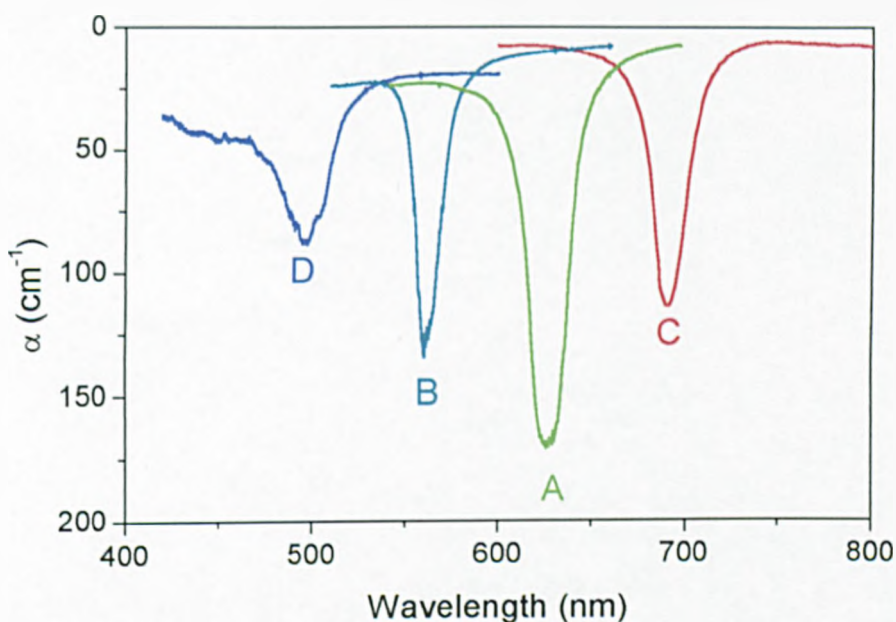


**Figure 2-10** Transmission spectra of samples A, B, C and D at normal incidence in cyclohexane.

To characterise samples A and B in more detail, we have measured the transmission spectra for both samples as a function of the position ( $h$ ) of the slice in the [111] direction with respect to the bottom of the original sample as can be seen in of Figure 2-11a. The results from sample A are presented in Figure 2-11b. The position, the depth and width of the stop band do not change with  $h$ , thus indicating the good uniformity of the sample for more than 1.5 cm along the growth direction. Very similar results have been obtained for sample B.

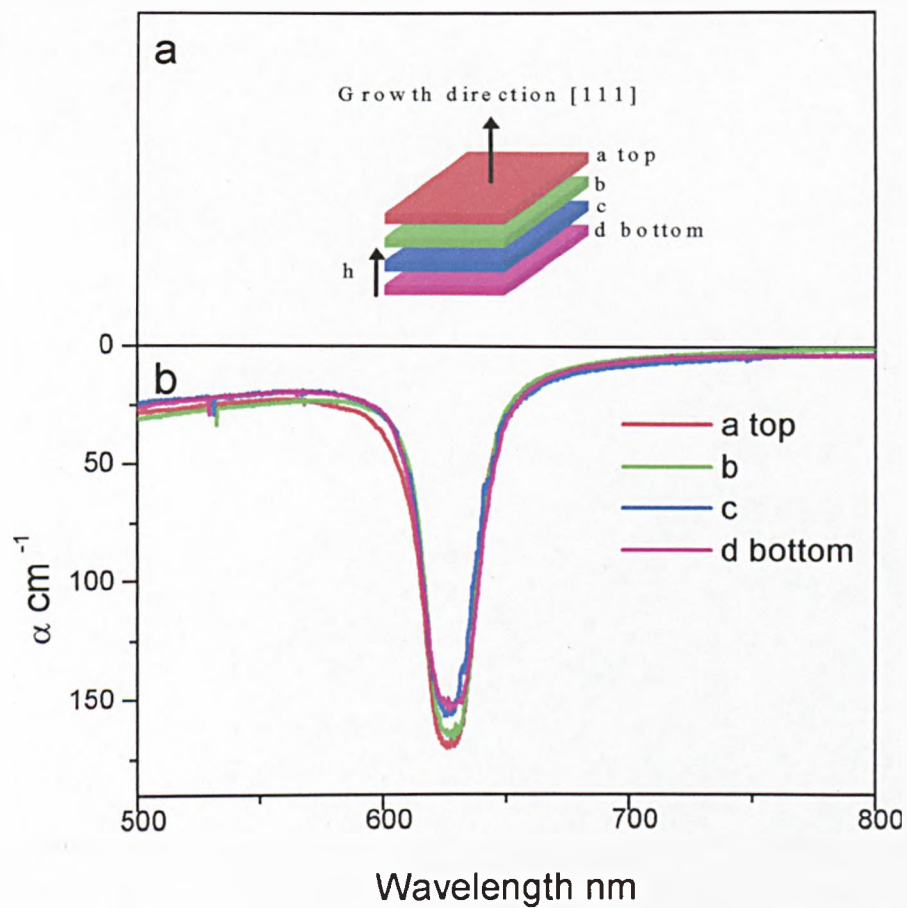


**Figure 2-11 (a) Schematic presentation of the sawing of the samples with base parallel to the (111) planes. (b) transmission spectra from sample A at normal incidence in cyclohexane for different slices along the growth direction as in (a).**

### 2.8.1 Dependence of the Stop Band on the Refractive Index Contrast

By filling the pores of the samples with materials having refractive indices different from that of the spheres, the spectral position and the contrast of the stop band can be controlled. We have used this fact to study the evolution of the stop band with the refractive index of the pores and to determine the refractive index ( $n_{\text{SiO}_2}$ ) of the silica spheres exactly. The transmission spectra of sample A filled with cyclohexane ( $n=1.43$ ), ethanol ( $n=1.36$ ) and methanol ( $n=1.33$ ), at normal incidence, are presented in Figure 2-12a. The sample becomes transparent when it is infiltrated with methanol due to refractive index matching between the silica spheres and methanol. By increasing the refractive index of the pores with respect to the refractive index of the spheres the stop band starts to appear. As the refractive index of the pores increases the stop band shifts to longer wavelengths and becomes broader. In Figure 2-12b the position of the stop band is plotted versus the refractive index of the pores. The experimental points are fitted to Bragg's law

$$\lambda = 2d_{111}n_{av} \quad (2.9)$$

with

$$n_{av} = \sqrt{fn_{\text{SiO}_2}^2 + (1-f)n_{\text{pores}}^2}$$

where  $d_{111}$  is the interpane distance and  $f$  is the  $\text{SiO}_2$  filling fraction. In the fit we used  $n_{\text{SiO}_2} = 1.33$  and  $f=74\%$  (for fcc structure). From the fit the plane spacing  $d_{111}$  is deduced and found to be equal to 233 nm. From  $d_{111}$  the diameter of the spheres can be calculated using the formula  $D = \sqrt{\frac{2}{3}}d_{111} = 285 \text{ nm}$ .

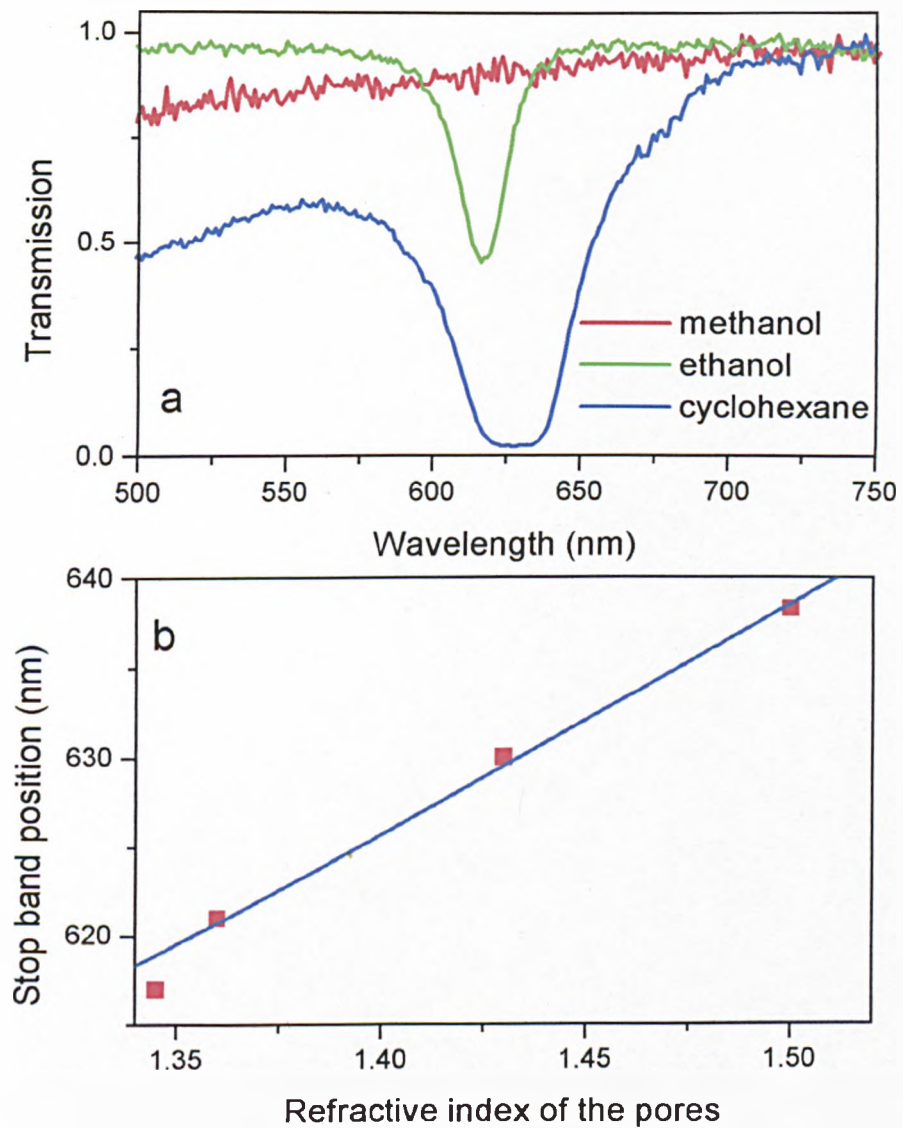


**Figure 2-12 (a) Transmission spectra of sample A at normal incidence in different liquids. (b) the measured stop band position as a function of the pores refractive index (square) and fit according to Bragg's law (full line) as in equation (2.9).**

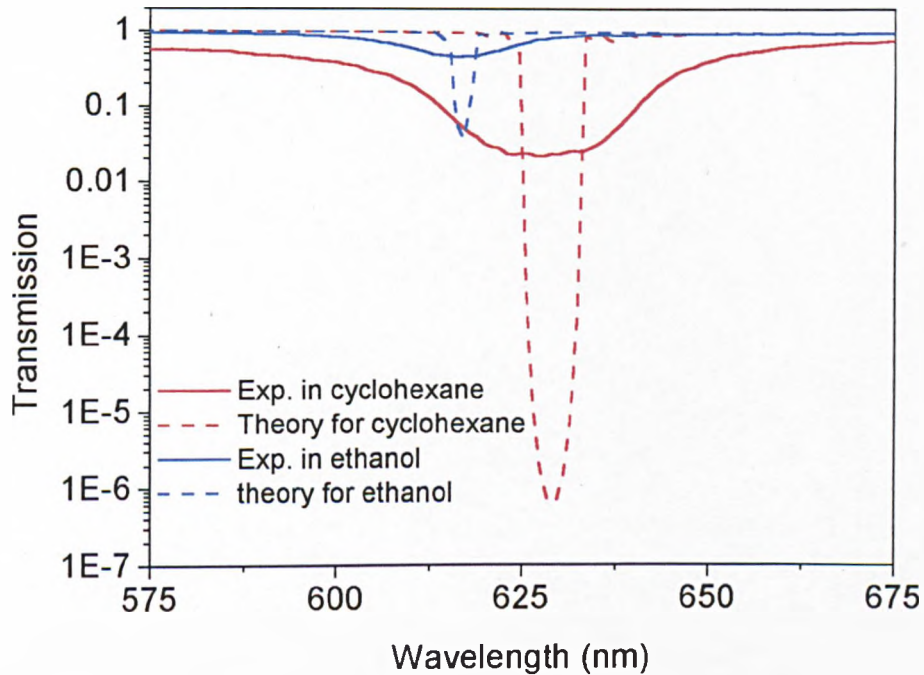
To investigate the effect of the disorder on the depth and width of the stop band of the sample, the transmission spectra for a perfectly ordered opal crystal were calculated. In the calculations the refractive index and the diameter of the spheres are assumed to be  $n_{SiO_2} = 1.33$  and  $D = 285$  nm, respectively, as estimated from the fitting to Bragg's law in Figure 2-12b. A comparison between the experimental and calculated transmission spectra for sample A infiltrated with cyclohexane and ethanol is illustrated in Figure 2-13. The slab thickness in the calculated spectra is  $90 \mu\text{m}$  smaller than the actual thickness of the  $300 \mu\text{m}$  sample. The experimental stop band is much wider and shallower than the calculated spectra. To compare precisely between the experimental and the calculated spectra, the stop band width ( $\Delta$ ) and Bragg attenuation length ( $L_B$ ) are extracted from the spectra and summarised in Table 1.

Table 1 parameters of Bragg attenuation length calculated for a perfectly ordered fcc lattice along the [111] direction and the measured Bragg attenuation length in the polycrystalline samples along the growth direction, width of the stop band in calculated and measured spectra.

Liquid	Refractive index	$L_B$ ( $\mu\text{m}$ )		$\Delta$ (nm)	
		Calculated	$L_{B_{exp}}$ (Measured)	Calculated	$\Delta_{exp}$ (Measured)
Ethanol	1.36	43	300	3	18
Cyclohexane	1.43	12	60	9	~50
Refractive index of the silica spheres is 1.33					

The experimental stop band is six times broader than the calculated stop band in both liquids. The experimental Bragg attenuation length in the ethanol case is 7 times larger than the calculated value while in the cyclohexane case it is 5 times larger than the measured value. This huge disagreement between the experimental and the calculated values represents the influence of the disorder, which we observed in

section 2.7 in the optical imaging results. The influence of the disorder on the properties of the stop band will be investigated in full detail in the next chapter.



**Figure 2-13 Comparisons between the measured (full line) transmission and calculated (dashed line) transmission spectra for infiltration with cyclohexane and ethanol at normal incidence. The calculation predicts significantly stronger attenuation and narrower spectra width of the stop band features, even though in the calculations the thickness of the structure was smaller (90  $\mu\text{m}$  corresponding to 384 close-packed (111) layers with interplane spacing  $d_{111}=233$  nm) than the actual thickness of the sample ( $t=300$   $\mu\text{m}$ ).**

The same experimental and calculation procedures have been carried out on sample B. In contrast with sample A we found that the refractive index of the silica spheres in sample B is  $n_{\text{SiO}_2} = 1.36$  as can be seen in Figure 2-14. The difference in the refractive index of the spheres from one sample to another can be attributed to the difference in internal substructure of the silica spheres. The detail of the results from sample B will be presented in chapter 4.

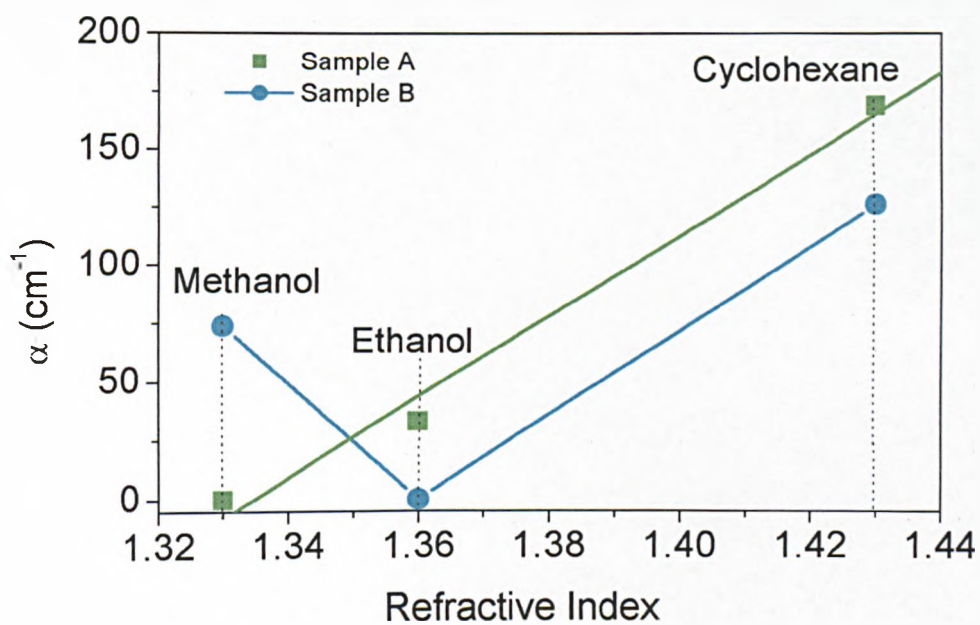


**Figure 2-14** The inverse of the Bragg attenuation length of sample A and B as a function of the refractive index of the pores.

### 2.8.2 Angular Dependence of the Stop Band

From the band structure calculations which have been presented in section 2.2.4 we found that the position of the stop band depends upon the angle between the light propagation direction and the crystal axes. To investigate this dependence the transmission spectra for an opal infiltrated with cyclohexane have been measured as a function of the angle of incidence with respect to the [111] direction. The results are illustrated in Figure 2-15a. As the angle of incidence increases the stop band shifts to shorter wavelengths. The stop band also becomes broader and less pronounced. To investigate the position dependence of the stop band with angle of incidence in more detail, we have used two models. In the first model Bragg's law has been used. The position of the stop band has been plotted against  $\cos(\phi)$  (where  $\phi$  is the angle of incidence inside the opal and can be related to the external angle of incidence  $\theta$  using Snell's law (see equation (2.10) ) in Figure 2-15b. The experimental points are very well fitted to Bragg's law

$$\lambda = 2n_{av}d_{111}\cos(\phi)$$

With  $\phi$  related to  $\theta$  by Snell's law

$$\cos(\phi) = \sqrt{1 - \frac{\sin^2(\theta)}{n_{av}^2}} \quad (2.10)$$

In this fit the following parameters have been used,  $n_{SiO_2} = 1.33$  as measured in section 2.8.1, and  $f = 74\%$ . From the fit  $d_{111}$  has been deduced and found to be equal to 233 nm exactly as in section 2.8.1. Bragg's law thus correctly describes the position of the experimentally observed stop band and its angular shift.

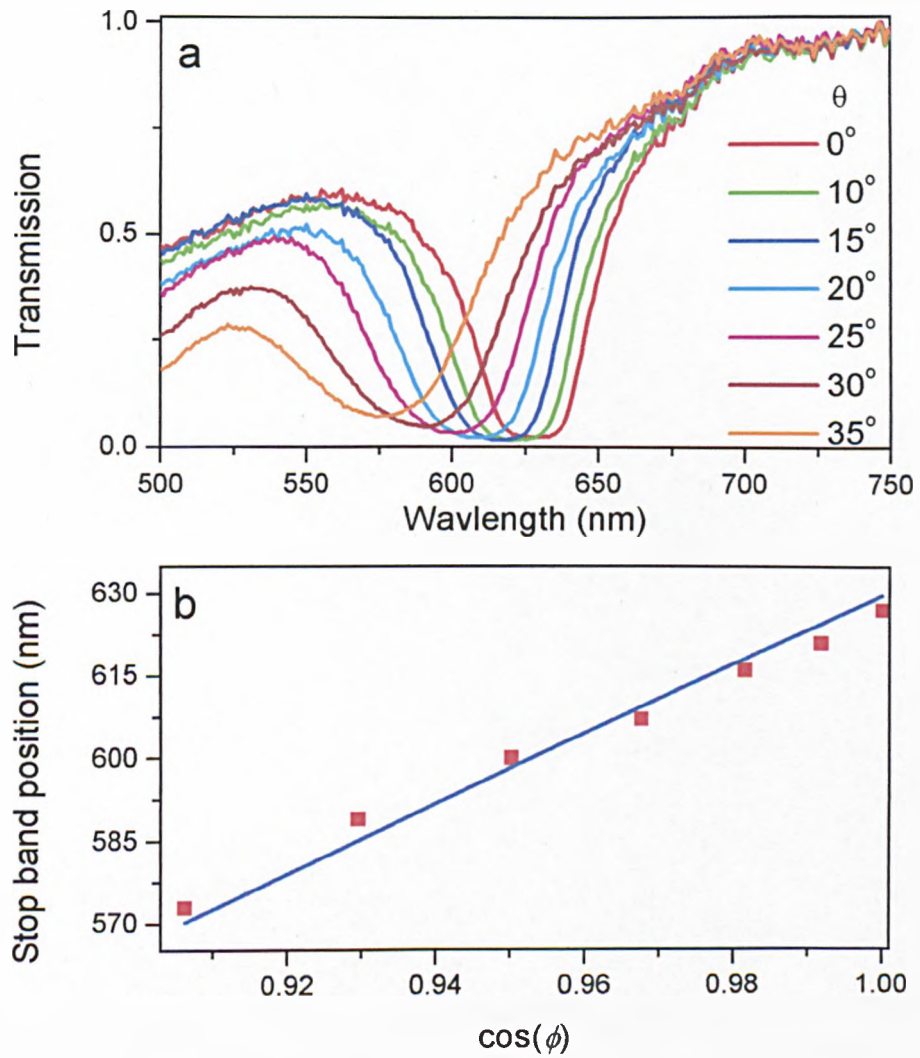
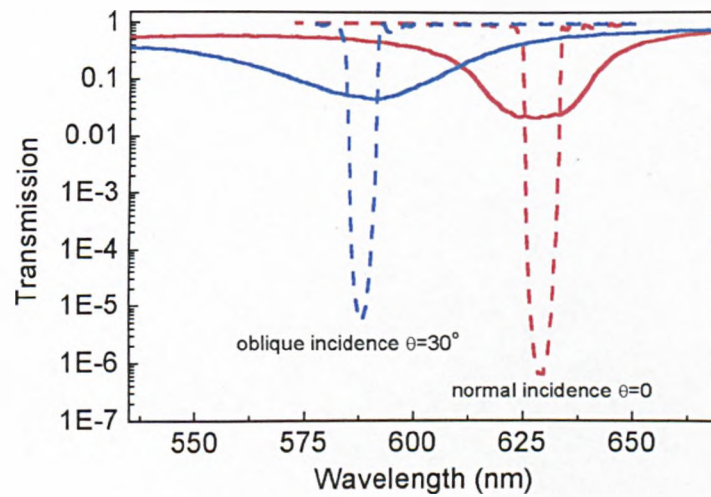


Figure 2-15 (a) Transmission spectra of sample A in cyclohexane as a function of the external angle of incidence ( $\theta$ ) with respect to the [111] direction. (b) The measured stop band position as a function of the internal angle of incidence (squares) and fit according to Bragg's law (full line) as in equation (2.10).

Secondly three dimensional calculations for a perfectly ordered fcc opal crystal have been used to model the transmission spectra as a function of the angle of incidence with respect to the [111] direction. Figure 2-16 shows a comparison between measured and calculated spectra for sample A infiltrated with cyclohexane at two external angles of incidence  $\theta = 0^\circ$  and  $\theta = 30^\circ$ . It is seen that the calculations correctly describe the position of the experimentally observed stop band and its angular shift. At the same time the calculations do not predict the width and the depth of the experimentally observed stop band and the observed broadening of the experimental stop band with angle of incidence. On the contrary the calculations predict some narrowing of the stop band with the angle of incidence. We attribute the failure of the perfect lattice model to predict the shape of the experimentally observed stop band to the polycrystalline nature of the samples. The effect of the polycrystallinity of the opals on the shape of the transmission stop band will be discussed in full detail in the next chapter.

Another important difference between the experimental and calculated spectra is that there is strong overlap between the experimental normal incidence transmission spectrum and the transmission spectra at angles up to  $25^\circ$  away from the [111] direction (see Figure 2-15a). By contrast the overlap between the normal incidence calculated transmission spectrum and the calculated transmission spectra at angles away from the normal only occurs for angles less than  $10^\circ$  away from the [111] direction (see Figure 2-17). Therefore the apparent occurrence of a complete photonic band gap in opals at low refractive index contrast stems from the inhomogeneous broadening in the stop band, a result of the disorder inside the material, and not from the order of the material.



**Figure 2-16.** Experimental (solid) and theoretical (dashed) zero-order transmission spectra for sample A infiltrated with cyclohexane at normal incidence ( $\theta=0^\circ$ ), and oblique incidence  $\theta=30^\circ$ . The calculations predict significantly stronger attenuation and narrower spectral width of the stop band features even though in the calculations the thickness of the structure was smaller ( $90\mu\text{m}$ , corresponding to 384 close-packed (111) layers with interplane spacing of  $d_{111}=233\text{nm}$ ) than the actual thickness of the sample ( $t=300\mu\text{m}$ ).

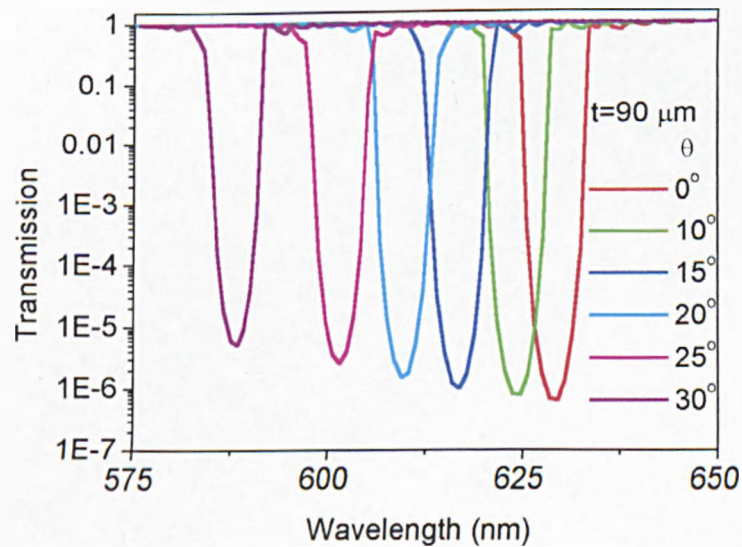


**Figure 2-17** Theoretical zero-order transmission spectra for sample A infiltrated with cyclohexane as a function of the external angle of incidence  $\theta$ . In the calculations the thickness of the structure was  $90\mu\text{m}$ , corresponding to 384 close-packed (111) layers with interplane spacing of  $d_{111}=233\text{nm}$ .

### 2.8.3 Thickness Dependence of the Stop Band

To study the thickness dependence of the transmission spectra, a sample of dimensions 6x5mm and thickness 500  $\mu\text{m}$  was polished in the form of a wedge of  $6^\circ$  with a base corresponding to the (111) plane. The thickness of the sample increases linearly with the distance along the base direction from 30 $\mu\text{m}$  to 500  $\mu\text{m}$ . To characterise the sample, the strength of the stop band has been measured as a function of the refractive index of the pores. The sample becomes transparent when it is infiltrated with ethanol ( $n=1.36$ ). The angular dependence of the stop band in cyclohexane has been investigated. The position of the stop bands is very well fitted to Bragg's law and gives  $d_{111}=186$  nm and  $D=228$  nm.

Figure 2-18a and b represent a comparison between the measured and calculated transmission spectra for the sample filled with cyclohexane at different thicknesses. The position of the experimental gap is unchanged along the base direction of the sample. This means that the sample is uniform and has the same periodicity along 6 mm on the base of the sample. In Figure 2-18c and d the minima of the transmission spectra are plotted as a function of thickness on a logarithmic scale. Both the experimental and calculated points show a linear variation. The values of the Bragg attenuation length have been deduced from Figure 2-18c and d and are summarised in Table 2.

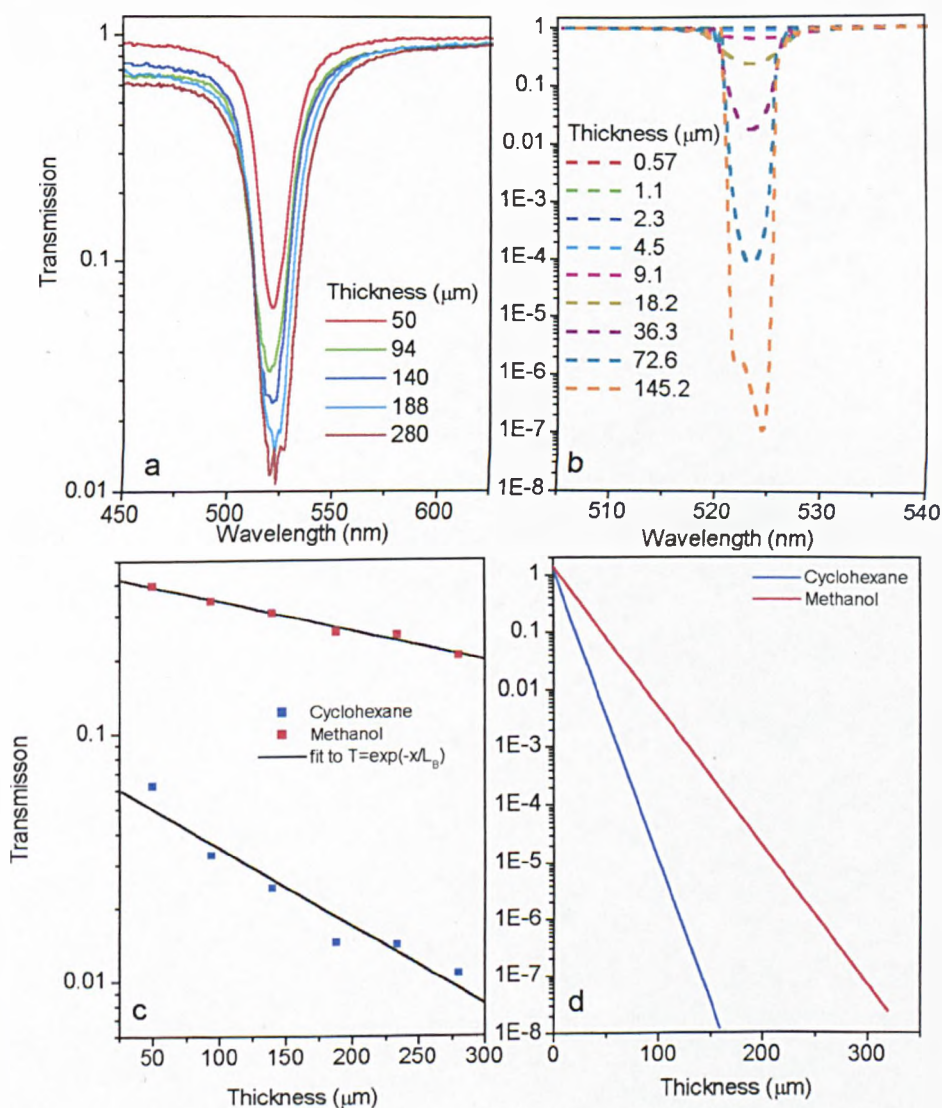


**Figure 2-18 (a)** Measured transmission spectra at normal incidence of the wedge sample infiltrated with cyclohexane. **(b)** calculated transmission spectra for opal infiltrated with cyclohexane at normal incidence to (111) planes as a function of structure thickness. In the calculations  $n_{\text{SiO}_2} = 1.36$  and  $d_{111} = 186$  nm. **(c)** the measured minimum of the transmission spectra as a function of the thickness in a logarithmic scale (square) with fit to exponential law (full line) infiltrated with different liquids **(d)** the calculated minimum of the transmission spectra as a function of the thickness in a logarithmic scale for different pores refractive index.

Table 2 Comparison between theoretical and measured optical parameters of the wedge sample for different pores refractive index.

Liquid	n	$L_B$ ( $\mu\text{m}$ ) Calculated	$L_{B_{exp}}$ ( $\mu\text{m}$ ) Measured
Methanol	1.36	36	365
Cyclohexane	1.43	15	137
Refractive index of the silica spheres is 1.36			

As can be seen in Figure 2-18a the width of the measured stop band increases with the sample thickness, Vlasov *et al*<sup>28</sup> have observed the same behavior for the variation of the stop band with thickness. In contrast the width of the calculated stop band initially decreases at the start with the crystal thickness until  $t = 18 \mu\text{m}$ , and then there is no further reduction in the width of the stop band with increased crystal thickness. The explanation of the behavior of the theoretical spectra is straightforward. When the crystal thickness ( $t$ ) is less than the Bragg attenuation length the stop band is homogeneously broadened due to the finite size of the crystal. Once the crystal thickness exceeds the Bragg attenuation length, the crystal reflects all the incident light (within the stop band) back and no more homogeneous broadening due to the size effect can be seen. Before going on to explain the experimental spectra we must remember that the sample consists of domains, and these domains do not just exist on the sample surface but also in the thickness direction. The thickness of the domains is unknown. However, we are still able to discuss the results for two limiting cases:

1. If the thickness of the domains is larger than the Bragg attenuation length, the stop band develops as a result of passing through one layer of domains across the sample thickness. The structural defects in the domains will determine the width of the stop band. Increasing the thickness of the sample beyond the thickness of the domain layer will not change the width of the stop band.

2. If the thickness of the domain is less than the Bragg attenuation length, a small part of the incident light will be reflected from each layer of domains. The measured transmission spectrum in this case can be considered as an accumulation of the transmitted light from each layer of domains. Therefore with increasing sample thickness the number of domains which the light passes through increases, and the measured stop band will consequently become deeper and wider.

From the above discussion we conclude that the samples consist of domains of size  $\sim 10 \mu\text{m}$  (less than the Bragg attenuation length in cyclohexane) in the thickness direction, and that is the reason for the observed broadening in the stop band width with increasing sample thickness.

The effect of the finite thickness of the domains ( $t_{\text{domain}} \geq L_B$ ) on the transmission stop band will be discussed in more detail in the next chapter.

## 2.9 Conclusions

In this chapter the structural and optical properties of self assembled opal photonic crystals have been investigated. Optical Microscopic Imaging and SEM techniques are used to study the structural properties of the samples and an angular transmission technique is used to investigate the optical properties of the samples.

The structural studies on self assembled opals indicate that self assembled opal photonic crystals consist of domains of sizes between 50 to 100  $\mu\text{m}$  and that these domains are misoriented with respect to each other. The SEM images showed that the domains contain different types of point defects such as vacancies or interstitial defects. The concentration of the point defects in the samples is about  $10^{-2}$  per unit cell.

The transmission spectra indicate that self assembled opals have a strong stop band gap along the [111] direction (growth direction). The position of the stop band depends on the sphere size, and the refractive index contrast. The angular transmission studies showed that opals only have stop bands due to the low refractive index contrast of the samples.

The experimental spectra are compared with three dimensional calculations based on the transfer matrix method. The calculations predict accurately the position of the experimental spectra and their shift with changing refractive index contrast or angle of incidence. The experimental spectra are found to be much broader and shallower than the calculated spectra. The failure of the perfect order crystal model to predict the width and depth of the experimental stop band is attributed to the polycrystalline nature of the samples.

The thickness dependence measurements of the stop band showed that the stop band gets wider with increased thickness, in contrast with the calculated spectra, where the stop band narrows with the thickness initially until the thickness exceeds the Bragg attenuation length then no further narrowing with the crystal thickness is observed. These results are attributed to the limiting size (less than the Bragg attenuation length) of the domains in the thickness direction.

In this chapter we have attributed the broadening and weakening of the transmission stop band to the disorder in the material without further detail about the nature of the interplay between light and disorder. The next chapter will be devoted toward studying the interplay of light with disorder in opals. Two experimental techniques will be used to study the disorder in opals (i) the angle resolved diffraction technique, and (ii) the angle resolved scattering technique. In the light of the experimental results, we will develop a model describing the propagation of light in polycrystalline photonic materials. Using this model, all the features of the transmission stop band will be explained.

## 2.10 References

- <sup>1</sup> - E. Yablonovitch, Phys. Rev. Lett. **58**, 2059 (1987).
- <sup>2</sup> - J. D. Joannopoulos, R. D. Meade and J. N. Win, Photonic Crystals (Princeton University press, 1995).
- <sup>3</sup> - E. Yablonovitch and T. J. Gmitter, Phys. Rev. Lett. **67**, 2295(1991).
- <sup>4</sup> - L. Zavieh and T. S. Mayer, Appl. Phys. Lett. **75**, 2533 (1999).
- <sup>5</sup> - S. Y. Lin *et al*, Nature **394**, 251 (1998).
- <sup>6</sup> - V.N. Astratov, V.N. Bogomolov, A.A. Kaplyanskii, A.V. Prokofiev, L.A. Samoilovich, S.M. Samoilovich, and Y.A. Vlasov, Nuovo Cimento D **17**, 1349 (1995).
- <sup>7</sup> - A. Stein, Microporous and Mesoporous Materials **44-45**, 227 (2001).
- <sup>8</sup> - G. Pan, R. Kesavamoorthy and S. A. Asher, Phys. Rev. Lett. **78**, 3860 (1997).
- <sup>9</sup> - V.N. Astratov, A.M. Adawi, M.S. Skolnick, V.K. Tikhomirov, V. Lyubin, D.G. Lidzey, M. Ariu, and A.L. Reynolds, Appl.Phys. Lett. **78**, 4094 (2001).
- <sup>10</sup> - K. Busch and S. John, Phys. Rev. E **58**, 3896 (1998).
- <sup>11</sup> - J. B. Pendry and A. Mackinnon, Phys. Rev. Lett. **69**, 2772 (1992).
- <sup>12</sup> - A.L. Reynolds, Modelling of Photonic Band Gap Materials for mm-wave & Optical Applications, Ph.D. thesis, University of Glasgow (2000).
- <sup>13</sup> - J. Jackson, Classical electrodynamics, third edition (John Wiley and Sons, 1998).
- <sup>14</sup> - S. John, Phys.Rev.Lett. **58**, 2486 (1987).
- <sup>15</sup> - H. S. Sozuer, J. W. Haus and R. Inguva, Phys. Rev. B **45**, 13 962 (1992).
- <sup>16</sup> - A. Moroz and C. Sommers. J. Phys.: Condens. Matter **11**, 997 (1999).
- <sup>17</sup> - A. Reynolds, F. Lopez-Tejeira, D. Cassagne, F.J. Garcia-Vidal, C. Joanin, and J. Sanchez-Daheza, Phys. Rev.B **60**, 11422 (1999).
- <sup>18</sup> - M. Campbell, D.N. Sharp, M.T. Harrison, R.G. Denning, A.J. Turberfield, Nature **404**, 53 (2000).
  
- <sup>19</sup> - Shawn-Yu Lin, J. G. Fleming, M. M. Sigalas, R. Biswas and K. M. Ho, Phys. Rev. B **59**, R15 579 (1999).
- <sup>20</sup> - S. Noda, K. Tomoda, N. Yamamoto, A. Chutinan, Science **289**, 604 (2000).
- <sup>21</sup> - A. Feigel, Z. Kotler, B. Sfez, A. Arsh, M. Klebanov and V. Lyubin, Appl. Phys. Lett. **77**, 3221 (2000).
- <sup>22</sup> - G. Subramania, K. Constant, R. Biswas, M. M. Sigalas and K. M. Ho,J. Lightwave Technology **17**, 1970 (1999).

- 
- <sup>23</sup> - M. Holgado *et al*, *Langmuir*, **15**, 4701 (1999).
- <sup>24</sup> - Y.A. Vlasov, X.-Z. Bo, J.C. Sturm, and D.J. Norris, *Nature* **414**, 289 (2001).
- <sup>25</sup> - P. V. Braun *et al*, *Adv. Mater.* **13**, 721 (2001).
- <sup>26</sup> - L. Samoilovich and M. Samoilovich, Institute for the Synthesis of Minerals, Alexandrov, Moscow region, Russia.
- <sup>27</sup> - Y.A. Vlasov, V.N. Astratov, A.V. Baryshev, A.A. Kaplyanskii, O.Z. Karimov, and M.F. Limonov, *Phys. Rev. E* **61**, 5784 (2000).
- <sup>28</sup> - Y.A. Vlasov, M.A. Kaliteevski, and V.V. Nikolaev, *Phys.Rev. B* **60**, 1555 (1999).

## Chapter 3

# Diffraction and Scattering of Light in Self Assembled Opals

### 3.1 Introduction

The optical properties of self assembled opal photonic crystals have been investigated by several groups<sup>1-4</sup> using transmission or reflection techniques. Typically the measured stop bands are much broader and shallower than the calculated stop bands for perfectly ordered structures as we have seen in the previous chapter. The broadening and weakening of the stop band have previously<sup>1-4</sup> been attributed to disorder in the samples without further investigation about mechanisms of the interaction of light with disorder inside opals. So far, there have been relatively few experimental studies<sup>5-7</sup> of the effects of the disorder on the optical properties of self assembled opal photonic crystals. In addition, in all of these studies the spatial and spectral characteristics of scattered light and polycrystallinity of opals were not studied in detail. Vlasov *et al*<sup>5</sup> have used the total transmission to study the disorder in opals. The results indicate that at energies far from the stop band region, the transmission is inversely proportional to the sample thickness ( $T = \frac{l}{t}$  where  $l$  is the mean free path of the photon), characteristic of classical diffusion. The mean free path,  $l = 20 \mu\text{m}$ , was estimated for bare opals. In order to model the experimental zero-order transmission spectra, Vlasov *et al* assumed that the disorder in opals arises from fluctuations in the size of spheres. A one dimensional model was used with a random distribution of sphere sizes inside the sample to fit the experimental spectra. It was found that in order to fit the experimental data, 15-20% size fluctuation is

required, three to four times greater than the fluctuation known to exist from structural studies. The reason for the overestimated parameters in the above model is that it did not take in account the three-dimensional nature of the scattering phenomena taking place in polycrystalline material such as opals. Megens *et al*<sup>6</sup> have studied the disorder in opals using built in light sources. The results of this experiment revealed that in the case of built in light sources the propagation of light in opals arises from a combination of ballistic transport along directions away from the stop band with diffuse scattering in thin near-surface region (more details about the propagation of light generated by built in light sources in opals will be given in the next chapter). However, the polycrystallinity of opals is completely ignored in Megens *et al*<sup>6</sup> work.

In this chapter a systematic study of the diffraction and scattering mechanisms taking place in the vicinity of the stop band of self assembled opal photonic crystals will be presented. In order to investigate all the diffraction and scattering mechanisms occurring in opals, scattering measurements have been performed in all directions around the sample. The results of the diffraction and scattering measurements in this study provide a full explanation of the disagreement observed between the measured and calculated stop bands in the previous chapter. This study shows that the shape of the stop band features in transmission, diffraction and scattering spectra are interlinked and must be studied jointly to obtain a comprehensive understanding of the optical phenomena in opals.

This chapter is organised as follows. Firstly a review of the transmission spectra measured in the previous chapter will be given. The angle resolved diffraction and scattering techniques used to study the order and disorder of the sample will be presented. The diffraction properties in front of the sample for the case of low and

relatively high refractive index contrast will be discussed. Then the mechanisms leading to the broadening of the stop band in zero-order transmission spectra will be discussed. The final part of this chapter will be devoted toward the properties of the scattered light behind the sample.

### 3.2 Review of the Transmission Spectra

In chapter 2, experimental transmission spectra were compared with calculated spectra within the stop band region. The experimental stop band was found to be broader and shallower than the calculated stop band. The results were attributed to the disorder in the sample. No details about the mechanisms of the interplay of the light with the disorder was given. In this section the mechanisms responsible for the broadening and weakening of the stop band will be introduced. The transmission spectra in Figure 3-1 can be divided into two regions, outside the stop band region and within the stop band region. The transport of the photons in the outside stop band region is characterised by a mean free path for photons ( $l$ : the average length that the wave propagates in between two collisions). The mean free path depends on the refractive index contrast of the sample. In the case of bare opals the refractive index contrast is relatively high ( $\frac{n_{\text{SiO}_2}}{n_{\text{air}}} = 1.33$ ), and therefore the mean free path is short ( $l \sim 20 \mu\text{m}$ )<sup>5</sup> and light is strongly attenuated within the first 20 microns. Thus the sample has a milky appearance if its thickness is more than 20  $\mu\text{m}$  as is the case for our samples. For opals infiltrated with cyclohexane or ethanol the refractive index contrast between the silica spheres and cyclohexane or ethanol is rather low (refractive index contrast = 1.07 or 1.02 respectively) and the mean free path ( $l$ ) is comparable to the sample thickness as can be seen from the transmission spectra (Figure 3-1), at high wavelengths where the transparency of the sample is about unity. At the shorter wavelengths out of the stop band region the transparency is less than unity, especially for cyclohexane infiltration due to the scattering of the light with lattice imperfections and impurities. In the stop band region the light undergoes Bragg reflection due to the periodic order of the silica spheres and appears as a dip in the transmission spectrum (Figure 3-1).

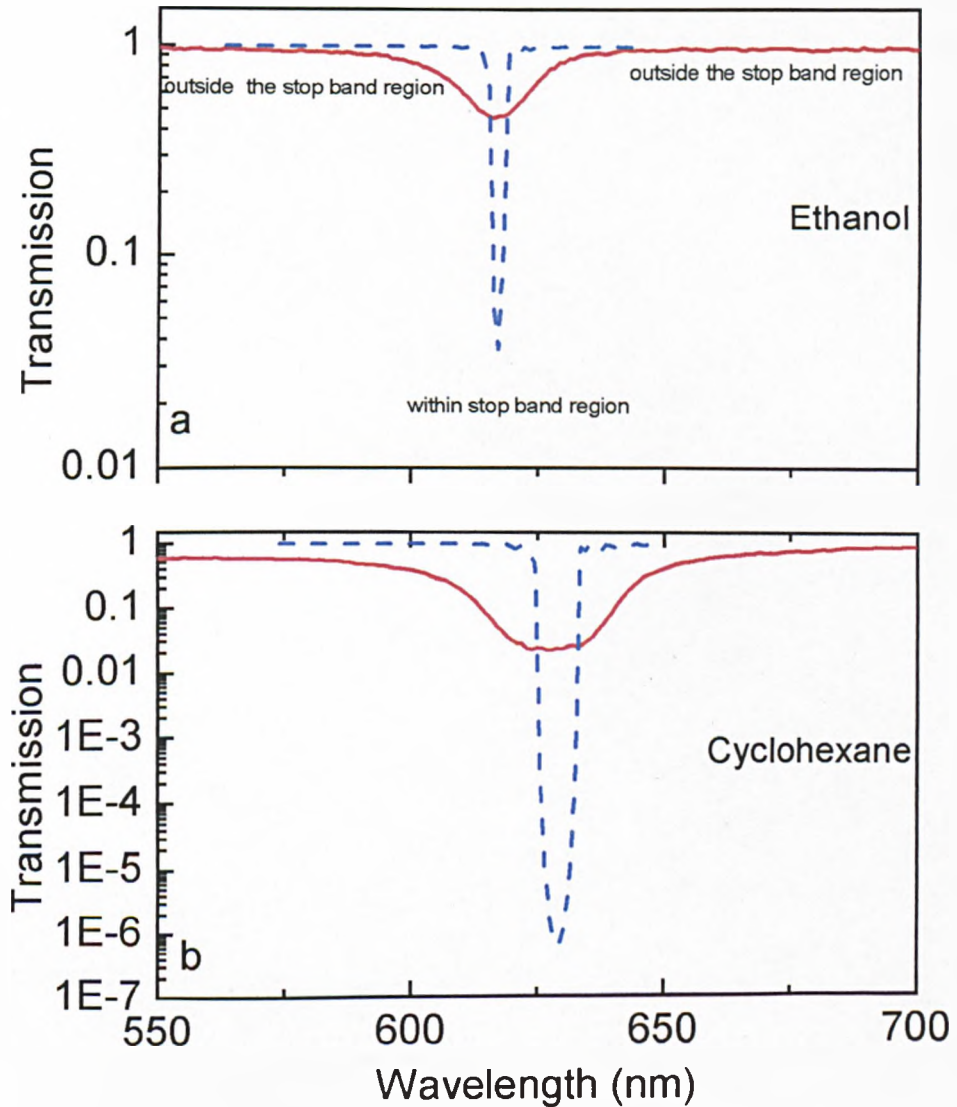


**Figure 3-1** Experimental (solid) and theoretical (dashed) zero-order transmission spectra at normal incidence (a) for infiltration with ethanol and (b) with cyclohexane. The calculations predict significantly stronger attenuation and narrower spectral width of the stop band features even though in the calculations the thickness of the structure was smaller ( $90\mu\text{m}$ , corresponding to 384 close-packed (111) layers with interplane spacing of  $d_{111} = 233\text{nm}$ ) than the actual thickness of the sample ( $t = 300\mu\text{m}$ ).

The transport of the photons is characterised by the Bragg attenuation length ( $L_B$ ) in this region ( $T = e^{-\frac{t}{L_B}}$ ). As we described in chapter 2, the transmission spectra of a perfectly ordered fcc structure along the [111] direction were calculated and compared with the experimental spectra (see Figure 3-1). The calculated transmission spectra are much deeper and narrower in comparison with the experimental spectra. The high signal at the center of the measured stop band in the transmission spectra in comparison with the calculated stop band indicates that there is light of wavelengths within the stop band propagating behind the sample along the [111] direction. The broadening of the measured stop band reveals that there is some light that is prevented from propagating throughout the sample. The absence of absorption in opal within the investigated region indicates that scattering takes place in the vicinity of the stop band, and was not taken into account in the previous chapter. In order to identify these scattering mechanisms, we have performed scattering measurements in all directions around the sample in space ( $4\pi$  steradian solid angle). Figure 3-2 represents all the mechanisms involved in the experiment. To simplify the discussion through the chapter, the experiments performed to measure the scattered light in front of the sample (see Figure 3-2) will be referred to as diffraction experiments because the experimental spectra in some sense follow Bragg's law. The experiments performed to measure the scattered light behind the samples will be called scattering experiments.

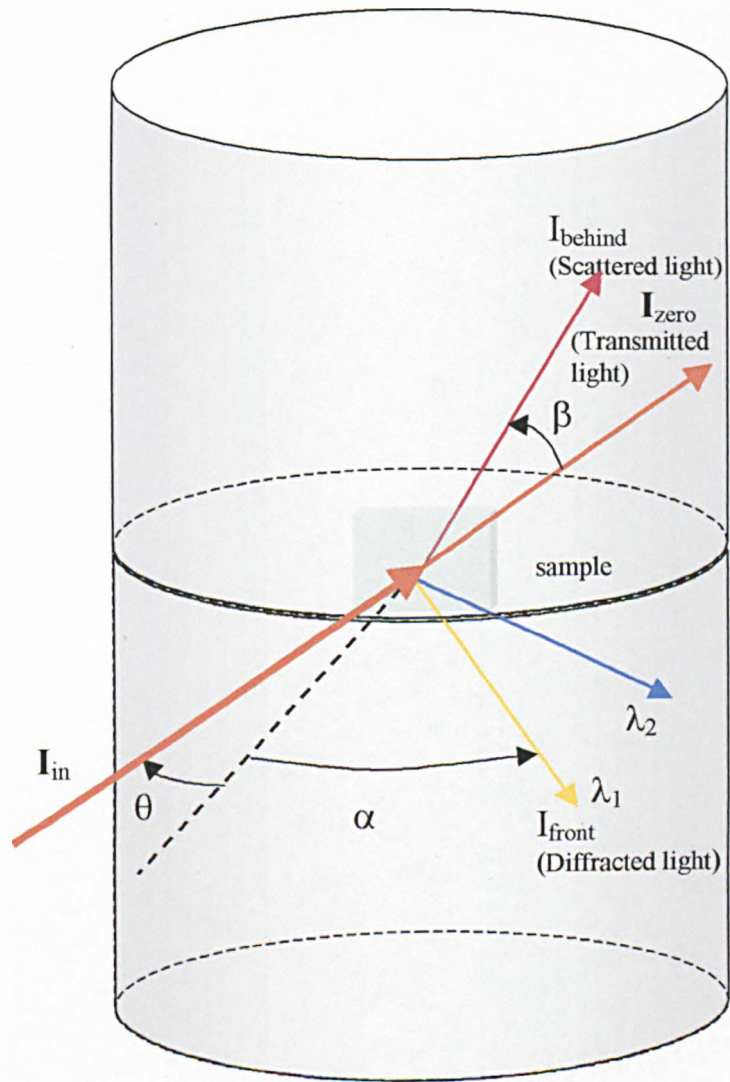


**Figure 3-2 Schematic representation of the scattering mechanisms in self assembled opal photonic crystals.**

### 3.3 Experimental Details

#### 3.3.1 Diffraction Measurement Setup

The same experimental setup described in section 2.5 was used to measure the diffracted light in front of the sample (see also Figure 3-3a). The principle of this set of experiments is to measure the diffracted light in front of the sample as a function of the angles of illumination ( $\theta$ ) and collection ( $\alpha$ ). In each set of experiments the angle of illumination ( $\theta$ ) was fixed at a certain value between  $0^\circ$  and  $60^\circ$  and the angle of collection ( $\alpha$ ) was varied between  $0^\circ$  and  $55^\circ$  to collect the diffracted light from the misoriented microcrystallites of the sample. This technique has analogy with the powder (Debye-Scherrer) method in x-ray diffraction<sup>8</sup> with one important difference. In the powder method the microcrystallites are equally present in the sample while in the case of opals the microcrystallites have a specific distribution in the sample as we will see in the discussion of the results. The size of the incident beam on the sample surface was about 2mm, resulting in a number of illuminated domains of the order  $10^3$ - $10^4$ . Light was collected in the front direction with angular resolution  $1^\circ$  degree using a flexible fiber coupled to a spectrometer (40Å/mm) with a photomultiplier (PMT). To be able to probe all the domains in the thickness direction, the samples were infiltrated with ethanol or cyclohexane during the experiment.

#### 3.3.2 Scattering Measurement Setup

Figure 3-3b represents the experimental setup used to measure the scattered light behind the sample. In this set of experiments the angle of illumination ( $\theta$ ) was fixed at a certain value between  $0^\circ$  and  $40^\circ$  and the angle of collection ( $\beta$ ) was varied between  $-40^\circ$  and  $40^\circ$ , with respect to the sample normal, to collect the scattered light. Throughout the measurements the sample was infiltrated with ethanol or cyclohexane.

In order to gain a deeper understanding of the properties of the scattered light behind the sample, the white light source in Figure 3-3b was replaced by a tunable dye laser in the range 600-650 nm using Rhodamine 6G or Sulforhodamine B. A 6 W Argon Ion laser was used as a pump source. During the experiments the emission power of the dye laser was about 400 mW with 3W pumping power. The flexible fiber was replaced by a camera to record the spatial pattern of the scattered light behind the sample as a function of wavelength, angle of incidence ( $\theta$ ), and refractive index contrast. In the measurements the camera was parallel to the (111) planes of the sample.

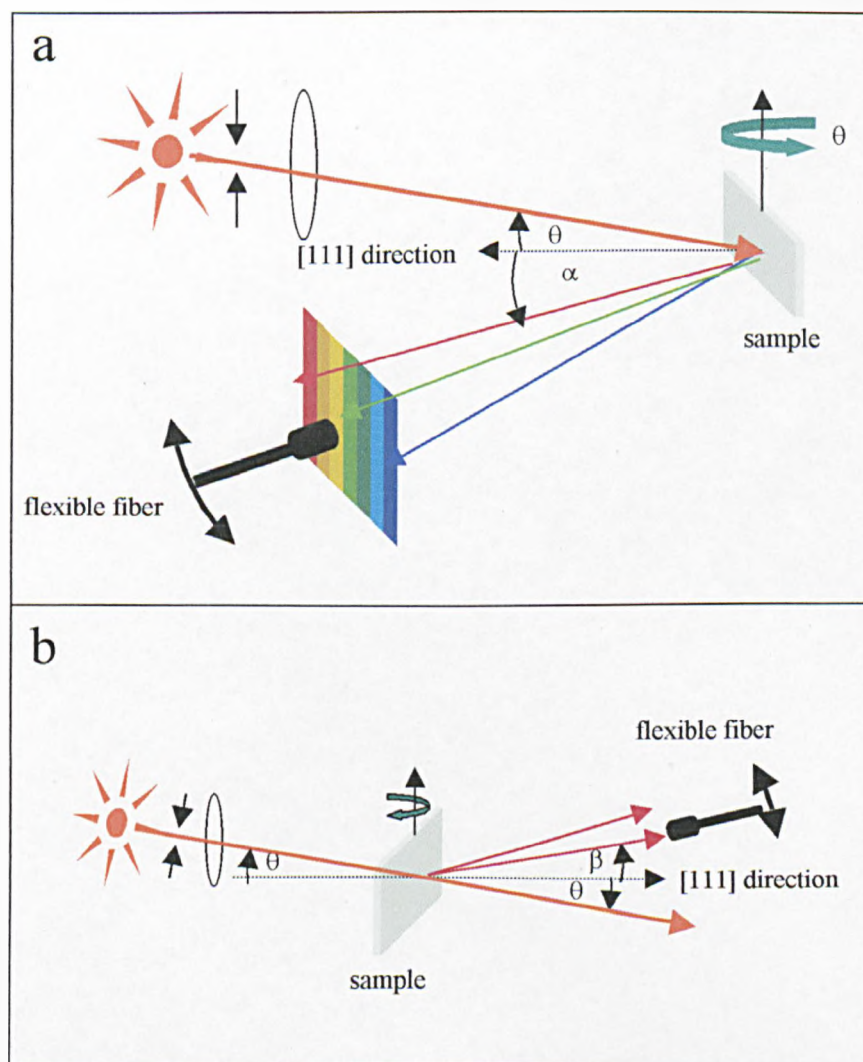


**Figure 3-3 (a) Diffraction measurements setup (b) Scattering measurements setup.**

### 3.4 Diffraction Results

In this section, the properties of the diffracted light in front of the sample (see Figure 3-2) will be discussed. Illuminating the sample at a certain angle of incidence ( $\theta$ ) gives rise to a particular diffraction pattern, found to be composed of coloured stripes as in Figure 3-3a. Simple characterisation of the diffracted pattern in front of the sample showed that as the angle of incidence ( $\theta$ ) increases the diffracted pattern becomes more dispersed and more coloured stripes appear. To study the diffracted pattern precisely, the angle resolved diffraction technique was implemented (see section 3.3.1) to measure the diffracted spectra in front of the sample. The spectra were measured as a function of angle of incident  $\theta$ , angle of collection  $\alpha$  and refractive index contrast.

#### 3.4.1 Results in Ethanol

Figure 3-4 shows the angle resolved diffraction spectra for sample A infiltrated with ethanol ( $n=1.36$ ) for fixed  $\theta$  of  $30^\circ$  and varying  $\alpha$  from  $9^\circ$  to  $45^\circ$  with  $4.5^\circ$  step. A well defined peak with width  $\sim 13$  nm is observed at all  $\alpha$ , peaking in intensity at the specular condition  $\theta = \alpha = 30^\circ$ . As the angle of collection  $\alpha$  increases the peak position shifts to shorter wavelengths. It is important to notice that the widths of the diffraction peaks in Figure 3-4 are three times less than the width of the transmission stop band for the same angle of incidence ( $\theta=30^\circ$ ). This point will be discussed in more detail in section 3.4.3.

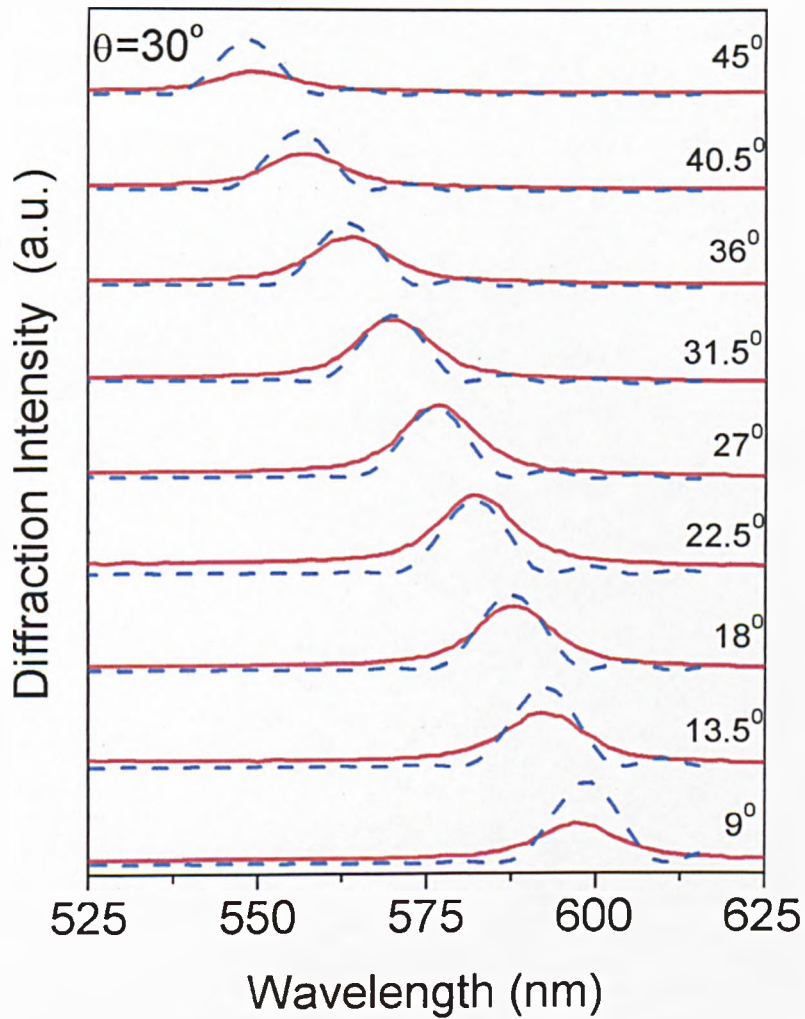


Figure 3-4 Experimental angle-resolved spectra on ethanol (full) for  $\theta = 30^\circ$  and  $\alpha$  varying from  $9^\circ$  to  $45^\circ$  compared with theoretical reflectivity spectra for fcc structures with  $n_{\text{void}}=1.36$  and  $n_{\text{SiO}_2}=1.33$  (dashed). In the calculations, the structure has a thickness of  $11.2 \mu\text{m}$  corresponding to 48 close-packed (111) layers with interplane spacing of  $d_{111} = 233\text{nm}$ . The measured peak intensities are normalised to fit the calculated spectra at the specular condition  $\alpha = \theta = 30^\circ$ .

The observed diffraction peaks are attributed to specular reflections from microcrystallites whose orientation fulfills the Bragg's law  $2d_{111}n_{av}\cos(\phi)=\lambda$  as represented schematically in Figure 3-5a. In order to give this interpretation quantitative support, we note that for each pair of  $\theta$  and  $\alpha$  there is a Bragg angle ( $\phi$ ) of incidence for the system of (111) planes inside the effective medium as presented in Figure 3-5b. The Bragg angle ( $\phi$ ) can be related to the external angles  $\theta$  and  $\alpha$  using Snell's law as follows:

$$\phi = \frac{1}{2}(\theta' + \alpha')$$

and from Snell's law

$$\phi = \frac{1}{2} \left[ \sin^{-1} \left( \frac{\sin(\theta)}{n_{av}} \right) + \sin^{-1} \left( \frac{\sin(\alpha)}{n_{av}} \right) \right] \tag{3.1}$$

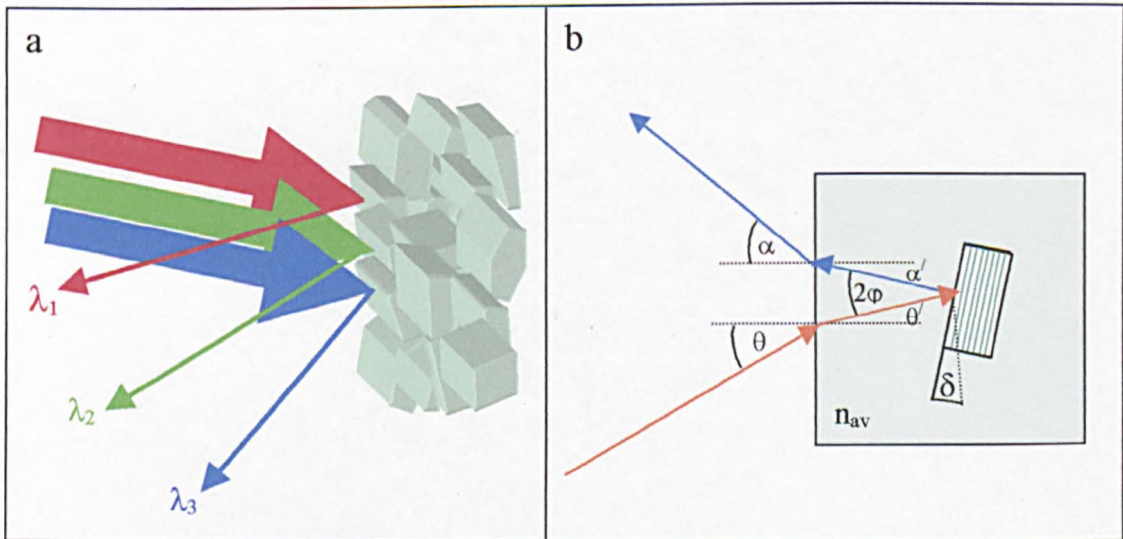


**Figure 3-5 (a) Schematic presentation of the diffraction phenomena in ensemble of polycrystalline opals (b) in a single domain.**

In Figure 3-6a the positions of the diffracted peaks are plotted against the angle of collection ( $\alpha$ ). The experimental data are well fitted to Bragg's law with equation (3.1). The combination between Bragg's law and equation (3.1) perfectly describe the

angular dispersions of the positions of the diffraction peaks for a very broad range of angles  $\theta$  and  $\alpha$  varying from 0 to 60° as shown in Figure 3-6a. In the fit the following parameters have been used,  $n_{\text{SiO}_2} = 1.33$  as the refractive index matching experiment indicated in section 2.8.1,  $n_{\text{pores}} = 1.36$ , and  $d_{111} = 233$  nm as extracted in section 2.8.1.

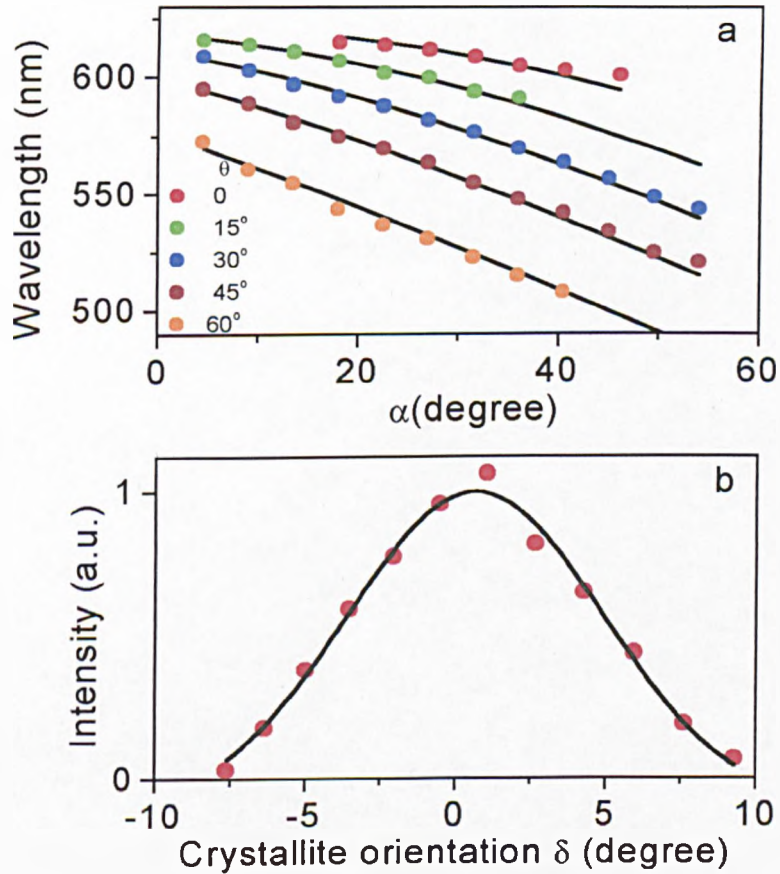


**Figure 3-6 (a) Measured angular dispersions of the center of the stop bands in ethanol for  $\theta = 0^\circ, 15^\circ, 30^\circ, 45^\circ,$  and  $60^\circ$  as a function of  $\alpha$  (symbols), and calculated using Bragg's law with equation (3.1) (full lines). (b) Measured intensity of the peak as a function of rotation of (111) planes relative to the plane of sedimentation (symbols), and Gaussian fit (full line).**

To go further in the analysis of the experimental spectra according to this model, the reflectivity spectra from a series of perfectly ordered fcc lattices were calculated. In the calculations, each lattice was slightly rotated to represent the domain structure of the material. The calculation procedure was as follow

1. Calculate the equivalent Bragg angle ( $\phi$ ) for each pair of  $\theta$  and  $\alpha$  according to equation (3.1). For example the equivalent Bragg angle for  $\theta=30^\circ$  and  $\alpha=9^\circ$  is  $\phi=14.3^\circ$ .
2. The calculated Bragg angle ( $\phi$ ) in step 1 was considered as an angle of incidence on the surface of the lattice in the calculations.
3. To avoid any refraction effect from the surface of the lattice and to fulfill the specular condition for each combination of the external angles  $\theta$  and  $\alpha$ , the electromagnetic waves were launched on the surface of the lattice from a medium of refractive index equal to the average refractive index of the lattice (1.34 in the case of opal infiltrated with ethanol).
4. The reflectivity spectra were calculated for lattices with different thickness (11.2  $\mu\text{m}$ , 22.4  $\mu\text{m}$ , 45  $\mu\text{m}$  and 90  $\mu\text{m}$ ).

Good agreement was achieved between the experimental and calculated spectra for lattices of thickness 11.2  $\mu\text{m}$  as illustrated in Figure 3-4. In Figure 3-4 the intensity of the experimental peaks are normalised to fit the calculated spectra at the specular condition  $\theta = \alpha = 30^\circ$ . The calculated spectra describe the position and the width of the experimental spectra very accurately. The thickness of the lattices used to fit the spectra in Figure 3-4 is less than the Bragg attenuation length (43  $\mu\text{m}$ ), which means that there is homogeneous broadening (FWHM =10 nm) in the calculated spectra due to the finite size of the lattices. At the same time the calculated spectra for thicker material show narrowing in the stop band by a factor 3 and rectangular shape for the

reflectivity spectra indicating 100% reflectance, which is not seen in the experimental spectra. These results show that the domains inside the sample are rather thin with thickness about 10  $\mu\text{m}$ , in agreement with the conclusion obtained from the thickness dependence measurements in section 2.8.3.

Figure 3-4 allows us to study the distribution of the domain orientations in the sample by comparing the intensities of the calculated and measured peaks. As can be seen in Figure 3-4 the intensities of the experimental spectra decay rapidly away from the specular condition ( $\theta = \alpha = 30^\circ$ ) for small and large values of  $\alpha$  in comparison with the calculated spectra, showing a preferential orientation around the [111] growth direction of the sample. Figure 3-6b shows the variation of the diffracted intensity

with the deviation angle of the domain  $\delta = \frac{1}{2} \left[ \sin^{-1} \left( \frac{\sin(30^\circ)}{n_{av}} \right) - \sin^{-1} \left( \frac{\sin(\alpha)}{n_{av}} \right) \right]$ . The

domains in the sample have an approximately Gaussian distribution with FWHM of  $10^\circ$  around the [111] direction.

From the above discussion, we conclude that self assembled opal is a polycrystalline material and consists of domains. The thickness of these domains is about 10  $\mu\text{m}$ . The domains inside opals are misoriented with a Gaussian distribution of  $10^\circ$  of FWHM around the [111] direction.

### 3.4.2 Results in Cyclohexane

Figure 3-7a shows the angle resolved diffraction spectra for sample A infiltrated with cyclohexane ( $n=1.43$ ) for fixed  $\theta=30^\circ$  and varying  $\alpha$ . As in the case of ethanol, the diffraction spectra in cyclohexane peak in intensity at the specular condition and decay rapidly away from the specular condition for small and large  $\alpha$ . The positions of the diffracted peaks are very well fitted to Bragg's law with equation (3.1) for a wide range of  $\theta$  and  $\alpha$  as shown in Figure 3-7b. To fit the diffraction spectra in Figure 3-7a, the reflectivity spectra from a series of perfectly ordered lattices were calculated according to the procedure described in the previous section. Good fits, in both position and width, are obtained to the experimental spectra when the thickness of the lattices in the calculations equals  $11.2 \mu\text{m}$  as shown in Figure 3-7a. Analysing the intensity of the diffracted peaks with angle of deviation ( $\delta$ ) gave a Gaussian distribution for the domains around the [111] direction of the sample with FWHM  $10^\circ$  as in the ethanol case (see Figure 3-6b).

In the last two sections, the angular resolved diffraction technique was used to study the diffracted light in front of the sample infiltrated with ethanol or cyclohexane. The results showed that self assembled opal consists of domains with Gaussian distribution of FWHM of  $10^\circ$  around the growth direction. Theoretical modeling of the diffraction spectra indicated that the thickness of the domains in the sample is about  $10 \mu\text{m}$ , which is smaller than the Bragg attenuation length in the case of ethanol and comparable to the Bragg attenuation length in the case of cyclohexane. Therefore the reflectivity spectra from the domains have homogeneous broadening due to the finite thickness of the domains. In the next section this information is used to explain the broadening effect in the zero order transmission spectra (Figure 3-1).

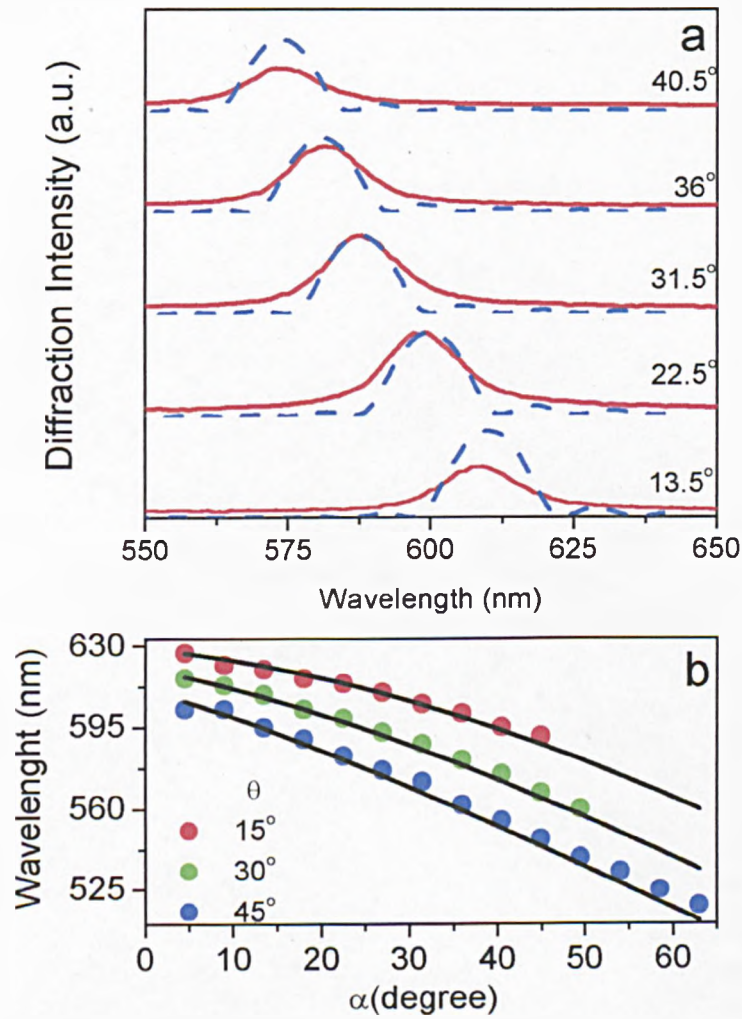


**Figure 3-7 (a)** Experimental angle-resolved spectra in cyclohexane (full) for  $\theta = 30^\circ$  and  $\alpha$  varying from  $13.5^\circ$  to  $40.5^\circ$  compared with theoretical reflectivity spectra for fcc structures with  $n_{\text{void}}=1.43$  and  $n_{\text{SiO}_2}=1.33$  (dashed). In the calculations, the structure has a thickness of  $11.2 \mu\text{m}$  corresponding to 48 close-packed (111) layers with interplane spacing of  $d_{111} = 233\text{nm}$ . The measured peak intensities are normalised to fit the calculated spectra at the specular condition  $\alpha = \theta = 30^\circ$ . **(b)** Measured angular dispersions of the center of the stop bands in cyclohexane for  $\theta = 15^\circ, 30^\circ$  and  $45^\circ$ , as a function of  $\alpha$  (symbols), and calculated using Bragg's law with equation (3.1) (full lines).

### 3.4.3 Interpretation of the Broadening Effect in the Transmission Spectra

As we discussed in section 3.2, light incident on the opal undergoes three mechanisms; Transmission ( $I_{zero}$ ); diffraction in front of the sample ( $I_{diff}$ ); and scattering behind the sample ( $I_{scat}$ ). Due to the absence of absorption in the silica within the investigated region, the balance of beams originated from the slab of opal can be represented as (see Figure 3-2):

$$I_{inc} = I_{zero} + I_{diff} + I_{scat} \quad (3.2)$$

where  $I_{inc}$  is the intensity of the incident beam,  $I_{zero}$  is the intensity of the zero order transmitted beam measured along the line-of-sight direction behind the sample,  $I_{diff} = \sum I_{front}$  is the integrated intensity of the beams diffracted in front of the sample,  $I_{scat} = \sum I_{behind}$  is the integrated intensity of beams scattered behind the sample. Equation (3.2) can be rewritten as

$$I_{inc} = I_{zero} + \sum I_{front} + \sum I_{behind} \quad (3.3)$$

#### 3.4.3.1 Ethanol Case

The observed inhomogeneous broadening in the transmission spectra stems from the fact that the total intensity of light rejected from the zero order beam at the stop band wavelengths does not arise from a single Bragg diffraction peak in front of the sample, but it arises from a series of Bragg diffraction peaks with different wavelengths resulting from the domain distribution inside the sample. Each diffraction peak is homogeneously broadened due to the finite thickness of the domains in the sample. To illustrate this mechanism of broadening clearly, the diffraction peaks measured at  $\theta = 30^\circ$  and different  $\alpha$  are combined on a single plot in Figure 3-8a. The envelope curve in Figure 3-8a represents  $I_{diff} = \sum I_{front}$  for  $\theta = 30^\circ$ .

The FWHM of envelope curve is 40 nm. From  $I_{diff}$  the forward transmission curve can be calculated using  $F = I_{inc} - \sum I_{front}$ . In Figure 3-8b  $F = I_{inc} - \sum I_{front}$  is compared with the transmission spectrum at  $\theta = 30^\circ$ . It is clearly seen that the position, width and strength of the envelope curve fit very well the shape of the transmission spectrum. This agreement between  $I_{zero}$  and  $F$  in Figure 3-8b indicates that the scattering term  $I_{scat} = \sum I_{behind}$  in the balance equation (3.2) does not play a significant role in the case of very low refractive index contrast. This conclusion agrees with the direct measurements of the scattered intensity behind the sample (discussed later in section 3.5) which showed that the scattered term  $I_{scat} = \sum I_{behind}$  constitutes only a few percent of  $I_{inc}$  at all frequencies, while  $I_{zero} \sim I_{diff} = \sum I_{front} \sim 50\% I_{inc}$ . From the above results we conclude that the broadening in the transmission spectra in the case of very low refractive index contrast is controlled by the coherent Bragg diffraction due to the polycrystalline structure of the sample and the homogeneous broadening due to the finite thickness of the domains. Understanding the dominant scattering mechanism of light inside the sample allows us to explain fully the transmission spectra in the case of ethanol. As we discussed in chapter 2, the experimental transmission spectra become broader with increasing the angle of incidence  $\theta$ . The explanation of this observation now becomes clear. The width of the stop band in the transmission spectra is proportional to the angle of the diffracted cone in front of the sample. As the angle of incident  $\theta$  increases, we access more domains with different orientations and thus the angle of the diffracted cone in front of the sample increases and consequently the width of the stop band. This argument can be easily seen by comparing the diffracted spectra for  $\theta = 30^\circ$  in Figure 3-8a and the diffracted spectra for  $\theta = 15^\circ$  in Figure 3-8c.

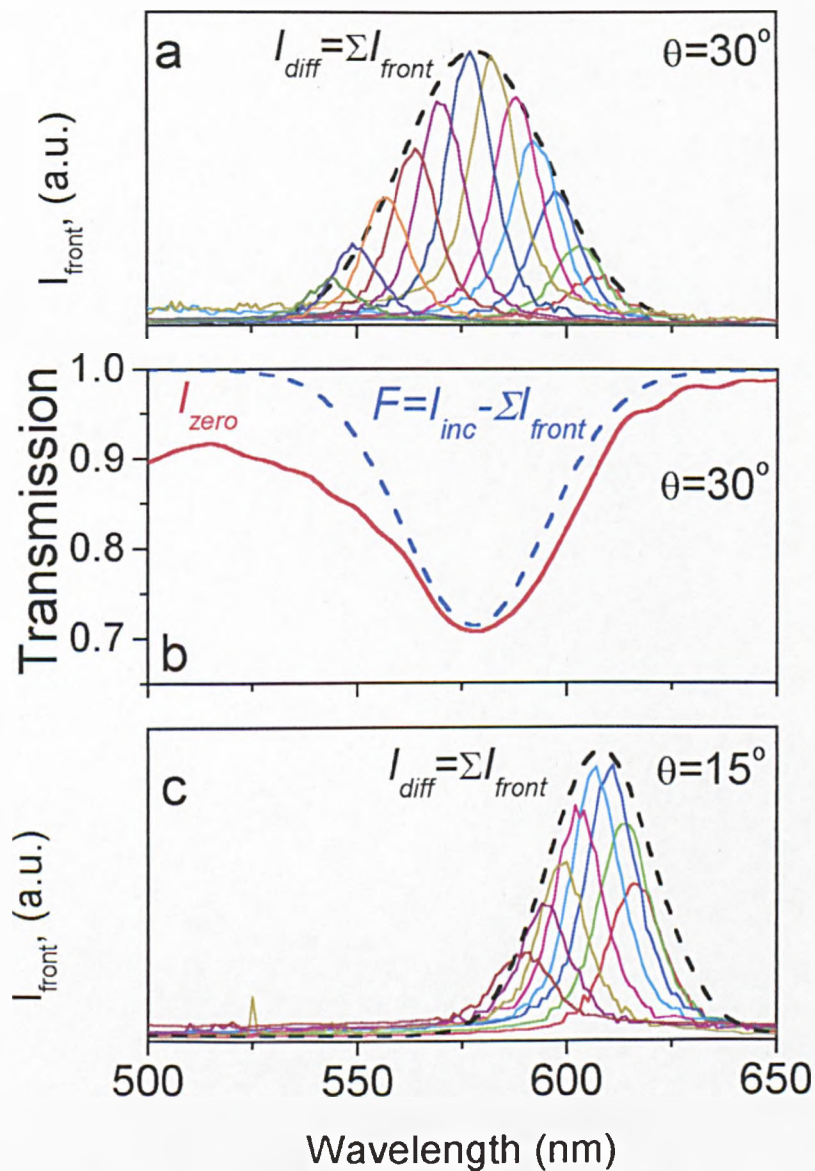


Figure 3-8 (a) Experimental diffraction peaks for  $\theta = 30^\circ$  in the case of infiltration with ethanol (same as in Figure 3-4) represented without vertical shift (full lines). The envelope function (dashed) represents the spectral shape of the term  $\sum I_{front}$  in the balance Equation (3.2). (b) Experimental zero-order transmission spectrum,  $I_{zero}$ , in ethanol at  $\theta = 30^\circ$  (full) and the function  $F = I_{inc} - \sum I_{front}$  (dashed). The function F is normalised for direct comparison with  $I_{zero}$ . (c) Experimental diffraction peaks for  $\theta = 15^\circ$  in the case of infiltration with ethanol. The envelope function (full line) represents the spectral shape of the term  $\sum I_{front}$  in the balance Equation (3.2).

### 3.4.3.2 Cyclohexane Case

The same procedure used to treat the ethanol data in section 3.4.3.1 was used to treat cyclohexane data where the refractive index contrast is large. The results for  $\theta=30^\circ$  are illustrated in Figure 3-9. The position of the envelope function ( $I_{diff} = \sum I_{front}$ ) agrees with the position of the stop band in the transmission spectrum. However, the function  $F=I_{inc}-\sum I_{front}$  can not explain the broadening, the strength, and the shape of the background especially at the short wavelengths in the transmission spectrum. The difference between the function  $F=I_{inc}-\sum I_{front}$  and the transmission spectrum indicates that the scattering behind the sample ( $I_{scat} = \sum I_{behind}$ ) plays an important role in the shape of the transmission spectrum in the case of large refractive index contrast. To have an idea about the scattered light behind the sample, the scattering term in the balance equation was calculated as  $I_{scat} = \sum I_{behind} = I_{inc} - I_{zero} - \sum I_{front}$  and is presented in Figure 3-9c. It is seen that the scattering term  $I_{scat} = \sum I_{behind}$  has a magnitude comparable with  $I_{zero}$  in the whole range of wavelengths, except at the stop band frequencies where  $I_{scat} = \sum I_{behind}$  completely dominates  $I_{zero}$ . The interesting feature in the scattering term  $I_{scat} = \sum I_{behind}$  is the enhancement in the scattering intensity at the edges of the stop band. This effect is thus responsible for the additional broadening in the transmission spectra.

To prove the argument above, we have performed scattering measurements behind the sample. The scattering spectra have been measured as a function of angle of illumination  $\theta$ , angle of collection  $\beta$ , and refractive index contrast. The results will be the subject of the next section.

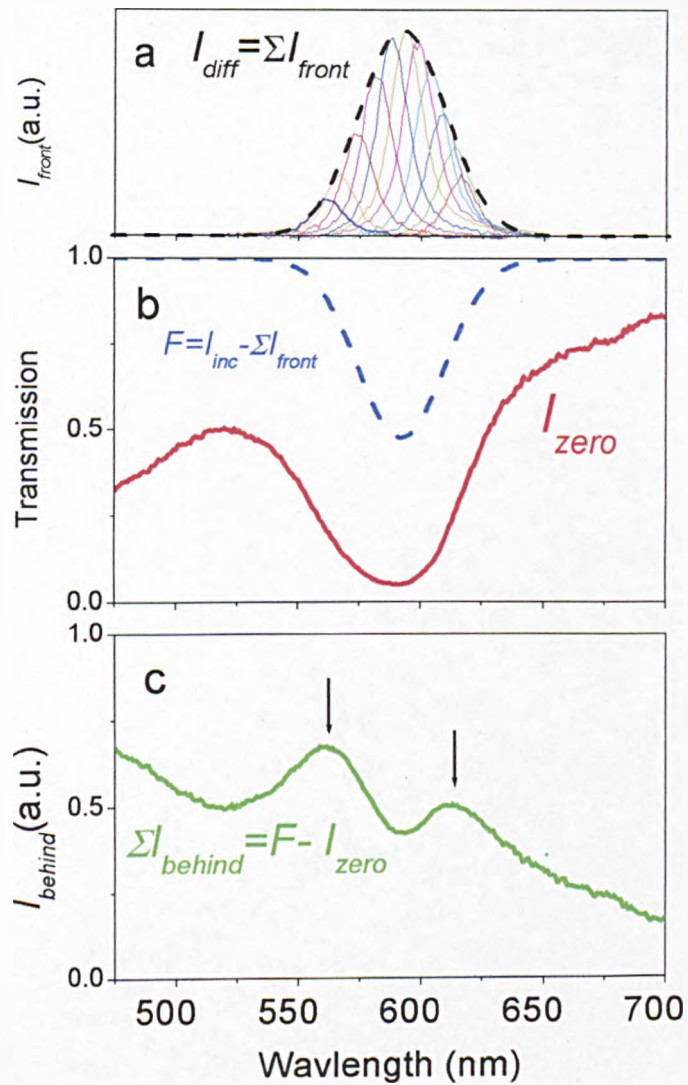


Figure 3-9 (a) Experimental diffraction peaks for  $\theta = 30^\circ$  in the case of infiltration with cyclohexane at different angles  $\alpha$  from  $9^\circ$  to  $45^\circ$  (full lines). The envelope function (dashed) represents the spectral shape of the term  $\sum I_{front}$  in the balance equation (3.2). (b) Experimental zero-order transmission spectrum,  $I_{zero}$ , in cyclohexane at  $\theta = 30^\circ$  (full) and function  $F = I_{inc} - \sum I_{front}$  (dashed). (c) The spectral shape of the angle-integrated scattering behind the sample, as deduced from  $\sum I_{behind} = F - I_{zero}$ . The two marked peaks indicate resonant enhancement of scattering at the stop band edges.

### 3.5 Scattering Results

From the results of section 3.4.3.2, we found that the scattering term ( $I_{scat} = \sum I_{behind}$ ) in the balance equation (3.2) plays an important role in determining the properties of the stop band in opals in the case of strong refractive index contrast (cyclohexane). In this section, we will discuss the results of the scattering measurements behind the sample in two cases: (i) weak Bragg attenuation length ( $L_{B_{exp}} \geq t$ ) as in the case of ethanol, (ii) strong Bragg attenuation length ( $L_{B_{exp}} < t$ ) as in the case of cyclohexane.

#### 3.5.1 Scattering in the Regime of Weak Bragg Attenuation Length

According to the analysis in section 3.4.3.1 (ethanol), the scattering term ( $I_{scat} = \sum I_{behind}$ ) is just a few percent and does not play an important role in the balance equation (3.2), thus determining the properties of the stop band in the case of weak Bragg attenuation length (ethanol). However, we found that the scattering in this case is still fully representative of the general properties of the light scattering in opals and very helpful in understanding the physical mechanisms of this type of scattering.

In order to characterise the spatial pattern of the scattered light behind the sample, the sample was illuminated using a single wavelength of light provided from a dye laser as described in section 3.3.2. The main observations are that the scattering is resonantly enhanced at the stop band energies, and in addition gives rise to an additional beam of light behind the sample as shown in Figure 3-10. The additional beam has very different properties from conventional scattering which gives rise to a diffuse halo surrounding the zero-order transmitted beam (see the difference between the scattering images at 620 nm and 650 nm in Figure 3-10).

The additional beam appears at the stop band energies, whilst the diffuse halo occurs for a wide range of wavelengths. The additional beam is characterised by a broad cone of directions, centred around the normal to the sample for any angle of incident  $\theta$ . In contrast the diffuse halo is scattered in a much narrower cone around the zero order beam. In the case of oblique incidence the additional beam is separated from the diffuse halo. Whilst for normal incidence ( $\theta=0$ ) the additional beam and the diffuse halo are superimposed forming a symmetrical (relative to the normal) spatial distribution of scattered light behind the sample

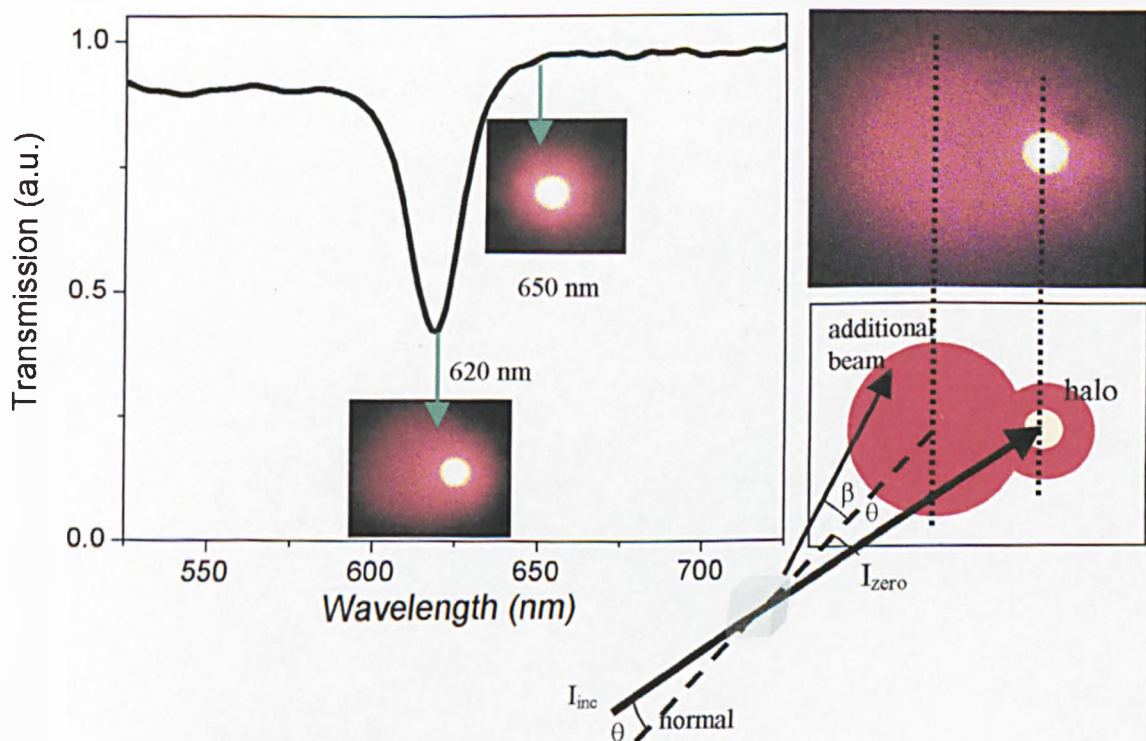


**Figure 3-10** Patterns of scattered light behind the sample (ethanol) observed in the case of illumination at  $\theta=15^\circ$  by a tunable dye laser of wavelength 620 nm in the stop band region and 650 nm out of the stop band region. The resonantly enhanced scattering manifests itself as an additional beam, shown for clarity in the schematic sketch. It is scattered in a broad cone of directions represented by the angle  $\beta$  (from the normal). The white circle represents the zero-order transmitted beam surrounded by a diffuse halo.

In order to characterise the additional beam, the angular-resolved scattering technique was implemented (see section 3.3.2). Scattering spectra were measured as a function of angle of incident  $\theta$  and angle of collection  $\beta$ .

Figure 3-11a and Figure 3-11b show scattering spectra for different angle of incidence  $\theta$  measured at  $\beta = 0$  and the scattering spectra for normal incidence  $\theta = 0$  measured at different angles of collection  $\beta$ , respectively. The spectra exhibit a peak due to the additional beam (see Figure 3-10) and an almost wavelength independent background from the diffuse halo. The amplitude of the peak is comparable with the background for small  $\theta$  and  $\beta$ . For increasing  $\theta$  or  $\beta$ , the background decreases rapidly and the peak increases relative to the level of the background by at least an order of magnitude, as seen in the green spectra in Figure 3-11a or b. The position (620 nm) and width (FWHM  $\sim 10$ nm) of the peak at small  $\theta$  and  $\beta$  correlate with that of the stop band in the zero-order transmission spectra at  $\theta = 0$ , as seen by comparison with Figure 3-11c. As the angle  $\theta$  or  $\beta$  increases the peak displays a slight shift to shorter wavelengths accompanied by weakening and broadening. It is important to stress that the shift of the peak position as a function of  $\theta$  or  $\beta$  is very weak compared to the shift of the stop band with the angle of incident see Figure 3-12.

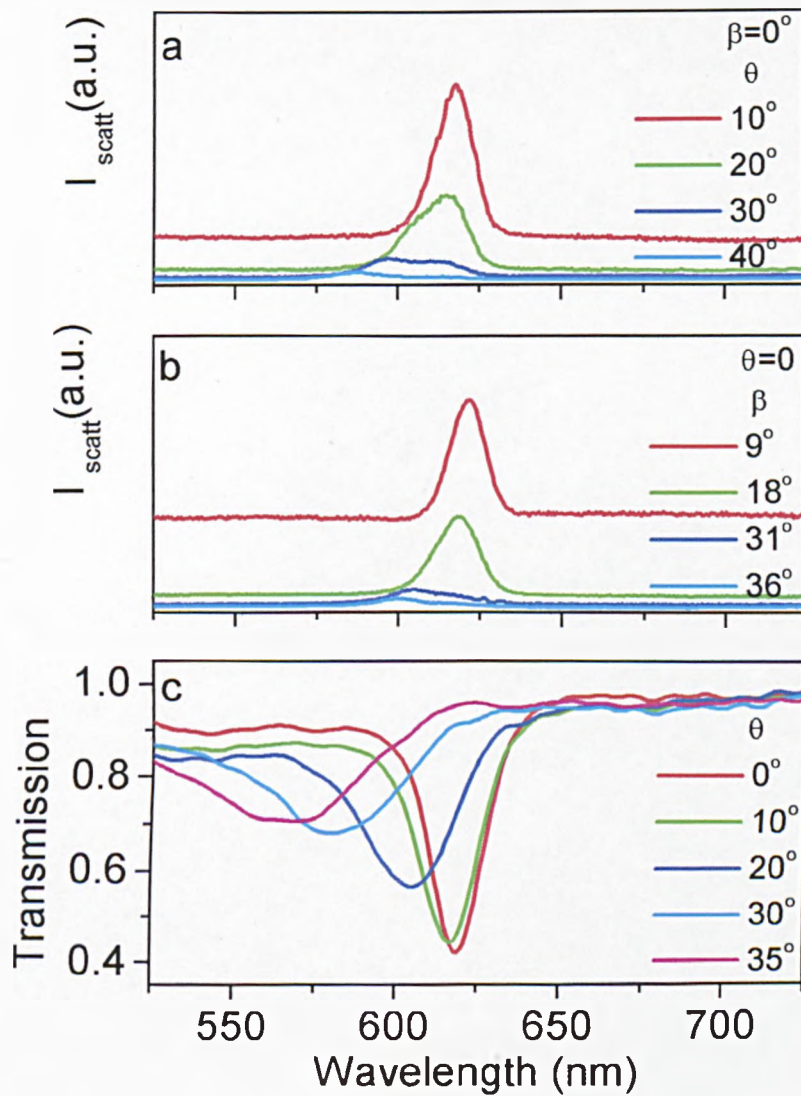
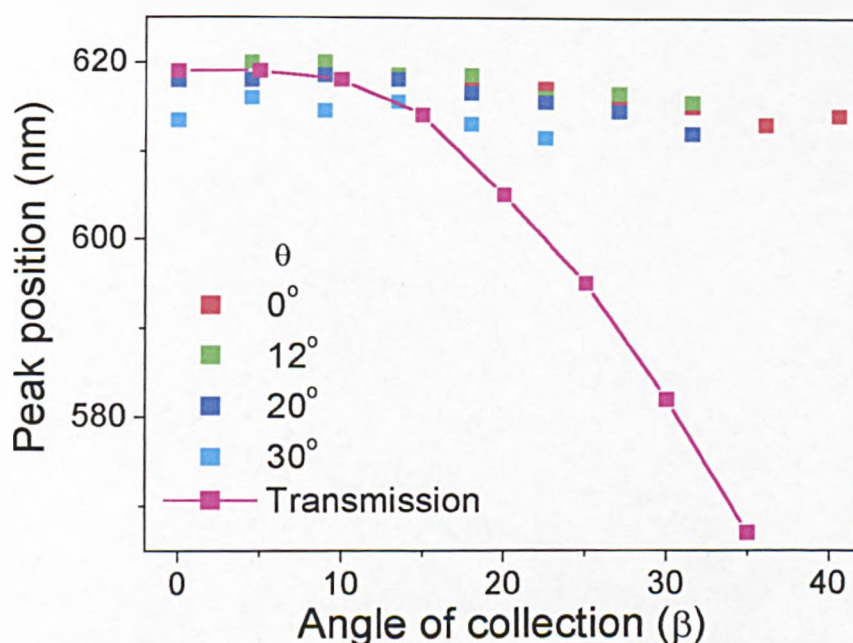


Figure 3-11(a) Experimental scattering spectra for various angle of incidence ( $\theta$ ) measured at  $\beta = 0^\circ$  in the case of infiltration with ethanol (b) Experimental scattering spectra for normal incidence ( $\theta = 0^\circ$ ) and various scattering angles  $\beta$  from  $9^\circ$  to  $36^\circ$  in the case of infiltration with ethanol. (c) Zero-order transmission spectra for various angles of incidence  $\theta$  from  $0^\circ$  to  $35^\circ$  in the case of ethanol.



**Figure 3-12 Comparison of the angular dependence of the position of the scattering peak and the stop band in ethanol.**

To investigate the directionality of the scattered light behind the sample, the intensity of the scattered peak (additional beam) and the background (the diffuse halo) were plotted versus the angle of collection  $\beta$  for different values of the incident angle  $\theta$  in Figure 3-13a and Figure 3-13b respectively. The amplitude of the peak was measured from the level of the background. It is seen for each  $\theta$ , the scattering peak occurs over a very broad range of angles  $\beta$  with angular width as large as  $\sim 40^\circ$ , centred either at normal direction for  $\theta < 15^\circ$  or close to the normal for  $\theta > 15^\circ$ . In contrast the background has narrow directionality of  $\sim 15^\circ$  with the direction of maximum intensity occurring along the direction of illumination, as illustrated in Figure 3-13b.

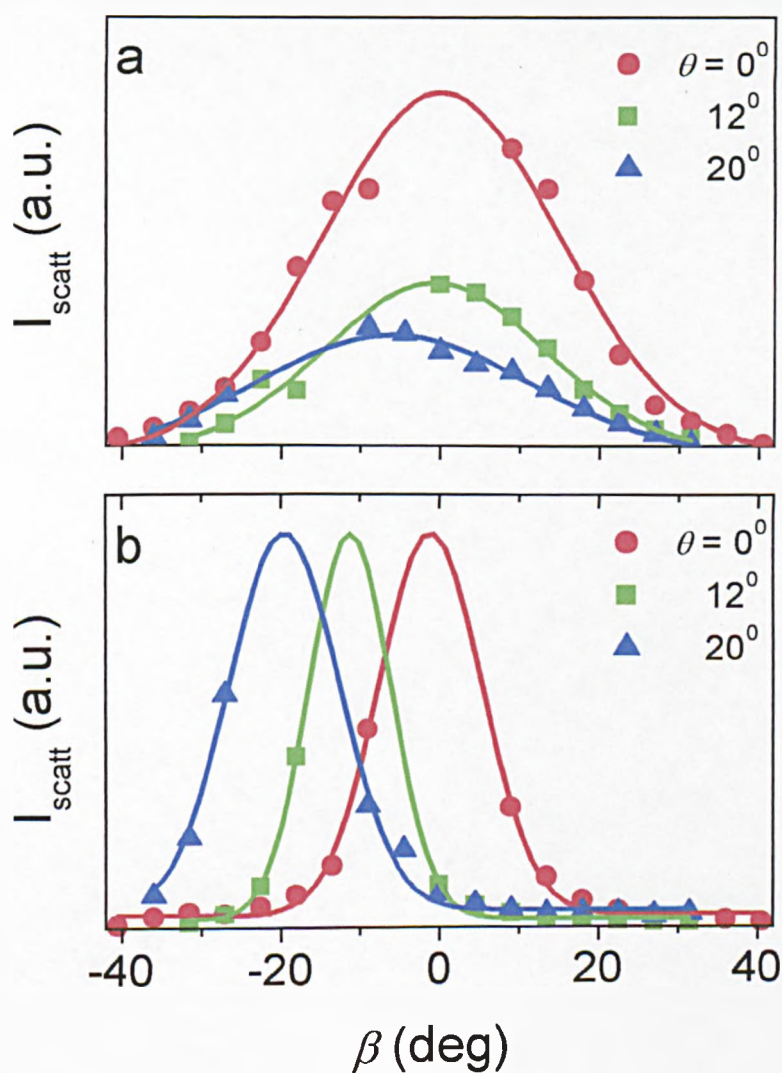


Figure 3-13 Measured angular ( $\beta$ ) distributions of the peak (a) and background at  $\lambda=700$  nm (b) in the scattering spectra (symbols). The amplitude of the peak was measured from the level of the background for  $\theta = 0^\circ, 12^\circ,$  and  $20^\circ$ . The solid lines represent a Gaussian fit to the experimental data.

### 3.5.2 Interpretation of the Scattering Results in Ethanol

In the previous section, we observed a very surprising spectral enhancement behind the sample at or close to the energies of the normal incidence ( $\theta = 0$ ) stop band, rather than spectral suppression as one might expect at this range of energies and along the [111] direction, where Bragg reflection has its maximum value. The analysis of the scattering spectra reveals the following characteristic features of the observed effect of resonant enhancement of scattering:

1. In the limit of small  $\theta$  and  $\beta$  the position of the scattering peak completely coincides with the position of the stop band at normal incident indicating that the Bragg reflectivity along the [111] direction is directly involved in the formation of the scattering peak.
2. The shift in the position of the scattering peak with  $\theta$  and  $\beta$  is very weak in comparison with the shift in the position of the stop band with the angle of illumination  $\theta$  (see Figure 3-12).
3. The peak possesses very broad directionality in comparison with the diffuse scattering around the zero-order beam as illustrated in Figure 3-13.
4. The background of the scattering spectra is wavelength independent (see Figure 3-11).

Before interpreting the scattering results the following points should be noted for opals:

1. Opal is a polycrystalline material and consists of domains. The thickness of each domain is about 10  $\mu\text{m}$  (see section 2.7 and 3.4.1).
2. The domains in opals are misoriented with respect to each other (see section 3.4.1) with a Gaussian distribution of  $10^\circ$  FWHM.

3. The [111] direction is the most important direction in opals since it has the largest structure factor. Hence the (111) plane can be considered as a highly reflecting mirror within the stop band region.

First we explain the background or the diffuse halo around the zero-order direction (see Figure 3-10 and Figure 3-11). This background arises from the structural imperfection in the samples. The fact that the background is wavelength independent indicates that it arises from scattering (mainly refraction and reflection) by particles of irregular shape, large compared to a wavelength<sup>9</sup>, rather than diffraction or scattering by defects of wavelength size. The structural study of the samples in section 2.7 showed that the samples consist of domains and these domains are large in size (50-100  $\mu\text{m}$ ) and irregular in shape. Therefore the main origin of the background or the diffuse halo is the scattering of the light by the sample domains. Another criteria for the background is that it has relatively narrow directionality ( $\sim 15^\circ$  and see as well Figure 3-13) and weak intensity showing that this type of scattering is a single scattering event, in agreement with the fact that the mean free path for the photon ( $l$ ) in the case of ethanol is larger than the sample thickness.

Figure 3-12 and Figure 3-13 show that the scattering peak (additional beam) has a totally different origin from the background (the diffuse halo). There are two parameters that control this phenomenon: (i) the Bragg attenuation length of the individual domain (which can be taken from the theoretical calculations  $L_{B_{\text{theory}}}$ ), (ii) the Bragg attenuation length of the sample (which can be taken from the experiment  $L_{B_{\text{exp}}}$ ). At the Bragg condition each domain can be considered as a highly reflective mirror if  $L_{B_{\text{theory}}} \leq t_{\text{domain}}$ . In the case of ethanol  $L_{B_{\text{theory}}} > t_{\text{domain}}$ , however the (111)

planes of each domain still work as a mirror with 10% reflectivity within the stop band region. This transforms the propagation path of the light within the stop band region into a series of incoherent forward/backward reflections between the different domains. As a result of the interaction length of the light with the sample, the time spent by the light within the scattering medium is enhanced. If  $L_{B_{theory}} \ll t_{domain}$  the incident light will be attenuated within the first layer of domains and the multireflection (forward/backward) of the light between the domains across the sample will not occur, and thus no resonant scattering enhancement will happen (like the case of single crystal). Since the opal system possesses a mechanism for nonresonant scattering (the diffuse halo described above), it is very likely that this mechanism will be resonantly enhanced if both the initial (zero-order beam) and final beams undergo efficient multiple reflection between the domains. The strength of the scattering depends on the total thickness of the sample compared with the Bragg attenuation length of the sample ( $L_{B_{exp}}$ ). For the situation where  $L_{B_{exp}} \ll t$  both the zero-order beam and the scattered light are strongly attenuated in the vicinity of the illuminated surface, hence no scattered light will occur. On the other hand in the case  $L_{B_{exp}} \gg t$  the scattered light will be insignificant in comparison with the zero order beam and no enhancement of the scattered light will occur. From the discussion of the two limiting cases above, we conclude that the strength of the scattering will be optimised if  $L_{B_{exp}} \sim t$ .

The above model allows us to explain the striking spectral enhancement at the centre of the stop band in the [111] direction where attenuation is greater as illustrated in Figure 3-11. For small  $\theta$  and  $\beta$  (around the normal incidence condition) most of the scattered light is reflected back by the domains according to Bragg's law, exactly as

in the case of the zero order beam within the stop band region (see the transmission spectra for  $\theta = 0$  and  $10^\circ$  in Figure 3-11c). Consequently both waves (zero-order and low-angle scattered) are resonantly trapped due to multiple reflections between the domains, at an energy corresponding to the centre of the stop band at normal incidence. In addition, for small  $\theta$  and  $\beta$  the condition  $L_{B_{exp}} \sim t$  is optimum for the incoming beam (incidence) and outgoing beam simultaneously (see table 1 in chapter 2) and resonant enhancement occurs at the centre of the stop band in the [111] direction where the attenuation is greater, explaining the unexpected spectral enhancement at the center of the stop band in the [111] direction as in Figure 3-11a and b.

For large  $\theta$  or  $\beta$  (more than  $30^\circ$ )  $L_{B_{exp}} \gg t$  because of the angular shift and the weakening of the corresponding stop bands (see Figure 3-11c), the amplitude of the peak decreases as has been observed in Figure 3-11a and b. In this case the position of the peak is determined by the convolution of the transmission spectra for the incoming and outgoing waves (for a given  $\theta$  or  $\beta$ ): this occurs very close to the intersection point of the short wavelength edge of the normal incidence stop band and long wavelength edge of the stop band at  $\theta = \beta$ . Therefore the shift in the peak in the scattering spectra is much smaller than the corresponding shift of the stop band in the zero-order transmission spectra.

The broad directionality of the peak in the scattering spectra (see Figure 3-13a) arises from the inhomogeneous broadening of the stop bands in the transmission spectra due to the domain distribution in the sample as has been discussed section 3.4.1. This provides good overlap between the stop bands for transmitted zero-order and scattered waves for a wide range of angles.

### 3.5.3 Scattering in the Regime of Strong Bragg Attenuation Length

As discussed in section 2.8.1 of chapter 2, infiltration of the opal with cyclohexane leads to strong attenuation of the zero-order beam at the stop band energies ( $I \sim 1\%I_{inc}$ ). Thus the Bragg attenuation length of the sample is smaller than the sample thickness ( $L_{B_{exp}} = 60\mu\text{m} < t = 300\mu\text{m}$ ). For opal infiltrated with cyclohexane  $L_{B_{theory}} = 12\mu\text{m} \sim t_{\text{domain}}$  and the (111) planes of each domain reflect  $\sim 63\%$  of the incident light at the stop band energies. Therefore the light will undergo a series of incoherent forward/backward reflections between the different domains inside the sample as in the ethanol case. Since the Bragg attenuation length of the sample is smaller than the sample thickness, resonant enhancement at the centre of the stop band does not occur as in the ethanol case, but it is still possible to observe resonant enhancement at the edges of the stop band, where the condition  $L_{B_{exp}} \sim t$  is satisfied.

Figure 3-14a shows the scattering spectra at normal incidence ( $\theta = 0$ ) and for different angles of collection  $\beta$ . The spectra display a relatively flat background, but now with a stronger intensity and broader directionality of the diffuse halo because of the large refractive index contrast in this case, leading to a reduced mean free path of the photon ( $l$ ) away from the stop band. The resonant behavior is different in this case, instead of a single peak at the centre of the stop band, several resonant features in the stop band region are observed. At small angles ( $\beta \sim 10^\circ$ ), two resonant enhancements of scattering at the stop band edges (peaks at 613 nm and 640 nm) with significant suppression of intensity at the mid gap energy (625 nm) are observed, as predicted in the analyses above. With increasing angle of detection, up to  $\beta = 36^\circ$ , the dip and the long wavelength peak weaken, while the short wavelength peak at 613 nm increasingly dominates the scattering spectra. Again in the case of cyclohexane we

have observed a very complicated spectral enhancement in the stop band region in the [111] direction where attenuation is stronger.

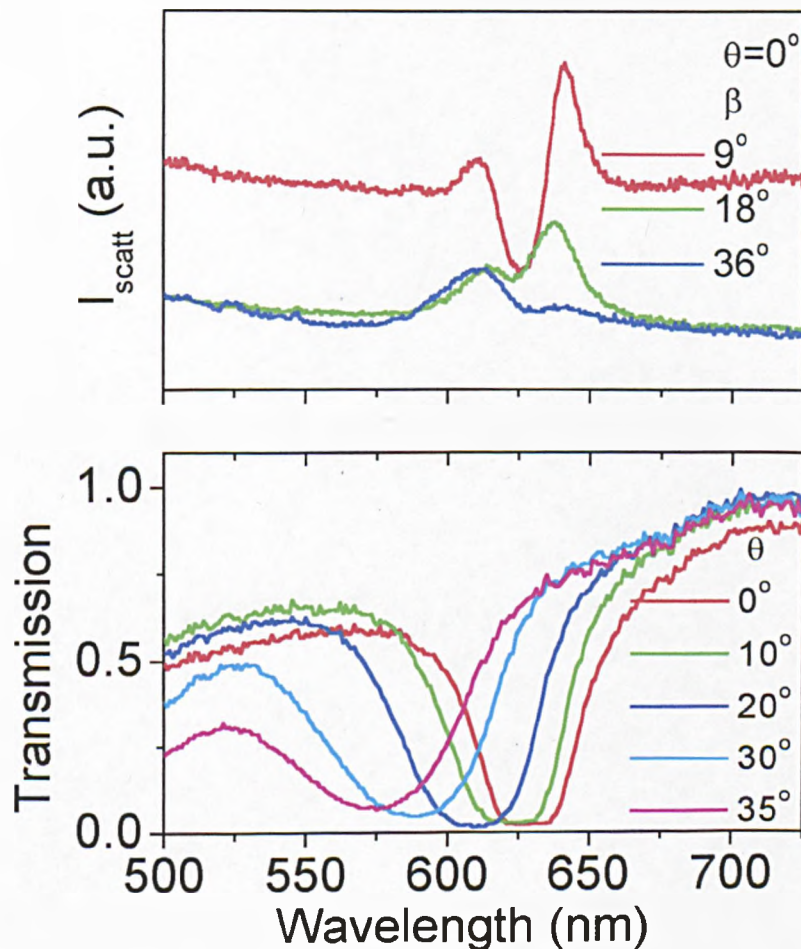


**Figure 3-14 (a) Experimental scattering spectra for normal incidence ( $\theta = 0^\circ$ ) and various scattering angles  $\beta$  from  $9^\circ$  to  $36^\circ$  in the case of infiltration with cyclohexane. (b) Zero-order transmission spectra for various angles of incidence  $\theta$  from  $0^\circ$  to  $35^\circ$  in the case of cyclohexane.**

Using the model which has been developed in section 3.5.2, the shape and the angular evolution of the scattering spectra in cyclohexane can be explained. For small  $\beta$  and at the centre of the stop band  $L_{B_{\text{exp}}} < t$ , the propagation length at the energy of the centre of the stop band is small and very little multiple reflection can occur, hence very little scattered light behind the sample is seen, which explains the appearance of the dip in

the scattering spectra. At the edges of the stop band the condition  $L_{B_{exp}} \sim t$  occurs, explaining the double peak structure in the spectra. For large  $\beta > 30^\circ$  due to the strong shift of the stop band (see Figure 3-14b), the condition  $L_{B_{exp}} \sim t$  can be met for the incoming and outgoing waves simultaneously only at the short wavelength edge of the stop band at normal incidence, leading to a single peak in large-angle scattering.

In order to confirm our model, we have measured the scattering spectra of a wedge sample infiltrated with cyclohexane as a function of the sample thickness. The results are illustrated in Figure 3-16. With increasing sample thickness the dip in the scattering spectra becomes more clear and deeper and the peak shifts toward longer wavelength, confirming our model.

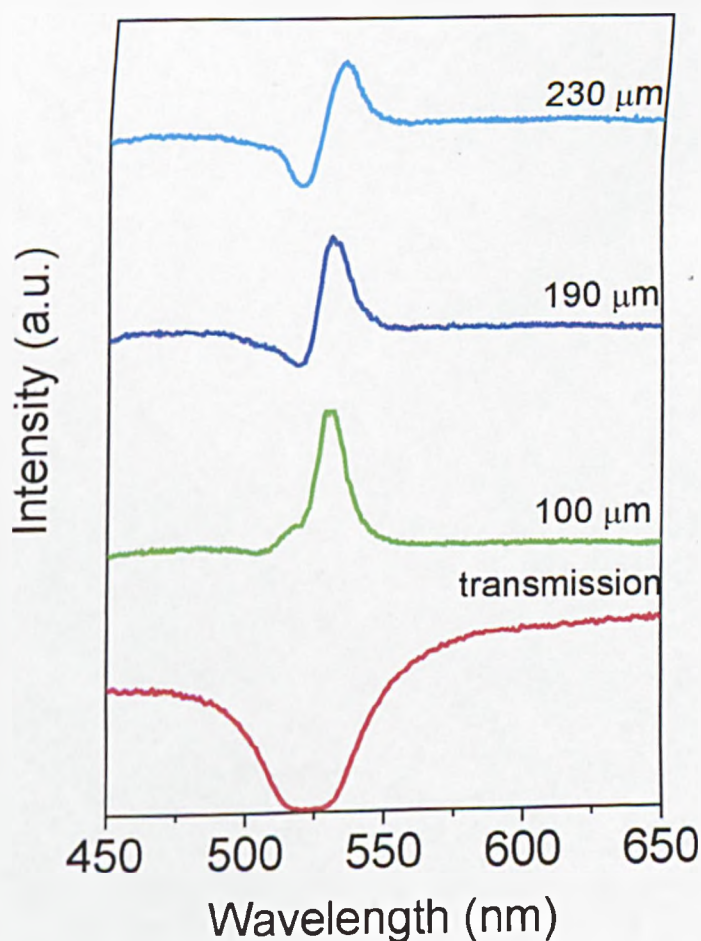
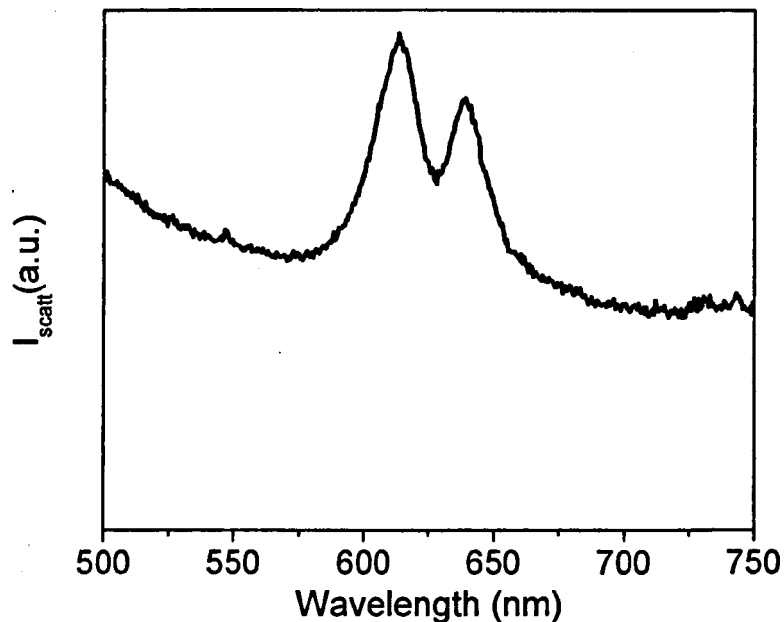


Figure 3-15 Scattering spectra as a function of the sample thickness at  $\theta=12^\circ$  and  $\beta=\text{zero}$ .

Integration of the scattering spectra in Figure 3-14a over all  $\beta$  leads to the term  $I_{scat} = \sum I_{behind}$  in the balance equation. The results are illustrated in Figure 3-16. The overall scattering spectrum consists of two peaks at the stop band edge energies as predicted in section 3.4.3.2 (see Figure 3-9c). The high similarity between the integrated scattering spectrum in Figure 3-16 and the predicted scattering spectrum ( $I_{scat} = \sum I_{behind} = I_{inc} - I_{zero} - \sum I_{front}$ ) in Figure 3-9c provides strong evidence of scattering contribution to total photon flux in the case of strong refractive index contrast and thus validity of the balance equation (equation (3.2)) is proved. These results support our conclusion in section 3.4.3.2 that scattering provides a major contribution to the inhomogeneous broadening of the zero-order stop band spectra for large refractive index contrast.



**Figure 3-16** The angle-integrated scattering behind the sample ( $I_{scat} = \sum I_{behind}$ ), deduced from Figure 3-14a.

From the above analysis we conclude that scattered light in the case of strong refractive index contrast contributes strongly to total photon flux passing through

opals and hence plays an important part of determining the final shape of the transmission spectra.

### 3.5.4 The Spatial Pattern of the Scattered Light in the Regime of Strong Bragg Attenuation Length

In order to investigate the spatial pattern of the scattered light behind the sample in the case of cyclohexane, the scattering patterns were recorded as described in section 3.3.2 for different wavelengths of the incident light. Figure 3-17 shows the scattering patterns measured at an angle of incidence  $15^\circ$  and for different wavelengths; 613 nm (position of the short wavelength peak), 625 nm (position of the dip) and 640 nm (position of the long wavelength peak).

At the position of the long wavelength peak (640 nm) the scattering image consists of a diffuse halo surrounding the zero-order beam and an additional beam close to the normal as in the case of ethanol. At  $\lambda \approx 640$  nm the condition  $L_{B_{\text{exp}}} \sim t$  is optimum and therefore a scattering spot appears as in the case of ethanol.

The scattering image at  $\lambda = 625$  nm (centre of the stop band in the [111] direction) is illustrated in Figure 3-17b. It consists of a bright ring with a dark spot in the range of angles  $-15^\circ < \beta < +15^\circ$ . The explanation of the dark spot in the angles range  $-15^\circ < \beta < +15^\circ$  is straightforward: within this range of angles the scattering is inefficient because  $L_{B_{\text{exp}}} < t$  as we discussed in section 3.5.3. For  $\beta > 15^\circ$  it is possible to approach the condition  $L_{B_{\text{exp}}} \sim t$  and thus the scattering becomes more efficient explaining the bright ring for  $\beta > 15^\circ$ . Also the scattering image at  $\lambda = 625$  nm (see

Figure 3-17b) illustrates the contribution of the scattered light relative to the zero order within the stop band region. It is clearly seen that at the energy of the stop band

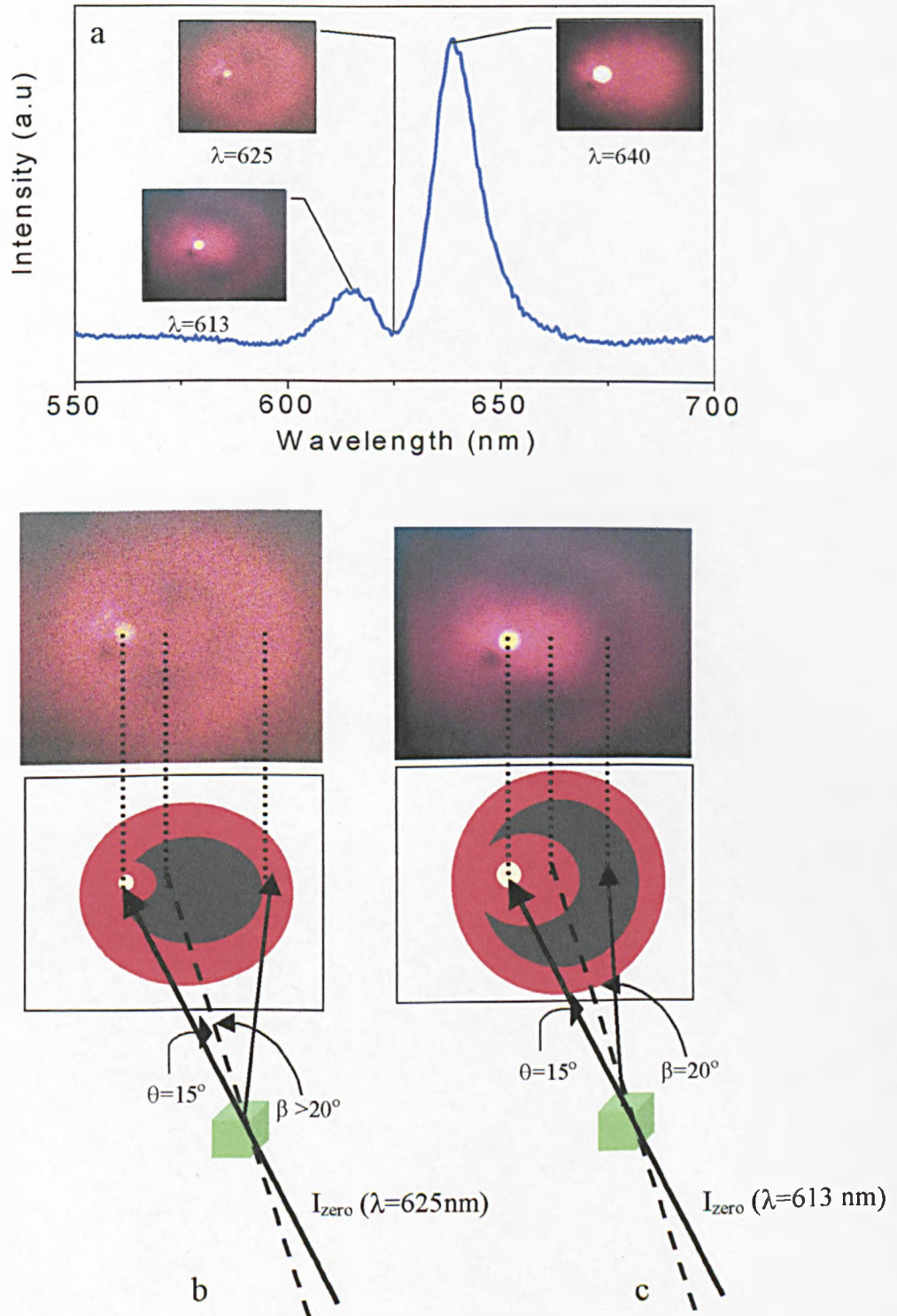


**Figure 3-17 (a) Scattering patterns observed in cyclohexane at  $\theta=15^\circ$  for different wavelengths, the blue curve is the scattering spectrum at  $\theta=15^\circ$  and  $\beta=zero$ . (b) A schematic sketch for the scattering pattern at  $\theta=15^\circ$  and  $\lambda= 625$  nm. (c) A schematic sketch for the scattering pattern at  $\theta=15^\circ$  and  $\lambda= 613$  nm.**

the scattered light exceeds the zero-order beam, in agreement with the conclusion of section 3.4.3.2.

At the position of the short wavelength peak ( $\lambda = 613$  nm), the scattering image is more complicated. It consists of (i) a bright spot around  $\beta \approx 0^\circ$  (ii) a dark ring in the range of angles  $15^\circ < \beta < 25^\circ$  and (iii) a weak bright ring for  $\beta > 25^\circ$ . Around  $\beta \approx 0^\circ$  the condition  $L_{B_{exp}} \sim t$  is optimum thus we have a bright spot. In the range of angles  $15^\circ < \beta < 25^\circ$ , the wavelength 613 nm is at the centre or close to the centre of the stop bands at these angles (see Figure 3-14b) for the incoming and outgoing beams simultaneously, thus we approach the condition  $L_{B_{exp}} < t$  explaining the dark ring in the range of angles  $15^\circ < \beta < 25^\circ$ . For  $\beta > 25^\circ$  the condition  $L_{B_{exp}} \sim t$  is approached again, explaining the weak bright ring for  $\beta > 25^\circ$ .

Furthermore the structure of the scattering image at  $\lambda = 613$  nm in Figure 3-17c can be understood on a more quantitative basis by analysing the intensity of the scattering spectra measured at  $\theta = 15^\circ$  and for different angle of collections  $\beta$ . The result is illustrated in Figure 3-18. In Figure 3-18 the amplitude of the scattered light was measured from the level of the background. From the angular dependence of the scattered intensity at  $\lambda = 613$  nm in Figure 3-18, it is clear that the scattered intensity increases with decreasing the angle of collection in the angular range  $0^\circ < \beta < 15^\circ$  representing a bright spot around  $\beta \approx 0^\circ$  and supporting the above conclusion, around  $\beta \approx 0^\circ$  the condition  $L_{B_{exp}} \sim t$  is optimum at  $\lambda = 613$  nm, thus a bright spot is observed. In the angular range  $15^\circ < \beta < 25^\circ$  the intensity in Figure 3-18 is minimum representing a dark spot in the scattering image (in Figure 3-17c) and proving that  $L_{B_{exp}} < t$  for

$15^\circ < \beta < 25^\circ$ . For  $\beta > 25^\circ$  the scattered intensity increases indicating that the condition  $L_{B_{exp}} \sim t$  is approached again, in agreement with the scattering image in Figure 3-17c.

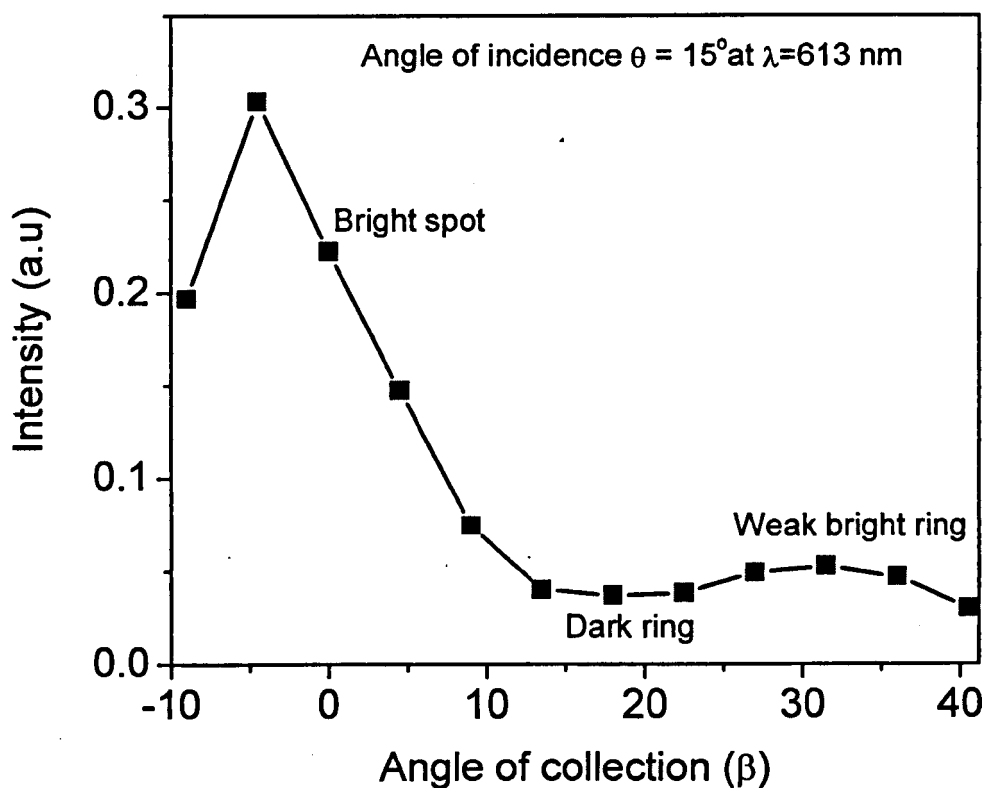


**Figure 3-18** The measured angular ( $\beta$ ) distribution of the scattered light at  $\theta=15^\circ$  and  $\lambda=613$  nm.

### 3.6 Conclusions

In this chapter, the mechanisms responsible for the broadening and weakening of the stop band in self assembled opal photonic crystals have been investigated. In order to understand these mechanisms we have developed experimental techniques, based on simultaneous investigation of the spatial and spectral characteristics of the diffracted and scattered light in all directions around the sample. It is found that the diffracted and scattered light play an important role in the understanding of the spectral form of the transmission stop band.

Due to the polycrystalline structure of the samples, there are two types of scattering in self assembled opal photonic crystals: (i) coherent scattering (Bragg diffraction) which comes from the order in each domain, (ii) incoherent scattering (diffusive propagation of photons) which comes from the disorder in opals. There exists a complex interplay between the coherent and incoherent scattering in opals in the vicinity of the stop band, which appears as a resonant enhancement of scattering at the stop band energies.

Analyses of the coherent diffracted light in front of the sample revealed full information about the polycrystalline structure of the self assembled opal photonic crystals. It is found that opals consist of domains of thickness about 10  $\mu\text{m}$  in the growth direction. The domains possess a Gaussian distribution around the [111] direction of the sample with FWHM of  $10^\circ$ .

The influence of the order and disorder on the properties of the transmission stop band in self assembled opal photonic crystals has been investigated in two cases:

- (i) Weak Bragg attenuation length ( $L_{B_{exp}} \geq t$ ). In this case we found that the broadening and weakening of the transmission stop band stems from the coherent Bragg diffraction of the light due to the domain distribution in the samples. The interplay between the coherent and incoherent scattering light in the vicinity of the stop band was found to be very weak (a few percent of the incident beam) and appeared as a peak in resonance with the centre of the transmission stop band in the [111] direction where the attenuation is greater. The results are attributed to the multiple reflectivity (forward/backward) between the (111) plans of the sample domains.
- (ii) Strong Bragg attenuation length ( $L_{B_{exp}} < t$ ). In this case the coherent Bragg diffraction in front of the sample could not explain the shape of the transmission stop band indicating that the scattering behind the sample plays an important role in determining the shape of the transmission spectra. Analysing the balance of the photon fluxes showed that the scattering term in the balance equation has a magnitude comparable with the zero-order beam for a wide range of wavelengths, except at the frequencies of the stop band where the scattering dominates the zero-order beam. The interplay between the coherent and incoherent scattering light appeared as resonant enhancement at the edges of the stop band in the [111] direction. The enhancement of the scattering at the edges of the stop band was found to be responsible for the additional broadening in the transmission spectra.

### 3.7 References

- <sup>1</sup> - V.N. Astratov, V.N. Bogomolov, A.A. Kaplyanskii, A.V. Prokofiev, L.A. Samoilovich, S.M. Samoilovich, and Y.A. Vlasov, *Nuovo Cimento D* **17**, 1349 (1995).
- <sup>2</sup> - W. L. Vos, M. Megens, C. M. van Kats and P. Bosecke, *J. Phys.: Condens. Matter* **8**, 9503 (1996).
- <sup>3</sup> - I. I. Tarhan and G. H. Watson, *Phys. Rev. Lett.* **76**, 315(1996).
- <sup>4</sup> - H. Miguez, C. Lopez, F. Meseguer, A. Blanco, L. Vazquez, R. Mayoral, M. Ocana, F. Fornes, and A. Mifsud, *Appl.Phys.Lett.* **71**, 1148 (1997).
- <sup>5</sup> - Y.A. Vlasov, M.A. Kaliteevski, and V.V. Nikolaev, *Phys.Rev. B* **60**, 1555 (1999).
- <sup>6</sup> - M. Megens, J.E.G.J. Wijnhoven, Ad Lagendijk, and W.L. Vos, *J.Opt.Soc.Am. B* **16**, 1403 (1999).
- <sup>7</sup> - J. Huang, N. Eradat, M.E. Raikh, and Z.V. Vardeny, *Phys.Rev.Lett.* **86**, 4815 (2001)
- <sup>8</sup> - W.H. Zachariasen, *Theory of X-Ray Diffraction in Crystals* (Dover Publications, New York, 1945).
- <sup>9</sup> - H. C. van de Hulst, *Light Scattering by Small Particles*, (Dover, New York, 1981), 1<sup>st</sup> ed.

## Chapter 4

# Self Assembled Opal Photonic Crystals Infiltrated with Fluorescent Materials and Chalcogenide Glasses

### 4.1 Introduction

Over the last decade the idea of controlling the spontaneous emission of excited atoms using a photonic crystal has attracted the attention of numerous researchers<sup>1-6</sup> due to the importance of this phenomenon for a variety of applications including low threshold laser and high efficiency light emitting devices. Self assembled opal photonic crystals are one of the candidates for the control of spontaneous emission in the ultraviolet and visible regions. The system of the interconnected pores in opals can be infiltrated with active materials such as laser dyes<sup>3,4-7</sup> or semiconductors<sup>8-11</sup>. Furthermore, controlling the spontaneous emission can be complete if a full band gap photonic crystal is used. Self assembled opal photonic crystals can also be used as a template to fabricate an inverted opal structure which is expected to have a complete band gap<sup>12</sup>. In this method the system of the interconnected pores is infiltrated with high refractive index material and then the silica spheres are etched out<sup>10,11</sup>. The air voids of the inverted structure can be used as a host for active materials<sup>4</sup> or sometimes the high refractive index material<sup>7</sup> itself can be used as a light source. However, controlling the spontaneous emission using opals<sup>6</sup> or inverted opals<sup>4,5</sup> depends strongly on the optical quality of the original host material.

In the first part of this chapter the possibility of using self assembled opal photonic crystals to control spontaneous emission will be investigated. Opals were infiltrated with active materials such as laser dyes to study the mechanisms which control the propagation of light generated deep inside a photonic environment. In contrast with the conventional transmission stop band, the fluorescence stop band is found to be much weaker and narrower. This observation is attributed to scattering events which take place inside opals, as we discussed in more depth in the previous chapters where the reflectivity and transmission properties were analysed.

In the second part of this chapter a study of infiltration of self assembled opals with high refractive index chalcogenide glasses will be presented. In this work opals were infiltrated through dipping the samples in a saturated solution of chalcogenide glass. Optical imaging of the samples after infiltration showed that chalcogenide glasses tend to aggregate into submillimeter areas inside opals. Spatially Resolved Reflectivity measurements showed that the distribution of the glass inside the infiltrated areas is uniform and the infiltration ratio inside these areas is about 40%. Further measurements indicated that the infiltration ratio is limited by the blocking of the thin connectivity channels inside opals.

## 4.2 Experimental Details

### 4.2.1 Fluorescence Measurement Setup

The experimental setup illustrated in Figure 4-1 was used to measure the fluorescence spectra of opals infiltrated with dye materials. Fluorescence spectra were obtained by exciting the dye inside the sample with an argon laser of power 40 mW, operating at a wavelength of 488 or 514.5 nm, from the front surface of the sample (see Figure 4-1). The fluorescence was collected from the back surface of the sample using an achromatic doublet lens of focal length 30 mm, and focused onto a slit of a spectrometer (40 Å/mm resolution) coupled to a photomultiplier (PMT).

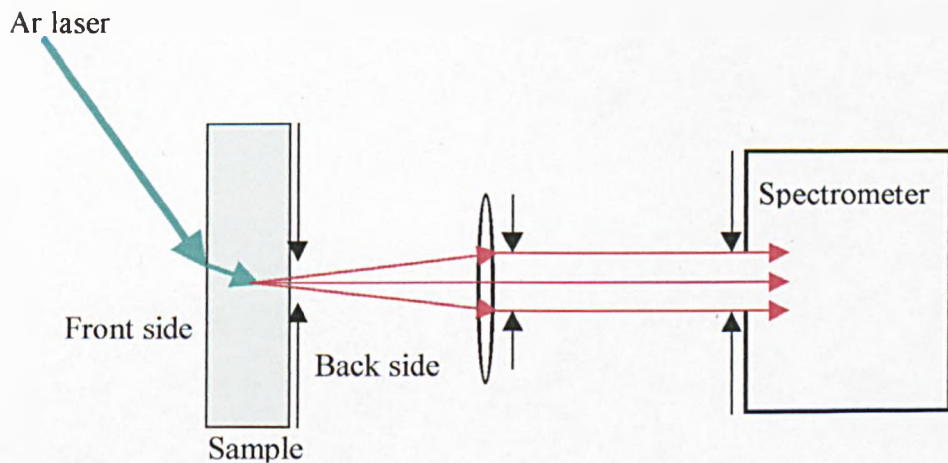


**Figure 4-1** Experimental setup used to measure the fluorescence spectra.

The dye solution was prepared by dissolving the wanted amount of the dye in ethyleneglycol ( $n=1.43$ ). For sample A, Rhodamine 6G and Sulforhodamine B were used. For sample B, Uranin was used.

### **4.2.2 Spatial Resolved Reflectivity Spectroscopy of Infiltrated Opals**

In this experiment opal samples were infiltrated with high refractive index chalcogenide glasses ( $\text{As}_2\text{S}_3$  and  $\text{AsSe}$ ). The infiltration was achieved by dipping opals into a saturated solution of chalcogenide glasses<sup>13</sup>. The glass solution was prepared<sup>14</sup> by dissolving 2 g of  $\text{As}_2\text{S}_3$  or  $\text{AsSe}$  in 10 ml of propylamine or ethylenediamine correspondingly. The dissolution was accomplished at room temperature in the dark and in a tightly closed chemical container. Total dissolution took several hours. In this procedure the precursor liquid with the dissolved glass penetrates the system of interconnected opal pores by capillary action within a few minutes. This leaves several percent of the total pore volume infiltrated with glass. The liquid evaporates over several hours and is accompanied by a dragging of the clusters of glass by the moving interface of the liquid, as well as by the processes of diffusion and agglomeration of clusters within the interconnected network of pores.

An optical microscope (LEICA DML) operating in the reflectivity mode was used to characterise the surface of the infiltrated samples. As we will discuss later, the chalcogenide glasses tend to aggregate into submillimeter areas in the samples. In order to study the infiltrated areas with chalcogenide glasses, spatial resolved reflectivity spectroscopy was implemented. In this experiment the optical microscope (LEICA DML) was coupled to a spectrometer (with 1 Å maximum resolution) combined with Charge Coupled Device (CCD) detection system. The spatial resolution during the measurements was  $10 \mu\text{m}^2$ .

### 4.3 Opal Infiltrated with Fluorescence Materials

Spontaneous emission of light is an important physical phenomenon, which is of great practical and commercial interest. For example, in a semiconductor laser, spontaneous emission is the major sink for threshold current, which must be surmounted in order to initiate lasing. The easiest way to understand the effect of a photonic band gap on spontaneous emission is to take note of Fermi's Golden Rule. The rate of spontaneous emission  $w$ , is given by<sup>15</sup>

$$w = \frac{2\pi}{\hbar} |\langle f | H_{int} | i \rangle|^2 \rho(\omega_f) \quad (4.1)$$

where  $|f\rangle$  and  $|i\rangle$  are the final and initial states,  $H_{int}$  is the interaction Hamiltonian and  $\rho(\omega_f)$  is the density of final states per unit energy.

In free space, the density of states is proportional<sup>16</sup> to  $\omega^2$  (see Figure 4-2), which determines the natural rate of spontaneous emission. In a photonic band gap of a perfect photonic crystal, however, no modes are available for the transition and the spontaneous emission can be suppressed<sup>15-17</sup> (see Figure 4-2). On the other hand, when a defect mode is introduced in the gap, the density of states at the resonance frequencies is greatly increased (see Figure 4-2), leading to enhancement of the spontaneous emission rate. If the band gap is incomplete as is the opal case, the light emitted in the direction of the stop band is attenuated, while the light can propagate perfectly well in other directions as in Figure 4-3. In the case of incomplete band gap photonic crystals, the influence of the stop band(s) on the spontaneous emission rate ( $w$ ) is very weak, about 2% as was reported by Megens *et al*<sup>18</sup>. Instead what happens as a result of the interaction of light with an incomplete photonic environment is a spatial redistribution of the spontaneous emission<sup>6,18</sup>.

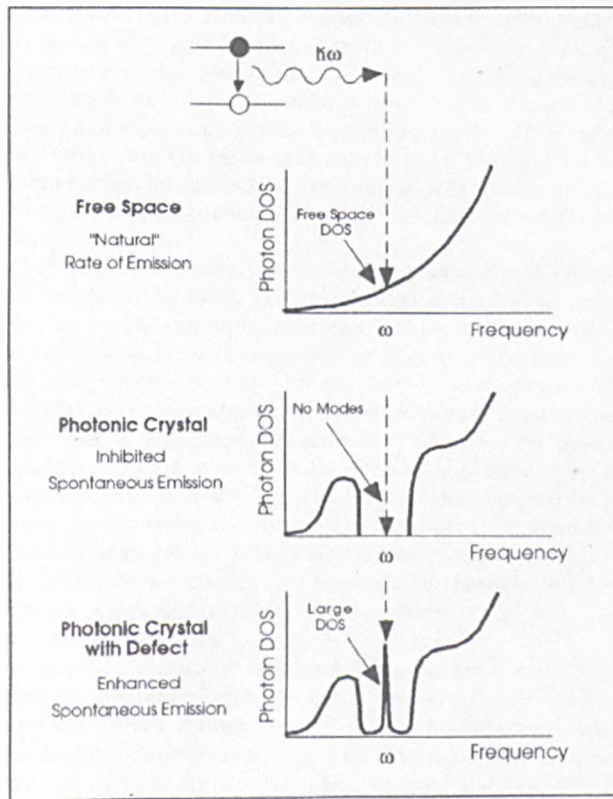


**Figure 4-2 Methods of controlling spontaneous emission with photonic crystals. (Reference 15).**

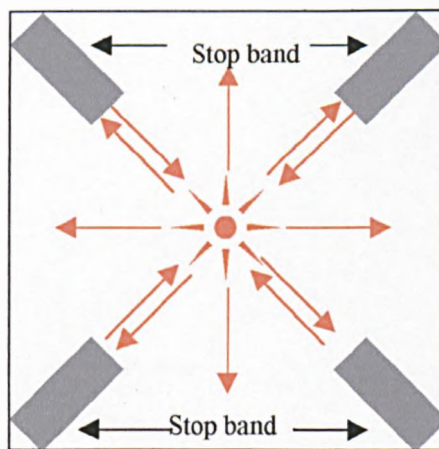


**Figure 4-3 Schematic presentation of propagation of light emitted inside incomplete band gap photonic crystals.**

In this section we will study the emission properties of light sources located deep inside self assembled opal photonic crystals. The interplay between the emitted light inside the sample and the sample order/disorder will be investigated. The effect of the concentration of the dye solution and the sample thickness on the fluorescence spectra will be studied.

Figure 4-4a shows the contrast between the fluorescence spectrum of Sulforhodamine B dye infiltrated in an opal (sample A) and the fluorescence spectrum of Sulforhodamine B dye without an opal for dye concentration equal to  $0.018 \text{ mol.L}^{-1}$ . Through the experiment the refractive index contrast was equal to 1.07. A strong dip in the emission spectrum of opal/dye system can be seen in comparison with the fluorescence spectrum of the Sulforhodamine B without an opal. The position of the dip in the fluorescence spectrum is in good agreement with the position of stop band in the transmission spectrum (see Figure 4-4), thus showing that the stop band of the opals has prevented part of the fluorescent light from leaving the sample.

To obtain the transmission spectrum of the light sources inside the opals, the ratio between the fluorescence spectrum of the opal/dye system and the reference spectrum has been taken and is illustrated in Figure 4-4b. The reference spectrum has been measured from an opal sample infiltrated with Sulforhodamine B dye with a stop band far from the emission peak of the dye. In order to compare between the fluorescence stop band and the conventional transmission stop band, the conventional transmission spectrum of the sample has been plotted in Figure 4-4b. It can be seen that the fluorescence stop band has the same position as the transmission stop band. The fluorescence stop band is narrower and shallower in comparison with the stop band in the conventional transmission spectrum.

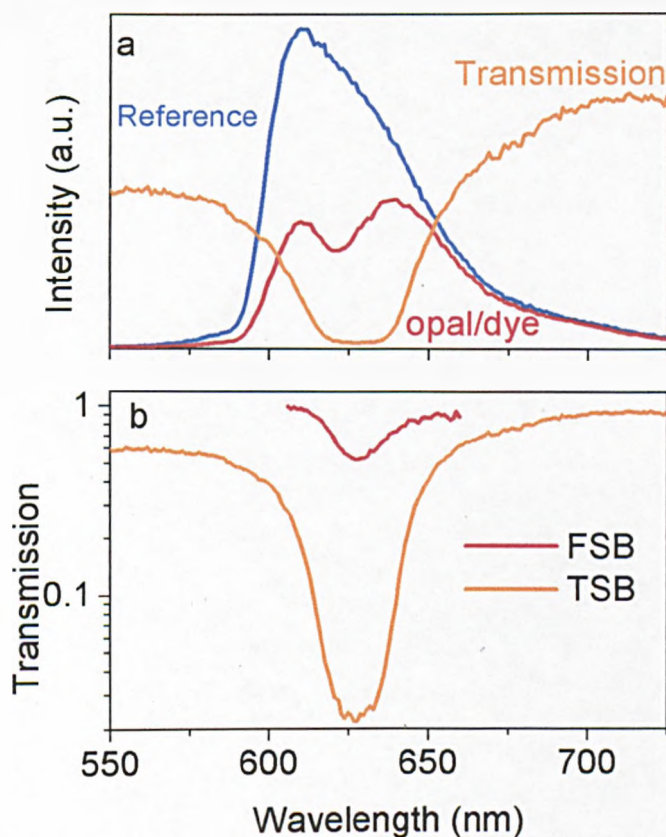


**Figure 4-4** A comparison between (a) fluorescence spectra of dye embedded in sample A and fluorescence spectra of dye without opals. (b) fluorescence stop band and transmission stop band.

In order to investigate the fluorescence stop band in more detail, the fluorescence spectra were measured as a function of the angle of collection. The results are illustrated in Figure 4-5a. With increasing angle of collection the dip in the fluorescence spectra shifts to shorter wavelengths. Figure 4-5b shows the position of the fluorescence stop band as a function of the angle of collection. For comparison the angular dependence of the transmission stop band is plotted on the same graph. Both the fluorescence and transmission stop band have the same angular dependence and follow Bragg's law.

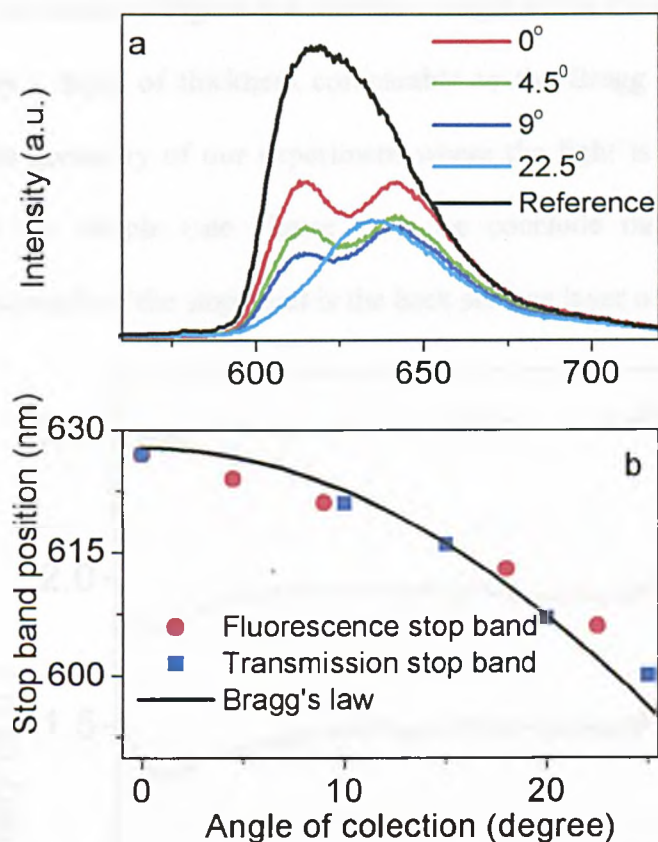


**Figure 4-5 (a) Angular dependence of the fluorescence spectra of dye embedded in opals (sample A) (b) comparison between the angular dependence of the fluorescence stop band and the transmission stop band.**

To investigate why the fluorescence stop band is shallower and narrower in comparison with the conventional transmission stop band, we studied the effect of the sample thickness on the fluorescence spectra using a wedge sample. The characterisation detail of the wedge sample used in this section can be found in chapter 2 section 2.8.3. The wedge sample was infiltrated with Uranin dye during the experiment. Figure 4-6 shows the thickness dependence of the fluorescence stop band. With increasing sample thickness, the depth of the fluorescence stop band increases until the thickness of the sample reaches  $\sim 120 \mu\text{m}$  (Bragg attenuation length as was measured in chapter 2 section 2.8.3). Then the depth does not increase with increasing the sample thickness. This behavior was reported before by Megens *et al*<sup>6</sup>. We

conclude from the results of Figure 4-6 that the strength of the fluorescence stop band is determined by a layer of thickness comparable to the Bragg attenuation length. According to the geometry of our experiment where the light is collected from the rear surface of the sample (see Figure 4-1), we conclude that the layer which determines the strength of the stop band is the back surface layer of the sample.

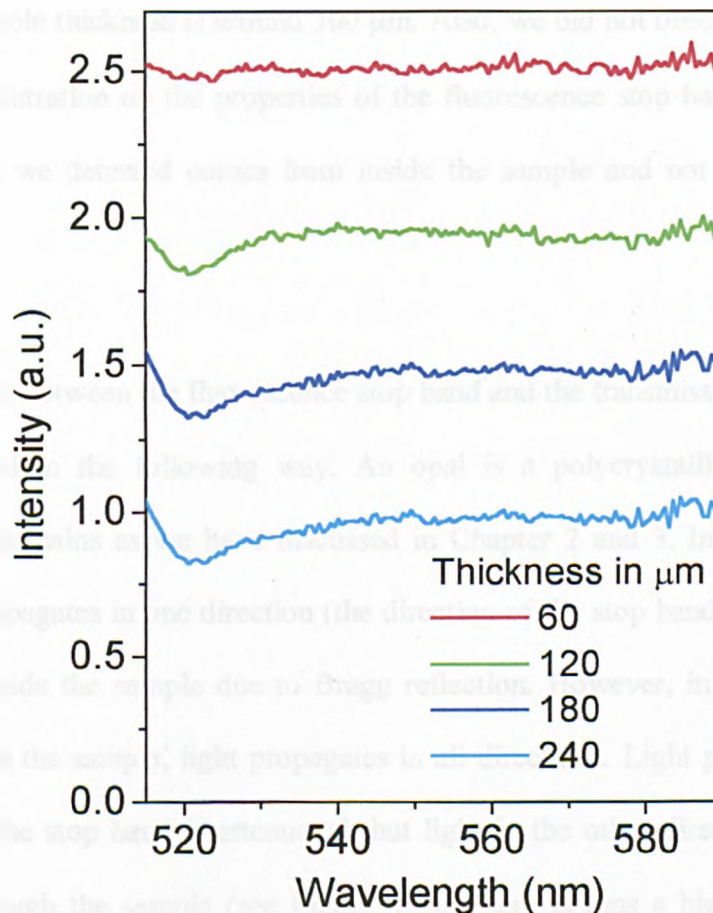


**Figure 4-6 Thickness dependence of the fluorescence stop band of a wedge sample infiltrated with Uranin dye. The curves for thicknesses 180  $\mu\text{m}$ , 120  $\mu\text{m}$  and 60  $\mu\text{m}$  have been offset by 0.5, 1 and 1.5, respectively.**

From the above results we observed that the fluorescence stop band is shallower and narrower than the transmission stop band. This means that there is light in the direction of the stop band which reaches the surface of the sample and is detected by the detection system. In our experiment we can not attribute the decrease in the depth of the fluorescence stop band to light which comes from the back surface of the

sample, for several reasons. We excited the dye from the front surface of the sample and the fluorescence light was collected from the back surface. To excite the dye at the back surface region of the sample, the absorption length of the laser light inside the sample due to the dye should be equal or greater than the sample thickness, which is not the case in our experiment. The absorption length of the laser is around 80  $\mu\text{m}$  while the sample thickness is around 300  $\mu\text{m}$ . Also, we did not observe any effect for the dye concentration on the properties of the fluorescence stop band. This suggests that the light we detected comes from inside the sample and not from the sample surface.

The difference between the fluorescence stop band and the transmission stop band can be understood in the following way. An opal is a polycrystalline material with misoriented domains as we have discussed in Chapter 2 and 3. In the transmission case light propagates in one direction (the direction of the stop band) and this light is attenuated inside the sample due to Bragg reflection. However, in the case of light sources inside the sample, light propagates in all directions. Light propagating in the direction of the stop band is attenuated, but light in the other directions propagates perfectly through the sample (see Figure 4-3). There is thus a high probability for light which propagates away from the sample normal to be scattered by disorder in the sample (mainly by the domains which were shown to exist from the analysis of the optical images and the SEM results in section 2.7 and also from the analyses the diffraction and scattering spectra in chapter 3). The light scatters in all directions including the direction of the stop band. If the scattering event happens deep inside the sample, the scattered light in the stop band direction will be attenuated due to Bragg reflections, see Figure 4-7. However, if the scattering event happens close to the back surface of the sample (within a layer of thickness less than the Bragg

attenuation length), the scattered light in the stop band direction will propagate out of the sample without attenuation, see Figure 4-7. This explains the weaker depth in the fluorescence stop band relative to that in transmission. The narrowing in the fluorescence stop band relative to that in transmission. The narrowing in the fluorescence stop band can be understood in the same way. The Bragg attenuation length is wavelength dependent and takes its minimum value at the centre of the stop band. As the wavelength shifts from the centre of the stop band toward the edges, the Bragg attenuation length increases (correspondingly, the geometrical thickness of the back surface layer). Hence the amount of scattered light which reaches the back surface of the sample without attenuation increases by shifting the wavelength far from the centre of the stop band, and explains why the stop band is narrower in the fluorescence case. This type of narrowing also is observed in the transmission spectra for thicknesses less than the Bragg attenuation length as we discussed in chapter 2 section 2.8.3.

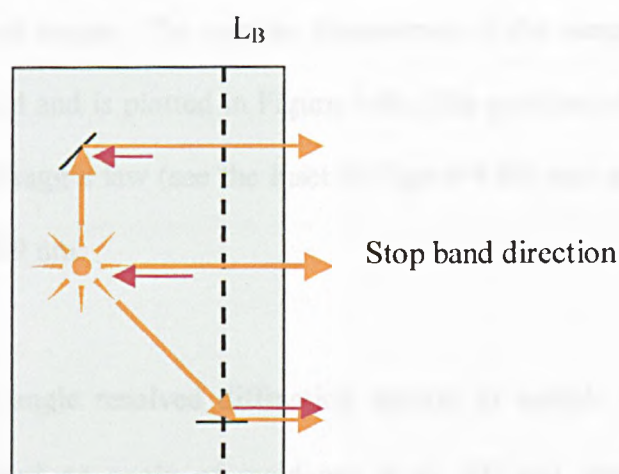


**Figure 4-7 Schematic presentation of propagation of light generated deep inside opals. The red arrow represents light within the stop band.**

From the above discussion we conclude that (i) it is possible redistribute the spatial properties of the fluorescent light of active materials such as dyes by embedding them into an incomplete photonic environment, (ii) the disorder in opals control the shape of the stop band in the fluorescence spectra.

## 4.4 Opal Infiltrated with Chalcogenide Glasses

### 4.4.1 Sample Characteristics

In this section we will characterise sample B (see section 2.8), which will be used as a host to the chalcogenide glasses ( $\text{As}_2\text{S}_3$  and  $\text{AsSe}$ ). In order to study the optical quality of the host material, the transmission technique and angle resolved diffraction spectroscopy are used. Figure 4-8a shows the transmission spectra at normal incidence of sample B as a function of the refractive index of the pores. The sample becomes transparent when it is infiltrated with ethanol ( $n=1.36$ ) due to refractive index matching between the silica spheres and ethanol. Since  $n_{\text{met}} < n_{\text{SiO}_2} < n_{\text{cy}}$ , the refractive index of the spheres has been surrounded from both sides in this experiment. As the average refractive index of the sample ( $n_{\text{av}} = \sqrt{fn_{\text{SiO}_2}^2 + (1-f)n_{\text{pores}}^2}$ ) increases the stop band shifts to longer wavelengths and becomes broader and deeper. The angular dependence of the sample in cyclohexane has been investigated and is plotted in Figure 4-8b. The position of the stop bands is fitted very well to Bragg's law (see the inset of Figure 4-8b) and gave  $d_{111} = 203$  nm and diameter  $D = 249$  nm.

Figure 4-9a shows angle resolved diffraction spectra of sample B infiltrated with cyclohexane for fixed an angle of incidence  $\theta$  of  $30^\circ$  and varying an angle of collection  $\alpha$  from  $10^\circ$  to  $40^\circ$  (see the experimental set up in chapter 3 section 3.3). As in the case of sample A in section 3.4, a well defined peak is observed from sample B with very similar width at all  $\alpha$ , peaking in intensity at  $\alpha=\theta=30^\circ$ , and decaying rapidly away from the specular condition. The peak position shifts to shorter wavelengths with increasing  $\alpha$ .

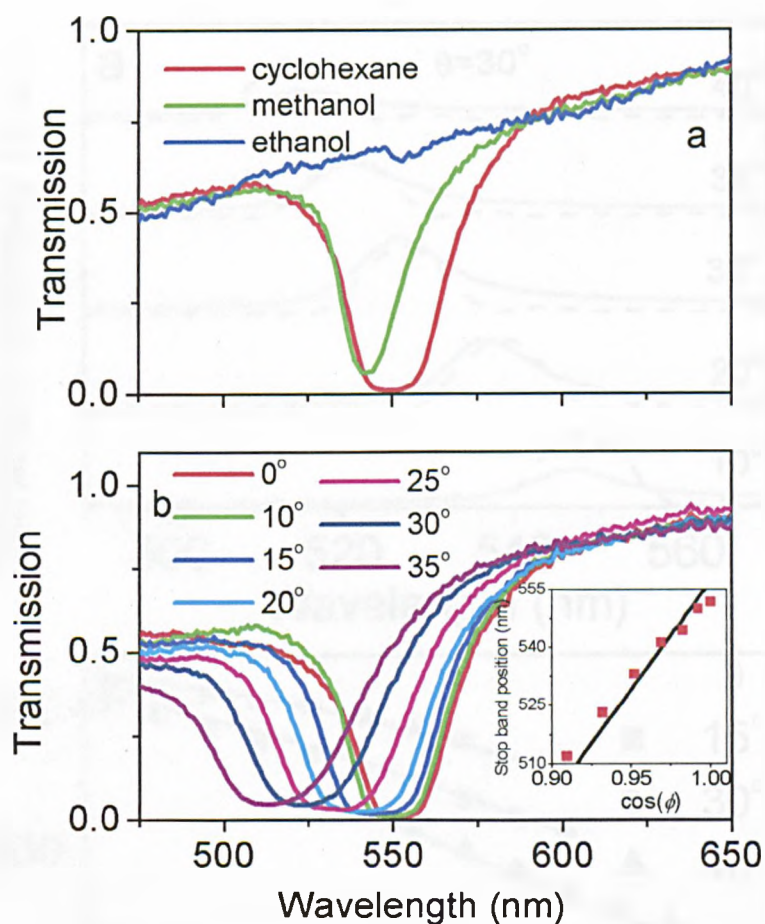


**Figure 4-8 (a) Refractive index dependence of the transmission spectra of sample B at normal incidence (b) transmission spectra of sample B in cyclohexane as a function of angle if incidence. The inset in (b) represents the position of the measured stop band (squares) and fit according to Bragg's law (full line).**

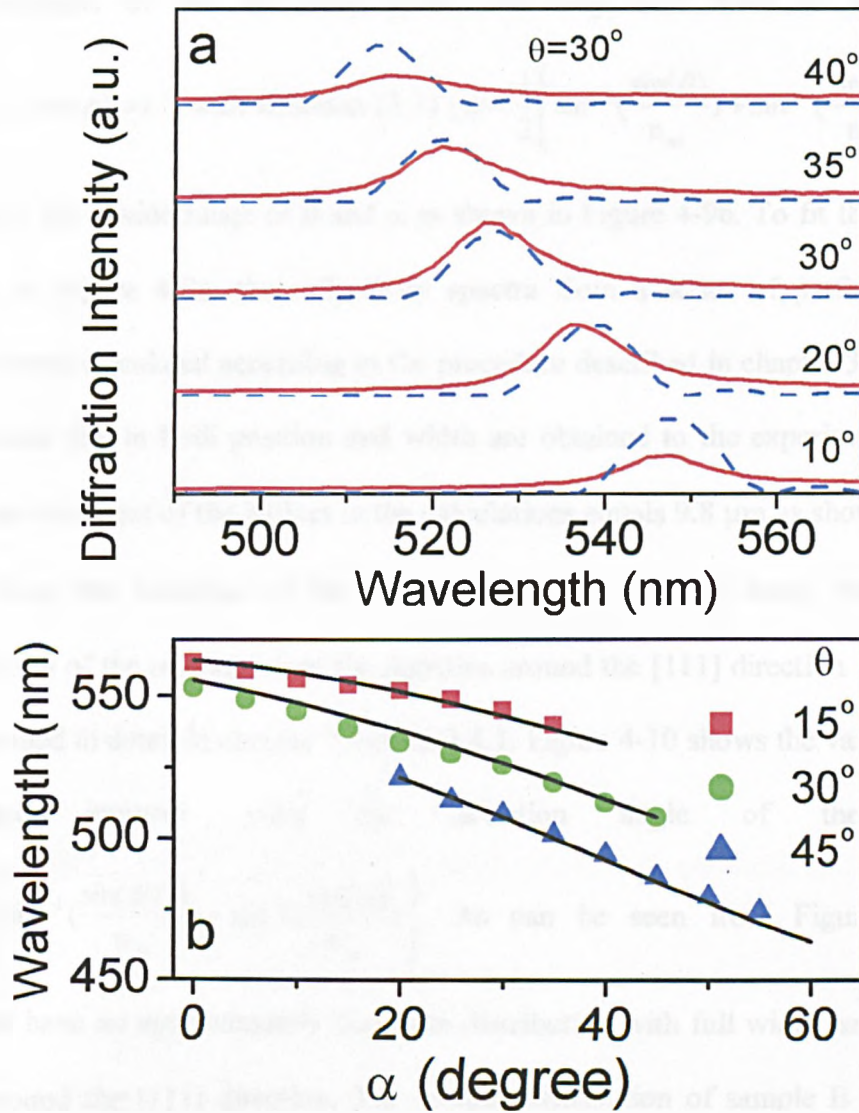


Figure 4-9 (a) Experimental angle-resolved spectra (full) for  $\theta=30^\circ$  and  $\alpha$  from  $10^\circ$  to  $40^\circ$  compared with theoretical reflectivity spectra for single crystal fcc structures with  $d=203\text{nm}$ ,  $n_p=1.43$ ,  $n_s=1.36$  (dashed). The measured peak intensities are normalised to fit the calculated spectra at the specular condition  $\alpha \sim \theta = 30^\circ$ . (b) Measured angular dispersions of the centre of the stop bands for  $\theta=15, 30, 45^\circ$  as a function of  $\alpha$  (symbols), and calculated using Bragg's law

$$2d_{111}n_{av}\cos(\phi) = \lambda \quad (\text{full lines}) \quad \text{with} \quad \phi = \frac{1}{2} \left[ \sin^{-1} \left( \frac{\sin(\theta)}{n_{av}} \right) + \sin^{-1} \left( \frac{\sin(\alpha)}{n_{av}} \right) \right].$$

The positions of the diffracted peaks are very well fitted to Bragg's law

$$(2d_{111}n_{av}\cos(\phi)=\lambda) \text{ with equation (3.1) } (\phi = \frac{1}{2} \left[ \sin^{-1}\left(\frac{\sin(\theta)}{n_{av}}\right) + \sin^{-1}\left(\frac{\sin(\alpha)}{n_{av}}\right) \right])$$

from chapter 3 for a wide range of  $\theta$  and  $\alpha$  as shown in Figure 4-9b. To fit the diffraction spectra in Figure 4-9a, the reflectivity spectra from a series of perfectly ordered lattices were calculated according to the procedure described in chapter 3 (see section 3.4). Good fits, in both position and width are obtained to the experimental spectra when the thickness of the lattices in the calculations equals  $9.8 \mu\text{m}$  as shown in Figure 4-9a. From the variation of the diffracted intensity with  $\alpha$  away from  $30^\circ$ , the distribution of the orientation of the domains around the [111] direction was deduced as described in detail in chapter 3 section 3.4.1. Figure 4-10 shows the variation of the diffracted intensity with the deviation angle of the domains

$$\delta = \frac{1}{2} \left[ \sin^{-1}\left(\frac{\sin(30^\circ)}{n_{av}}\right) - \sin^{-1}\left(\frac{\sin(\alpha)}{n_{av}}\right) \right].$$

As can be seen from Figure 4-10 the

domains have an approximately Gaussian distribution with full width half maximum of  $5^\circ$  around the [111] direction. The domain distribution of sample B is narrower than the domain distribution of sample A ( $\sim 10^\circ$  see Figure 3-6b) indicating that the crystallinity of sample B is better than sample A. In the next section sample B will be used to investigate the effect of infiltration with chalcogenide glasses on the optical properties of opals.

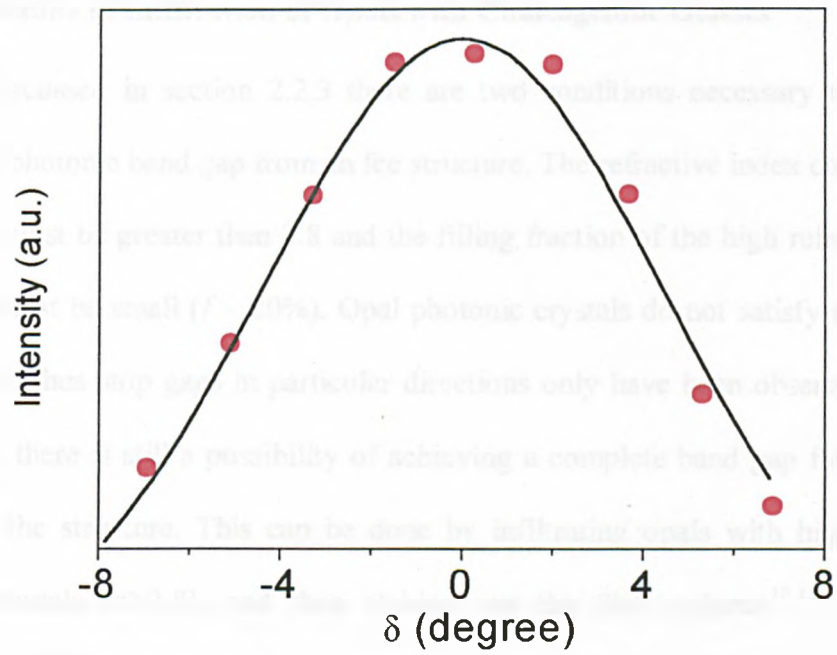


**Figure 4-10 Measured intensity of the peak as a function of rotation of (111) planes relative to the plane of sedimentation**

$$\delta = \frac{1}{2} \left[ \sin^{-1} \left( \frac{\sin(30^\circ)}{n_{av}} \right) - \sin^{-1} \left( \frac{\sin(\alpha)}{n_{av}} \right) \right] \text{ (symbols), and Gaussian fit (full line).}$$

#### 4.4.2 Results of Infiltration of Opals with Chalcogenide Glasses

As we discussed in section 2.2.3 there are two conditions necessary to achieve a complete photonic band gap from an fcc structure. The refractive index contrast of the structure must be greater than 2.8 and the filling fraction of the high refractive index material must be small ( $f \sim 20\%$ ). Opal photonic crystals do not satisfy any of these conditions, thus stop gaps in particular directions only have been observed in opals. However, there is still a possibility of achieving a complete band gap from opals by inverting the structure. This can be done by infiltrating opals with high refractive index materials ( $n > 2.8$ ), and then etching out the  $\text{SiO}_2$  spheres<sup>10,11</sup>. Theoretical calculations<sup>12,19</sup> on structures like this predict a complete band gap between the eighth and ninth bands (see Figure 4-11).

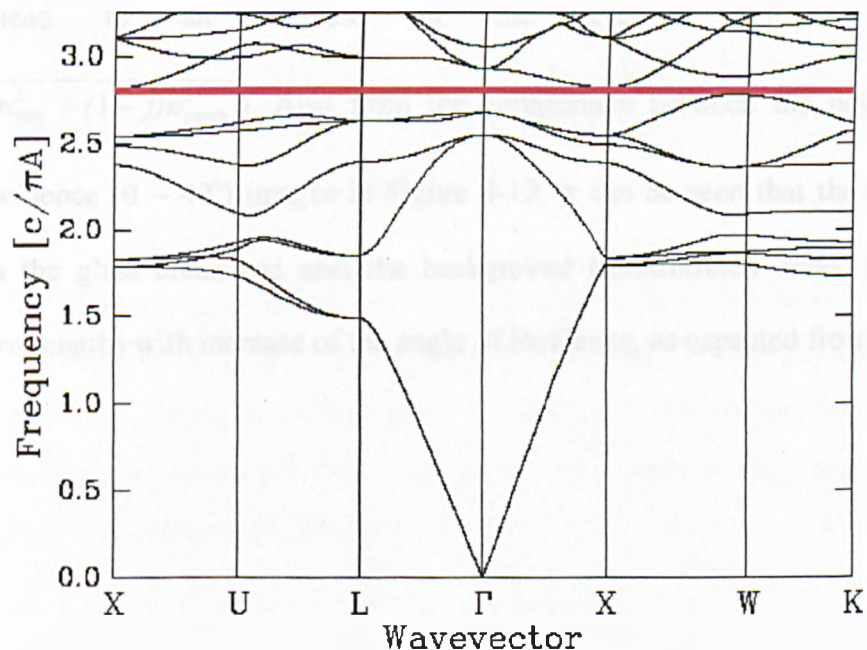


**Figure 4-11** The photonic band structure for a closed-packed fcc lattice of air spheres in a background of  $\epsilon_b=9$ , (Reproduced from reference 19).

In this section we will investigate the optical properties of opals infiltrated with high refractive index chalcogenide glasses ( $\text{As}_2\text{S}_3$  and  $\text{AsSe}$ ). Such materials are currently attracting considerable interest for photonic applications<sup>20,21</sup> as a result of their

high refractive index ( $n$ ) up to 3.6, strong photorefractive effect ( $\Delta n$  up to 0.2 easily achievable) which make them in high interest to be used to achieve tunable band gap photonic crystals, optical nonlinearity (nonlinear index  $n_2 \sim 10^{-14} \text{ cm}^2/\text{W}$ ) and electro-optic properties<sup>22</sup>. Optical Microscope Imaging and Spatial Resolved Reflectivity Spectroscopy techniques were used in this study.

Figure 4-12 shows the optical micrographs of sample B infiltrated with  $\text{As}_2\text{S}_3$  ( $n=2.45$ ) and  $\text{AsSe}$  ( $n=2.7$ ) at normal and oblique incidence. Aggregation of the glasses into submillimetre areas can be seen directly from the presence of the bright orange regions on a blue-green background (uninfiltrated areas). The bright orange areas in Figure 4-12 arise from regions containing large concentrations of glass, which lead to an increase in the average refractive index ( $n_{av} = \sqrt{fn_{\text{SiO}_2}^2 + (1-f)n_{\text{pores}}^2}$ ). Also from the comparison between the normal and oblique incidence ( $\theta \sim 40^\circ$ ) images in Figure 4-12, it can be seen that the reflected light from the glass areas and also the background (uninfiltrated areas) shifts to shorter wavelengths with increase of the angle of incidence, as expected from Bragg's law.

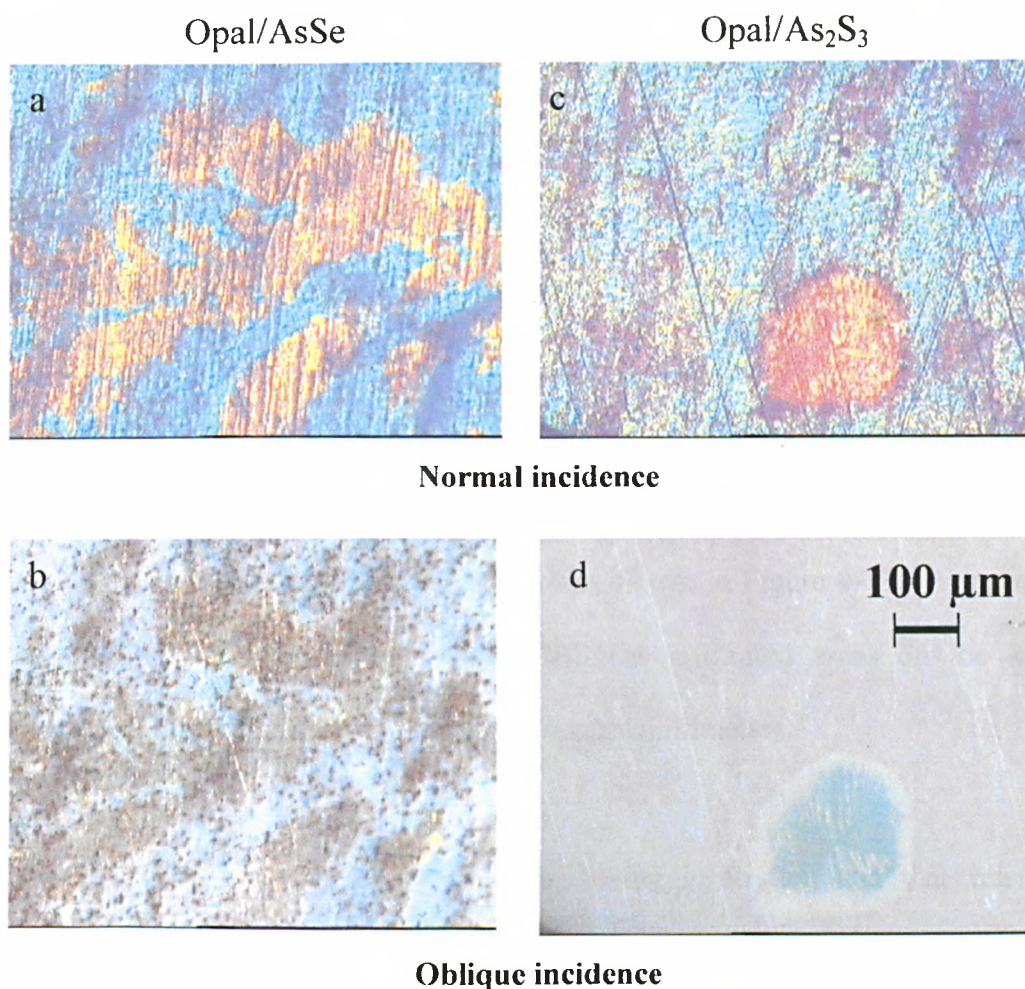
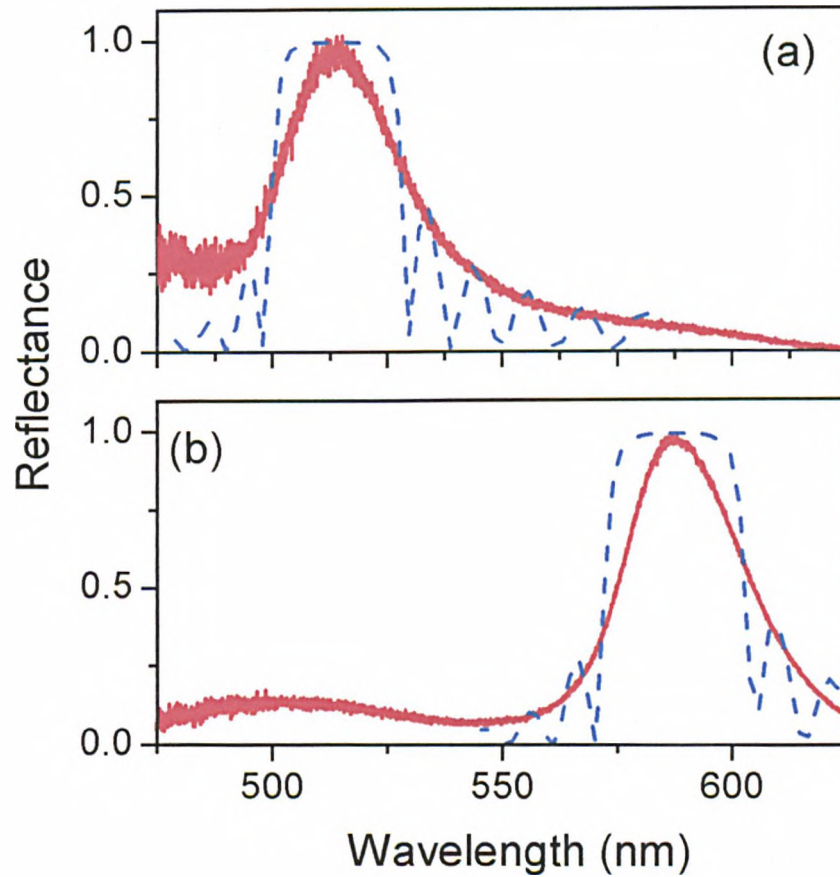


**Figure 4-12** Optical micrographs at normal and oblique incidence showing surface of samples infiltrated with (a) and (b) AsSe and (c) and (d) As<sub>2</sub>S<sub>3</sub> after removing the top ~100μm by polishing. In (a) and (c) the green-blue background arises from domains which are free from glass. The bright orange regions arise from the domains infiltrated with glass.

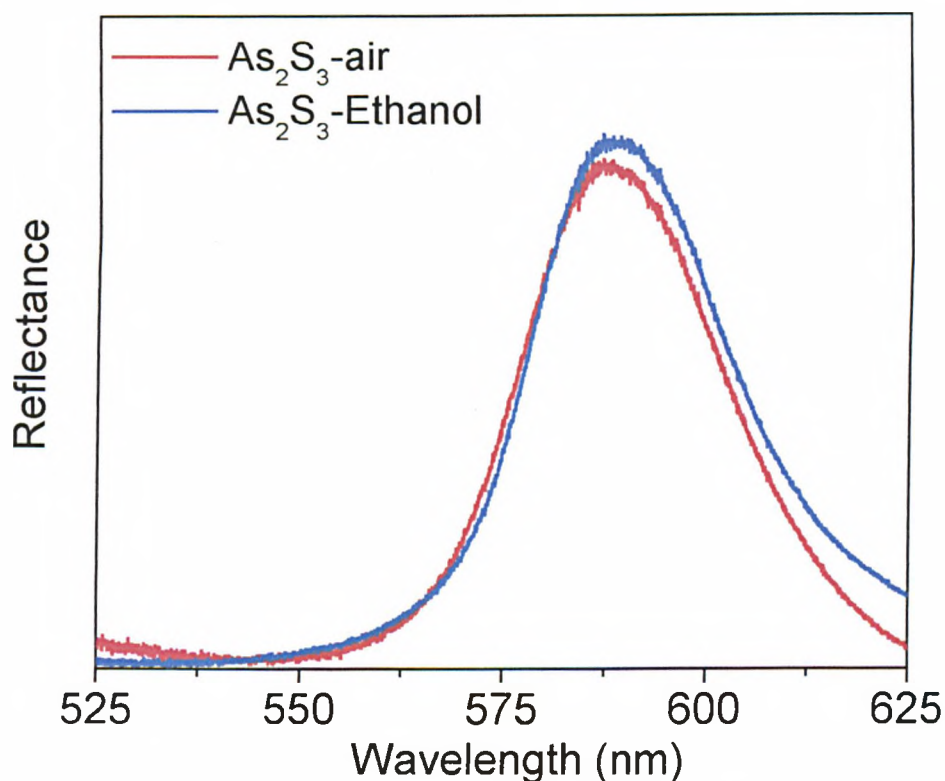
Spectra taken from the blue/green background (uninfiltrated areas) regions show that they contain nearly no infiltration since the stop band measured from different domains in Figure 4-12c agrees well with that measured from the templates before infiltration. This is further confirmed by the good agreement of the position of the stop band with that calculated for a pore refractive index  $n_{\text{pore}}=1$  as in Figure 4-13a.

Figure 4-13b shows the reflectivity from an infiltrated area with  $\text{As}_2\text{S}_3$ . The stop band is shifted relative to the reflectivity spectrum from the background (uninfiltrated areas) by up to 80 nm to longer wavelength as shown in Figure 4-13b. Very similar reflectivity results were obtained from different infiltrated areas on the sample surface, spatially separated by distances of several millimeters.

Good agreement between the spectrum following infiltration and that calculated theoretically is obtained using a value for  $n_{\text{pore}}$  of 1.7, as shown in Figure 4-13b. The reasonable agreement with the measured width, shows that microscopically, the filling of individual pores is uniform within the infiltrated areas. From the value for  $n_{\text{pores}}$ , and a value of  $n=2.45$  for  $\text{As}_2\text{S}_3$ , it is concluded that the filling factor of the infiltrated pores is  $\sim 40\%$ . We believe that this value is limited by the topology of opal crystals which consists of thin channels connecting larger voids. When the channels are filled by glass, further diffusion and agglomeration of the precursor materials is blocked. This conclusion is confirmed by additional experiments involving in-filling with various liquids; no shifts in wavelength of the stop bands were observed from the glass-infiltrated areas (see Figure 4-14), providing clear evidence for blocking of flow into the infiltrated regions. Similar restrictions may be an intrinsic limitation on the filling factors that can be achieved in opals by the differing infiltration techniques reported in the literature<sup>23-25</sup>.



**Figure 4-13** Typical experimental (full) spatially resolved spectra measured at normal incidence from (a) domains in the background area, and (b) from a region infiltrated with  $\text{As}_2\text{S}_3$ . The dashed curves are theoretical reflectivity spectra for a single crystal fcc structure with  $n_{\text{SiO}_2}=1.36$  and (a)  $n_{\text{pores}}=1$ , (b)  $n_{\text{pores}}=1.7$ . Experimental spectra are normalised with theoretical spectra for direct comparison.



**Figure 4-14 Comparison between the reflectivity spectra of the infiltrated areas ( $\text{As}_2\text{S}_3$ ) in different liquids.**

Figure 4-15a shows a comparison between reflectivity spectra measured from sample B before infiltration and from areas infiltrated with AsSe (the orange areas in Figure 4-12a). Also reflectivity spectra from the blue/green areas in Figure 4-12a indicate that these areas are free of glass confirming that chalcogenide glasses tend to aggregate into submillimetre areas. The stop band after infiltration with AsSe is shifted by 66 nm to longer wavelength relative to the stop band before the infiltration. Using the same theoretical procedure described above to fit reflectivity spectra measured from infiltrated areas with  $\text{As}_2\text{S}_3$ , a good agreement in the position of the reflectivity spectra measured from infiltrated areas with AsSe and that calculated theoretically is obtained using  $n_{\text{pore}}=1.57$  (see Figure 4-15). From the values of  $n_{\text{pore}}=1.57$  and  $n_{\text{AsSe}} = 2.7$ , the filling factor of the infiltrated pores with AsSe is estimated and found to be ~25%.

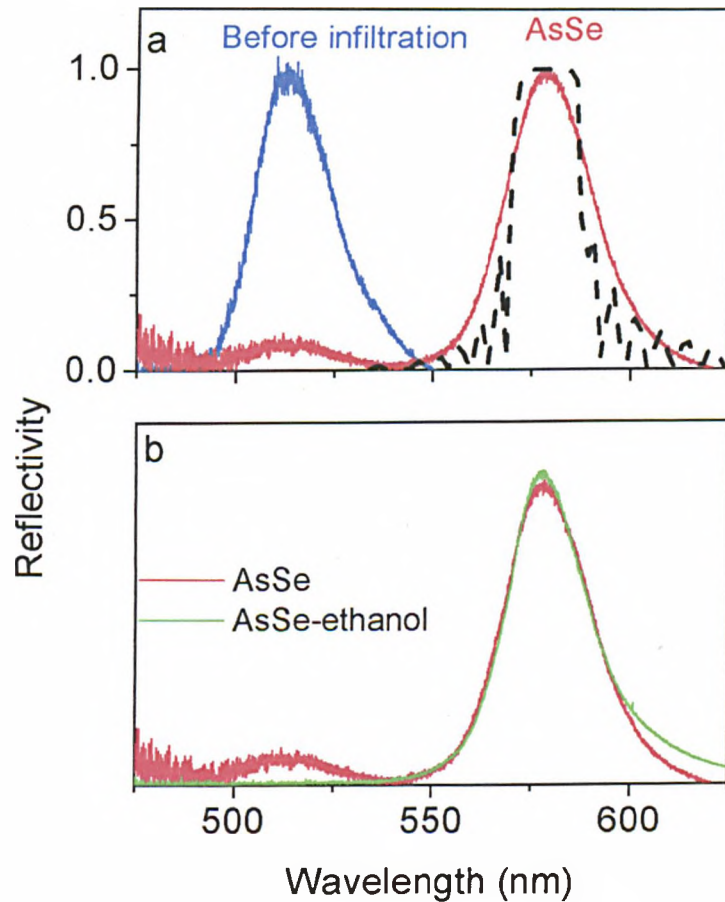


**Figure 4-15 (a) Experimental spatially resolved spectra at normal incidence from the sample before infiltration (blue) and from a region infiltrated with AsSe (red). The dashed curve is a theoretical reflectivity spectrum for a single crystal fcc structure with  $n_{\text{SiO}_2}=1.36$  and  $n_{\text{porc}}=1.57$ . (b) Comparison between the reflectivity spectra of the infiltrated areas (AsSe) in different liquids.**

Figure 4-15b shows the reflectivity spectra measured from the infiltrated areas of AsSe in different liquids. No shifts in the position of the stop band were observed as in the case of  $\text{As}_2\text{S}_3$ , providing further evidence of the blocking of the flow into the infiltrated regions. So far we do not have complete explanation of why the infiltrated filling factor of  $\text{As}_2\text{S}_3$  is higher than AsSe, possibly due to a difference in the viscosity of the solution of  $\text{As}_2\text{S}_3$  and solution of AsSe solution, and also to the difference in the surface tension for the two solutions.

In conclusion, we have studied the structural and optical properties of opal infiltrated with high refractive index chalcogenide glasses. The room temperature method used in this work to infiltrate opals is simple, rapid, and cheap compared with many other methods such as low-pressure chemical vapour deposition<sup>11</sup> or metal-organic chemical vapour deposition<sup>10</sup> which are very complicated and expensive. It allows uniform infiltration to be obtained over submillimeter areas. An 80 nm shift to longer wavelengths is observed in the infiltrated samples in comparison with the uninfiltrated samples, representing a 40% infiltration. We also suggest that repeating the infiltration procedure several times could improve the size of the infiltrated area and the infiltration ratio.

## 4.5 Conclusions

In this chapter the optical properties of opals infiltrated with fluorescent materials and high refractive index chalcogenide glasses were investigated. Angular dependent fluorescence and spatially resolved reflectivity techniques were employed.

The optical properties of opals infiltrated with fluorescent materials were investigated. The fluorescence experiment indicated that redistribution of spatial properties of the fluorescent light of active materials such as dyes is possible by embedding them into an incomplete photonic environment. Analysing the fluorescence spectra showed that the fluorescence stop band is much weaker and narrower than the conventional transmission stop band. This observation is attributed to the scattering events inside opals taking into account the spectral dependence of the Bragg attenuation length.

Chalcogenide glasses are very high refractive index ( $n$  is up to 3.6) materials, which make them very suitable to be used to infiltrate opal photonic crystals to achieve complete photonic band gap inverted opal structure in the visible region. Also chalcogenide glasses have strong photorefractive effect ( $\Delta n$  is up to 0.2), with optical nonlinearity (nonlinear index  $n_2 \sim 10^{-14} \text{ cm}^2/\text{W}$ ), which make them of high interest to achieve tunable band gap photonic crystals. The structural and optical properties of opals infiltrated with chalcogenide glasses have also been investigated. The structural studies indicated that the chalcogenide glasses tend to aggregate in submillimeter areas inside opals. An 80 nm shift to longer wavelengths is observed in the infiltrated samples in comparison with the samples before infiltration, representing a 40% infiltration. The aggregation of the glass in submillimeter areas inside opals and the incomplete infiltration are attributed to the topology of opals.

## 4.6 References

- <sup>1</sup> - E. Yablonovitch, Phys. Rev. Lett. **58**, 2059 (1987).
- <sup>2</sup> - S. John, Phys.Rev.Lett. **58**, 2486 (1987).
- <sup>3</sup> - M. N. Shkunov, M.C. Delong, M. E. Raikh, Z. V. Vardeny, A. A. Zakhidov and R. H. Baughman, Synthetic Metals **116**, 485 (2001).
- <sup>4</sup> - H. P. Schriemer, H. M. van Driel, A. F. Koenderink and W. L. Vos, Phys. Rev. A **63**, 011801(R) (2000).
- <sup>5</sup> - A. Femius Koenderink, Lydia Bechger, H. P. Schriemer, Ad Lagendijk, and Willem L. Vos, Phys. Rev. Lett. **88**, 1433903-1(2002).
- <sup>6</sup> - M. Megens, J.E.G.J. Wijnhoven, Ad Lagendijk, and W.L. Vos, J.Opt.Soc.Am. B **16**, 1403 (1999).
- <sup>7</sup> - V. N. Bogomolov *et al*, Phys. Rev. E **55**, 7619 (1997).
- <sup>8</sup> - V. N. Astratov, V. N. Bogomolov, A. A. Kaplyanskii, A. V. Prokofiev, L. A. Samoilovich, S. M. Samoilovich, and Y. A. Vlasov, Nuovo Cimento D **17**, 1349 (1995).
- <sup>9</sup> - Y.A. Vlasov, N. Yao, and D.J. Norris, Adv.Mater. **11**, 165 (1999).
- <sup>10</sup> - A. Blanco, E. Chomski, S. Grabtchak, M. Ibsate, S. John, S.W. Leonard, C. Lopez, F. Meseguer, H. Miguez, J.P. Mondia, G.A. Ozin, O. Toader, and H.M. van Driel, Nature **405**, 437 (2000).
- <sup>11</sup> - Y. A. Vlasov, X.-Z. Bo, J. C. Sturn, and D.J. Norris, Nature **414**, 289 (2001).
- <sup>12</sup> - K. Busch and S. John, Phys. Rev. E **58**, 3896 (1998).
- <sup>13</sup> - V.N. Astratov, A.M. Adawi, M.S. Skolnick, V.K. Tikhomirov, V. Lyubin, D.G. Lidzey, M. Ariu, and A.L. Reynolds, Appl.Phys. Lett. **78**, 4094 (2001) and also in reference 14.
- <sup>14</sup> - S. Shtutina, M. Klebanov, V. Lyubin, S. Rosenwaks, and V. Volterra, Thin Solid Films **261**, 263 (1995)
- <sup>15</sup> - J. Joannopoulos, in Confined photon systems: fundamentals and applications: lectures from the summerschool, held in Cargèse, Corsica, 3-15 August 1998, H. Benisty, J. M. Gerard, R. Houdie, J. Rarity, and C. Weisbuch eds. (Springer, Heidelberg, 1999).
- <sup>16</sup> - J. Joannopoulos, P. Villeneuve and S. Fan, Nature **386**,143 (1997).
- <sup>17</sup> - J. D. Joannopoulos, R. D. Meade and J. N. Win, Photonic Crystals (Princeton University press, 1995).

- <sup>18</sup> - M. Megens, J. E. G. J. Wijnhoven, Ad Lagendijk, W. L. Vos, Phys. Rev. A **59**, 4727 (1999).
- <sup>19</sup> - A. Moroz and C. Sommers, J. Phys.:Condens. Matter **11**, 997 (1999).
- <sup>20</sup> - A. Feigel, Z. Kotler, B. Sfez, A. Arsh, M. Klebanov and V. Lyubin, Appl. Phys. Lett. **77**, 3221 (2000).
- <sup>21</sup> - V.N. Astratov, A.M. Adawi, M.S. Skolnick, V.K. Tikhomirov, V. Lyubin, D.G. Lidzey, M. Ariu, and A.L. Reynolds, Appl.Phys. Lett. **78**, 4094 (2001)
- <sup>22</sup> - V.Pruneri, P.G.Kazansky, D.Hewark, J.Wang, H.Takebe, and D.N.Payne, Appl.Phys.Lett. **70**, 155 (1997)
- <sup>23</sup> - Y. A. Vlasov, V. N. Astratov, O. Z. Karimov, A. A. Kaplyanskii, V. N. Bogomolov, and A. V. Prokofiev, Phys. Rev. B **55**, 13357 (1997)
- <sup>24</sup> - J. Wijnhoven and W.L.Vos, Science **281**, 802 (1998).
- <sup>25</sup> - A. A. Zakhidov, R. H. Baughman, Z. Iqbal, C. Cui, I. Khairulin, S. O. Dantas, J. Marti, and V. G. Ralchenko, Science **282**, 897 (1998).

## Chapter 5

# Intersubband Spectroscopy of In(Ga)As/GaAs Self Assembled Quantum Dots

### 5.1 Introduction

Self-assembled quantum dots (SAQDs) are semiconductor heterostructures in which the carriers are spatially confined in all three dimensions. This confinement provides a variety of novel properties, many of which have a direct analog with those found in atoms<sup>1</sup>. The formation of SAQDs is based on the strain between highly mismatched semiconductors<sup>1</sup>. Over the last few years, the optical properties of SAQDs have been widely studied, both for basic physical understanding<sup>2-8</sup>, and for development of novel devices such as low threshold current quantum dot lasers<sup>9</sup>, optical memory systems<sup>10</sup> and quantum dot infrared photodetectors<sup>11</sup>(QDIPs). However, the electronic structure of SAQDs remains unclear. Several techniques such as photoluminescence<sup>2,3,5</sup> (PL), photoluminescence excitation<sup>4</sup> (PLE), direct absorption<sup>8</sup>, photocapacitance<sup>4</sup>, and interband photocurrent spectroscopy<sup>6,7</sup> have been used to investigate the electronic structure of such dots. In the above methods, both electrons and holes are involved (electron-hole transitions), thus they do not provide separate information about the number of the bound states in each band of the quantum dot. Also these techniques do not provide direct information about either: (i) the binding energy of the lowest electron level with respect to the GaAs conduction band minimum (CBM) (or the binding energy of the lowest hole level with respect to the GaAs valence band maximum (VBM)) or (ii) the position of the wetting layer band minima with respect to GaAs. In addition, the selection rules that control the intersubband transitions in

each band can not be studied using these methods. All this information is critical to understanding the electronic structure of SAQDs and to enable them to be modeled theoretically.

Another motivation to study intersubband transitions in SAQDs is the possibility of using them to fabricate high quality infrared photodetectors<sup>12,13</sup>. QDIPs have several advantages compared with quantum well infrared photodetectors (QWIPs), including sensitivity to normal incidence radiation (due to relaxation of intersubband polarisation selection rules), higher gain and broader spectral response range due to the inhomogeneous broadening in SAQDs.

In this work we present the results of intersubband spectroscopy<sup>12,13</sup>, which provides a direct and relatively unambiguous measurement of the energy level structure of the valence band and/or the conduction band of the dots. Two techniques have been used, namely direct intersubband absorption and intersubband photocurrent spectroscopy. A range of experiments have been carried out to investigate the dependence of the intersubband transitions in the valence band or the conduction band on factors such as polarisation of the incident light, external applied electric field and temperature. The last section of this chapter is devoted to studying of the effect of the coupling between multiple stacked dot layers on intersubband transitions within the conduction band.

The experimental results indicate that radiative intersubband transitions in the conduction band of isolated SAQDs are polarised in the growth direction, similar to that found for quantum wells. In contrast with the results for the conduction band, intersubband transitions in the valence band are found to be strongly polarised in the growth plane. We found by employing strongly coupled SAQDs in the vertical

direction that the selection rules in the conduction band could be modified to give strong absorption in the dot plane.

## 5.2 Growth of Self Assembled Quantum Dots

Since the 1980s considerable efforts have been devoted to the realization of semiconductor heterostructures that provide carrier confinement in all three dimensions and hence behave as electronic quantum dots. The most straightforward technique is to laterally pattern a two dimensional quantum well structure through the combination of high-resolution electron beam lithography and dry or wet etching<sup>14</sup>. The smallest lateral dimensions achievable for this type of structure are of order of 100 nm, very large in comparison to the vertical dimensions of the quantum well (<10 nm). Due to the large lateral size of these structures, they still behave essentially as quantum wells. Furthermore, lithography and etching cause unavoidable damage to the structure, producing impurity contamination, defect formation and poor interface quality.

Recently, self-assembly<sup>1</sup> techniques, have attracted the attention of researchers as a novel way to fabricate good quality and defect-free quantum dots. The dots form during the growth of certain strained heterostructures using techniques such as molecular beam epitaxy (MBE) or metal-organic chemical vapour deposition (MOCVD). Depending on the lattice mismatch between the two semiconductor materials, there are three modes of heteroepitaxial growth. These are shown in Figure 5-1.

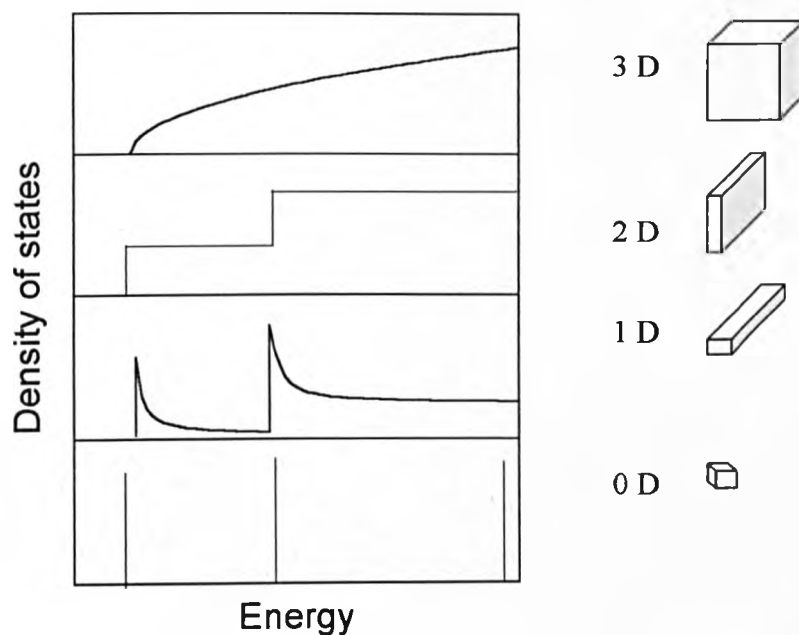


Figure 5-1 Schematic diagrams of the three possible growth modes.

In unstrained material systems, basic layer by layer growth occurs, referred to as the Frank-van der Merwe (FvdM) growth mode. In case of highly strained materials, islands of the second material form at the top of the first one. This mode is known as the Volmer-Weber (VW) growth mode. The third mode is a combination of the first two modes. It occurs for heterostructures with a moderate lattice mismatch (less than 10%) and is known as the Stranski-Krastanov (SK) mode. In this mode, the second material initially grows as strained planar layers (called wetting layers) until it reaches a critical thickness ( $\sim 2\text{ML}$ ). After reaching the critical thickness, it becomes energetically favorable for the strain to relax forming three dimensional islands. These islands are known as self-assembled quantum dots (SAQDs). The growth of InAs upon a GaAs substrate (with a lattice mismatch  $\sim 7\%$ ) is a typical example of the growth of dislocation-free high-density SAQDs with a 1.7 ML wetting layer formed by SK mode. The shape, size, and areal density of the dots depends strongly on the growth conditions<sup>1</sup>. Typically, the dots have lateral sizes of 10-25 nm with heights of 3-8 nm. These dots are lens shaped or pyramid shaped with an areal density of the dots which ranges from  $10^9$ - $10^{11}$   $\text{cm}^{-2}$ .

### 5.3 Theory

Confining the carrier motion in a solid to length scales of the order of the de Broglie wavelength in one, two or three dimensions produces unique electronic and optical properties for these artificial systems<sup>1</sup>. Variation of the energy ( $E$ ) dependence of the density of states with the dimensionality of the system is illustrated in Figure 5-2. In contrast with bulk solids the density of states for a two dimensional system (quantum well) is a step function. For a one dimensional system (quantum wire) the density of states is proportional to  $E^{-1/2}$ . In the case of a zero dimensional system (quantum dot), the density of states has atomic-like, delta function characteristics. In this theoretical section, a general introduction into the electronic and optical properties of self assembled quantum dots will be given.



**Figure 5-2 Schematic representation of the density of states with the variation of the dimensionality of the system.**

### 5.3.1 Electronics of Quantum Dots

The electronic states of the quantum dots can be calculated by solving the Schrodinger equation, which is given by

$$-\frac{\hbar^2}{2m}\nabla^2\psi(\mathbf{r})+V(\mathbf{r})\psi(\mathbf{r})=E\psi(\mathbf{r}) \quad (5.1)$$

where  $\hbar$  is Planck's constant divided by  $2\pi$ ,  $m$  is the effective mass of the carrier,  $V(\mathbf{r})$  is the confinement potential and  $\psi(\mathbf{r})$  is the carrier wavefunction. Due to our limited knowledge of the exact shape, size, strain distribution and composition of the dots, an exact solution for Schrodinger's equation is unavailable so far. Therefore, several approximate approaches have been used, such as the effective mass approximation<sup>15</sup>,  $\mathbf{k}\cdot\mathbf{p}$  theory<sup>16</sup> and the pseudopotential method<sup>17</sup>. A detailed comparison between the experimental results and theoretical calculation can be found in references 19 and 20.

#### 5.3.1.1 Strain in Self Assembled Quantum Dots

As we discussed in section 4.2, the growth of self assembled InAs/GaAs quantum dots depends on the lattice mismatch between InAs and GaAs. Therefore, the electronic structure of such dots is profoundly affected by their strain profile. An example for this is that the ground state transition energy in InAs/GaAs dots is  $\sim 1$  eV, even though the band gap of bulk InAs is  $\sim 0.4$  eV. Theoretically there are two methods<sup>20</sup> to model the strain in self assembled quantum dots; the continuum mechanical (CM) model and valence-force-field (VFF) model. In this section I will summarise the strain calculations which were performed by Cusack *et al*<sup>21</sup> using the VFF model as a function of aspect ratio  $Q=b/2h$  of the dot width ( $b$ ) and height ( $h$ ). In their model, they assumed the dot has pyramidal geometry with square base (Figure 5-3).

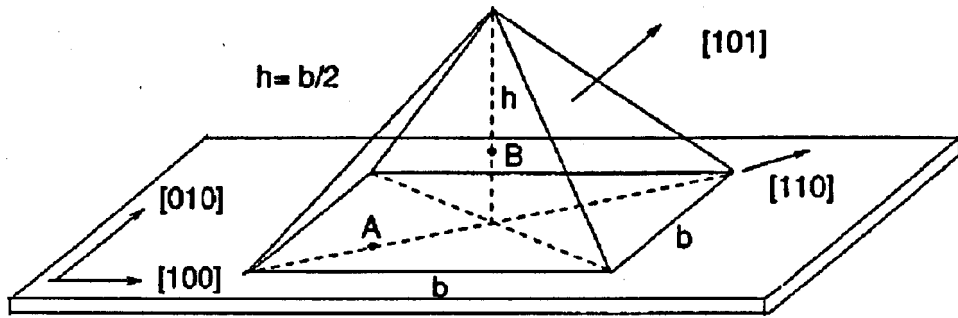


Figure 5-3 Schematic view of the pyramidal quantum dot, ( $Q=b/2h$ ). (Reference 17).

Figure 5-4 shows the strain tensor components ( $\epsilon_{xx} = \epsilon_{yy}$  and  $\epsilon_{zz}$ ) along the z-axis (the growth direction) for two structures. Structure 1 with  $b=12$  nm and  $h=6$  nm ( $Q=b/2h=1$ ) and structure 2 with  $b=20$  nm and  $h=2.5$  ( $Q=b/2h=4$ ). Changing  $Q$  changes the strain of the dots. For example near the centre of structure 1 there is a region under purely compressive stress ( $\epsilon_{xx} = \epsilon_{yy} = \epsilon_{zz}$ ). There is no such region like this in structure 2. Near the base of structure 1, the substrate material compresses the x-y lattice constant of InAs giving a negative  $\epsilon_{xx}$  strain and positive  $\epsilon_{zz}$  strain. However, at the apex of pyramid, the barrier material to the sides compresses the dot along the z-axis producing a negative  $\epsilon_{zz}$  component and a positive  $\epsilon_{xx}$  component. In structure 2 the pyramid is flatter and the dot is wider, therefore the influence of the barrier material on the InAs pyramid apex is smaller. As a result the strain components do not cross.

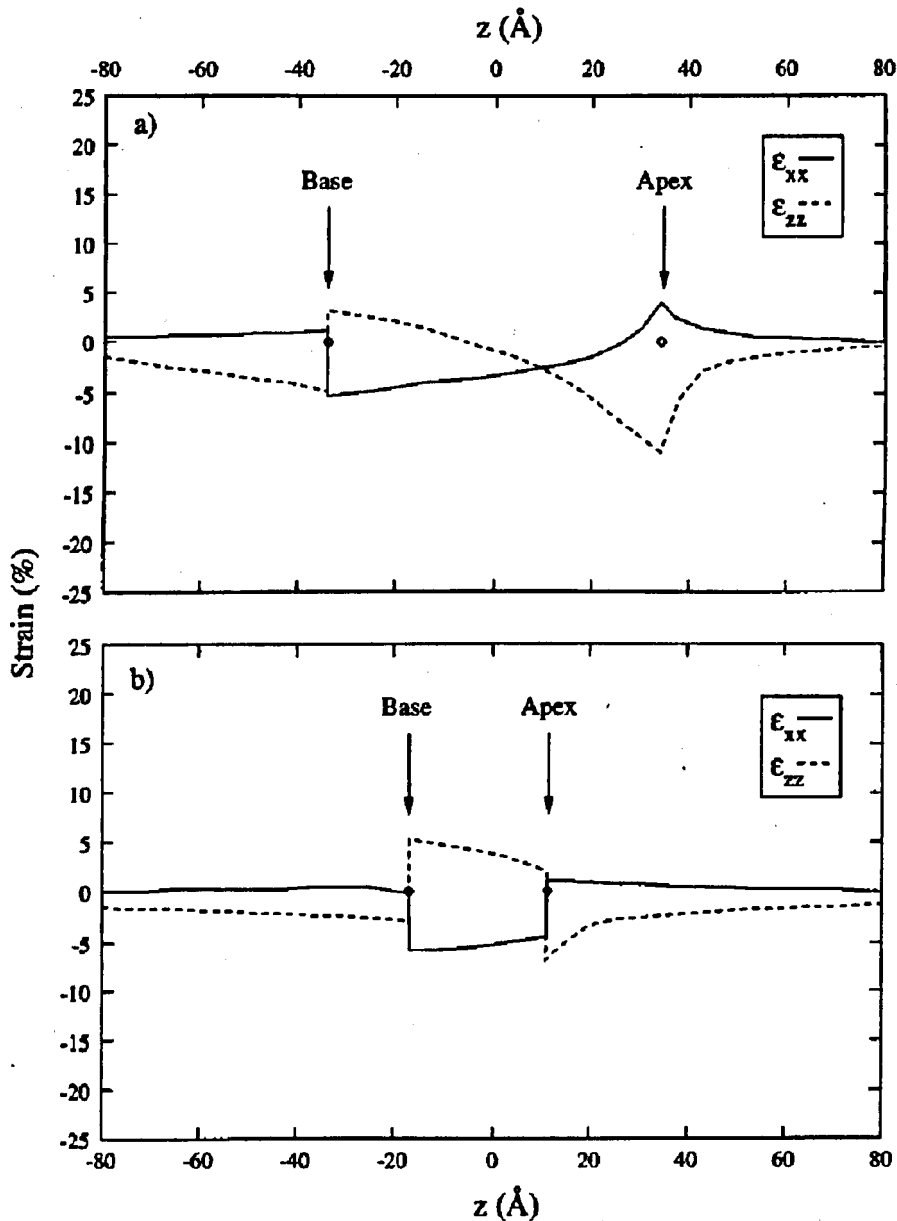
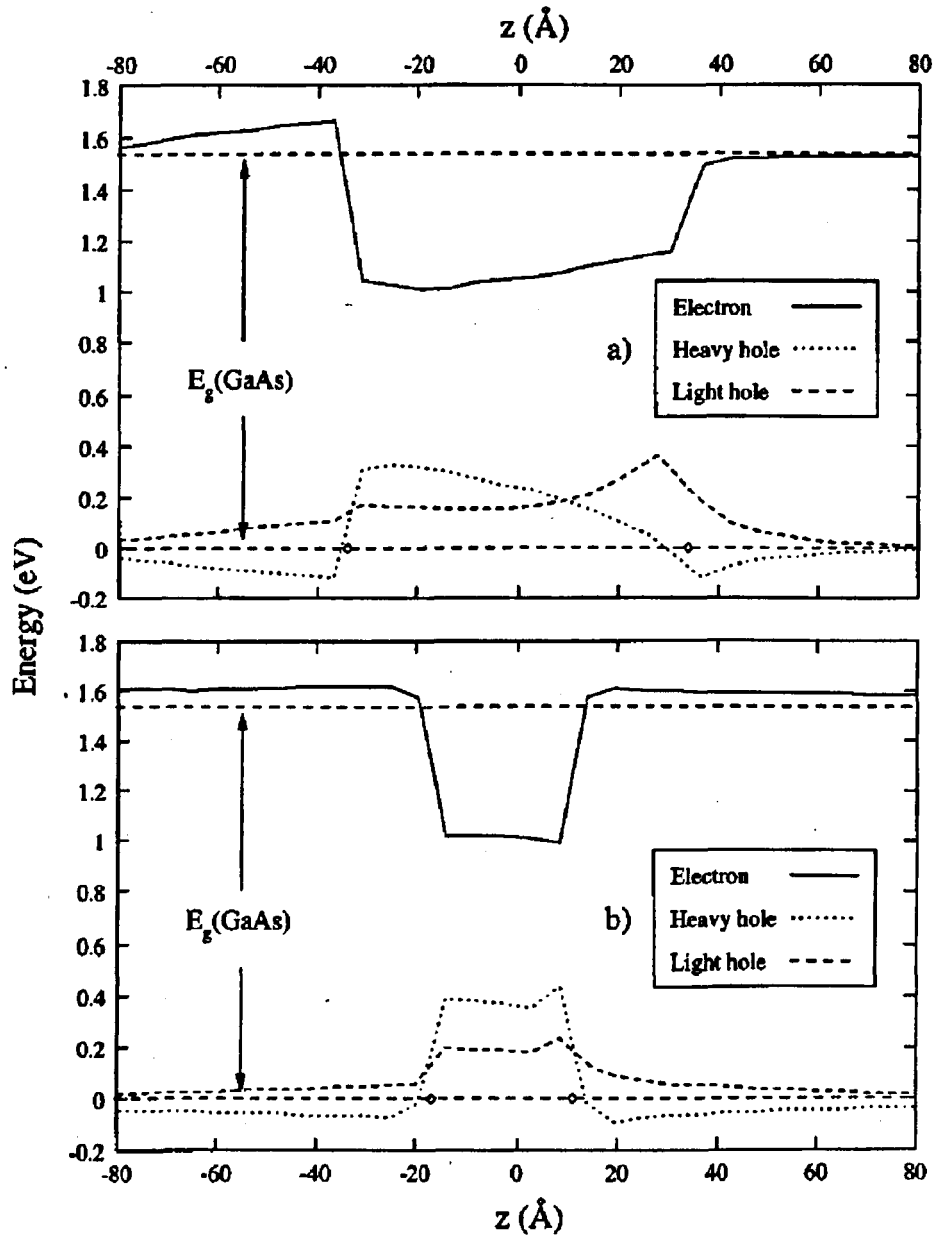


Figure 5-4 Strain tensor components for (a) structure 1 ( $b=12$  nm,  $h=6$  nm and  $Q=1$ ) and (b) structure 2 ( $b=20$  nm,  $h=2.5$  nm and  $Q=4$ ). (Reference 21).

### 5.3.1.2 Effect of the Strain on the Band Structure of Quantum Dots

The InAs dot and the wetting layer act as a potential well for the carriers. In the case of an unstrained dot the well profile is given by the offset between the band edges in InAs and GaAs ( $V_{CB}=0.83$  eV and  $V_{VB}=0.26$  eV)<sup>22</sup>. Figure 5-5 shows the effect of the strain on the confining potential profiles for electrons and holes along the growth direction in structure 1 ( $b=12$  nm,  $h=6$  nm and  $Q=1$ ) and structure 2 ( $b=20$  nm,  $h=2.5$

nm and  $Q = 4$ ). In structure 1, it can be seen that the heavy hole and light hole confining potentials have a similar energy near the centre of the dot. In structure 2 the heavy hole and light hole potentials are well separated. The reason for this is that at the centre of structure 1,  $\epsilon_{xx} = \epsilon_{yy} = \epsilon_{zz}$ . There is no such strain condition like this in structure 2.



**Figure 5-5** The confining potentials for electron, heavy hole, and light hole carriers in (a) structure 1 ( $b=12$  nm,  $h=6$  nm and  $Q=1$ ) and (b) structure 2 ( $b=20$  nm,  $h=2.5$  nm and  $Q=4$ ). (Reference 21).

### 5.3.1.3 Energy Levels in Quantum Dots

Energy levels in self assembled dots depend on dot size, shape, composition and strain distribution. Here I will present theoretical calculations for energy levels of squared pyramidal InAs/GaAs quantum dots. Figure 5-6<sup>23</sup> shows the electron and hole energy levels as a function of the dot base length ( $b$ ). For  $b \leq 12$  nm there is at most one electron bound state in the conduction band and at least four hole bound states in the valence band. The dependence of the hole energy levels on the dot size is weaker than that of the electrons. This is due to the larger effective mass of the holes. The energy separation between the electron energy levels decreases with increasing the dot size.

Figure 5-7<sup>17</sup> represents the wavefunction amplitude for the electron and hole states. The conduction band ground state is an s-like state, while the next two conduction band states are p-like. The fourth conduction band state is d-like. The valence band states are confined to the bottom of the pyramid and as such, do not reach the tip of the structure. These states represent such strong band mixing that they can not be classified as s-like, p-like, etc.

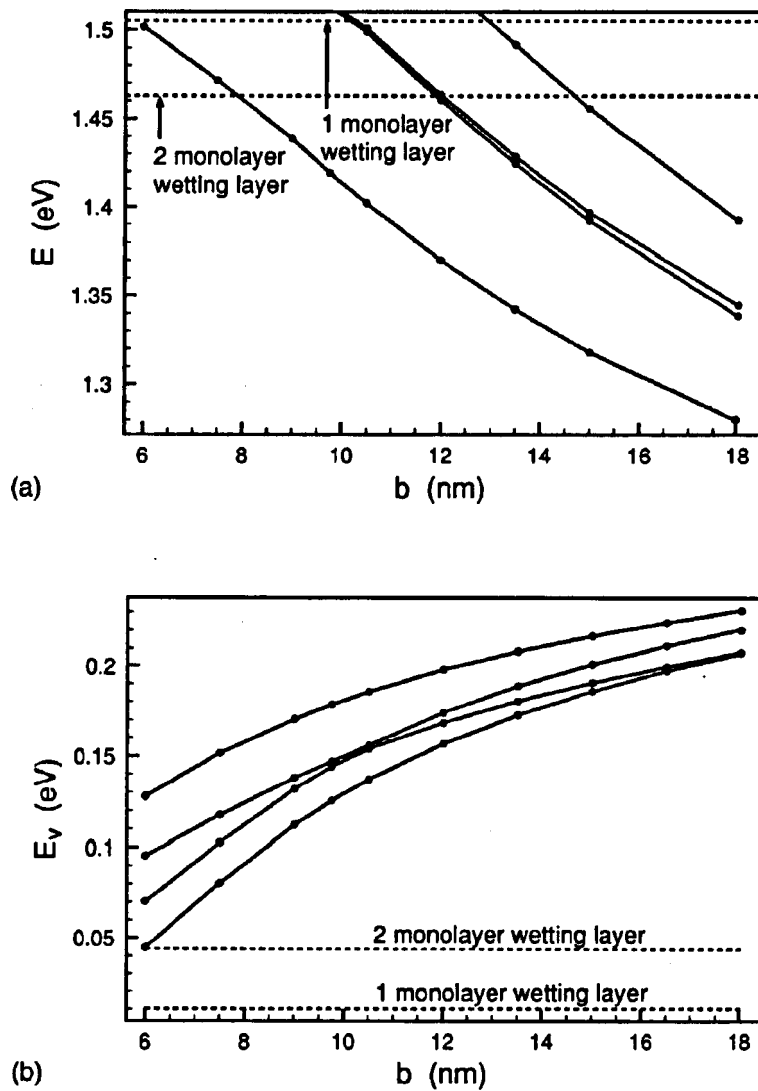
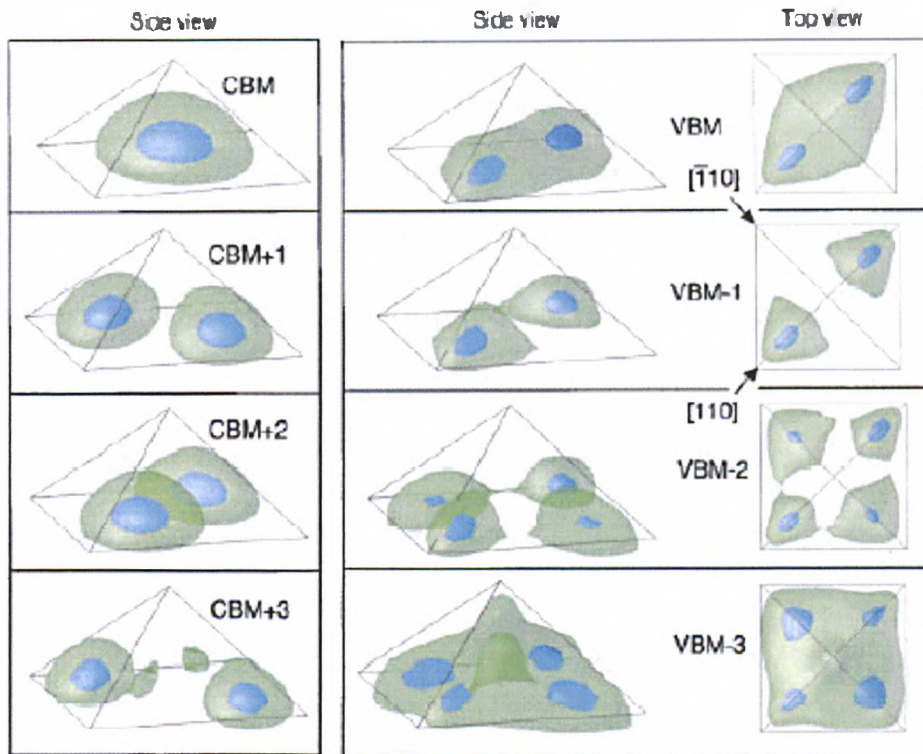


Figure 5-6 The conduction and valence band bound state energies as functions of the pyramid base length  $b$ . (Reference 23).



**Figure 5-7** Isosurface plots of the charge densities of the conduction and valence band states for the  $b=11.3$  nm pyramids. The charge density equals wavefunction square, including the spin-up and -down components. The level values of the green and blue isosurfaces equal 0.25 and 0.75 of the maximum charge density, respectively. (Reference 17).

### 5.4 Optical Transitions in Quantum Dots

There are two types of optical transitions in quantum dots as illustrated in Figure 5-8. Interband transitions take place between the discrete levels in the conduction and valence bands. In these transitions both electrons and holes are involved (electron-hole transitions). The energy of this transition is the band gap energy plus the confinement energies of the electrons and holes, minus the exciton binding energy. Typical interband transitions have energies of the order of 1eV. For more details about interband transitions, see references 2 to 8.

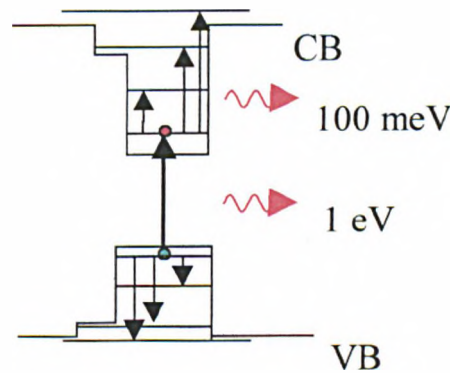


**Figure 5-8 Schematic presentation of the interband and intersubband transitions in quantum dots.**

Intersubband transitions occur entirely within either the conduction band or the valence band, and involve only one type of carrier (electron or hole). The energy of the intersubband transitions is typically around 100 meV, which is equivalent to an emission or absorption wavelength of  $\sim 12.5 \mu\text{m}$ .

The Hamiltonian, which describes the interaction between the electron (or hole) and the electromagnetic waves can be written as<sup>24</sup>

$$\hat{H} = \frac{e^2 E_0}{2m\omega} \hat{\varepsilon} \cdot \hat{p} \exp(-i\omega t) \quad (5.2)$$

where  $e$  is the electron charge,  $E_o$  is the amplitude and  $\hat{\varepsilon}$  the polarisation vector of the electric field associated with the electromagnetic radiation, respectively, and

$p = \frac{\hbar}{i} \left( \frac{\partial}{\partial x} + \frac{\partial}{\partial y} + \frac{\partial}{\partial z} \right)$  is the momentum operator.

From Fermi's golden rule, the radiative transition probability from a state  $|i\rangle$  to a state  $|f\rangle$ , with energy  $E_i$  and  $E_f$ , respectively, is

$$w_{if} = \frac{\pi}{2\hbar} \left( \frac{eE_o}{m\omega} \right)^2 \left| \langle f | \hat{\varepsilon} \cdot \hat{p} | i \rangle \right|^2 \delta(E_f - E_i - \hbar\omega) \quad (5.3)$$

The absorption coefficient ( $\alpha$ ) is defined as the ratio of the absorbed electromagnetic energy per unit time and volume,  $u = \hbar\omega w_{if}/V$ , and the intensity of the incident radiation  $I = \frac{1}{2} \varepsilon_o c n E_o^2$ , summed over all occupied initial and empty final states<sup>24</sup>.

$$\alpha(\hbar\omega) = \frac{u}{I} = \frac{2\pi e^2 \hbar}{m^2 \varepsilon_o c n V} \sum_i \frac{\left| \langle f | \hat{\varepsilon} \cdot \hat{p} | i \rangle \right|^2}{E_f - E_i} \delta(E_f - E_i - \hbar\omega) \quad (5.4)$$

where  $n$  is the refractive index of the material and  $c$  is speed of light. The quantity

$\frac{2 \left| \langle f | \hat{\varepsilon} \cdot \hat{p} | i \rangle \right|^2}{m(E_f - E_i)}$  is defined as the oscillator strength  $f$  of the transition<sup>24</sup>. From Eq (5.4)

intersubband absorption is proportional to  $f$  and the polarisation selection rules are determined by the nonzero terms of the matrix element  $\langle f | \hat{\varepsilon} \cdot \hat{p} | i \rangle$ .

First we will discuss the selection rules of the intersubband transition in quantum wells.

### 1. Selection rules in the conduction band of a quantum well:

To understand the selection rules in the conduction band of a quantum well, a single band infinite potential well model will be used<sup>25</sup>. In this model the confining potential of the well can be described as follows:  $V(z) = 0$  between  $z = 0$  and  $z = L$  and infinite elsewhere, where the  $z$ -axis represents the growth direction and  $L$  is the width of the quantum well (see Figure 5-9a),  $V(x) = V(y) = 0$  for all  $x$  and  $y$ . The wavefunction of the above system is given by

$$\psi_{nk_1}(x, y, z) = \sqrt{\frac{2}{AL}} \sin\left(\frac{n\pi z}{L}\right) \exp(ik_x x + ik_y y) \quad (5.5a)$$

because  $\psi$  is ortho-normal function

$$\langle \psi_{nk_1} | \psi_{n'k'_1} \rangle = \langle nk_{\parallel} | n'k'_{\parallel} \rangle = \delta_{nn'} \delta_{k_1, k'_1} \quad (5.5b)$$

where  $A$  is the area of the well and  $n = 1, 2, 3, \dots$ . Using the wavefunction in equation (5.5), the matrix element in equation (5.4) becomes

$$\langle f | \hat{\epsilon} \cdot \hat{p} | i \rangle = \frac{2}{AL} \int \exp(-ik'_x - ik'_y) \sin\left(\frac{m\pi z}{L}\right) (\epsilon_x p_x + \epsilon_y p_y + \epsilon_z p_z) \exp(ik_x + ik_y) \sin\left(\frac{n\pi z}{L}\right) dx dy dz$$

or

$$\langle f | \hat{\epsilon} \cdot \hat{p} | i \rangle = (\epsilon_x \hbar k_x + \epsilon_y \hbar k_y) \delta_{n,m} \delta_{k_1, k'_1} + \epsilon_z \delta_{k_1, k'_1} \sqrt{\frac{2}{L}} \int \sin\left(\frac{m\pi z}{L}\right) [p_z] \sin\left(\frac{n\pi z}{L}\right) dz$$

where  $(k_x, k_y, n)$  represents the initial state and  $(k'_x, k'_y, m)$  represents the final state. In the above equation the terms proportional to  $\epsilon_x$  and  $\epsilon_y$  vanish for all  $n \neq m$  (see equation (5.5b)) and the term proportional to  $\epsilon_z$  yields a contribution to the matrix element if  $k_x = k'_x, k_y = k'_y$  and  $n \neq m$  with changing parity (odd to even or even to odd). Thus the matrix element  $\langle f | \hat{\epsilon} \cdot \hat{p} | i \rangle$  in the conduction band of a quantum well reads

$$\langle f | \hat{\epsilon} \cdot \hat{p} | i \rangle = \frac{2}{L} \epsilon_z \int \sin\left(\frac{m\pi z}{L}\right) [p_z] \sin\left(\frac{n\pi z}{L}\right) dz \quad (5.6)$$

From equation (5.6) we conclude that intersubband transitions in the conduction band of a quantum well are allowed if the electric field of the incident radiation is parallel to the  $z$ -axis (growth direction) as illustrated in Figure 5-10.

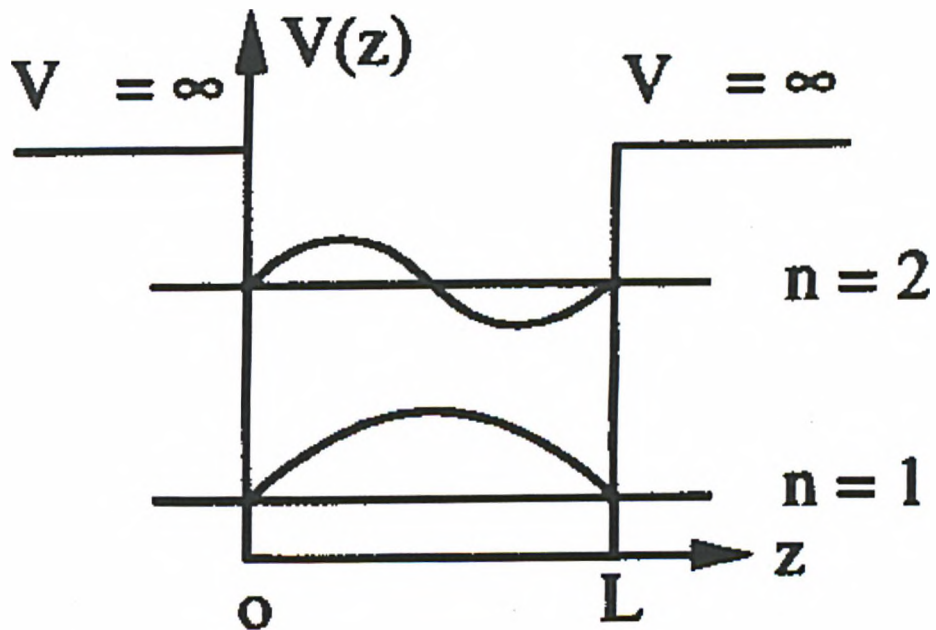


Figure 5-9 Simplified potential profile of the conduction band of a quantum well, (Reference 26).

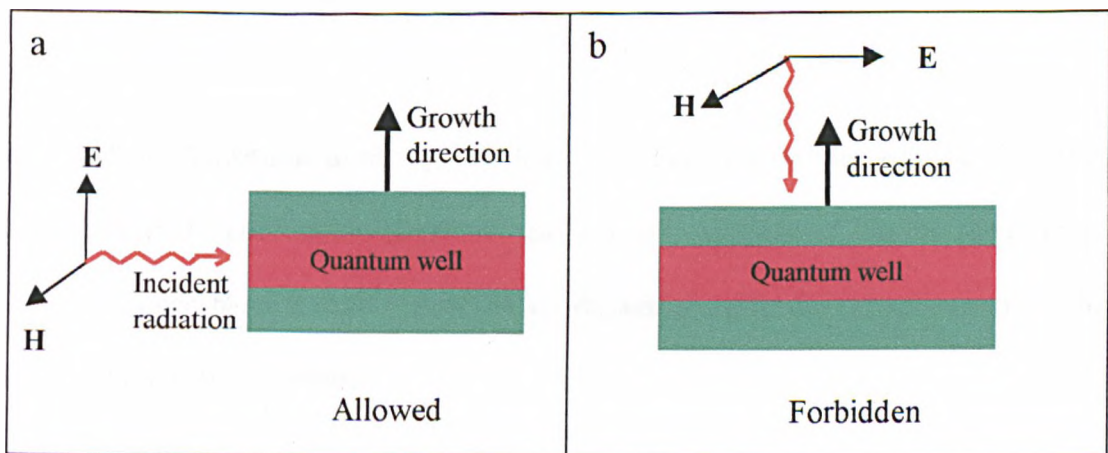
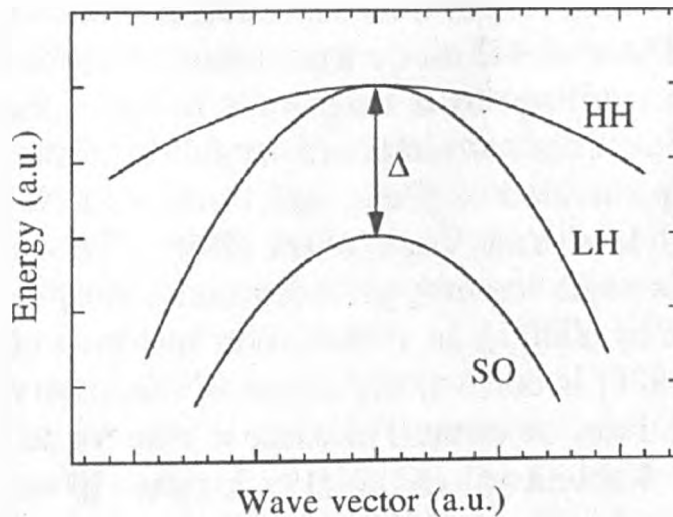


Figure 5-10 Schematic presentation of the selection rules in the conduction band of a quantum well.

## 2. Selection rules in the valence band of a quantum well:

The valence band of a bulk semiconductor consists of three bands (six bands with spin): heavy-hole (HH), light-hole (LH) and split-off (SO) as illustrated in Figure 5-11.



**Figure 5-11 Schematic of the valence band of most common semiconductors at the  $\Gamma$  point. HH, LH, SO indicate heavy hole, light hole, and spin-orbit split-off band, respectively. (Reference 24).**

Intersubband transitions in the valence band of a quantum well are more complicated than those in the conduction band of a quantum well because of<sup>27</sup> (i) the band mixing (in the valence band and also with the conduction bands), (ii) the anisotropy of the valence hole subband states.

In order to calculate the intersubband transitions in the valence band accurately, a multi-band theory such as the eight-band  $\mathbf{k}\cdot\mathbf{p}$  must be used<sup>24,27</sup>. In the multi-band framework the total wavefunction is written as a linear combination of the product of the envelope wavefunctions and the zone-centre Bloch wavefunctions<sup>24</sup>

$$\psi_{nk}(r) = \sum_{\nu} F_{\nu nk_1}(r) u_{\nu k}(r) \quad (5.7)$$

where  $\nu$  runs over all the bands included in the calculations,  $n$  indicates the subband levels,  $u_{\nu k}(r)$  is the Bloch wavefunctions and  $F_{\nu nk_1}(r)$  is the envelope wavefunction which can be found by solving the Schrodinger equation for the Luttinger-Kohn hamiltonian<sup>24</sup>

$$\sum_{\nu} [H_{\nu\nu}^{LK} + V(z)\delta_{\nu\nu'}] F_{\nu nk_1}(r) = E_{nk_1} F_{\nu nk_1}(r) \quad (5.8)$$

where  $V(z)$  is the quantum well potential and  $H_{\nu\nu}^{LK}$  is the Luttinger-Kohn Hamiltonian.

In the case of four band model (HH and LH)  $H_{\nu\nu}^{LK}$  is given by<sup>24</sup>

$$H_{\nu\nu}^{LK} = \begin{pmatrix} P+Q & -S & R & 0 \\ -S^* & P-Q & 0 & R \\ R^* & 0 & P-Q & S \\ 0 & R^* & S^* & P+Q \end{pmatrix} \quad (5.9)$$

where

$$P = \frac{\hbar^2}{2m_0} \gamma_1 (k_x^2 + k_y^2 + k_z^2)$$

$$Q = \frac{\hbar^2}{2m_0} \gamma_2 (k_x^2 + k_y^2 - 2k_z^2)$$

$$R = -\frac{\hbar^2 \sqrt{3}}{2m_0} [-\gamma_2 (k_x^2 - k_y^2) + 2i\gamma_3 k_x k_y]$$

$$S = \frac{\hbar^2 \sqrt{3}}{m_0} \gamma_3 (k_x - ik_y) k_z$$

where  $k_z = -i \frac{d}{dz}$  and  $\gamma_1$ ,  $\gamma_2$  and  $\gamma_3$  are the Luttinger parameters and depend on the material.

The anisotropy of the valence bands arises from the difference in the value of  $\gamma_2$  and  $\gamma_3$  (see the expression for  $R$ ) and also from terms such as  $k_x k_z$  and  $k_y k_z$  (see the expression for  $S$ ) in the Luttinger-Kohn Hamiltonian.

In the light of the four band model described above, the matrix element in equation (5.4) can be calculated explicitly<sup>24</sup>

$$\langle \psi_{nk}(\mathbf{r}) | \hat{\varepsilon} \cdot \mathbf{p} | \psi_{n'k}(\mathbf{r}) \rangle = \frac{m_0}{\hbar} \hat{\varepsilon} \cdot \sum_{v,v'=1}^4 (I_{vv'} O_{vv'}^{nn'} + J_{vv'} D_{vv'}^{nn'}) \quad (5.10)$$

where  $I_{vv'}$  is a function of  $\gamma_1, \gamma_2, \gamma_3$ , and  $k_{\parallel} = (k_x, k_y)$ .  $J_{vv'}$  is a function of  $\gamma_1, \gamma_2$  and  $\gamma_3$  only (see reference 24).  $O_{vv'}^{nn'}$  and  $D_{vv'}^{nn'}$  are given by<sup>24</sup>

$$O_{vv'}^{nn'} = \int F_v^*(n, k_{\parallel}, z) F_{v'}(n', k_{\parallel}, z) dz \quad (5.11)$$

and

$$D_{vv'}^{nn'} = \int F_v^*(n, k_{\parallel}, z) \left(-i \frac{d}{dz}\right) F_{v'}(n', k_{\parallel}, z) dz \quad (5.12)$$

The results of the calculations of the matrix element in equation (5.10) for x (y) and z polarisation are summarised in Table 1<sup>24</sup> and Table 2<sup>24</sup>, respectively.

Table 1 x (y) polarisation (in-plane). (Reference 24)

	HH(3/2)	HH(-3/2)	LH(1/2)	LH(-1/2)
HH(3/2)	$\hbar k_x (\gamma_1 + \gamma_2) O^{nn'}$	0	$-\sqrt{3} \gamma_3 D^{nn'}$	$-\sqrt{3} \hbar (\gamma_2 k_x - i \gamma_3 k_y) O^{nn'}$
HH(-3/2)	0	$\hbar k_x (\gamma_1 + \gamma_2) O^{nn'}$	$-\sqrt{3} \hbar (\gamma_2 k_x + i \gamma_3 k_y) O^{nn'}$	$\sqrt{3} \gamma_3 D^{nn'}$
LH(1/2)	$-\sqrt{3} \gamma_3 D^{nn'}$	$-\sqrt{3} \hbar (\gamma_2 k_x - i \gamma_3 k_y) O^{nn'}$	$\hbar k_x (\gamma_1 - \gamma_2) O^{nn'}$	0
LH(-1/2)	$\sqrt{3} \hbar (\gamma_2 k_x + i \gamma_3 k_y) O^{nn'}$	$\sqrt{3} \gamma_3 D^{nn'}$	0	$\hbar k_x (\gamma_1 - \gamma_2) O^{nn'}$

Table 2 z polarisation (growth direction). (Reference 24)

	HH(3/2)	HH(-3/2)	LH(1/2)	LH(-1/2)
HH(3/2)	$\hbar(\gamma_1 - 2\gamma_2)D^{nn'}$	0	$-\sqrt{3}\gamma_3(k_x + ik_y)O^{nn'}$	0
HH(-3/2)	0	$\hbar(\gamma_1 - 2\gamma_2)D^{nn'}$	0	$\sqrt{3}\gamma_3(k_x + ik_y)O^{nn'}$
LH(1/2)	$-\sqrt{3}\gamma_3(k_x - ik_y)O^{nn'}$	0	$\hbar(\gamma_1 + 2\gamma_2)D^{nn'}$	0
LH(-1/2)	0	$\sqrt{3}\gamma_3(k_x + ik_y)O^{nn'}$	0	$\hbar(\gamma_1 + 2\gamma_2)D^{nn'}$

The results in Table 1 and Table 2 can be understood as follows<sup>24</sup>: the terms containing  $JD^{nn'}$  contain the dipole matrix element of the envelope function ( $D^{nn'}$  see equation (5.12)). Due to the dipole matrix element only transitions between states of different parity are allowed. Because  $J$  is independent of  $k_{||}$ , they are allowed at  $k_{||} = 0$ . The  $JD^{nn'}$  terms give rise to HH→HH and LH→LH transitions for light polarised in the z direction (growth direction) and to HH→LH transitions for light polarised in the x (y) direction (in-plane). The terms containing  $IO^{nn'}$  include an envelope integral between envelope wavefunctions ( $O^{nn'}$  see equation (5.11)), and thus only transitions between states of the same parity are allowed.  $I$  is  $k_{||}$  dependent, and thus the transitions are allowed only for  $k_{||} \neq 0$ . The  $IO^{nn'}$  terms give rise to HH→HH and LH→LH transitions for light polarised in the x (y) direction (in-plane) and to HH→LH transitions for light polarised in the x (y) and z directions.

From the above discussion we conclude that due to the band mixing in the valence band and the anisotropy of the valence hole subband states, intersubband transitions in the valence band are allowed for light polarised in the growth direction and also for light polarised in the in-plane direction.

More sophisticated calculations were performed by F. Szmulowicz and G. Brown<sup>27</sup> using the eight-band  $k \cdot p$  theory showed that the admixture of the s-type conduction band states into the valence bands enhances the in-plane transitions between  $HH1 \rightarrow LH2$  at  $k_{\parallel}=0$  as illustrated in Figure 5-12.

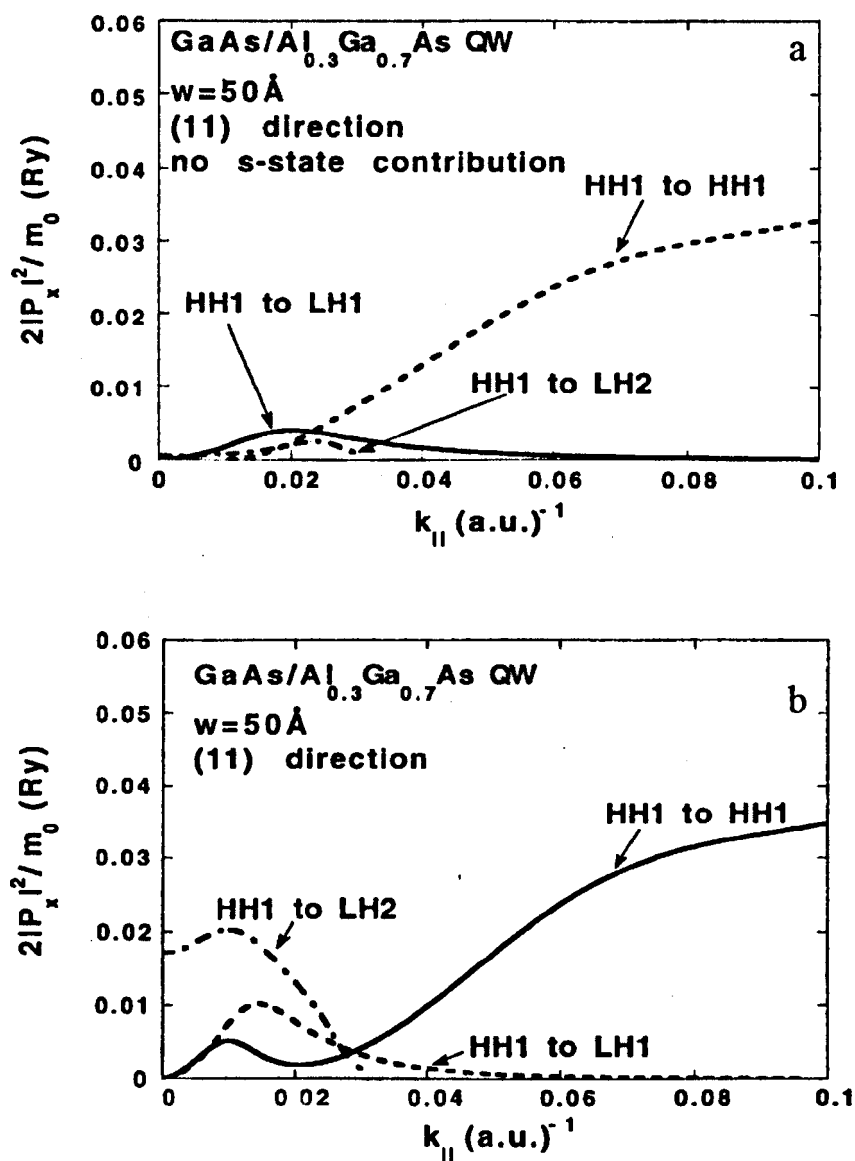


Figure 5-12 Effect of conduction band-valence band coupling on the intersubband transitions in the valence band of a quantum well. (a) without conduction band valence band-coupling (b) with conduction band-valence band coupling. (Reference 27).

### 3 Selection rules in quantum dots:

For simplicity the selection rules will be discussed in the case of a cubic quantum dot with dimensions  $L_x=L_y=L_z=L$ . The eigenfunctions and eigenvalues of this system are given by

$$\psi_{nml}(\mathbf{r}) = \sqrt{\frac{8}{L^3}} \sin\left(\frac{n\pi x}{L}\right) \sin\left(\frac{m\pi y}{L}\right) \sin\left(\frac{l\pi z}{L}\right)$$

with

$$\langle nml | n'm'l' \rangle = \delta_{nn'} \delta_{mm'} \delta_{ll'} \quad (5.13)$$

and

$$E_{nml} = \frac{\hbar^2 \pi^2}{2mL^2} (n^2 + m^2 + l^2), \text{ with } n, m, l = 1, 2, 3, \dots \quad (5.14)$$

The matrix element in equation (5.4) is given by

$$\langle f | \hat{\mathbf{p}} | i \rangle = \frac{8}{L^3} \int \sin\left(\frac{n'\pi x}{L}\right) \sin\left(\frac{m'\pi y}{L}\right) \sin\left(\frac{l'\pi z}{L}\right) (\varepsilon_x p_x + \varepsilon_y p_y + \varepsilon_z p_z) \sin\left(\frac{n\pi x}{L}\right) \sin\left(\frac{m\pi y}{L}\right) \sin\left(\frac{l\pi z}{L}\right) dx dy dz$$

$$\langle f | \hat{\mathbf{p}} | i \rangle = \varepsilon_x \delta_{mm'} \delta_{ll'} \langle n' | p_x | n \rangle + \varepsilon_y \delta_{nn'} \delta_{ll'} \langle m' | p_y | m \rangle + \varepsilon_z \delta_{nn'} \delta_{mm'} \langle l' | p_z | l \rangle \quad (5.15)$$

Equation (5.15) indicates that intersubband transitions are allowed for all polarisation directions in a cubic quantum dot. Intersubband transitions are allowed for light polarised in the x direction if  $m=m'$ ,  $l=l'$  and for all  $n \neq n'$  with changing parity (odd-even or even-odd). In the same way intersubband transitions are allowed for light polarised in the y direction if  $n=n'$ ,  $l=l'$  and for all  $m \neq m'$  with changing parity and for light polarised in the z direction if  $n=n'$  and  $m=m'$  for all  $l \neq l'$  with changing parity. Figure 5-13 shows some of the allowed transitions in a cubic quantum dot and their polarisation. From the above discussion we conclude that in contrast to the transitions in the conduction band of a quantum well, intersubband transitions in quantum dot are allowed for all polarisations.

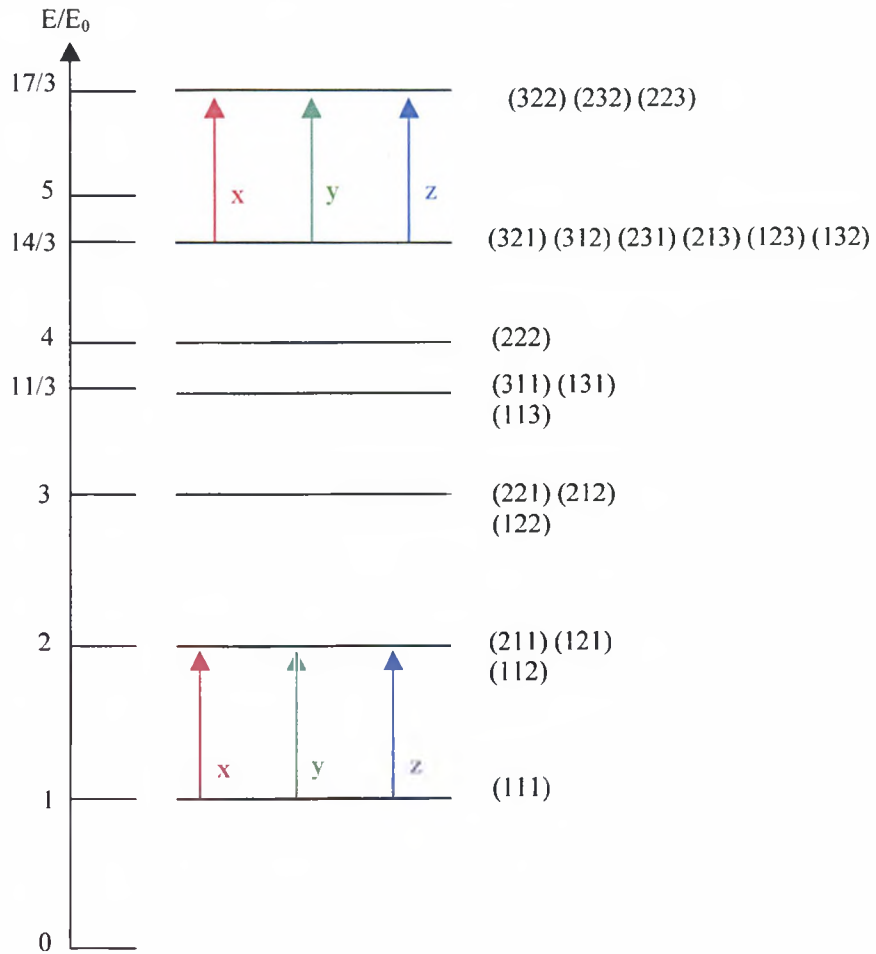


Figure 5-13 Energy levels and the polarisation directions associated with

intersubband transitions in a cubic quantum dot,  $E_0 = E_{111} = \frac{3\hbar^2\pi^2}{2mL^2}$ .

## 5.5 Experimental Methods

The experimental techniques used to obtain the results of this chapter will be summarised in this section. All the intersubband measurements are carried out using an evacuated Fourier transform infrared (FTIR) spectrometer. Two types of measurements are performed, namely direct absorption and photocurrent spectroscopy. First an introduction to FTIR spectroscopy will be given.

### 5.5.1 FTIR Spectroscopy

FTIR spectrometer is composed of the following components: a mid infrared radiation (MIR) source, an interferometer with beamsplitter (Michelson interferometer) and a detector. The beam produced by the MIR source passes through an aperture, then through an optical filter to the interferometer. When the beam exits the interferometer, it is led to the sample, and finally focused on the detector (see Figure 5-14)

As can be seen in Figure 5-15, the interferometer consists of a fixed mirror, moving mirror (scanner) and beamsplitter (which transmits 50% of the beam and reflects 50%). The beam entering the interferometer is divided into two beams: one is transmitted (T) to the moving mirror while the second is reflected (R) to the fixed mirror. The transmitted part is reflected by the moving mirror and returns to the beamsplitter where again one part is transmitted to the source (TT) while the second is reflected (TR) to the sample. The reflected part is reflected by the fixed mirror and returns to the beamsplitter where it also divided: one part is reflected (RR) back to the source while the second is transmitted (RT) to the sample. The output of the interferometer incident on the sample is TR+RT.

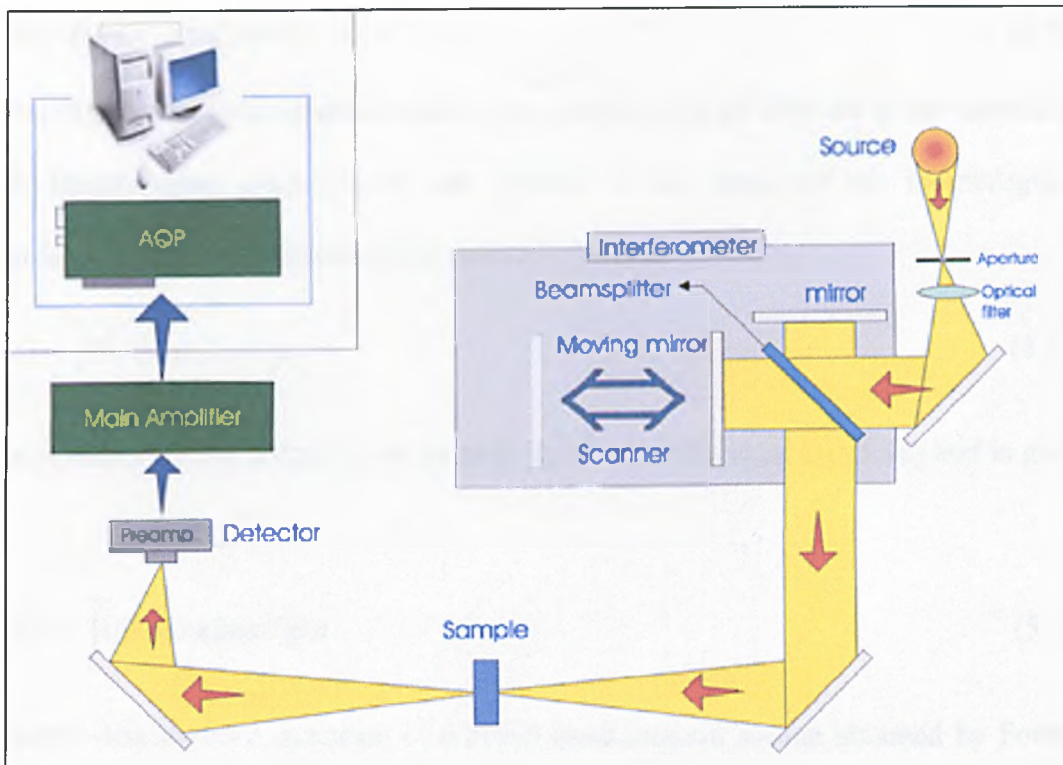


**Figure 5-14 Schematic diagram representing the working principle of the FTIR spectrometer. (Reference 28).**

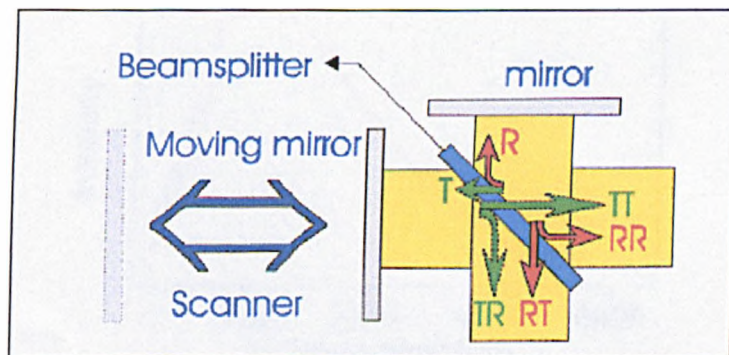


**Figure 5-15 Schematic diagram representing the working principle of the interferometer. (Reference 28).**

In the case of a monochromatic light source of intensity  $B(\nu)$ , where  $\nu$  is the frequency of the light in  $\text{cm}^{-1}$  units, the phase difference between TR and RT varies with time and is given by  $\phi = 2\pi\delta\nu$ .  $\delta$  is called the retardation and equals  $2vt$ , where  $v$  is the scanner velocity (cm/sec). Therefore, the intensity of the beam at the detector (or the so called interferogram) is

$$I(\delta) = B(\nu)(1 + \cos(2\pi\delta\nu)) \quad (5.16)$$

When a polychromatic source is used, many frequencies are emitted at the same time. The interferogram measured by the detector is the result of the interferograms corresponding to each wavenumber and can be written

$$I(\delta) = \int_{-\infty}^{+\infty} B(\nu) \cos(2\pi\nu\delta) d\nu \quad (5.17)$$

The intensity of the source is the inverse Fourier transform of Eq (5.18) and is given by

$$B(\nu) = \int_{-\infty}^{+\infty} I(\delta) \cos(2\pi\nu\delta) d\delta \quad (5.18)$$

Figure 5-16a shows a spectrum of a broad band infrared source obtained by Fourier transforming the measured interferogram in Figure 5-16b.

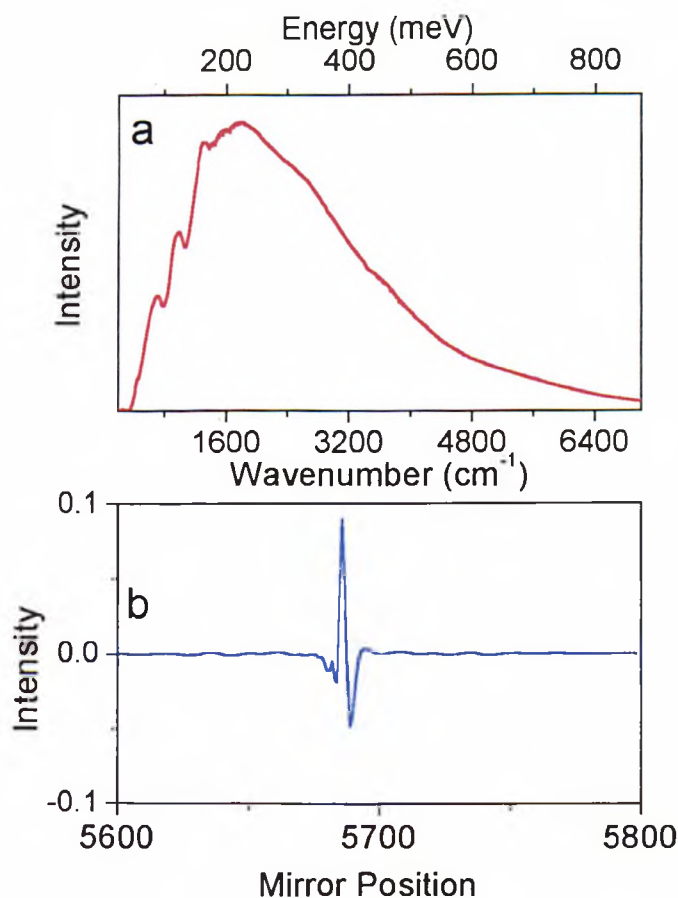


**Figure 5-16 (a) Spectrum of a broad band MIR source obtained from Fourier transforming the interferogram in (b).**

The measurements in this work were carried out using a step-scan lock-in amplifier technique. In this technique the moving (scanning) mirror (see Figure 5-15) moves in discrete steps and performs a measurement at each step or retardation point. Also the device is modulated and a lock-in amplifier is used to demodulate the signal at each retardation point. The advantage of this technique is that it can measure a weak signal or a signal hidden beneath an intense background. Additionally, multiple reading may be taken at each retardation point to improve the signal to noise ratio.

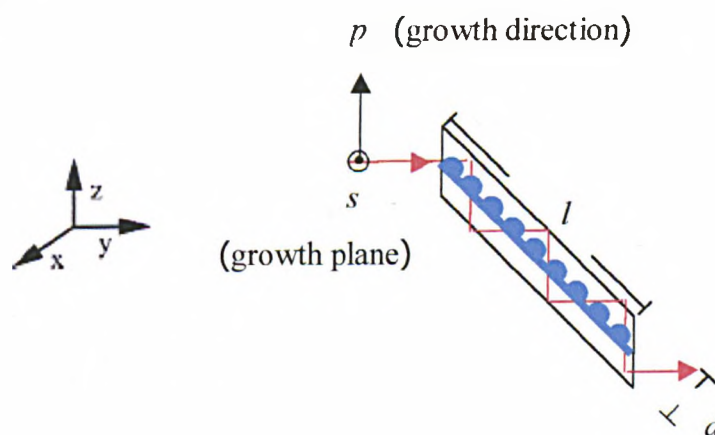
The specifications of our Bruker IFS 66v/S vacuum FTIR spectrometer have been summarised in Table 3.

Table 3 Specifications of IFS 55 FTIR spectrometer

Item	Spectral Range (cm <sup>-1</sup> )	Description
Light Source	7500-30	MIR Source (Globar)
Beamsplitter	7500-370	Ge on KBr beamsplitter
Detector	545 cm <sup>-1</sup> cutoff	HgCdTe (MCT)
The maximum resolution of the IFS 66v/S is 0.1 cm <sup>-1</sup>		

### 5.5.2 Direct Absorption Measurements

Intersubband absorption of doped quantum dot samples can be measured by illuminating the sample with broad band MIR, and detecting the transmitted signal through the sample using an MCT detector. When the energies of the incident light match the energy separations of the quantized levels in the dots, carriers (electrons or holes) absorb the radiation and undergo transitions from their lowest state to higher states. The absorption will appear as a dip in the transmission spectrum. The advantage of this technique is that it is a direct measurement and can be used to probe both bound-to-bound and bound-to-continuum transitions. The disadvantage of the technique is that the absorbed signal is generally weak relative to the background. To enhance the observed absorption signal and to be able to study the polarisation dependence of the intersubband absorption, the facets and the backside of the sample were polished to form a 45° multipass waveguide of dimensions 0.5 cm x 0.5 cm (see Figure 5-17).



**Figure 5-17 45° multipass waveguide geometry for absorption measurements.**

In this geometry the light is coupled to the 45° polished facet of the sample. The incident radiation undergoes several internal reflections in the sample. The number of passes through the active region of the sample is determined by  $M = \frac{l}{d}$ , where  $l$  is the sample length and  $d$  is the sample thickness. In our geometry  $M=10$ .

Figure 5-18 shows the experimental set up used for the direct absorption experiment with the FTIR spectrometer in step-scan mode using a lock-in amplifier. The incident beam is mechanically modulated at frequency of 177 Hz and focused onto the sample. An MCT detector is used to detect the transmitted signal through the sample. The lock-in amplifier demodulates the detected signal at the reference frequency of the chopper. Finally the demodulated signal is sent to the spectrometer's digitizer to perform the Fourier transform. The spectral resolution of the measurements is set at  $16\text{ cm}^{-1}$ .

In the *s* polarisation, the electric field of the incident light is in the layer plane. In *p* polarisation half of the electric field is along the growth direction and the other half is in the layer plane (see Figure 5-17).

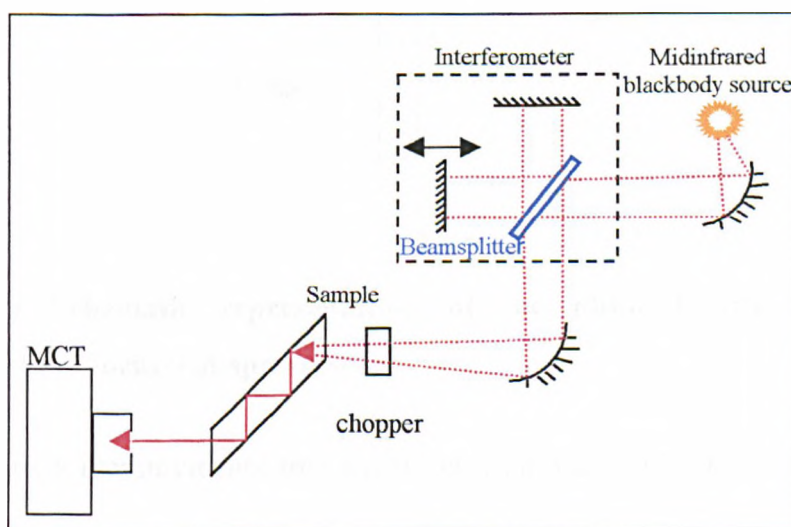


**Figure 5-18 Experimental setup of the absorption measurements.**

### 5.5.3 Photocurrent Measurements

Intersubband photocurrent spectroscopy involves a two step mechanism. Photoexcitation of the carriers (electrons or holes) occurs first, then the carriers escape out of the dots and are collected and give rise to a measurable photocurrent as illustrated in Figure 5-19. This technique can therefore probe both bound-to-bound and bound-to-continuum transitions. The advantage of this technique is that it is highly sensitive because there is no current background in this type of measurement and also it is easy to measure the current signal with high sensitivity. However, the photocurrent signal depends on the transport properties as well as the absorption characteristics of the device.

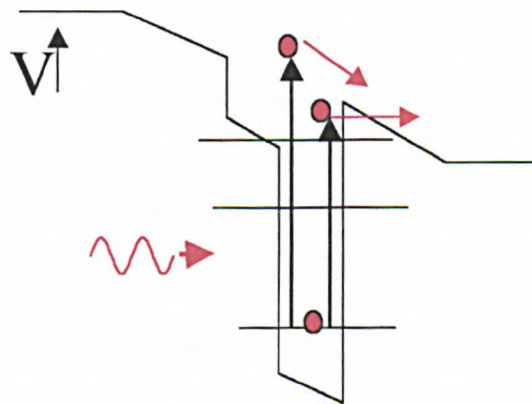


**Figure 5-19 Schematic representation of the physical principle of the intersubband photocurrent spectroscopy.**

The photocurrent measurements are carried out using the FTIR spectrometer in step-scan mode using a lock-in amplifier. The experimental setup is shown in Figure 5-20. The samples are mounted in a helium flow cryostat model ST-50C (Janis Research Co.) with ZnSe window. The spectrometer's broad band MIR source (globar) is mechanically modulated at frequency of 177 Hz and focused onto the sample. The device is connected in series with the current input of the lock-in amplifier. The device can be biased using a Keithley 230 voltage source which is connected across the sample. The lock-in amplifier demodulates the detected signal at the reference

frequency of the chopper. Finally the demodulated signal is sent to the spectrometer's digitizer to perform the Fourier transform. The spectral resolution of the measurements is set at  $16 \text{ cm}^{-1}$ .

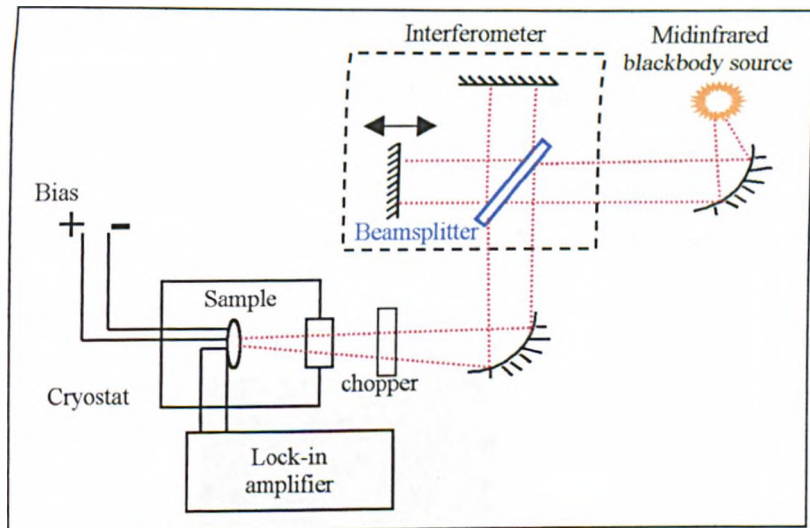


**Figure 5-20** Experimental setup of the photocurrent measurements.

The photocurrent measurements were performed in two configurations, normal incidence geometry and  $45^\circ$  polished facet geometry as shown in Figure 5-21. The second geometry allows us to study the polarisation dependence of the photocurrent.

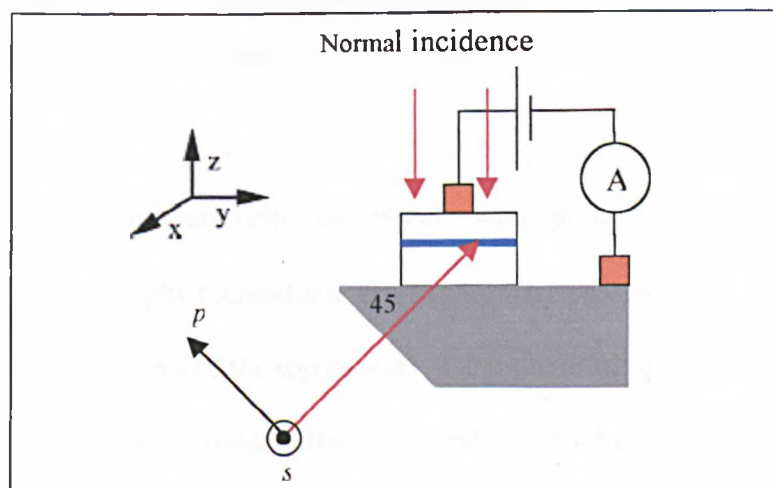


**Figure 5-21** Sample configuration used in photocurrent measurements.

## 5.6 Samples

Four sets of samples have been investigated in this work. All samples were grown by molecular beam epitaxy on (100) undoped GaAs substrates at the EPSRC Central-Facility for III-V Semiconductors at Sheffield. The structure of the samples is illustrated schematically in Figure 5-22. The investigated samples are n-i-n or p-i-p infrared photodetector structures. Silicon was used to dope n-type samples and beryllium to dope p-type samples. The structural detail of the samples will be given within the results section.

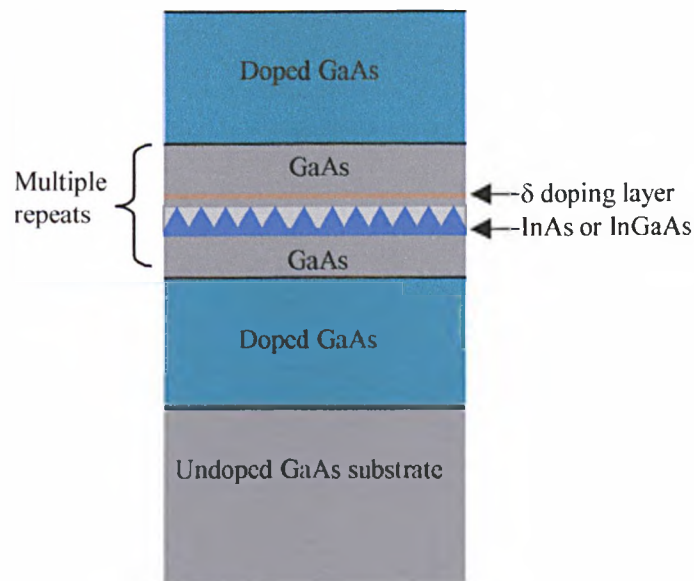


**Figure 5-22 Schematic structure of the samples.**

For photocurrent measurements the wafers were processed into 400  $\mu\text{m}$  diameter mesas using lithography techniques. The lithography process is a five step procedure.

- 1- Defining the pattern of the top contact, using photolithography.
- 2- Metallising the top contact. InGe-Au and Au-Zn-Au were used to make n-type ohmic contacts and p-type ohmic contacts respectively.
- 3- Forming and etching the mesa. 1:8:80 of  $\text{H}_2\text{SO}_4 : \text{H}_2\text{O}_2 : \text{H}_2\text{O}$  etching solution was used. The etching rate is about 0.5 micron/min.

- 4- Evaporating the bottom contacts. InGe-Au and Au-Zn-Au were used to make n-type and p-type ohmic contacts, respectively.
- 5- Annealing the processed samples in nitrogen environment at 420C for about one minute to diffuse the metals into GaAs.

After the processing, the edge of the sample was polished to form a 45° wedge. Finally the samples were glued onto ceramic, then mounted and bonded onto TO-5 headers.

## 5.7 Results

In the next three subsections the results of intersubband transition measurements on SAQDs will be presented. In section 5.7.1 we will discuss intersubband transitions in the conduction band from doped and undoped active regions of isolated SAQD samples. A full comparison between intersubband absorption and photocurrent spectroscopy will be presented. Section 5.7.2 will be directed toward the intersubband transitions in the valence band of SAQDs. Section 5.7.3 will be devoted to the effects of vertical dot coupling on intersubband transitions in the conduction band.

### 5.7.1 Intersubband Transitions in the Conduction Band of Quantum Dots

In this section intersubband transitions in the conduction band of isolated SAQDs will be presented. Two experimental techniques will be used in this study; direct absorption measurements and photocurrent spectroscopy. We will present the results from two samples (i) M1698, consisting of 15 layers of InAs dots with undoped active region (see Table 4) (ii) M2303 consisting of 30 layers of InAs dots with doped active region (see Table 5). The dots in both samples are uncoupled.

Table 4 Structural detail of n-i-n undoped active region sample (M1698)

Repeats	Thickness (Å)	Material	Dopant	Type	Concentration (cm <sup>-3</sup> )
1	4000	GaAs	Si	n	7.0x10 <sup>+17</sup>
1	1000	GaAs	Si	n	1.0x10 <sup>+17</sup>
1	200	GaAs		ud	
15	6	InAs 2.5 ML		ud	
15	200	GaAs		ud	
1	1000	GaAs	Si	n	1.0x10 <sup>+17</sup>
1	20000	GaAs	Si	n	1.0x10 <sup>+18</sup>

Table 5 structural detail of n-i-n doped active region sample (M2303)

Repeats	Thickness (Å)	Material	Dopant	Type	Concentration (cm <sup>-3</sup> )
1	5000	GaAs	Si	n	3.0x10 <sup>+18</sup>
1	1700	GaAs		ud	
30	280	GaAs		ud	
30	6	InAs 2.5 ML		ud	
30	20	GaAs			
30	3	Si -δ			3.0x10 <sup>+18</sup>
1	2000	GaAs		ud	
1	5000	GaAs	Si	n	3.0x10 <sup>+18</sup>

Figure 5-23 shows a cross-section TEM micrograph of an uncapped InAs quantum dot grown under very similar conditions (the active region was grown at 520°C with growth rate 0.4 ML/s) to the dots used in this work. As can be seen from Figure 5-23 the dot is flat with lateral dimensions ~5 times larger than vertical dimension.

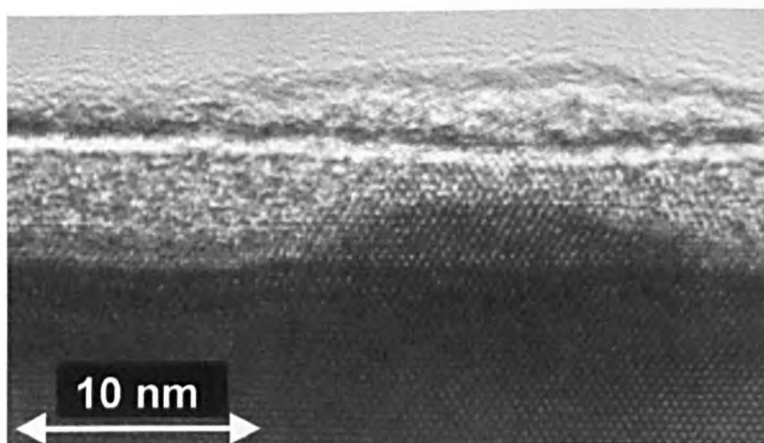
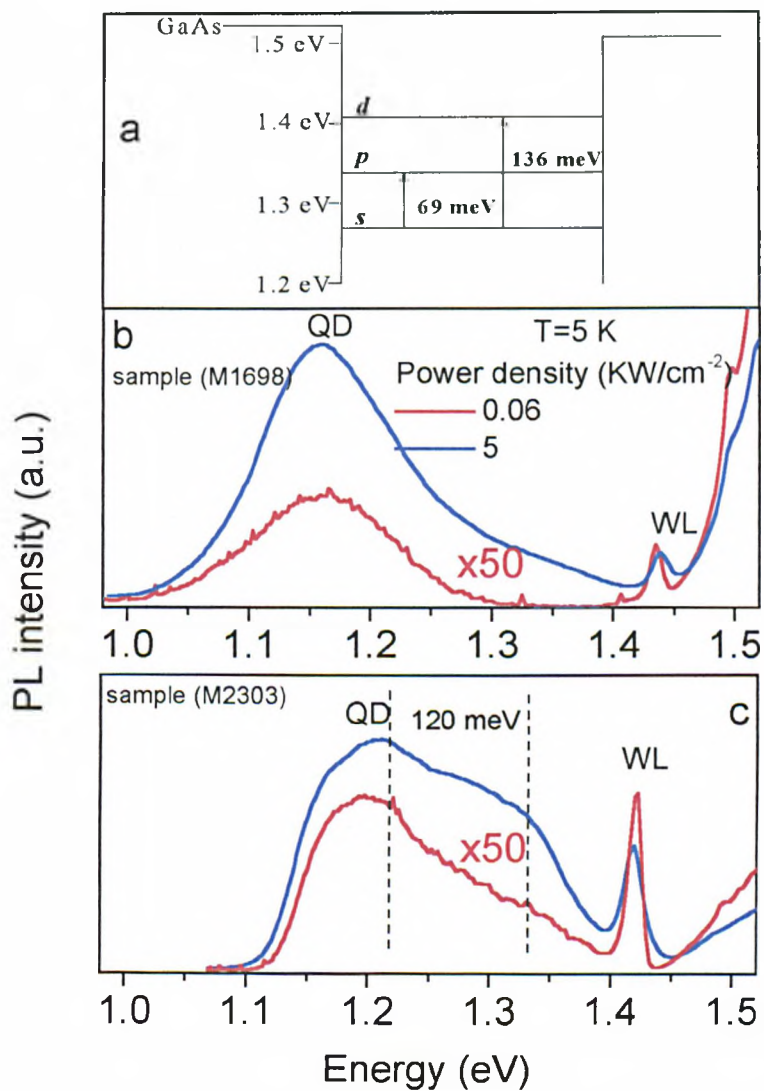


Figure 5-23 cross-section TEM micrograph of an uncapped InAs quantum dot was grown at 0.4 ML/s growth rate.

### 5.7.1.1 Photoluminescence

Figure 5-24b and Figure 5-24c show the PL spectra of samples M1698 (undoped active region), and M2303 (doped active region) at 5K for two different excitation power densities. It is clear from the comparison between the low and high power excitation spectra of sample M2303 that sample M2303 has at least one excited state. Theoretical calculations<sup>18</sup> on flat dots such as those used in this work gave 69 meV energy separation between the ground state (*s*-state) and the first excited state (*p*-state), and 136 meV energy separation between the ground state and the *d* excited state (see Figure 5-24a) indicating that the first resolved PL peak at 120 meV-130 meV above the ground state from sample M2303 in Figure 5-24 is due to transitions to the *d* excited state. By contrast, the PL spectra of sample M1698 do not show well resolved excited states. This is perhaps due to the doping in sample M2303 helping to observe excited states at lower excitation power compared with sample M1698. However, it is possible that the high energy tail (1.27 eV to 1.4 eV) in the high power PL spectrum of sample M1698 is due to transitions to excited states. For sample M2303 (doped active region), besides the PL associated with the dots, we observed a transition at 1.42 eV from the wetting layer, which indicates that the dot density in this sample is less than the dot density of sample M1698. The 70 meV red shift in the ground state PL peak position of sample M1698 relative to the ground state PL peak position of sample M2303 indicates that the dots of sample M1698 are larger than those in sample M2303.



**Figure 5-24** (a) Conduction energy levels of a single dot of base length 25 nm and height 2.5 nm (From reference 18). (b) 5 K power dependent PL spectrum of sample M1698, (c) PL spectra from M2303 under the same conditions

### 5.7.1.2 Direct Absorption

Figure 5-25a shows the transmission spectra in the intersubband region measured at room temperature from sample M1698 (undoped active region, see Table 4) for  $p$  and  $s$  polarisation as described in section 5.5.2 (see also Figure 5-18). In Figure 5-25a

$T_p = \frac{T_{QD,p}}{T_{GaAs,p}}$ , where  $T_{QD,p}$  is the transmittance of the sample and  $T_{GaAs,p}$  is the

transmittance of a GaAs waveguide with dimensions exactly the same as the dot

sample (see Figure 5-17) for  $p$  polarised light and  $T_s = \frac{T_{QD,s}}{T_{GaAs,s}}$  are presented. A clear

dip can be seen in Figure 5-25a in the  $p$  polarised transmission spectrum compared with the  $s$  polarised transmission spectrum indicating that there is an intersubband transition from the sample in the energy range 108 meV to 160 meV polarised in the growth direction. A very similar dip is observed in the  $p$  polarised transmission spectrum of sample M2303 (doped active region, see Table 5) relative to the  $s$  polarised transmission spectrum in the energy range 85 meV to 160 meV. In order to calculate the absorption from the transmission spectra, we used the expression

$$\text{Absorbance} = \log\left(\frac{T_s}{T_p}\right) \quad (5.19)$$

The advantage of this definition for absorption is that it is sensitive to the polarisation dependence of the signal and thus it allows us to eliminate the free carrier absorption and also any background effects. It is important to stress that by using equation (5.19) we calculate the strength of the  $p$  absorption relative to the  $s$  absorption. This method to obtain the absorption spectra is very similar to techniques previously published by Sauvage *et al*<sup>12</sup>.

Figure 5-25b and Figure 5-25c show intersubband absorption spectra from samples M1698 and M2303. From Figure 5-25b and Figure 5-25c we conclude that sample

M1698 has an absorption peak around 111 meV polarised in the growth direction, and sample M2303 has an absorption peak around 102 meV also polarised in the growth direction. The energy position of the absorption peak from each sample suggests that it is due to bound-to-bound transitions. The position of the intersubband transition peak at 102 meV from sample M2303 (doped active region) agrees well with the energy separation between the ground state and the first resolved excited state in the PL results for this sample (see Figure 5-24c). However, as discussed in the previous section, theoretical calculations<sup>18</sup> show that the energy separation between the ground state and the first excited state in flat dots such as those used in this work is between 50 meV and 70 meV. This energy separation is outside the detection range of the experiment (70 meV-800 meV). Thus the observed bound-to-bound absorption peaks in samples M1698 and M2303 are probably not due to transitions between ground state and first excited state but most likely arise from transitions between the ground state and a higher excited state (probably the  $d$  state). The energy calculations in Figure 5-24a showed that the energy separation between the ground state and the  $d$  excited state is 136 meV, very close to what is observed from the intersubband absorption spectra in Figure 5-25. The energy position of the observed transitions from our dots agree very well with the experimental results of Pan *et al*<sup>29</sup>, and Mukhametzhanov *et al*<sup>30</sup> for dots exhibiting similar PL energies. The temperature dependent absorption measurement indicated that the position of absorption peaks in Figure 5-25 are insensitive to temperature, with a red shift of only 3 meV being observed as temperature is increased from 12 K to 300K.

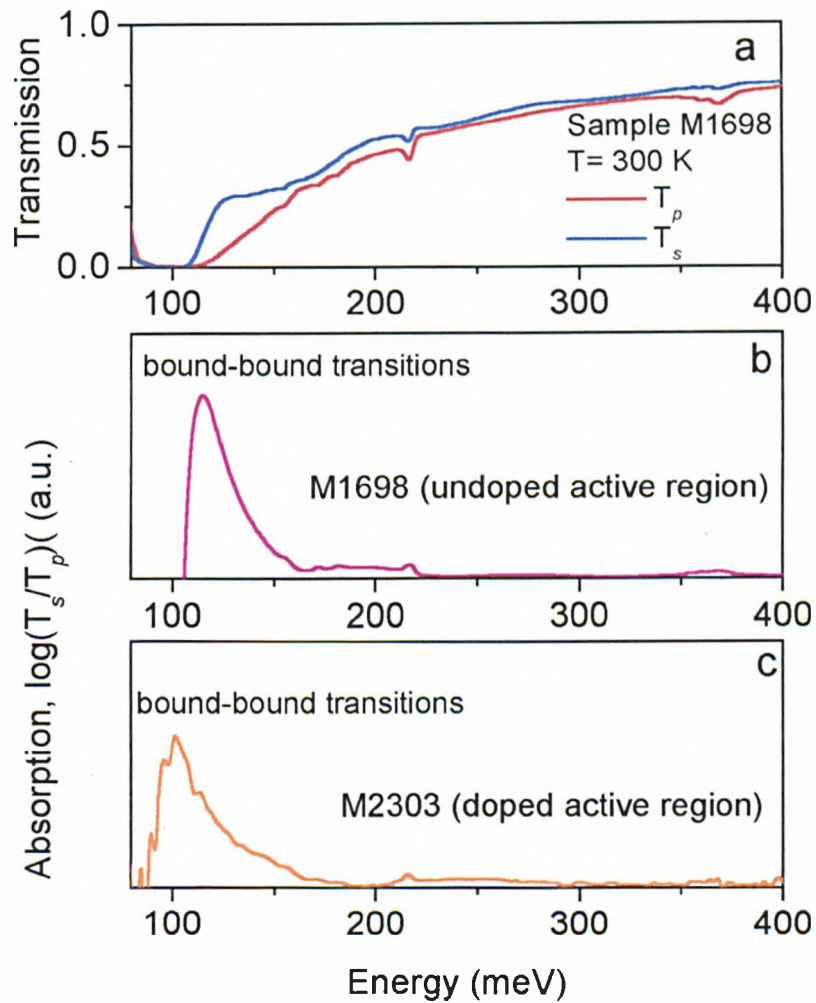
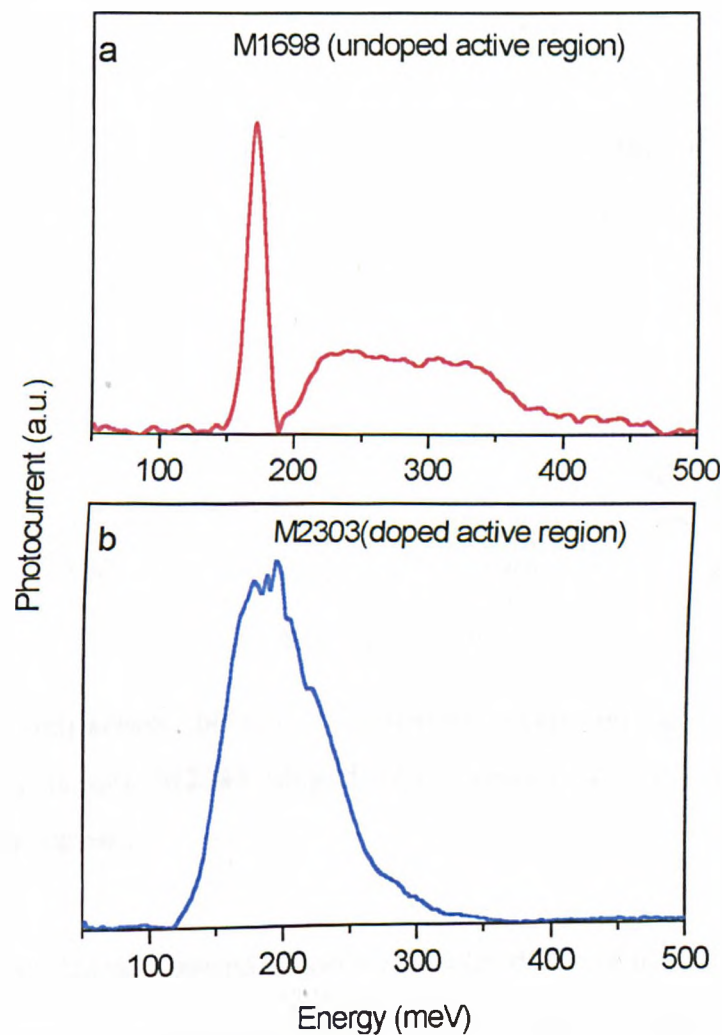


Figure 5-25 (a) Room temperature transmission spectra for  $p$  and  $s$  polarised light from sample M1698 (b) intersubband absorption ( $\log(T_s/T_p)$ ) spectra of sample M1698 and (c) M2303.

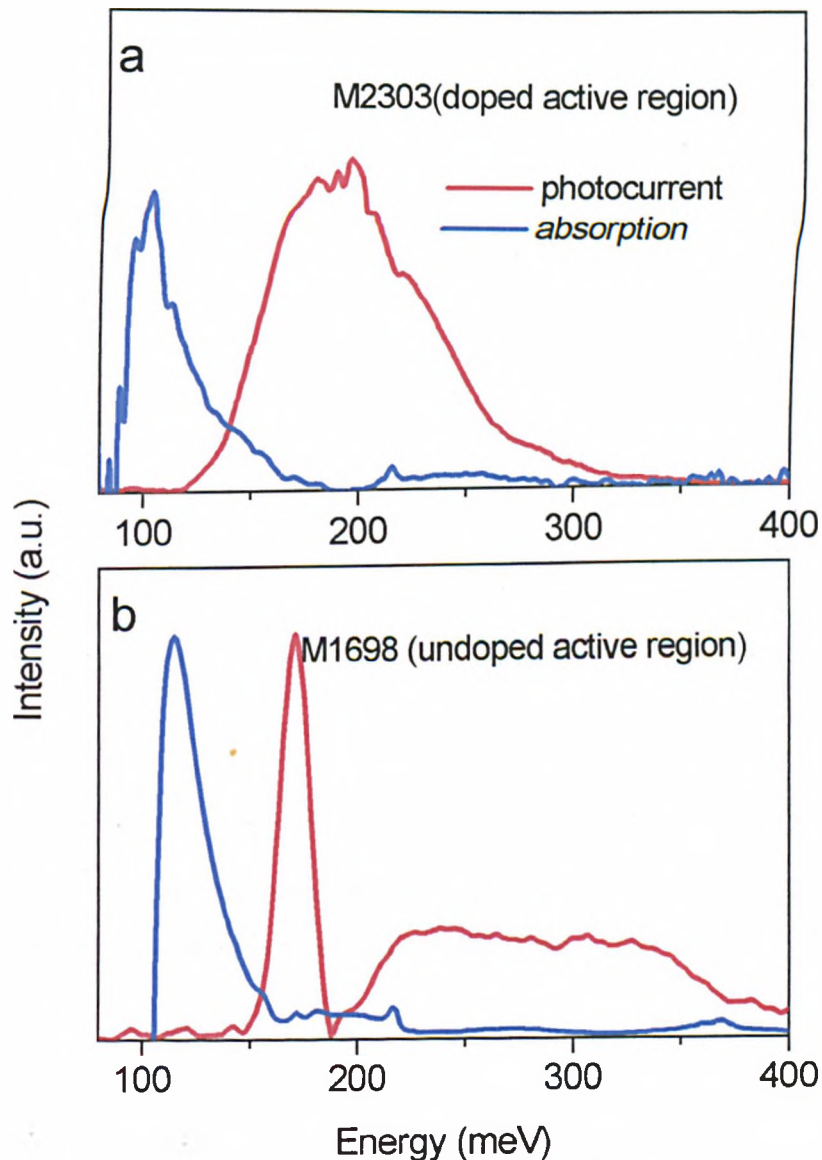
### 5.7.1.3 Photocurrent Measurements

Figure 5-26 shows photocurrent results from samples M1698 (undoped active region, see Table 4), and M2303 (doped active region, see Table 5) at 5 K and zero bias for  $p$  polarised MIR excitation (see the experimental set up in section 5.5.3 and also Figure 5-21). The photocurrent from sample M1698 consists of two peaks, the first peak centered at 170 meV and the second with onset at 220 meV. The photocurrent from sample M2303 consists of a single broader peak with maximum at 193 meV.



**Figure 5-26** 5 K  $p$  polarised photocurrent spectra of samples M1698, and M2303.

In order to attribute the observed transitions in the photocurrent spectra correctly, the absorption spectra and the photocurrent spectra from both samples (M2303 and M1698) were plotted on the same graph as shown in Figure 5-27.



**Figure 5-27 Comparison between absorption spectrum and photocurrent spectrum of (a) sample M2303 (doped active region) and (b) sample M1698 (undoped active region).**

Figure 5-27 shows that the absorption spectra are very different from the photocurrent spectra. For example the photocurrent spectrum of sample M2303 consists of a relatively broad single peak with maximum at 193 meV, while the absorption spectrum consists of two peaks, one at 102 meV, and another broad and weakly peak with onset at 210 meV. Such differences were reported previously by Sauvage *et al*<sup>32</sup>. Intersubband absorption is a direct measurement and depends mainly on the oscillator

strength ( $f$ ) of the transition. Therefore the direct absorption technique can be used to probe bound-to-bound and bound-to-continuum transitions (see Figure 5-28). However, the oscillator strength ( $f_{b-b}$ ) of bound-to-bound transitions is much larger than the oscillator strength ( $f_{b-c}$ ) of bound-to-continuum transitions.

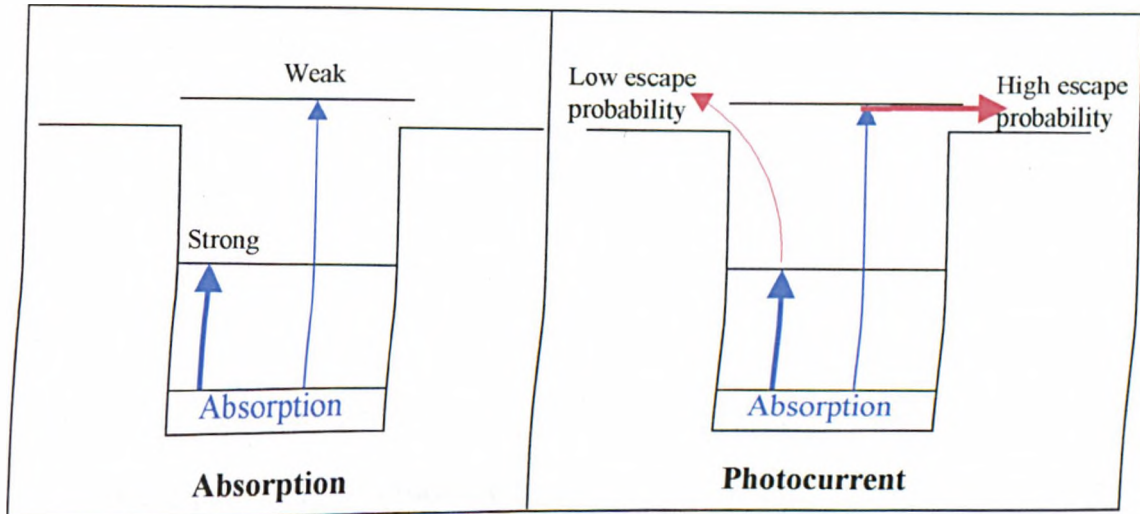


**Figure 5-28 Schematic representation of the difference between direct absorption and photocurrent measurements at low temperature.**

Photocurrent, by contrast, is a two step process (see Figure 5-28) (i) absorption, which depends mainly on the oscillator strength of the transition as it was discussed above (ii) the carrier escape probability out of the dot. At low temperature it is difficult to observe bound-to-bound transitions using photocurrent spectroscopy because the escape probability for this transition is low (see Figure 5-28). However, this technique is relatively sensitive to bound-to-continuum (or wetting layer) transitions at low temperature because the escape probability for these transitions is very high (see Figure 5-28). By increasing the temperature, the sensitivity to bound-to-bound transitions improves, because the escape probability for the carrier increases due to thermal activation.

Figure 5-29a shows the temperature dependence of the photocurrent spectra from sample M1698. For temperatures higher than 80 K a third peak starts to emerge on the low energy side of the low-temperature peak. As the temperature is raised, the intensity of the new peak increases and its position shifts slightly to lower energy. The position of the high temperature photocurrent peak at 150K agrees with the position of the absorption peak at the same temperature (see Figure 5-29b), strongly suggesting that the high temperature peak in the photocurrent spectra is due to bound-to-bound transitions. The explanation of this observation is as follows. As we discussed above, at low temperature the escape probability for the carrier as a result of bound-to-bound transitions is very low (see Figure 5-28). By increasing the temperature, the escape probability increases due to the thermal activation process, and thus the possibility of observing bound-to-bound transitions using photocurrent spectroscopy at high temperature increases.

The natural logarithm of the intensity of the high temperature peak is plotted versus the reciprocal of temperature ( $\frac{1000}{T}$ ) in Figure 5-30. The result is a straight line indicative of a well-defined activation energy for thermal escape of carriers which contribute to the photocurrent occurs. From the slope of the straight line, an activation energy  $E_{act}=101$  meV is deduced. (see the inset in Figure 5-30).

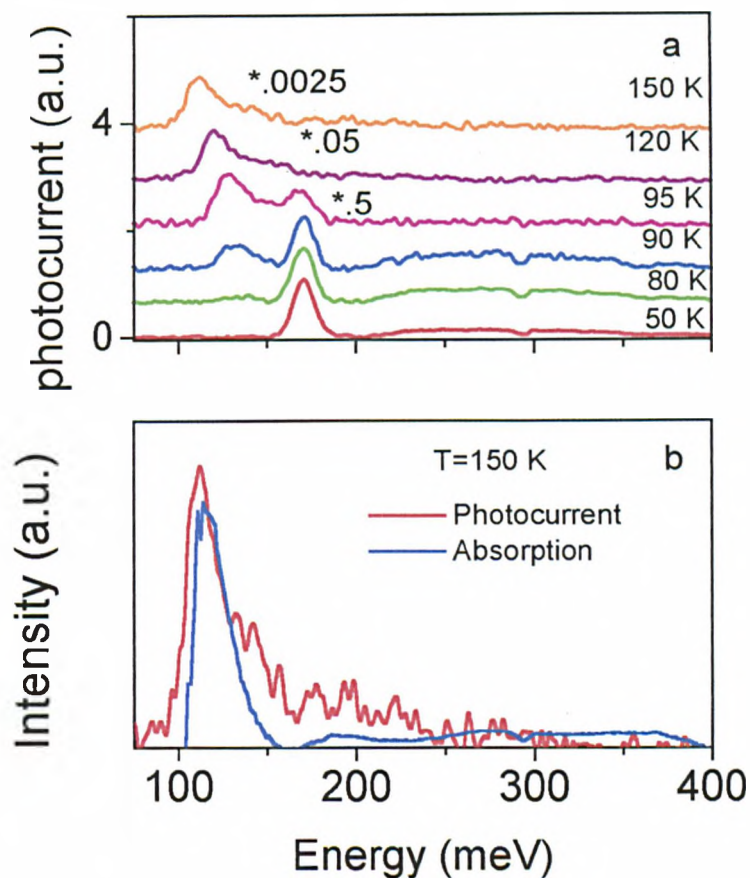


Figure 5-29 (a) Photocurrent temperature dependence of sample M1698. (b) Comparison between absorption spectrum and photocurrent measured at 150 K for sample M1698.

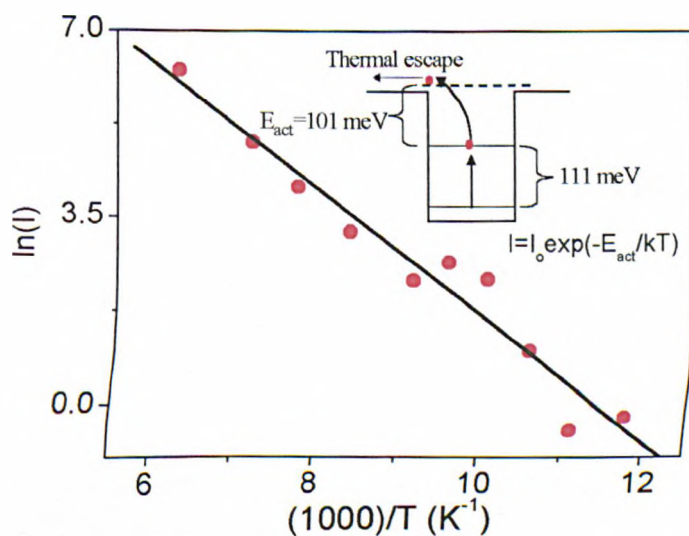


Figure 5-30  $\ln(I)$  versus  $1000/T$  for the high temperature photocurrent peak from sample M1698. The inset shows the mechanism for carrier escape from the dot.

In the light of the above discussion, all the differences between absorption and photocurrent spectra in Figure 5-27 can be explained. The photocurrent spectrum of sample M2303 at low temperature consists of a broad single peak with maximum at 193 meV, while the absorption spectrum consists of two peaks: one at 102 meV, which was attributed to bound-to-bound transitions, and another broader and relatively weak peak with onset at 210 meV. Both absorption peaks are polarised in the growth direction. The photocurrent peak from sample M2303 shows a relatively sharp increase on the low energy side and a broader tail on the high energy side. The occurrence of this peak at very low temperature, together with its asymmetric shape<sup>24,31</sup>, suggest that it is due to bound-to-continuum transitions. We also attribute the broad weak peak in the absorption spectrum with onset at 210 meV to bound-to-continuum transitions. The bound-to-bound transition at 102 meV in the absorption spectrum (see Figure 5-27a) was not observed in photocurrent spectra at low temperature because the escape probability from the upper state of this transition is low.

The photocurrent from sample M1698 at low temperature consists of two peaks, the first peak centered at 170 meV and the second with onset at 220 meV (see Figure 5-27b). The energy position and the shape of the second peak suggests that it is due to bound-to-continuum transitions. The sum of energy of the bound-to-bound transition energy (111 meV) and the activation energy ( $E_{act}=101$  meV) is 212 meV, very close to the energy position of the onset of the second peak in Figure 5-27b, supporting that the second peak in Figure 5-27b is due to bound-to-continuum transitions. The energy separation between the two peaks in Figure 5-27b is 50 meV, close to the PL (see Figure 5-24b) separation between the wetting layer and continuum (80 meV). Also the energy separation between the two peaks in Figure 5-27b is close to what was

reported before for the energy separation between the wetting layer and continuum using photocurrent spectroscopy by Sauvage *et al*<sup>32</sup> (65 meV) and Chu *et al*<sup>33</sup> (60 meV). Furthermore the absorption spectrum in Figure 5-27b shows very weak absorption around 170 meV. However, this transition became the dominant transition in the photocurrent spectrum at low temperature indicating that the escape probability for this transition at low temperature is high, as is typical for bound-to-wetting layer/continuum transitions. From the above discussion we conclude that the photocurrent peak at 170 meV is due to bound-to-wetting layer transitions and the second photocurrent peak with onset at 220 meV is due to bound-to-continuum transitions. Bound-to-wetting layer and continuum transitions are hardly visible in the absorption spectrum (see Figure 5-27b), because the oscillator strength ( $f_{bc}$ ) for these transitions is small. On the other hand bound-to-bound transitions are strongly visible in the absorption spectrum (see Figure 5-27b), because the oscillator strength ( $f_{bb}$ ) of bound-to-bound transitions is large. In contrast, photocurrent spectra at low temperature exhibit bound-to-wetting layer and bound-to-continuum transitions (see Figure 5-27b), because the escape probability for these transitions is high. Bound-to-bound transitions are not observed in photocurrent at low temperature, because the escape probability for bound-to-bound transitions is low. However, At T~80 K bound-to-bound, bound-to-wetting layer, and bound-to-continuum transitions can be seen in photocurrent spectra (see Figure 5-29a).

The photocurrent spectra in Figure 5-29a show a 20 meV red shift in the energy position of the bound-to-bound transitions with increasing temperature from 80K-150K. However, the temperature dependent absorption measurement indicates only 3 meV red shift with increasing temperature from 12K to 300K. At this stage we do not have a full explanation for this difference in the temperature dependence of the

photocurrent and absorption spectra. Sauvage *et al*<sup>34</sup> have reported a 5 meV red shift in the energy position of bound-to-bound transitions in the valence band of quantum dots with increasing temperature from 28K to 150K using photoinduced absorption spectroscopy. They attributed the observed red shift to the depopulation of the smaller dots with increasing temperature. In the work of Sauvage *et al*<sup>34</sup> only 5 meV red shift is observed, while in our experiment a 20 meV red shift is observed. This difference may in part be due to the fact that the hole energy levels in the valence band are less sensitive to the dot size compared with the electron energy levels in the conduction band (see Figure 5-6).

The PL spectra in Figure 5-24 show a strong inhomogeneous broadening (~100 meV) due to the fluctuation of the dot size, indicating that the density of states of the system is broadened by ~100 meV. The red shift (~ 20 meV) in the position of the high temperature peak in Figure 5-29a is less than the inhomogeneous broadening in the PL spectra. Thus a further contribution to the red shift may arise from the influence of the inhomogeneous broadening of the density of the excited states on the escape probability. At  $T \sim 80$  K not all the electrons which undergo bound-to-bound transitions can escape. The electrons undergo transitions from the ground state to the high energy tail of the excited states have more chance to escape compared with the electrons which undergo transitions to lower energy states (see Figure 5-31). However, by increasing temperature, the escape probability for electrons to undergo transitions from ground state to lower energy excited state increases and starts to dominate the photocurrent signal, because there are many more dots of energy close to the centre of the excited state energy distribution than the high energy tail of the excited states in the sample. In the absorption spectra we mainly measure the energy separation between the ground state the centre of the density distribution of the

excited state, providing a further contribution to the temperature dependence of the photocurrent peak.

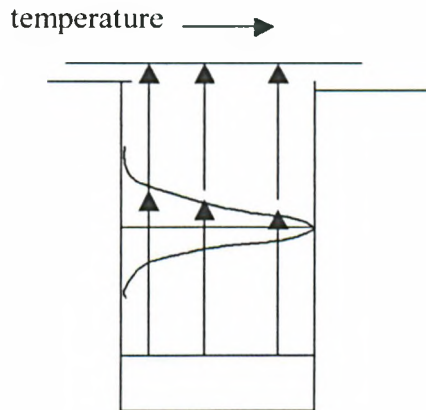


**Figure 5-31** Schematic presentation of the effect of the inhomogeneous broadening the thermally activated escape probability.

To investigate the polarisation dependence of the photocurrent signal, measurements were taken as a function of the polarisation angle  $\theta$  defined as  $\theta = 0^\circ$  for  $p$  polarised light and  $90^\circ$  for  $s$  polarised light (see Figure 5-21). The results from sample M2303 (doped active region) are illustrated in Figure 5-32. The  $p$  polarised photocurrent signal is significantly stronger than the  $s$  polarised component. This observation is very similar to what has been reported in quantum wells<sup>24</sup>.

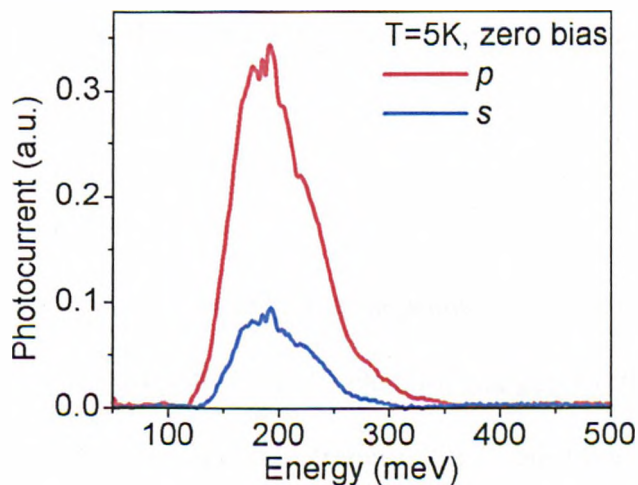


**Figure 5-32** Comparison between  $p$  and  $s$  polarisation photocurrent spectra for sample M2303 (doped active region).

To understand the polarisation dependence in more detail, we first consider the dependence of the electric field vector of the incident radiation on the polarisation angle  $\theta$  (see Figure 5-33). The component of electric field vector in the dot plane for a given angle of polarisation  $\theta$  can be written as

$$\mathbf{E}_{\parallel} = E_0 (\sin(\theta)\hat{x} - \frac{1}{\sqrt{2}}\cos(\theta)\hat{y}) .$$

Also the component in the growth direction can be written as

$$\mathbf{E}_{\perp} = \frac{E_0}{\sqrt{2}}\cos(\theta)\hat{z}$$

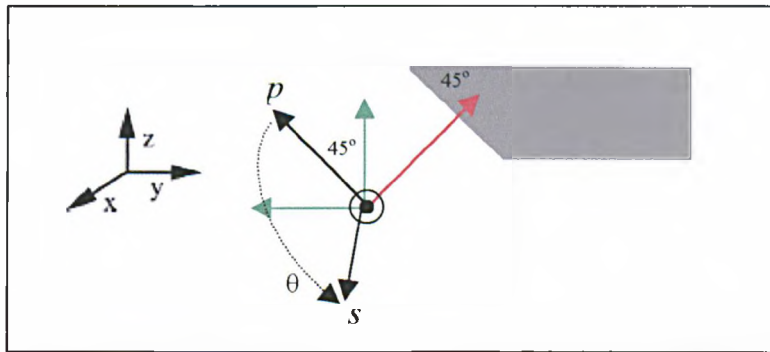


**Figure 5-33** Analysis of the electric field components in the case of *p* and *s* polarised incident light for the 45° wedge configuration used in the photocurrent experiment.

The photocurrent in the dot plane direction is proportional to the square of the electric field in that direction, thus

$$I_{\parallel} = \alpha A f_{\parallel} E_0^2 \left(1 - \frac{\cos^2(\theta)}{2}\right)$$

where  $\alpha$  is a constant of proportionality that depends on the power of the incident radiation, the energy of the transition and the electron charge,  $A$  is the cross section of the illuminated area and  $f_{\parallel}$  is the oscillator strength of the transitions in the dot plane.

In the same way the photocurrent in the growth direction can be written as

$$I_{\perp} = \frac{1}{2} \alpha A f_{\perp} E_0^2 \cos^2(\theta)$$

where  $f_{\perp}$  is the oscillator strength of the transitions in the growth direction.

The total photocurrent signal is therefore given by

$$I(\theta) = \alpha A E_0^2 \left( f_{\parallel} \left( 1 - \frac{\cos^2(\theta)}{2} \right) + \frac{f_{\perp}}{2} \cos^2(\theta) \right) \quad (5.20)$$

In Figure 5-34 the amplitude of the photocurrent signal from sample M2303 (doped active region, see Table 5) at 193 meV is plotted against the angle of polarisation  $\theta$ .

The experimental points are very well fitted by equation (5.20). From the fitting we

deduce the ratio  $\frac{f_{\perp}}{f_{\parallel}} \approx 6$ . The photocurrent data from sample M1698 (undoped active

region, see Table 4) have been analysed in the same way and give  $\frac{f_{\perp}}{f_{\parallel}} \approx 13$  for this

sample.

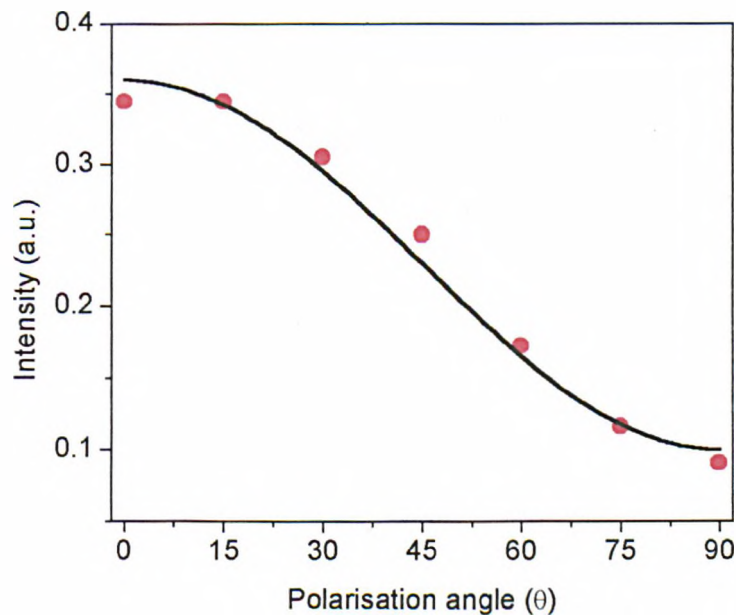


**Figure 5-34** Photocurrent signal of sample M2303 as a function of polarisation angle (circle), fit to equation (5.20) (full line).

From the above analysis we conclude that radiative intersubband transitions in the conduction band of isolated self assembled InAs/GaAs quantum dots are strongly

polarised along the growth direction, which corresponds to the direction of strongest confinement in the dots. These selection rules are very similar to the selection rules in the conduction band of quantum wells (see section 5.4). The reason behind that is the dots used in this work are rather flat, with the lateral dimensions 5 times larger than the vertical dimension (see Figure 5-23). Thus the lateral confinement is weak leading to intersubband transitions mainly polarised in the growth direction.

### 5.7.2 Intersubband Transitions in the Valence Band of Quantum Dots

Intersubband transitions in the valence band of SAQDs are much less studied by comparison with those in the conduction band. To the best of my knowledge there is no reported study of intersubband transitions in the valence band of SAQDs using photocurrent spectroscopy. Sauvage *et al* have studied intersubband transitions in the valence band of SAQDs using direct absorption measurements<sup>35</sup> from p-doped samples and photoinduced absorption techniques<sup>34,35</sup> from undoped samples. Bound-to-bound transitions at 100 meV polarised in the growth direction have been observed from the direct absorption measurements<sup>35</sup>. An *s* polarised transition around 280 meV has been observed by the photoinduced technique from an undoped sample. Sauvage *et al*<sup>36</sup> attributed the transitions at 280 meV to bound-to-continuum transitions in the valence band of the dots. In-plane polarised intersubband absorption in the valence band of quantum wells has been theoretically predicted<sup>27,37</sup> as we discussed in section 5.4 and also experimentally observed<sup>38,39</sup>. As we discussed in section 5.4, the in-plane absorption in the valence band of a quantum well is due to the anisotropy of the valence hole subbands and the band mixing in the valence band, and also the admixture of *s*-type, conduction band states into valence wavefunctions.

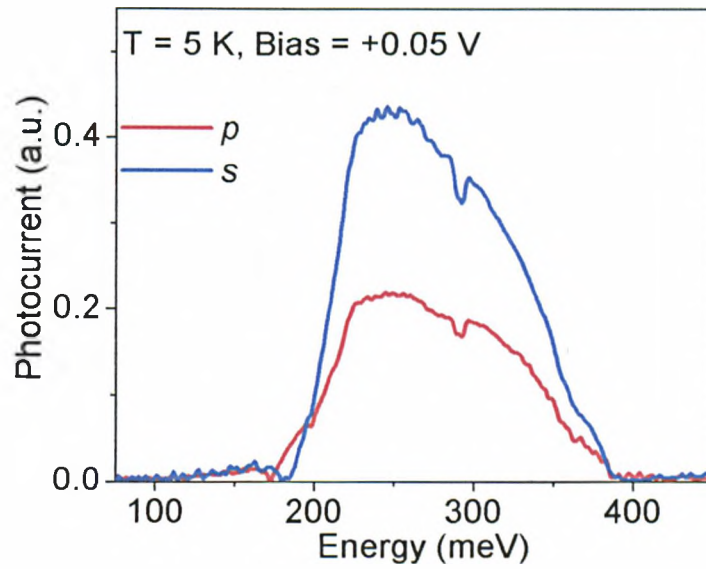
In this section experimental results are presented from a detailed study of the polarisation dependence of intersubband photocurrent spectroscopy for the valence band confined states of InAs SAQDs. We find that intersubband transitions in the valence band are strongly polarised in the dot plane. The structural detail of the sample used in this study is given in Table 6.

Table 6 structural detail of p-i-p sample (M2073)

Repeats	Thickness (Å)	Material	Dopant	Type	Concentration (cm <sup>-3</sup> )
1	4000	GaAs	Be	p	2.0x10 <sup>+18</sup>
1	380	GaAs		ud	
4	3	Be-δ(4x10 <sup>10</sup> cm <sup>-2</sup> )	Be		
4	20	GaAs		ud	
4	7	InAs 2.5 ML		ud	
4	400	GaAs		ud	
1	4000	GaAs	Be	p	2.0x10 <sup>+18</sup>

The photocurrent was measured from sample M2073 at 5 K, and +0.05 V bias for *p* and *s* polarised light as described in section 5.5.3 (see also Figure 5-21). The results are illustrated in Figure 5-35. A broad peak with a steep increase at the low energy side and a broad tail on the high energy side with maximum at 247 meV is observed. As discussed in the previous section, this asymmetric shape of the intersubband transitions is characteristic for bound to continuum transitions<sup>24,31</sup>. The energy position of the photocurrent peak in Figure 5-35 is close to what Savage *et al*<sup>34</sup> have measured for bound to continuum transitions (280 meV) in the valence band using photoinduced techniques. Also, the measured energy separation between ground state and continuum (247 meV) is close to what was calculated (174-203 meV, depending on the dot size and degree of Ga diffusion) by Williamson *et al*<sup>18</sup>.

In contrast with what was observed from the conduction band in photocurrent spectra (see Figure 5-32), we find that the observed transitions in the valence band are strongly polarised in the dot plane (*s*-polarised).



**Figure 5-35 Comparison between  $p$  and  $s$  polarised photocurrent spectra measured at 5 K and 0.05 V bias from p-i-p sample (M2073).**

The absorption spectra were measured from the same sample (M2073) at 300 K as described in section 5.5.3. Figure 5-36a shows a comparison between the transmission spectra for  $p$  and  $s$  polarisation. The transmission spectra were calculated as described in section 5.7.1.2. In contrast with the absorption results from n-i-n samples (see Figure 5-25), in-plane ( $s$ -polarised) absorption from the p-i-p sample is stronger than the growth direction ( $p$ -polarised) absorption. The absorption spectrum was calculated from the transmission spectra in Figure 5-36a using the equation

$$\text{Absorbance} = \log\left(\frac{T_p}{T_s}\right) \quad (5.21)$$

The result is illustrated in Figure 5-36b. It is clear that the p-i-p sample exhibits two absorption peaks, the first peak is at 145 meV and polarised in the dot plane, and the second peak at 420 meV, polarised in the same direction. Also it is clear from the comparison between Figure 5-35 and Figure 5-36b that the photocurrent spectra are different from the absorption spectra, as was observed for the n-type samples.

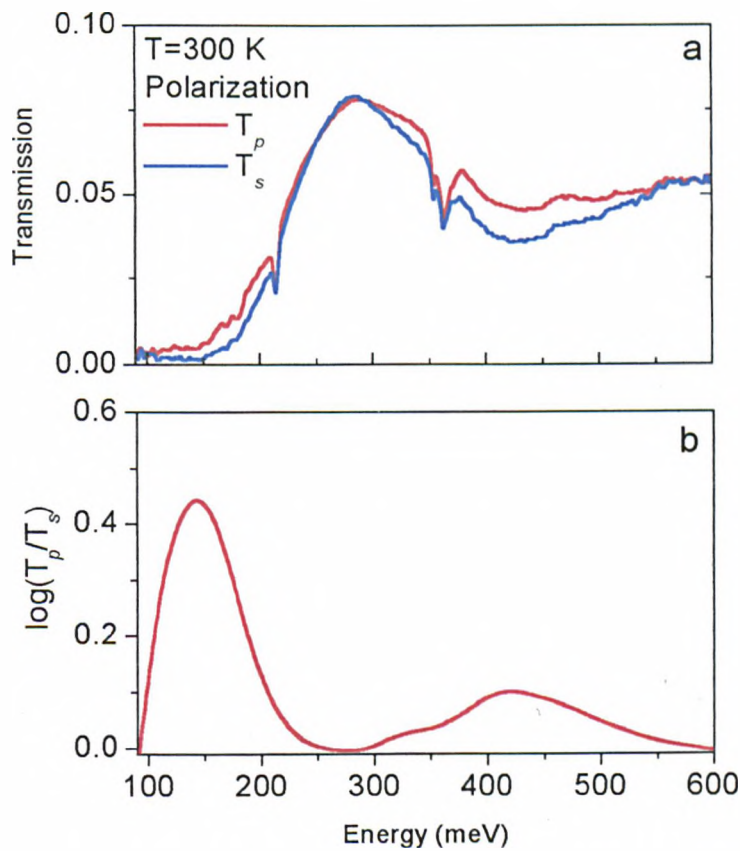


**Figure 5-36 (a) Room temperature transmission spectra from p-i-p sample (M2073) for  $p$  and  $s$  polarised light. (b) Absorption spectrum calculated from the transmission spectra in (a) using  $A=\log(T_p/T_s)$ .**

The peak observed in direct absorption at 145 meV is hardly visible in the photocurrent spectra in Figure 5-35, indicating that the escape probability for the carrier out of the dot due to this transition is small. The energy separation between the absorption peak (in Figure 5-36b) and the photocurrent peak (in Figure 5-35) is 102 meV, which is much larger than the energy separation between the wetting layer and continuum in the valence band. PL spectroscopy shows an 80 meV total energy separation between the wetting layer and continuum (see for example Figure 5-24b). From the results of the previous section, we found that the energy separation between the wetting layer and continuum in the conduction band is  $\sim 50$  meV indicating that the energy separation between the wetting layer and continuum in the valence band is

~30 meV, much less than the energy separation (102 meV) between the absorption peak and the photocurrent peak. From the above discussion we conclude that the absorption peak at 145 meV in Figure 5-36b is due to bound-to-bound transitions. However, the absorption peak at 145 meV is much too high in energy to arise from transitions between the ground state and first excited state. We therefore suggest that it is due to transitions between ground state and very highly excited states (from Figure 5-6 it can be seen that the energy separation between the ground state and the fourth excited state is between 40 meV and 80 meV).

The energy position of the second peak in the absorption spectrum is very high (420 meV). We attribute this peak to transitions between the heavy hole ground state and spin-orbit split-off hole states, by comparison with the PL experiments of Silva *et al*<sup>40</sup>. The results of this work, carried out on very small (R=2.7 nm) InAs self assembled quantum dots are illustrated in Figure 5-37a. The PL peak at 1.72 eV can not be attributed to heavy hole-electron or light hole-electron transitions. Silva *et al*<sup>40</sup> attributed the PL peak at 1.72 to spin-orbit hole-electron transitions. From the PL results in Figure 5-37a the energy separation between the heavy hole and the spin-orbit hole bands  $E_{hh-so}=350$  meV is deduced. From the band structure calculations for a single InAs quantum dot in Figure 5-37b<sup>41</sup>, it can be seen that the confinement potential of the spin-orbit hole is a 500 meV away from that of the heavy hole, and close to energy position (420 meV) of the second peak in the absorption spectrum (see Figure 5-36b). Furthermore the energy position of the second absorption peak in Figure 5-36b is close to the energy separation (410 meV) between heavy hole and spin-orbit hole bands in bulk InAs<sup>42</sup>.

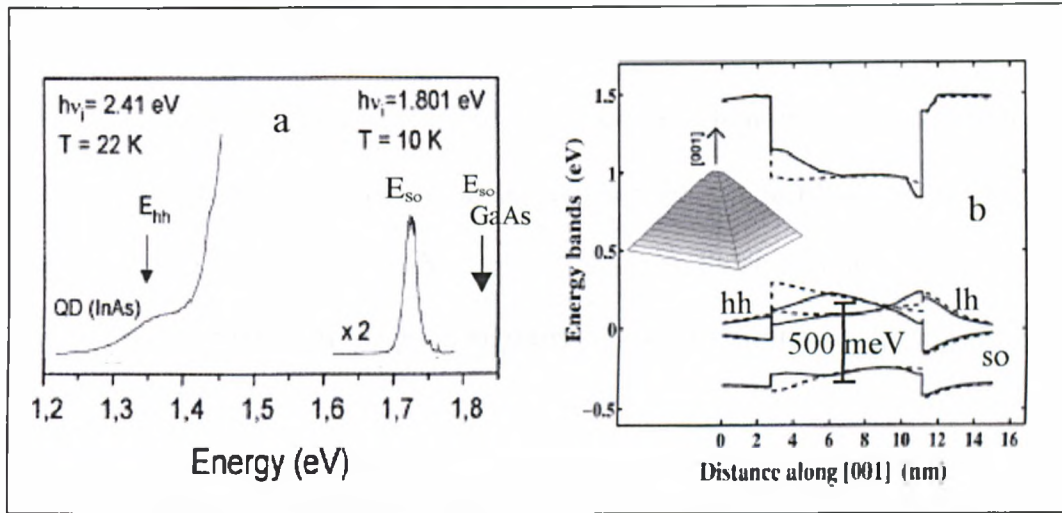


**Figure 5-37 (a)** The PL spectra of InAs quantum dot with excitation energy of 2.41 eV (off-resonance) and 1.801 eV (close to resonance) (reference 40). **(b)** Band structure of a quantum dot along the [001] direction through the center of the dot. Dashed lines for InAs and the solid lines for  $\text{In}_{1-x}\text{Ga}_x\text{As}$  (reference 41).

The polarisation dependence of the photocurrent signal in Figure 5-35 was investigated. The amplitude of the photocurrent signal is plotted against polarisation angle in Figure 5-38. The experimental points are very well fitted by equation (5.20).

From the fitting we deduced the ratio  $\frac{f_{\parallel}}{f_{\perp}} \approx 11$ . The oscillator strength of in plane

bound-to-continuum transitions is eleven times stronger than the oscillator strength of growth direction bound-to-continuum transitions in the valence band.

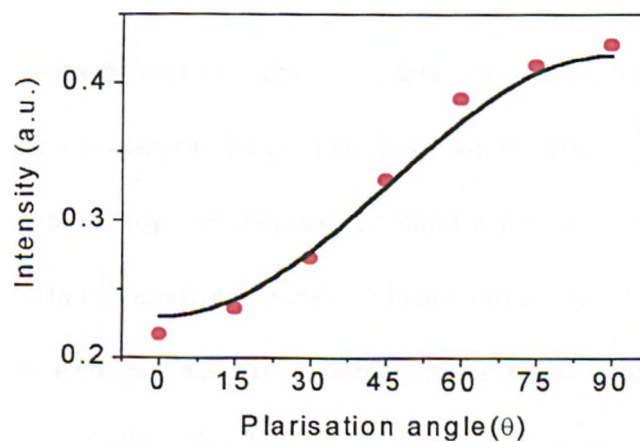


**Figure 5-38** Photocurrent signal of p-i-p sample (M2073) as a function of polarisation angle (circle), fit to equation (5.20) (full line).

In order to compare between the in-plane absorption in the valence band and the conduction band, photocurrent spectra for *s*-polarised light were measured for the p-i-p sample (M2073) and an identical (except for the doping) four layer n-i-n sample (M2071) at 5 K and +0.05 V. The results are illustrated in Figure 5-39. The photocurrent signal from the p-i-p structure is four times more intense than from the n-i-n sample.

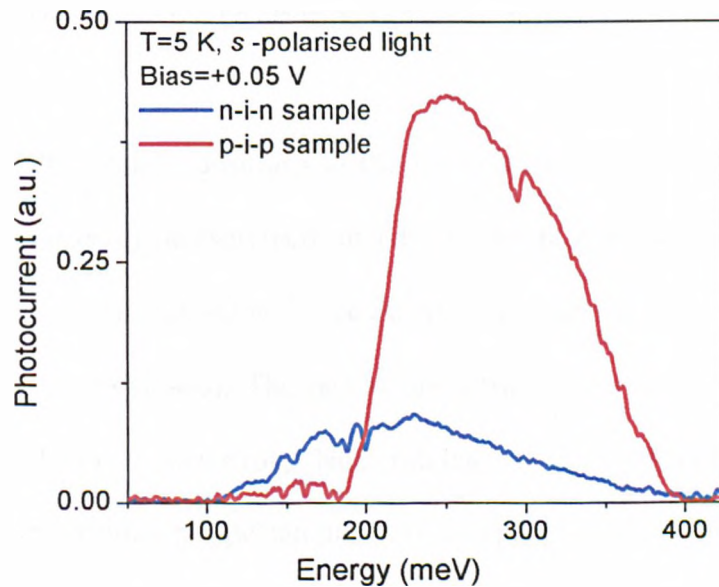


**Figure 5-39 Comparison between photocurrent spectra measured at 5 K, +0.05 V bias and using *s*-polarised light from 4 layer n-i-n sample (blue) and 4 layer p-i-p sample (red). Both samples were grown under the same conditions.**

There are two reasons behind the strong in-plane absorption from the valence band compared with the conduction band. The first comes from the anisotropy of the valence band. The anisotropy of the valence band arises from mixed terms such as  $k_x k_z$  and  $k_y k_z$  in the Hamiltonian, as discussed in section 5.4 for the case of the valence band of a quantum well (see also the expressions for  $R$  and  $S$  in the Luttinger-Kohn Hamiltonian equation (5.9)). This breaks the in-plane symmetry of the intersubband structure, opening channels for in-plane intersubband transitions. The second reason is the band mixing in the valence band and also the admixture of *s*-type, conduction

band states into valence wavefunctions. As we discussed in section 5.4 (see also Table 1 and Figure 5-12), in-plane intersubband transitions in the valence band of a quantum well are allowed due to the band mixing. In the same way it is probable that band mixing enhances in-plane intersubband transitions in the valence band of SAQDs. Furthermore the effect of the band mixing on the hole wavefunctions of SAQDs is very strong as can be seen in Figure 5-7. Due to the strong band mixing in SAQDs the hole states in Figure 5-7 can not be classified as s-like, p-like, etc.

In conclusion, intersubband transitions in the valence band were investigated using both the direct absorption measurement and photocurrent spectroscopy. The results showed that intersubband transitions in the valence band are mainly polarised in the dot plane direction (*s*-polarised). The results are attributed to the anisotropy of the hole subbands and also to the strong band mixing between the valence subbands. Photocurrent spectra from a p-type sample were compared with photocurrent spectra from an identical n-type sample for *s*-polarised light. The comparison showed that photocurrent signal from the p-type sample is four times stronger than the photocurrent signal from the n-type sample, suggesting the possibility of using p-type samples to fabricate large area normal incident infrared photodetectors.

### 5.7.3 Intersubband Absorption in Strongly Coupled Quantum Dots

From the results of section 5.7.1 we concluded that intersubband transitions in the conduction band of isolated SAQDs are strongly polarised in the growth direction (see Figure 5-32). This observation is attributed to the weak lateral confinement in the relatively flat dots used in this study.

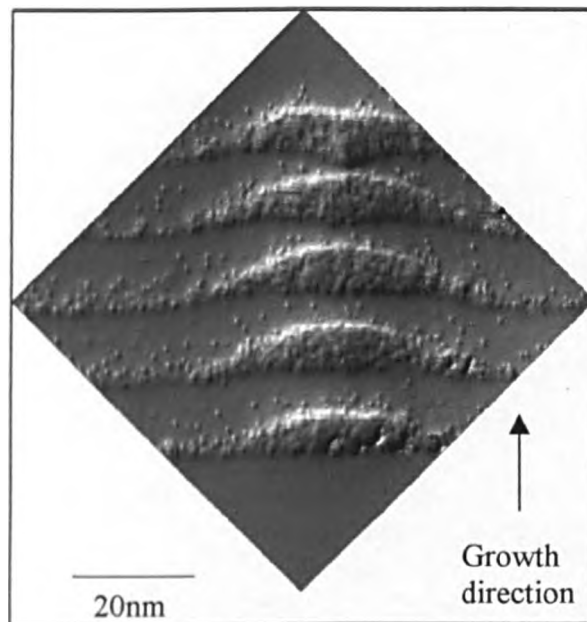


**Figure 5-40** Scanning tunneling microscope image of five vertically aligned InAs quantum dots grown in Sheffield.

Recently, several theoretical groups<sup>43,44</sup> have predicted a strong enhancement in the in-plane intersubband transitions in the conduction band of vertically stacked SAQDs. Experimentally, SAQDs can align on top of each other in the vertical direction (see Figure 5-40) if the thickness of the GaAs barrier between successive dot layers is less than 50 ML  $\approx$  15 nm<sup>45</sup>. The strain field of the first dot forces the new dot to form directly over the first dot. In addition to the structural coupling (see Figure 5-40) the dots can be electronically coupled. Fonseca *et al*<sup>46</sup> have studied the effect of the GaAs barrier thickness on the electronic coupling between two vertically stacked InAs/GaAs dot layers, using the effective mass approximation. For GaAs barriers less

than 5 nm thick, the ground state of the vertically stacked dots starts to split into bonding (b) and antibonding (a) states as illustrated in Figure 5-41. Solomon *et al*<sup>47</sup> have reported experimental evidence (red shift in the PL peak position of the coupled sample compared with the uncoupled sample) for an electronic coupling between vertically stacked quantum dots when the GaAs barrier thickness is less than 10 nm.

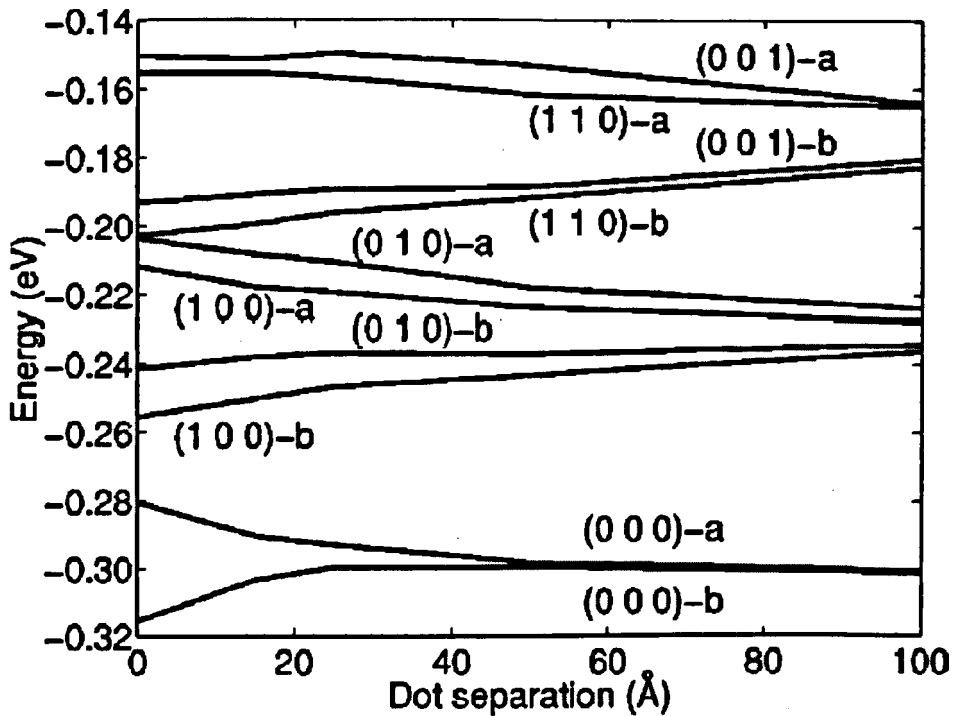


**Figure 5-41 Eigenenergies as a function of dot distance for pyramidal dot with base length 20 nm and height 6 nm. (Reference 47).**

In this section, the study of intersubband transitions in strongly coupled  $\text{In}_{0.5}\text{Ga}_{0.5}\text{As}$  dots (10 Å GaAs barrier) is described. We find that in-plane intersubband absorption is the dominant transition within the conduction band of strongly coupled dots. Two samples grown one after the other were used in this work. The first sample consisted of two strongly coupled  $\text{In}_{0.5}\text{Ga}_{0.5}\text{As}$  dot layers, while the second sample contained a single layer of  $\text{In}_{0.5}\text{Ga}_{0.5}\text{As}$  dots. The structural detail of the used samples is illustrated in Table 7.

Table 7a structural details of an n-i-n coupled sample (M2163)

repeats	Thickness (Å)	Material	dopant	type	Concentration (cm <sup>-3</sup> )
1	4000	GaAs	Si	n	2x10 <sup>+18</sup>
1	980	GaAs		ud	
1	3	Si delta 2.2x10 <sup>10</sup> cm <sup>2</sup>	Si	n	3.9x10 <sup>17</sup>
1	20	GaAs		ud	
1	9	In <sub>0.5</sub> Ga <sub>0.5</sub> As 3ML		ud	
1	10	GaAs		ud	
1	17	In <sub>0.5</sub> Ga <sub>0.5</sub> As 6ML		ud	
1	1000	GaAs		ud	
1	4000	GaAs	Si	n	2x10 <sup>+18</sup>

Table 7b structural detail of a single layer n-i-n sample (M2162)

repeats	Thickness (Å)	Material	dopant	type	Concentration (cm <sup>-3</sup> )
1	4000	GaAs	Si	n	2x10 <sup>+18</sup>
1	980	GaAs		ud	
1	3	Si delta 2.2x10 <sup>10</sup> cm <sup>2</sup>	Si	n	3.9x10 <sup>17</sup>
1	20	GaAs		ud	
1	17	In <sub>0.5</sub> Ga <sub>0.5</sub> As 6ML		ud	
1	1000	GaAs		ud	
1	4000	GaAs	Si	n	2x10 <sup>+18</sup>

Figure 5-42 shows a cross sectional TEM image for the coupled sample. The total height of the coupled dots is 8 nm. Each dot is 20 nm wide and 3 nm high. The GaAs spacer thickness between the dots appears to be larger than 1 nm (1.5 nm) which is possibly due to strain effects on the TEM image.

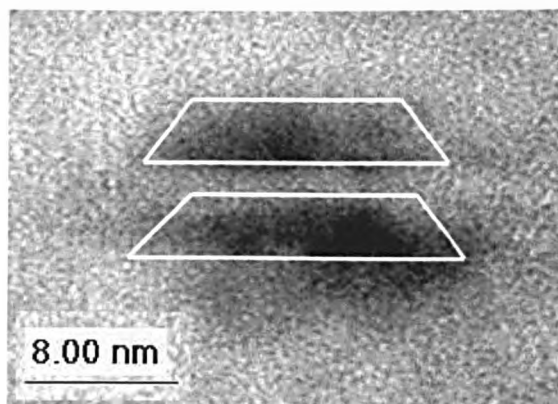


**Figure 5-42 TEM image of two coupled dots in sample (M2163).**

To characterise samples M2162 and M21623, we first measured the PL at 5 K, excited with a 633nm HeNe laser at low power. As shown in Figure 5-43a, the spectral peak position of the coupled sample shifts to lower energies by 70meV in comparison with the single dot layer sample (centered at 1.30eV). The red shift in the PL peak position is attributed to the reduction in vertical confinement due to the increase of the dot height as a result of the vertical coupling<sup>47</sup>.

To investigate the samples further, the PL was measured as a function of the excitation power density. The results are illustrated in Figure 5-43. From the PL spectra at high excitation power density it is clear that each sample has at least one excited state.

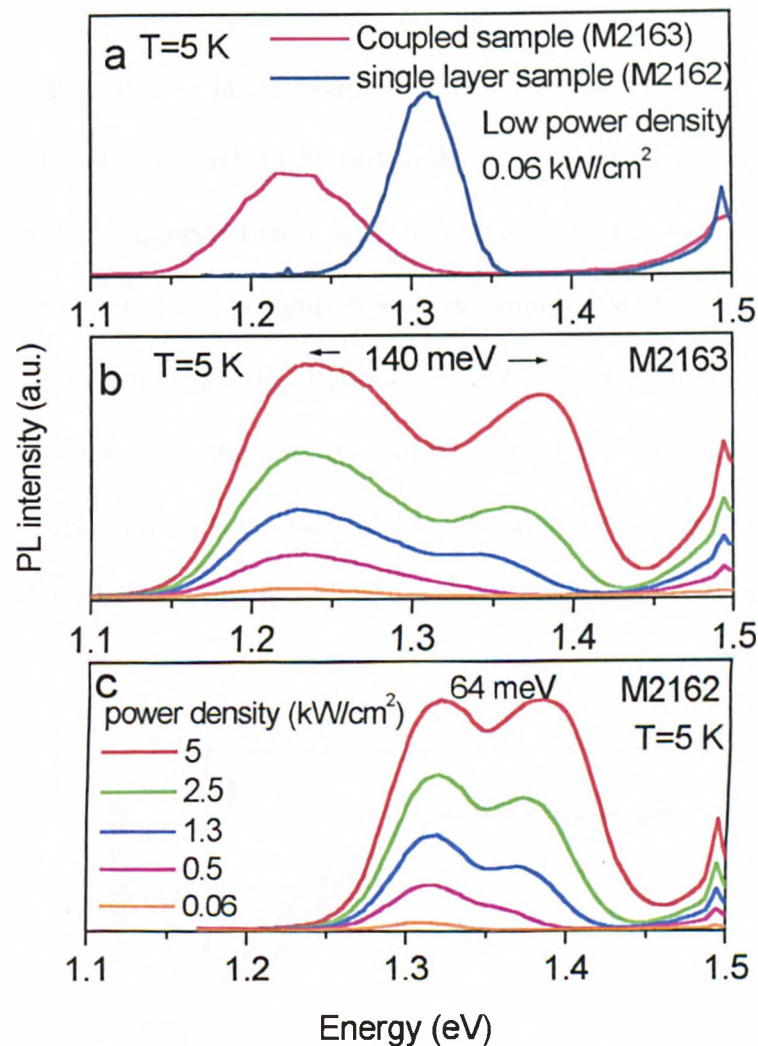


**Figure 5-43** (a) PL spectra obtained at 5K and excitation low power density (0.06 KW/cm<sup>-2</sup>) for samples M2162 and M2163, (b) power dependent PL spectra of the coupled sample (M2163) and (c) single layer dots sample (M2162)

Figure 5-44a shows a comparison between the transmission spectra of the coupled dot sample (M2163) for *s* and *p* polarization. The transmission spectra were calculated as described in section 5.7.1.2. A clear dip is observed between 100 meV and 250 meV in the *s* polarised transmission spectrum in comparison with the *p* polarised transmission spectrum. To study this absorption peak in more detail, we calculated the absorbance using the equation:  $\text{Absorbance} = \log\left(\frac{T_p}{T_s}\right)$ . The result is shown in

Figure 5-44b. A strong absorption peak, polarised in the dot plane with maximum at

141 meV, can be seen. The in-plane polarisation of the absorption peak proves that the absorption peak is due to intersubband transitions in the conduction band of the dots and not due to intersubband transitions in the wetting layer. The energy position of the absorption peak suggests that it arises from either transitions between the two bound states observed in the PL (Figure 5-43a) or bound-to-wetting layer transitions. From the PL results of the single layer sample (M2162, see Figure 5-43b), we expect to observe absorption due to intersubband transitions for energies larger than 65 meV. However, no absorption peak was observed for this sample. This could be due to the fact that the sample has only one layer of dots, rendering the absorption too weak to be observed.

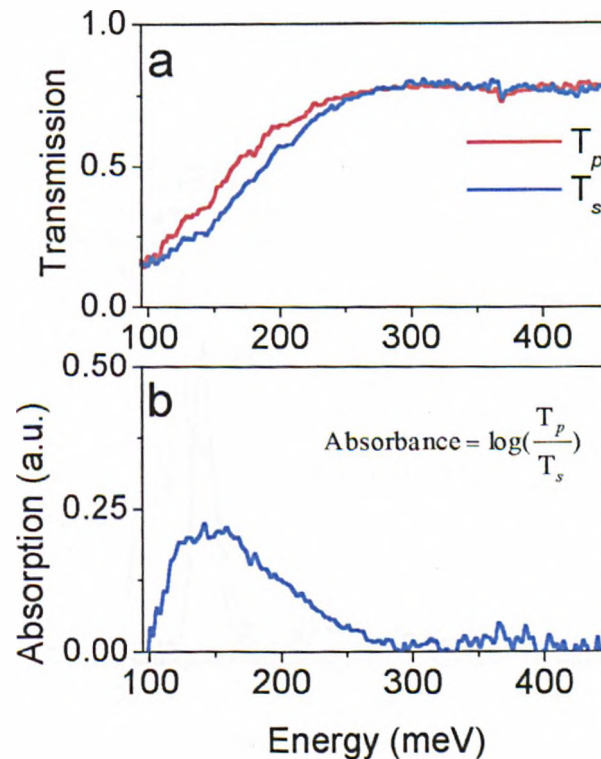


**Figure 5-44 (a) Room temperature transmission spectra for  $s$  and  $p$  polarisation from the coupled sample M2163. (b) The absorption spectrum of the coupled sample deduced using  $A = \log\left(\frac{T_p}{T_s}\right)$ .**

To investigate further the effect of the coupling, we carried out normal incidence photocurrent measurements M2162 and M2163 at 12 K with zero bias. The results are shown in Figure 5-45. The coupled sample gave a strong photocurrent signal centered at 140 meV, the same position as the absorption peak (see Figure 5-44b). The dip in photocurrent from the coupled sample at 136 meV is due to the beamsplitter. No photocurrent was observed from the single layer sample (M2162). For further comparison we plot in Figure 5-45 normal incidence photocurrent spectrum from the sample containing 15 layers of uncoupled dots (sample M1698 see Table 4). The photocurrent from the coupled sample is ten times stronger than the photocurrent from M1698. The photocurrent results confirm the absorption results in Figure 5-44b and also indicate that by coupling the dots in the vertical direction, the absorption is greatly enhanced.

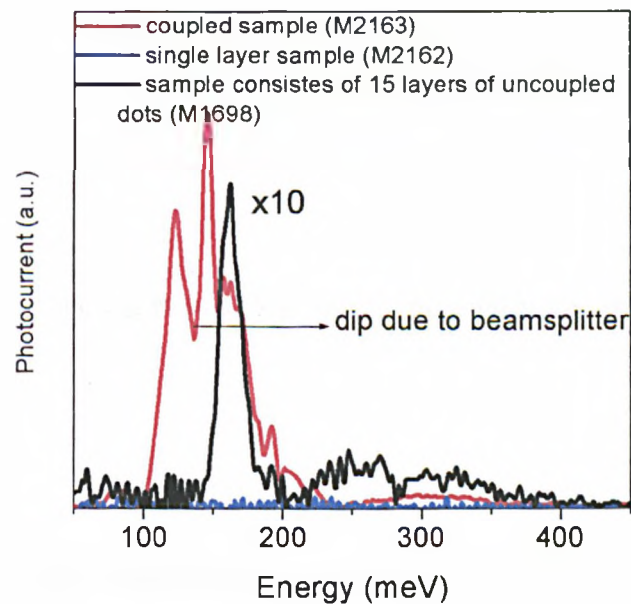


**Figure 5-45** A comparison between normal incidence photocurrent of the coupled sample (M2163), single dot layer sample (M2162) and 15 layers uncoupled sample (M2303).

This enhancement of the in-plane absorption as a result of the vertical coupling agrees qualitatively with the theoretical calculations of Sheng and Leburton<sup>44,48</sup> carried out

using eight-band strain dependent  $\mathbf{k}\cdot\mathbf{p}$  theory. They predicted a factor of 3 enhancement for the oscillator strengths of 1s-2p conduction intersubband transitions, for in-plane polarisation, due to the dot coupling in the vertical direction. This enhancement is attributed to the very different composition of the basis wave functions in the conduction band states for coupled and uncoupled dots due to differences in the conduction-valence band mixing. This effect enhances the oscillator strength of transitions between the ground and excited states in the conduction band for coupled dots

The importance of the conduction-valence band mixing in InAs/GaAs SAQDs can be understood from the following points<sup>49</sup>: (i) the band gap of bulk InAs is 0.4 eV, while the energy of the ground state transition of the InAs dot is  $\sim 1$  eV; (ii) the strain has a strong spatial variation (see Figure 5-4); (iii) the strain components are very large and the resultant splittings in the bands are comparable to the interband separations in the bulk material.

In the framework of the eight-band  $\mathbf{k}\cdot\mathbf{p}$  theory the total wavefunction can be written as<sup>44</sup>

$$\psi = \sum_{k=1}^8 u_k(R)\phi_k(r) \quad (5.22)$$

where  $u_k$ 's are the bulk band-edge Bloch functions at the  $\Gamma$  point (central cell). The explicit form of  $u_k$  can be found in reference 26.  $\phi_k$  are the envelope functions and can be found by solving the Schrodinger equation for the  $H_{k,p}$  Hamiltonian including the strain.

$$H_{k,p}\phi = E\phi \quad (5.23)$$

The explicit form of  $H_{k,p}$  including strain can be found in reference 23.

As we discussed in section 5.4 the intersubband absorption is proportional to the oscillator strength between the initial  $|i\rangle$  and final  $|f\rangle$  states, which is given by<sup>24</sup>

$$f = \frac{2|\langle f|\hat{\varepsilon}\cdot\hat{p}|i\rangle|^2}{m(E_f - E_i)} \quad (5.24)$$

The momentum matrix element in the oscillator strength expression above is given by<sup>44</sup>

$$\langle f|\hat{\varepsilon}\cdot\hat{p}|i\rangle = \sum_k \langle \phi_{fk}|\hat{\varepsilon}\cdot\hat{p}|\phi_{ik}\rangle + \sum_{kk'} \langle u_k|\varepsilon\cdot p|u_{k'}\rangle \langle \phi_{fk'}|\phi_{ik}\rangle \quad (5.25)$$

The momentum matrix element in equation (5.25) consists of two parts: the envelope function part  $\sum_k \langle \phi_{fk}|\hat{\varepsilon}\cdot\hat{p}|\phi_{ik}\rangle$  and the central cell part  $\sum_{kk'} \langle u_k|\varepsilon\cdot p|u_{k'}\rangle \langle \phi_{fk'}|\phi_{ik}\rangle$ . The band mixing comes from the central cell part. Sheng and Leburton's calculations<sup>44</sup> showed that the contribution of the central cell part to the total matrix element in equation (5.25) is one order of magnitude larger than the envelope function part. Thus the momentum matrix element in equation (5.25) can be approximated to

$$\langle f|\hat{\varepsilon}\cdot\hat{p}|i\rangle \approx \sum_{kk'} \langle u_k|\varepsilon\cdot p|u_{k'}\rangle \langle \phi_{fk'}|\phi_{ik}\rangle \quad (5.26)$$

The term  $\langle u_k|\varepsilon\cdot p|u_{k'}\rangle$  is the same for single dot and coupled dots. The solution ( $\phi_k$ ) of the Schrodinger equation for the  $H_{k,p}$  Hamiltonian in the case of coupled dots is different from the solution for the case of a single dot, simply due to the electronic coupling and to the difference in the strain distribution between the two cases. Consequently the overlap term  $\langle \phi_{fk'}|\phi_{ik}\rangle$  for the single dot is different from the overlap term for the coupled dots, and thus the final summation in equation (5.26) is different. The calculations also showed that the conduction-valence band mixing has a very similar effect on  $1s$  and  $1s^+$  states (compare the weight of the envelopes of the  $1s$  state and  $1s^+$  state in Figure 5-46). However the band mixing significantly changes the  $2p^+$  state compared with the  $2p$  state, which can be also be seen in Figure 5-46. From

Figure 5-46 it may be seen that the weights of the first and the fifth envelopes in the  $2p^+$  state are twice those in the  $2p$  state, while the other envelopes have smaller weight. The difference in behaviour between the  $1s$  and  $2p$  state is possibly due to their different symmetry.

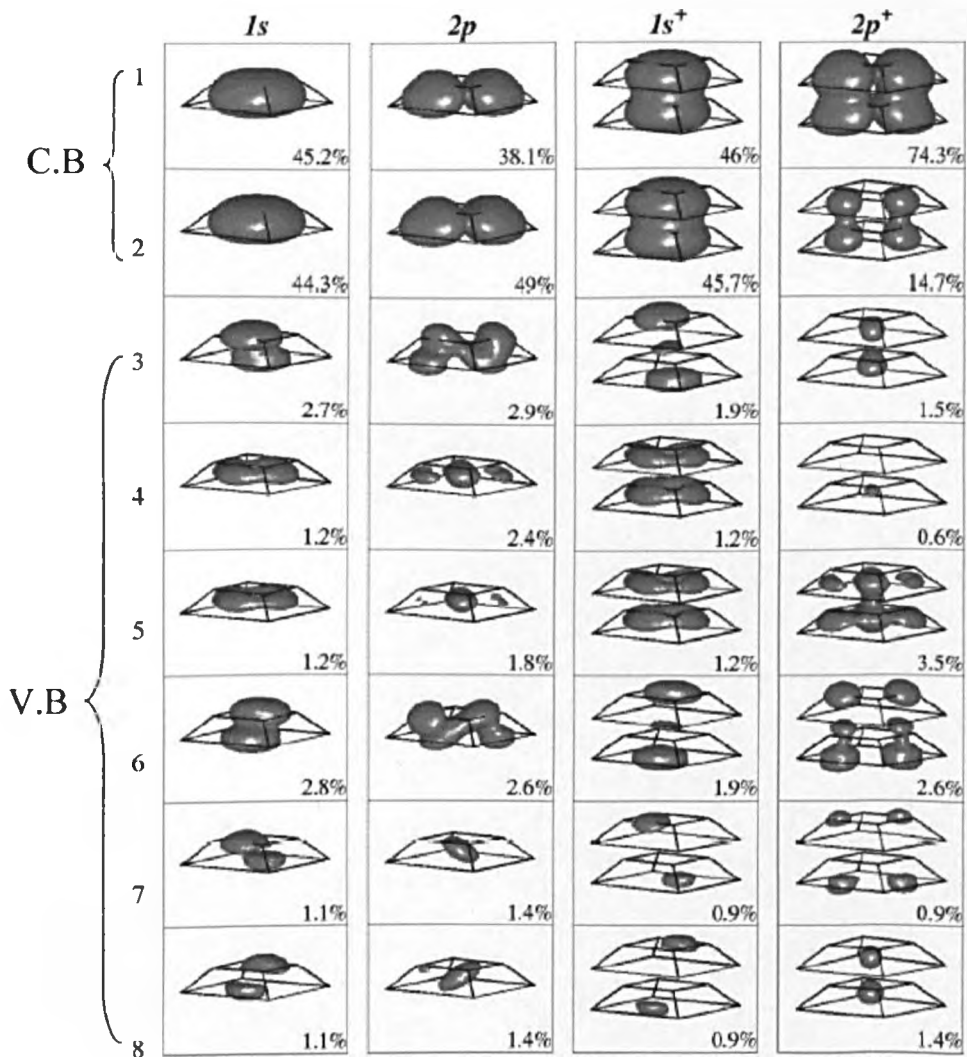


**Figure 5-46** Probability density isosurfaces of the ground  $1s$  states and excited  $2p$  states in single InAs SAQD (left two columns) and stacked coupled InAs SAQD's ( $1s^+$  and  $2p^+$  in right two columns). The first two envelopes belong to the  $s$ -type Bloch functions that originate from the conduction bands and the other six to the  $p$ -type Bloch functions that originate from the valence bands (heavy hole, light hole and spin-orbit hole including spin). Each column shows the decomposition of the wave function into its single envelope components. (Reference 44).

The detailed calculations<sup>45</sup> for the matrix element for the  $1s$ -to- $2p$  transition in single dots showed that most of the overlaps ( $\langle \phi_{jk} | \phi_{ik} \rangle$ ) tend to cancel each other in the summation of equation (5.26). However, in the case of coupled dots some of the overlaps between  $\phi_{ik}$  and  $\phi_{jk}$  that are from conduction bands and valence bands, respectively, are strongly enhanced, increasing the overall summation in equation (5.26) for the transition  $1s^+$ -to- $2p^+$ .

The above procedure can be generalised to calculate the momentum matrix element (equation (5.26)) for transitions between the ground state and some higher excited states such as  $3d$  ( $3d^+$  for coupled dots). Sheng and Leburton<sup>50</sup> have calculated the matrix element for transitions between ground state and very high excited states. Their results indicate that the transitions from ground state ( $1s$ ) to first excited states ( $2p$ ) are two to three times stronger than the transitions from ground state to high states such as  $3d$ . In the case of a single dot they found that the transitions to higher states are polarised in the growth direction (see Figure 5-47a). In contrast, for coupled dots the transitions are stronger for in-plane polarised light (see Figure 5-47b). The difference in the energy position of the transitions in the experimental spectra (Figure 5-44) and the energy position of the transitions in the calculated spectra (Figure 5-47) comes from the difference in the dot size between the experiment and the calculations.

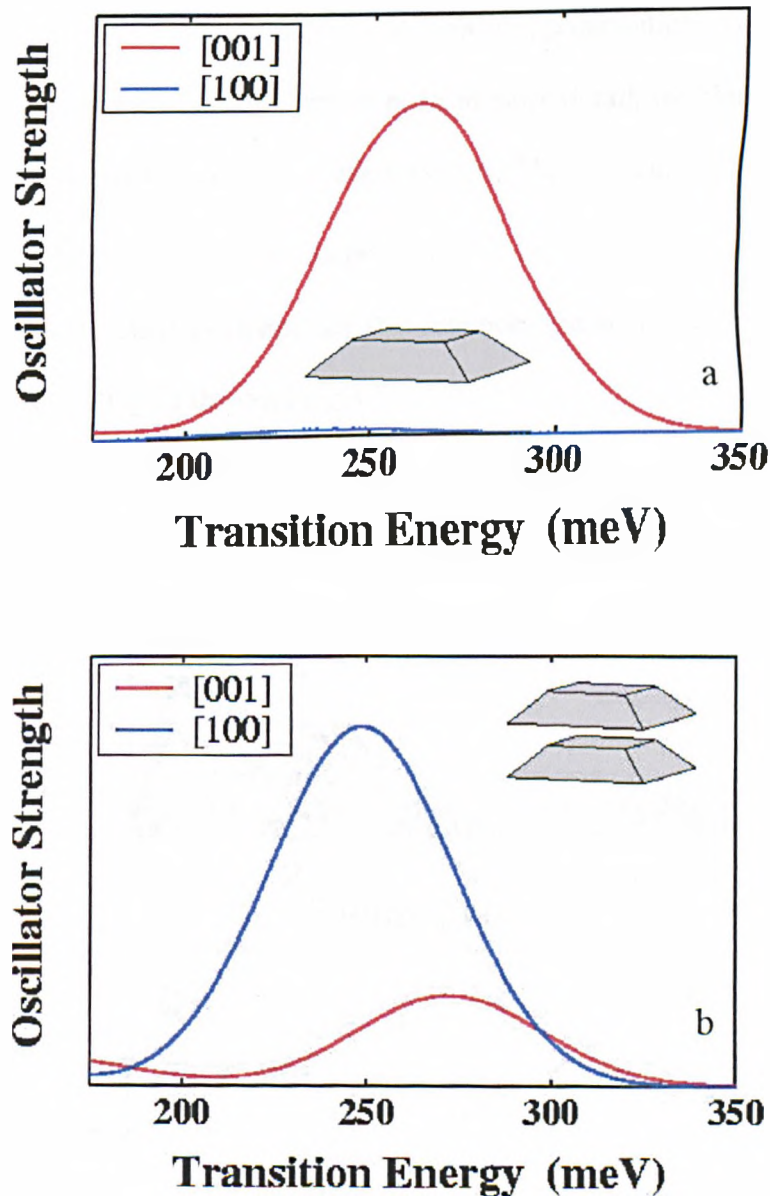
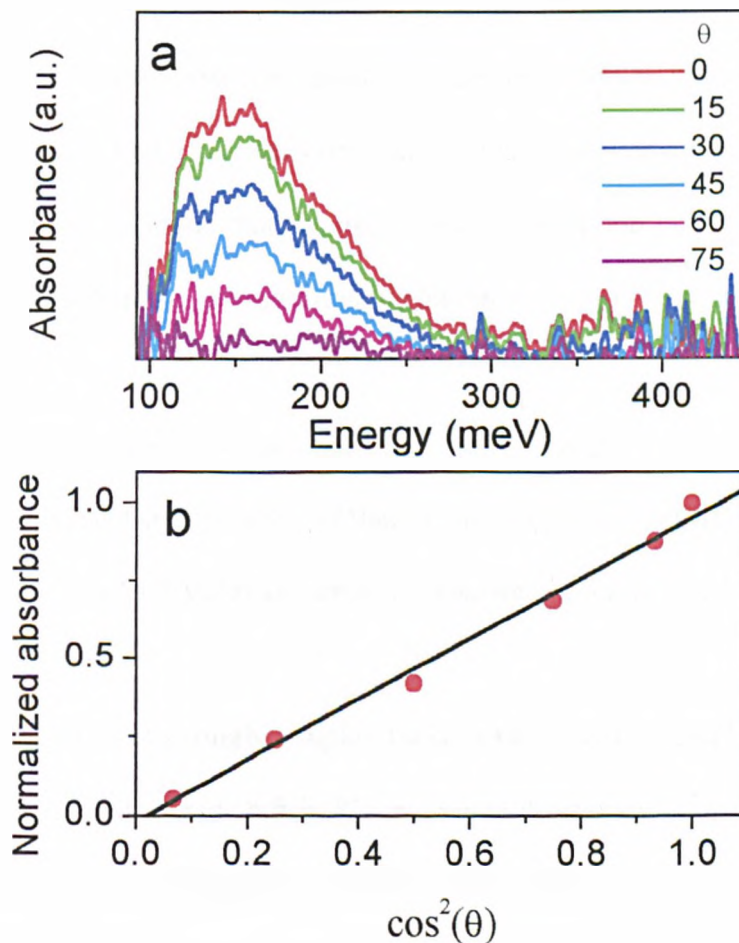


Figure 5-47 Oscillator strength for the optical transitions between ground state and high excited states calculated using the eight band strain dependent  $k,p$  theory for (a) a single dot and two coupled dots (b). [001] represents the growth direction and [100] represents the in-plane direction. (Reference 50)

Figure 5-48a shows the absorption spectra of the coupled dot sample of Figure 5-44b as a function of polarisation angle  $\theta$ , where  $\theta$  is zero for  $s$  polarised light and  $90^\circ$  for  $p$  polarised light. The absorption feature is observed to show strong polarisation dependence in agreement with the results presented in Figure 5-44b and the calculations in Figure 5-47b. As the polarisation angle  $\theta$  increases, the absorption

peak intensity decreases, and disappears for vertical polarisation. To investigate the polarisation dependence of the absorption peak in more detail, we plot in Figure 5-48b the normalised absorption intensity versus  $\cos^2(\theta)$ . The experimental points fit very well to a straight line. The  $\cos^2(\theta)$  dependence of the absorption spectra in Figure 5-48b provides very clear evidence for the enhancement of the in-plane absorption due to vertical coupling of the dot layers.



**Figure 5-48 (a) Polarisation angle ( $\theta$ ) dependence of the absorption spectra from the coupled sample (M2163) at room temperature. (b) Normalised absorption intensity as a function of  $\cos^2(\theta)$  (square), linear fit (full line).**

## 5.8 Conclusions

In conclusion, we have studied intersubband transitions in the conduction band and the valence band of In(Ga)As/GaAs SAQDs using a direct absorption technique and photocurrent spectroscopy. The intersubband transitions have been investigated as a function of polarisation angle and temperature.

The polarisation dependence of the intersubband transitions in the conduction band of isolated SAQDs indicates that the transitions are polarised in the growth direction, similar to quantum wells. By analysing the angular polarisation dependence of the photocurrent signal we found that the intersubband absorption in the growth direction is 6 times stronger than the absorption in the lateral direction.

In contrast to the results from the conduction band, direct absorption measurements and photocurrent spectroscopy showed that the intersubband transitions in the valence band of In(Ga)As/GaAs SAQDs are strongly polarised in the dot plane.

The optical properties of strongly coupled InGaAs/GaAs self assembled quantum dots have been investigated. A red shift in PL spectra peak position is observed due to the coupling of the dots in the vertical direction. Mid-infrared absorption measurements and photocurrent show a strong in-plane absorption feature at 141 meV. This result contrasts with measurements on uncoupled dots, which show intersubband absorption in the growth direction. The experimental results are in good agreement with the eight-band  $\mathbf{k}\cdot\mathbf{p}$  calculations.

The results of intersubband absorption measurements from two strongly coupled InGaAs dots showed a strong enhancement in the in-plane absorption due to the dot

coupling in the vertical direction. Also the absorption and photocurrent measurements from the p-type samples showed strong in-plane intersubband absorption. These results are of significant importance for development of normal incidence infrared photodetectors.

## 5.9 References

- <sup>1</sup> - D. Bimberg, M. Grundmann, and N. N. Ledentsov, *Quantum Dot Heterostructures*, John Wiley and Sons (1998).
- <sup>2</sup> - J.-Y. Marzin, J.-M. Gerard, A. Izrael and D. Barrier, *Phys. Rev. Lett.* **73**, 716 (1994).
- <sup>3</sup> - S. Farfad, R. Leon, D. Lenonard, J. L. Merz and M. Petroff, *Phys. Rev. B* **52**, 5752 (1995).
- <sup>4</sup> - K. H. Schmidt, G. Medeiros-Ribeiro, M. Oestreich, P. M. Petroff and G. H. Dohler, *Phys. Rev. B* **54**, 11 346 (1996).
- <sup>5</sup> - I. E. Itskevich, M. S. Skolnick, D. J. Mowbray, I. A. Trojan, S. G. Lyapin, L. R. Wilson, M. J. Steer, M. Hopkinson, L. Eaves and P. C. Main, *Phys. Rev. B* **60**, R2185 (1999).
- <sup>6</sup> - L. Chu, M. Arzberger, A. Zrenner, G. Bohm and G. Abstreiter, *Appl. Phys. Lett.* **75**, 2247 (1999).
- <sup>7</sup> - P. W. Fry *et al*, *Phys. Rev. Lett.* **84**, 733 (2000).
- <sup>8</sup> - S. Cortez, O. Krebs, P. Voisin and J. M. Gerard, *Phys. Rev. B* **63**, 233306 (2001).
- <sup>9</sup> - Y. Arakawa and S. Sakaki, *Appl. Phys. Lett.* **40**, 939 (1982).
- <sup>10</sup> - G. Yusa and H. Sakaki, *Appl. Phys. Lett.* **70**, 345 (1997).
- <sup>11</sup> - S. Tang, S. Lin and S. Lee, *Appl. Phys. Lett.* **78**, 2428 (2001).
- <sup>12</sup> - S. Sauvage, P. Boucaud, F. H. Julien, J.-M. Gerard and V. Thierry-Mieg, *Appl. Phys. Lett.* **71**, 2785 (1997).
- <sup>13</sup> - S. Maimon, E. Finkman, G. Bahir, S. E. Schacham, J. M. Garica and P. M. Petroff, *Appl. Phys. Lett.* **73**, 2003 (1998).
- <sup>14</sup> - A. Schere, H. G. Craighead, *Appl. Phys. Lett.* **49**, 1284 (1986).
- <sup>15</sup> - M. Grundmann, O. Stier and D. Bimberg, *Phys. Rev. B* **52**, 11969 (1995).
- <sup>16</sup> - O. Stier, M. Grundmann, and D. Bimberg, *Phys. Rev. B* **59**, 5688 (1999).
- <sup>17</sup> - L. W. Wang, J. Kim and A. Zunger, *Phys. Rev. B* **59**, 5678 (1999).
- <sup>18</sup> - A. J. Williamson, L. W. Wang and A. Zunger, *Phys. Rev. B* **62**, 12963 (2000).
- <sup>19</sup> - W. Yang, H. Lee, T. J. Johnson and P. C. Sercel, *Phys. Rev. B* **61**, 2784 (2000).
- <sup>20</sup> - C. Pryor, J. Kim, W. Wang, J. Williamson and A. Zunger, *J. Appl. Phys.* **83**, 2548 (1998).
- <sup>21</sup> - M. A. Cusack, P. R. Briddon and M. Jaros, *Phys. Rev. B* **56**, 4047 (1997).
- <sup>22</sup> - C. G. Van de Walle, *Phys. Rev. B* **39**, 1871 (1989).
- <sup>23</sup> - C. Pryor, *Phys. Rev. B* **57**, 7190 (1998)

- <sup>24</sup> - M. Helm, H. C. Liu, S. D. Gunapala and S. V. Bandara, in Intersubband Transition in Quantum wells: Physics and Device Applications I, edited by H. C. Liu and F. Capasso (Academic Press, 2000).
- <sup>25</sup> - J. H. Davies, The Physics of Low Dimensional Semiconductors, Cambridge University Press (1998).
- <sup>26</sup> S. L. Chuang, Physics of Optoelectronic Devices, John Wiley and Sons, 1995.
- <sup>27</sup> - F. Szmulowicz and G. Brown, Phys. Rev. B **51**, 13203 (1995).
- <sup>28</sup> - A short introduction to FT-IR, Bruker Optik.
- <sup>29</sup> - D. Pan, E. Towe and S. Kennerly, Appl. Phys. Lett. **73**, 1937 (1998).
- <sup>30</sup> - I. Mukhametzhanov, Z. H. Chen, O. Baklenov, E. T. Kim and A. Madhukar, Phys. Stat. Sol. (b) **224**, 697 (2001).
- <sup>31</sup> - L. Chu, A. Zrenner, G. Bohm and G. Abstreiter, Appl. Phys. Lett. **75**, 3599 (1999).
- <sup>32</sup> -S. Sauvage, P. Boucaud, V. Immer, E. Finkman and, J.-M. Gerard, Appl. Phys. Lett. **78**, 2327 (2001).
- <sup>33</sup> - L. Chu, A. Zrenner, G. Bohm and G. Abstreiter, Appl. Phys. Lett. **76**, 1944 (2000).
- <sup>34</sup> - S. Sauvage, P. Boucaud, J.-M. Gerard and V. Thierry-Mieg, J. Appl. Phys. **84**, 4356 (1998).
- <sup>35</sup> - S. Sauvage, P. Boucaud, F. H. Julien, J.-M. Gerard J.-Y, Marzin, J. Appl. Phys. **82**, 3396 (1997).
- <sup>36</sup> - S. Sauvage, P. Boucaud, J.-M. Gerard, and V. Thierry-Mieg, Phys. Rev. B **58**, 10562 (1998).
- <sup>37</sup> - Y. C. Chang and R. B. James, Phys. Rev. B **39**, 12672 (1989).
- <sup>38</sup> - B. F. Levine, S. D. Gunapala, J. M. Kuo, S. S. Pei and S. Hui, Appl. Phys. Lett. **59**, 1864 (1991).
- <sup>39</sup> - H. C. Liu, F. Szmulowicz, Z. R. Wasilewski, M. Buchanan and B. J. Brown, J. Appl. Phys. **85**, 2972 (1999).
- <sup>40</sup> - S W da Silvay, Yu A PusepZ, J C GalzeraniZ, D I LubyshevY, P P Gonz'alez-BorreroY and P Basmajiy, J. Phys.: Condens. Matter **9**, L13 (1997).
- <sup>41</sup> -Weidong Sheng and Jean-Pierre Leburton, Phys. Rev. B **63**, 161301-1, (2001).
- <sup>42</sup> - S. Adachi, Physical properties of III-V semiconductor compounds: InP, InAs, GaAs, GaP, InGaAs, and InGaAsP, New York; Chichester : Wiley, 1992.
- <sup>43</sup> - Shu-Shen Li and Jian-Bai Xia, Phys. Rev. B **55**, 15 434 (1997).

- 
- <sup>44</sup> - W. Sheng and J. P. Leburton, Phys. Rev. B **64**, 153302-1 (2001).
- <sup>45</sup> - M. A. Migliorato, L. R. Wilson, D. J. Mowbray, M. S. Skolnick, M. Al-Khafaji, A. G. Cullis and M. Hopkinson, J. Appl. Phys., **90**, 6374 (2001).
- <sup>46</sup> - L. R. C. Fonseca, J. L. Jimenez, and J. P. Leburton, Phys. Rev. B **58**, 9955 (1998).
- <sup>47</sup> G. S. Solomon, J. A. Trezza, A. F. Marshall, and J. S. Harris, Jr. Phys. Rev. Lett. **76**,952 (1996).
- <sup>48</sup> - W. Sheng and J. P. Leburton, Appl. Phys. Lett. **78**, 1258 (2001).
- <sup>49</sup> - Hongtao Jiang and Jasprit Singh, Appl. Phys. Lett. **71**, 3239 (1997).
- <sup>50</sup> - W. Sheng and J. P. Leburton, Private communication.

## Chapter 6

### Future Work

In the first part of this thesis, the optical properties of three dimensional opal photonic crystals were investigated. The results showed that opals are polycrystalline materials consisting of misoriented domains. The form of the transmission stop band in this type of photonic crystals was shown to be determined by the diffraction and scattering events that occur in the polycrystalline structures. The key to improve the optical properties of opal photonic crystals lies in improving the structural quality of this type of photonic crystal. Better structural quality can be achieved by improving the growth method by either (i) growing the samples on a patterned substrate, (ii) growing the samples on a vertical substrate, (iii) implementing an electric field or temperature gradient to control the sedimentation speed. The results of chapter 4 showed that infiltration of the opal with high refractive index chalcogenide glasses is possible. The infiltration method used in this work can be improved by repeating the infiltration procedure several times or by performing the infiltration at higher temperature to improve the size of the infiltrated area and the infiltration ratio.

In the second part of this thesis the intersubband optical selection rules in the conduction band of uncoupled and strongly coupled In(Ga)As/GaAs quantum dots and also in the valence band of In(Ga)As/GaAs dots were investigated. By strongly coupling quantum dots in the growth direction (10 Å spacer between the dots) we achieved a reversal of the mid-infrared intersubband selection rule for optical transitions between conduction band states, compared with that observed for uncoupled dots. However, in this work only the two extreme cases, uncoupled dots

and strongly coupled dots, were investigated. As future work the intersubband selection rule for optical transitions in the conduction band of In(Ga)As self assembled quantum dots will be investigated as a function of the spacer thickness between the dots. This study allows us to understand how the electronic coupling influences the intersubband selection rules in the conduction band of In(Ga)As dots. Also to understand the influence of size and shape of the upper dot on the intersubband transitions and their selection rule, intersubband transitions in the conduction band will be investigated as a function of the number of monolayers deposited during the growth of the upper dot. The large  $s$  polarised absorption from the strongly coupled dots suggests their suitability for use in high efficiency, normal incidence infrared photodetectors. Additional future work will involve designing and studying normal incidence infrared photodetectors using coupled quantum dots.